Investigation Of Optical Beam Shifts For Two-Dimensional (2D) Materials

A thesis submitted for the award of the degree of

Doctor of Philosophy

in

Physics (Experimental)

by

Akash Das

Department of Physics

University of Calcutta

Kolkata, India

December 2021

Dedicated to my Parents and Teachers…

"Around here, however, we don't
look backwards for very long.
We keep moving forward, opening up new doors and
doing new things, because we're curious
and curiosity keeps leading us down new paths."

- Walt Disney

Acknowledgement:

It has been five memorable years of my Ph.D. here at S. N. Bose National Centre for Basic Sciences, and now is the time to submit my thesis. I was never alone in this, and I would like to take this opportunity to acknowledge and thank the people without whom this thesis would not have been possible.

First and foremost, I want to express my deepest gratitude to my thesis supervisor for his inspiring guidance, continuous motivation, and invaluable instructions for my research. His patience and encouragement through the ups and downs during these years were the major impetus for me to forge ahead. In the last five years, he has enriched me with a gulf of self-confidence and optimism that has done wonders not only in my research activity but also in my personal life. I also pay my heartfelt respect to Prof. Akhlesh Lakhtakia and Prof. Mark Horn (Pennsylvania State University, USA) for guiding me towards a new direction in my research. Their active collaboration and suggestions have helped me a lot in the later stages of my research.

I owe much, perhaps most, to my teachers in the dawn of my study in science. I am privileged to have a science teacher like Sajahan Babu (Sk. Sajahan) at my early school days who not only ignited my interest in science but also taught me the basic morality and ethics of life. I am also thankful to my English teacher Ramesh Babu (Ramesh Pal) who valued lively reasoning and scientific thinking above pedagogy. I can't forget the contribution of my Biology tutor Sampad Da (Susanta Kunkry) who has always boosted up my confidence and inspired me to be a researcher. My Maths tutor Kashi babu (Kashinath Ghosh) was the first who had suggested to pursue my career in Physics with a goal to be a researcher. I also pay my respect to our beloved college teacher P.S. sir (Dr. Prasenjit Sarkar, Serampore College) who thoroughly addressed my queries and thereby introduced me to a systematic approach for seeking an answer. I also thank my B.Sc. teacher Sattar Da (Abdus Sattar) without whom such a lucid understanding of Physics would not have been possible. I also owe my heartfelt respect to Prof. Debnarayan Jana (University of Calcutta) who largely guided me in the beginning my research career and is still helping me in my academia and beyond. I am really fortunate to have found such good teachers in my academic journey. I cannot dare thank them, nor their debts to be repaid. But these memories that irreversibly shaped my evolution continue to push me to try to become a student worthy of such rare teachers.

I am thankful to my junior lab mates Biswajit, Ardhendu, Soumen, Manik, Swarnabha, Sayoni, Debatri for keeping this group vibrant and making the work enjoyable. Soumen (Mandal) has especially helped me a lot in my final two projects with his tireless data taking. During my initial days, I was fortunate to have seniors like Suman Som, Gourab Datta Banik, Chiranjit Ghosh, Abhijit Maity, Mithun Pal, Santanu Mandal, Sanchi Maithani who have always provided me with a homely feeling. In my final days, I was privileged to come across seniors like Arpan Da, Saptarshi Da, Pushpendu Da, and Joyita Di who were always helpful. I share a special relation with Suman Da who has always shared his knowledge, motivated me to do better, and listened to all my academic and non-academic views, mistakes, and non-sense talks all through these years like an elder brother.

Apart from my lab mates, I have spent a delightful five-year journey at S. N. Bose Institute with some charming friends without whom the life here would have been dull and boring, hence, I thank Sudipta, Sayan (Routh), Saikat, Sasthi, Koushik, Sayan (Pal), Dipanjan, Ikbal, Samrat, Anuvab, Khata, Supriyo Da, and Sankar Da. I cannot ever forget the night walks with Saikat (Pal) and Sayan (Routh) with all types of discussions that freed up the mind at the end of the tiring days. The ordinary expression of thanks does not suffice, for the unequivocal support and affection that I have received from Sudipta Chatterjee. He is the '*friend, philosopher and guide*' who is always there to listen to me and with whom I have spent a plethora of unforgettable moments both inside and outside our campus.

I am blessed with many loving and caring friends. I must thank my college friends Subhajit, Suman (Kundu), Snehasish with whom I still share a very special connection. How can I forget my IITKGP (Kharagpur) friends who have enriched me with the nicest memories? I am indebted to my KGP buddies, especially Aritra, Chinmoy, Satyajit, Dibyendu Da, Monodeep Da, Snehasish, Ambaresh, Mendel (Suman), Abhijit, Abinash, Pratap, Narayan Da, Swagata Da, Krishno Da, Debanjan Da, Suman (Chatterjee) Da, Soumya Da, Siddhartha Da and many more (sincere apologies if I forgot to mention anyone). I must acknowledge some of my close and old school mates Surajit, Pritam, Dipannita, Ranajit, and Sourav. I also thank my village friends Toton, Papai, Soumya, Pradip, Bittu, Pallab, and Niharendu who have given me many cherishable moments back at my home and enriched my life with a pool of happiness. Thank you all for the unforgettable time together. It is really difficult to express my deepest thanks and the appreciation I feel toward all of you.

I also acknowledge the influence of several books that have altered my thinking a lot. I specially mention two books '*God Talks with Arjuna: The Bhagavad Gita*' by Sri Paramahansa Yogananda and '*Man's Search for Meaning*' by Dr. Viktor Frankl that have helped me tremendously in my difficult times. This five-year journey would not have been so smooth without the much needed entertainment that I found in watching football and hence, I also acknowledge the '*Real Madrid Football Club*' that has always kept me fresh and entertained.

Being a very lucky person, I was born in such a caring and supportive family. No words can describe the influence of the '*guardian angels*' in my life - my parents. All my achievements belong to my parents who had to go through a lot of struggles and sacrifices to make me what I am now. I have also received never-ending support, love and care from my maternal uncles (Chotomama and Boromama) and grandparents (Dadu and Dida). A warm thanks go to my 'Chotomama' (Sukalyan Das) who was my second teacher after my mother. And my 'Boromama' (Surajit Das) was always my go-to friend since my childhood days. I am also thankful to my Dadu and Dida for their love, care, and blessings.

I would like to acknowledge University Grant Commission (India) for providing me doctoral fellowship and S. N. Bose National Centre for Basic Sciences for giving me an opportunity to work. I acknowledge the wonderful students mess, institute canteen, the cooking team, library members, the vulnerable group-D staffs, and the security staffs, who without recognition worked hard to make our life in the campus healthy, habitable, actually a clean, beautiful and safe one.

Finally, I want to thank almighty God for holding my hand in the ups and downs of my life all through this wonderful journey.

Preface:

A light beam with a finite transverse extent suffers diffractive corrections and may indicate subtle deviations from the prediction of geometrical optics. Unlike plane waves, a finite beam of light may undergo longitudinal (in the plane of incidence) and transverse (perpendicular to the plane of incidence) shifts, which are known as Goos-Hänchen (GH) and Imbert-Fedorov (IF) shifts, respectively. Such shifts may manifest as spatial displacement or angular deflection depending upon the nature of interaction.

Optical beam shifts have created a lot of interest in modern research lately. Using this wavelength scale phenomenon advanced optoelectronic devices and sensors are being proposed and subsequently entering into the real domain. In contemporary research, it is becoming more and more essential to investigate the details of the interaction of light and any physical surfaces. In this thesis, we will show the importance of this interaction. Depending upon the surface of interaction optical beam shifts can behave entirely in a different way. We have demonstrated the behaviour of the longitudinal (GH) and transverse (IF) shifts after reflection from a 2D material interface. The location of maximum and minimum shift is of utmost importance before going to apply this phenomenon for technological purposes. Tuning this optical shift gives us extra freedom to work with. Besides the surface of interaction, the optical beam shift can be controlled by the wavelength of the incident light, mode of polarization, angle of incidence as will be described in detail in this thesis.

In recent years, the advancement of science and technology has generated immense curiosity in layered materials. A whole new branch of two-dimensional (2D) materials has emerged in the community. There are several members in 2D materials such as graphene, transition metal di-chalcogenides (TMDC) and more are being added day by day. Due to their inherent properties, TMDCs show a lot of interesting phenomena like charge density waves, magnetism, and superconductivity making them a focus of the research community. Molybdenum disulphide (MoS_2) is one of the most studied TMDCs which have great potential in nano-electronics and optoelectronics. Keeping in mind the importance of 2D materials in optics and optical applications, we have chosen them as the basic system to study optical beam shift both theoretically and experimentally.

Chapter 1 starts with the basic introduction to the phenomena of the optical beam shift. Different types of the optical beam shifts, their cause of occurrence and related controversy, their application areas and difficulty in the experimental measurement are discussed in detail.

Additionally, the characteristic details of 2D materials, different types of 2D materials, their synthesis process, and field of application are also demonstrated.

In Chapter 2, we start with a theoretical calculation of the Goos-Hänchen shift in MoS_2. A general model is proposed to calculate the GH shifts in monolayer MoS_2 coated surfaces for the reflection of a Gaussian light beam. The GH shift is conventionally found for total internally reflected light. But, in this *Chapter*, we theoretically invent non-zero GH shift for both partially reflected and total internally reflected light. Our findings discovered the existence of giant spatial GH shift in monolayer MoS_2. This giant shift which is attributed to its surface optical conductivity. Also, the uncommon behaviour of GH shift near Brewster's and the critical angle is confirmed and explained.

Chapter 3 describes the more general Transfer Matrix Method approach for determining longitudinal Goos-Hänchen and transverse Imbert-Fedorov shifts in different transition metal di-chalcogenides (TMDCs). By considering a dielectric slab coated with a monolayer of TMDCs, we theoretically examine the influence of different TMDC monolayers on the GH & IF shifts. For total internally reflected beam giant negative GH shifts are reported. The role of the complex surface conductivity of TMDC monolayers on optical beam shift response is also described. We have also studied the difference in the optical beam shift nature in the bulk sample compared to the monolayers.

In Chapter 4, we calculate the GH and IF shifts for fundamental Gaussian beam of differing wavelengths (400-1300 nm) reflected from graphene-coated dielectric surface. The GH and IF shifts turn out to be extremely dependent upon the chemical potential of graphene along with the wavelength of the incident light, thus enabling one to appropriately choose the operating wavelength and tune the chemical potential in the desired region to obtain maximum beam shifts in graphene.

Chapter 5 deals with the conventional ways of experimental determination of the GH and IF shifts. The typical difficulties associated with the optical beam shift measurements are pointed out. Different techniques with their corresponding advantages and disadvantages are discussed in detail.

In Chapter 6, we discuss the development of quantum weak measurement technique to determine the Goos-Hänchen shift for the total internal reflection of a Gaussian beam from a glass prism. The condition to achieve maximum GH shift is established. GH shift is also dependent on the incident angle with maximum shift adjacent to critical angle.

Chapter 7 describes the effective way of applying quantum weak measurement technique for the measurement of the GH shift in monolayer MoS_2. The unusual behaviour in the neighbourhood of the critical angle is well-explained. The critical angle also gets slightly shifted in presence of monolayer MoS_2. A comparison of GH shift between monolayer MoS_2 and graphene-coated prism is also demonstrated in this Chapter.

In Chapter 8, transverse IF shift is determined experimentally in monolayer MoS_2 with modified quantum weak measurement technique. The theoretical formulation along with the experimental details is explained making it a very general method for the measurement of beam shift in any layered materials. The special characteristics of the IF shift for different incident polarization states are elaborated.

In Chapter 9, we have described the development of another simple indirect time-effective technique for prompt measurement of GH and IF shift. Using this Stokes Polarimetric method, the nature of GH & IF shift for different states of polarized light is thoroughly discussed.

Chapter 10 deals with a very new phenomenon of the photonic spin Hall effect that has attracted a lot of attention lately. Monolayer MoS_2 system deposited upon Si/SiO_2 substrate is found to be a good candidate showing non-trivial photonic spin Hall effect. A connection to the non-zero geometric curvature is also suggested from the zero-crossing of the spin Hall shifts.

List of Abbreviations:

2D	: Two-Dimensional
3D	: Three-Dimensional
TMDC	: Transition Metal Di-chalcogenides
GH	: Goos-Hänchen
IF	: Imbert-Fedorov
PSHS	: Photonic Spin Hall Shift
PSHE	: Photonic Spin Hall Effect
PR	: Partial Reflection
TIR	: Total Internal Reflection
ML	: Monolayer
QWM	: Quantum Weak Measurement
WVA	: Weak Value Amplification
BSS	: Beam Splitter Scanning
SP	: Stokes Polarimetry
HWP	: Half-wave Plate
QWP	: Quarter-wave Plate
GLP	: Glan-Thompson Linear Polarizer
BP	: Beam Profiler
L1 / L2	: Plano-convex lens

List of Symbols:

Δ_{GH}	: Spatial GH Shift
Θ_{GH}	: Angular GH Shift
Δ_{IF}	: Spatial IF Shift
Θ_{IF}	: Angular IF Shift
θ	: Angle of incidence / Incident angle
n	: Refractive index
ω	: Frequency of incident light
λ	: Wavelength of incident light
σ	: Complex surface optical conductivity
ε	: Angle of deviation / rotation from exact orthogonality
α	: Pre-selection angle
β	: Post-selection angle
δ	: Relative phase difference between P & S components
η	: Initial phase difference between P & S components
r	: Complex Fresnel reflection coefficient
R	: Amplitude of the reflection coefficient
ϕ	: Phase of the reflection coefficients
Ψ	: Wave function representing the electric field of light
ω_0	: Beam waist
S_0, S_1, S_2, S_3	: Stokes Parameters
y^{λ}	: Spin Hall shift for $\lambda(p,s)$ polarization

List of Publications:

[1] **A. Das** and M. Pradhan, "Goos-Hänchen shift for Gaussian beams impinging on monolayer-MoS_2-coated surfaces," **Journal of the Optical Society of America B** 35 (8), 1956-1962 (2018).

[2] **A. Das** and M. Pradhan, "Exploring the optical beam shifts in monolayers of transition metal dichalcogenides using Gaussian beams," **Optics Communications** 437, 312-320 (2019).

[3] **A. Das** and M. Pradhan, "Quantum weak measurement of Goos-Hänchen effect of light in total internal reflection using a Gaussian-mode laser beam," **Laser Physics Letters** 17 (6), 066001 (2020).

[4] **A. Das** and M. Pradhan, "Investigation of the optical beam shifts for monolayer MoS_2 using polarimetric technique," **Journal of Optics** 22 (10), 105004 (2020).

[5] **A. Das** and M. Pradhan, "Wavelength and chemical potential dependence of optical beam shifts in graphene," **Journal of Modern Optics** 68 (3), 146-152 (2021).

[6] **A. Das** and M. Pradhan, "Quantum weak measurement of Goos-Hänchen shift in monolayer MoS_2," **Journal of the Optical Society of America B** 38 (2), 387-391 (2021).

[7] **A. Das**, S. Mandal and M. Pradhan, "Observation of Imbert-Fedorov shift in monolayer MoS_2 via quantum weak measurement," **Optics Letters** 46 (23), 5826-5829 (2021).

[8] **A. Das**, S. Mandal and M. Pradhan, "Photonic signature of spin Hall shift in monolayer MoS_2 via quantum weak measurement" (**Under Review**)

Table of Contents

Section-A: Theoretical Study

Section-B: Experimental Investigation

Chapter 1 Optical Beam Shifts & 2D-Materials

This introductory Chapter consists of a detailed literature review of various works that motivated me to start my investigation in this particular field and also a brief outline of the entire work done in this thesis.

1 Optical Beam Shifts & 2D-Materials

1.1 Introduction

We will discuss the nature of optical beam shifts, their cause of generation, different types, controlling parameters, and applications in different areas of modern research.

1.1.1 Laws of reflection

The Ancient Greek mathematician Euclid was the first to describe the law of reflection long ago in about 300 BCE. We are already well aware of it since our school days. We can summarise them as follows:

(a) The incident ray, the reflected ray, and the normal to the reflecting surface at the point of the incidence lie in the same plane.

(b) The angle which the incident ray makes (angle of incidence) with the normal is equal to the angle which the reflected ray makes to the same normal (angle of reflection).

There are different types of reflection such as:

(*i*) Specular reflection (mirror-like),

(*ii*) Diffuse reflection (light is scattered away in different directions),

(*iii*) Retro reflection (light returns in the direction from which it came),

(*iv*) Multiple reflections (presence of multiple mirrors), and

(*v*) Complex conjugate reflection (non-linear optical process).

The inherent reason for the reflection of light lies in Maxwell's equations as light is an electromagnetic wave. As the light wave is incident upon a material surface, it induces oscillation of the electrons which generates polarization of atom. These oscillating electrons re-radiate secondary wavelets in all directions. Following the *Huygens-Fresnel principle*, all these secondary waves superimpose to give rise to reflection and refraction phenomena.

1.1.2 Laws of refraction

The Roman astronomer Ptolemy first tried to experimentally derive the law of refraction in the 2nd century CE. But he only predicted that the angle of refraction is proportional to the angle of incidence. The Iraqi mathematician Ibn Sahl discovered the full law of refraction. Sahl showed that the angle of incidence is related to the angle of refraction using the law of sines. Later, the Dutch mathematician Snellius (1621) and the French philosopher Rene Descartes (1637) rediscovered and originally formulated the law, independently. The law states that:

In case of two different media, the ratio of the sines of the angle of incidence (θ_i) and angle of refraction / transmission (θ_t) is constant and is equal to the ratio of phase velocities (v_1/v_2) in the two media, or equivalently, to the indices of refraction (n_2/n_1) of the two media.

$$\frac{\sin\theta_1}{\sin\theta_2} = \frac{v_1}{v_2} = \frac{n_2}{n_1} \tag{1.1}$$

This is popularly known as *Snell's Law*.

The primary cause of refraction is the difference in light speed in two different media. This change in light speed as it refracts from one medium to another causes the light to bend.

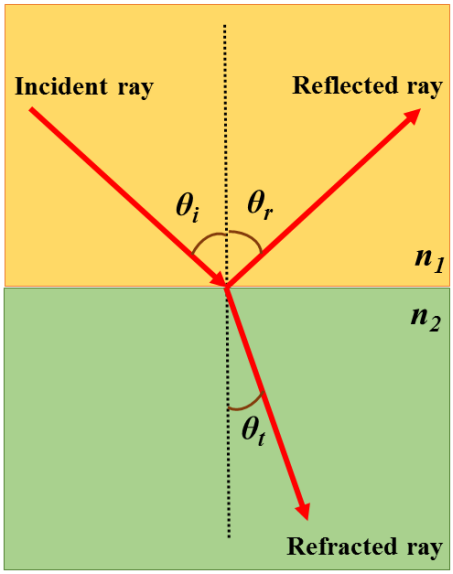

Figure 1.1. Laws of reflection and refraction for two media having refractive indices n_1 & n_2 .

1.2 Optical beam shift

The celebrated laws of reflection and refraction provide the geometrical optics picture of light evolution. The situation becomes complex for a real optical beam with a definite distribution of plane wave spectrum i.e. real light beam with finite transverse extent. There is a finite departure from the geometrical optics picture of the light beam if we look at the wavelength scale [1]. The reflected and/or refracted beam undergoes a non-zero shift from the position predicted by the common geometrical optics picture. In general, these shifts can be classified into two different categories. The shift longitudinal or parallel to the plane of incidence is called *Goos-Hänchen* (GH) shift [2], and the corresponding transverse or out of plane shift is termed *Imbert-Fedorov* (IF) shift [3,4]. Both of these shifts can also manifest as spatial (lateral or longitudinal displacements) and angular (angular deflections) [5] forms. There is also a transverse *Photonic spin Hall* (PSH) shift of the beam [6], but it has close similarity with the Imbert-Fedorov shift (discussed later in detail).

Different types of optical beam shifts can be pictorially demonstrated as shown in Figure 1.2 below. It turns out that these beam shifts (GH and IF) are present in almost all optical systems.

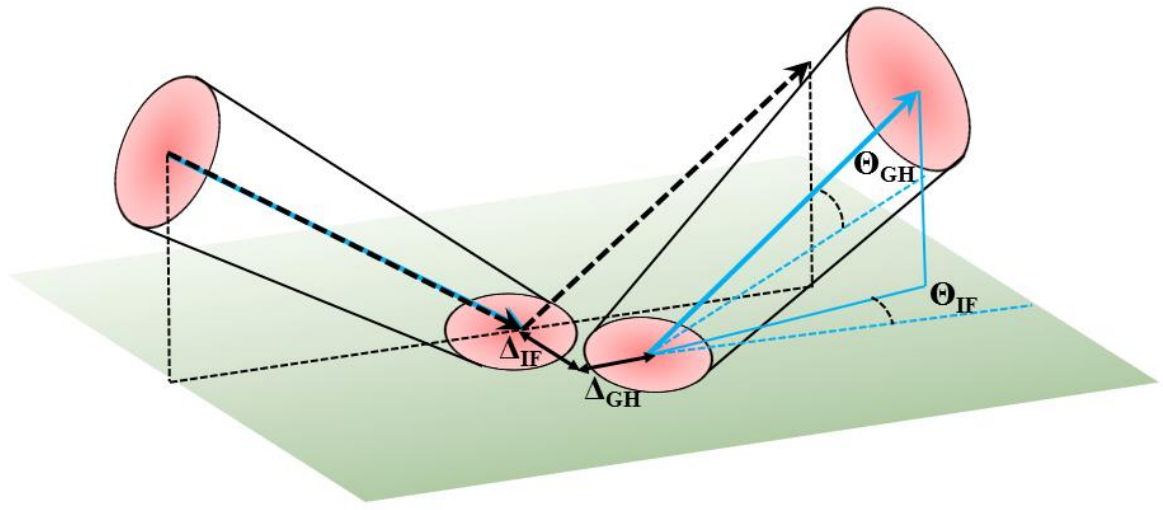

Figure 1.2. Pictorial representation of the Goos-Hänchen (GH) and Imbert-Fedorov (IF) shifts, both spatial (**Δ**) and angular (**Θ**) shifts are shown explicitly.

1.2.1 Goos-Hänchen shift

Newton first predicted the occurrence of the shift in reflection of a light beam in his famous book '*Opticks*' (1704). He presented a theoretical basis as well as experimental proof for the penetration of light into the second medium in case of total internal reflection of light between two media of different refractive indices. Nevertheless, Newton's picture is based on the mechanical model only. But German astronomer Fritz Goos with his Ph.D. student Hilda Hänchen (1947) first discovered experimentally that this in-plane (longitudinal) shift is linked with the wave nature of the radiation field [2]. Actually, any form of wave-like phenomena can be associated with the occurrence of the Goos-Hänchen effect. Motivated by their experimental investigation, Artmann (1948) and Fragstein (1949) published the first theoretical model [7]. Lateral shifts were first calculated in their work, with different shifts predicted for electric field polarization parallel to or perpendicular to the plane of incidence. Since then, the field of Goos-Hänchen effect has continued its evolution and created immense interest in modern research.

1.2.2 Imbert-Fedorov shift

After the invention of the GH shift, Soviet physicist Fedor Fedorov [4] (1955) first pointed out that during total internal reflection, the time-averaged Poynting vector in the evanescent wave has a component perpendicular to the plane of incidence in the lower refractive index medium. Hence, a transverse (out of plane) shift of the beam is also expected. Later, French scientist Cristian Imbert experimentally observed such transverse shifts. Applying Renard's energy flux conservation [8], a mathematical expression of such transverse shifts was also derived by Imbert subsequently. The proposed theory of Imbert follows the same assumptions as considered in the case of longitudinal shift. The Imbert-Fedorov (IF) shift is also found to be dependent upon the polarization state of the incident light beam. Imbert derived the following expression for the transverse shift for the simple case of the incident circular polarized beam.

$$y_T = \pm\left(\frac{\lambda}{\pi}\right)\left(\frac{1}{1-n^2}\right)\left(\frac{sin^3\theta\, cos\theta}{sin^2\theta - n^2 cos^2\theta}\right) \tag{1.2}$$

Here (+) & (-) signs stand for the right and left circularly polarized beam, λ is the wavelength of the incident beam.

1.3 Cause of the optical beam shift

As pointed earlier, the spatial Goos-Hänchen (GH) & Imbert-Fedorov (IF) shifts were originally discovered in the case of total internal reflection of light beam [2,3,9,10]. Both of

these effects are dependent on the polarization states of the light. The eigenmodes of the GH shift are the horizontal or P (or Transverse magnetic field) and vertical or S (or Transverse electric field) linearly polarized light beam. Whereas the eigenmodes of the IF shift are given by elliptically or circularly polarized light beams. A few years later, evidence of angular shifts was also found [11-14] for partial reflection and refraction of the light beam.

The authors dealing with this topic were divided into two theoretical classes at that time, firstly the stationary phase approximation method and secondly, energy flux conservation method. Both of these approaches produce almost identical results for longitudinal shift (GH) at angles of incidence surrounding the critical angle of incidence (θ_C). Unfortunately, both treatments give rise to different results for transverse (IF) shifts at all angles of incidence. At that time, experimental limitations allowed them to measure the shifts in the vicinity of the critical angle of incidence only. Hence, a lot of controversies were there for the proper explanation of the optical beam shift. But, with experimental advances, gradually results for a larger range of angles of incidence were found out, and proper explanation of the GH & IF shifts became feasible. Here, we would not go to the detailed mathematics for the origin of optical beam shifts, but explain only the physical mechanism behind these phenomena.

1.3.1 Cause of GH shift

The first concrete theoretical evidence of the Goos-Hänchen shift in total internal reflection came from Artman (1948) [7], who used stationary phase treatment, and from von Fragstein (1949) [15], who used the energy flux conservation principle. Later Schilling (1956) [16] modified and extended Artmann's model of Stationary phase approximation. Subsequently, Renard, Onoda, Yasumoto [8,17,18] modified the energy flux conservation model and tried to remedy the inconsistencies associated with the theory.

In the energy flux conservation approach, the time-averaged Poynting vector in the evanescent wave above a totally reflecting surface acquires a finite non-zero value. Figure 1.3 shows pictorially the concept of energy flux conservation. The center of the reflected beam is denoted by O. The reflected beam is displaced from the incident beam by distance *d*. Across the OB plane, an energy flux crossing takes place. Since the incident and reflected beam has the identical intensity in the total internal reflection, mathematically it can be proved by applying the energy conservation principle that this energy flux crossing is only allowed if the reflected beam is displaced from the position predicted by the geometrical optics, leaving a downward flux component of the incident beam. This downward component is not

compensated by the upward flux component of the reflected beam through the COD plane. It is argued that this flux difference is carried by the strip (having width *d*) near the incident beam center. By conservation principle, it should be equal to the energy flux across the OB carried by the evanescent wave.

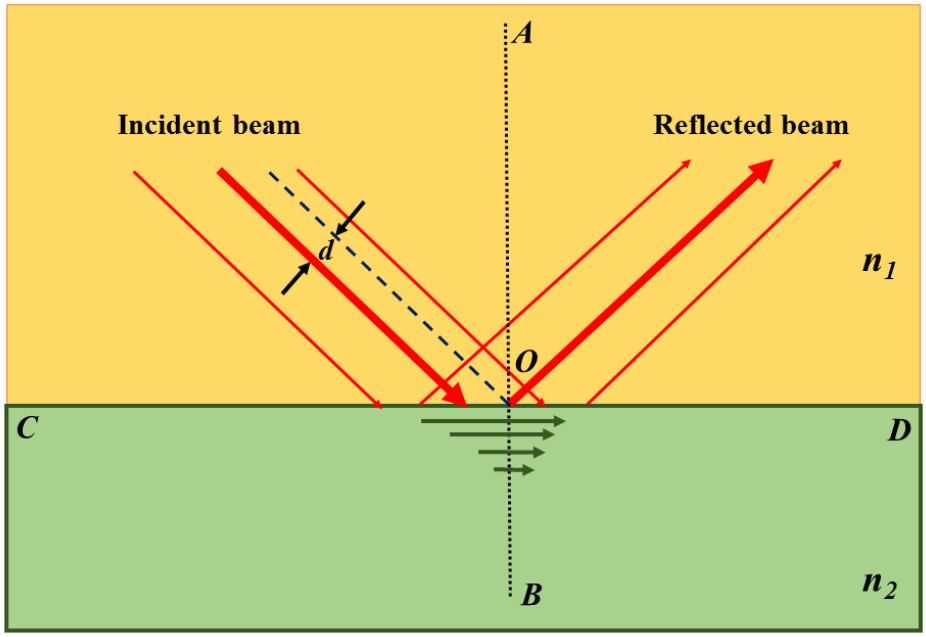

Figure 1.3. The beam is displaced for the requirement of the energy conservation principle.

Applying the above concept general expressions of the GH shift for the P & S wave can be derived:

$$d_S = \left(\frac{\lambda}{\pi}\right)\left(\frac{1}{1-n^2}\right)\left(\frac{\sin\theta\cos^2\theta}{\sqrt{\sin^2\theta - n^2}}\right) \tag{1.4}$$

$$d_P = \left(\frac{\lambda}{\pi}\right)\left(\frac{1}{1-n^2}\right)\left(\frac{\sin\theta\cos^2\theta}{\sqrt{\sin^2\theta - n^2}}\right)\left(\frac{n^2}{\sin^2\theta - n^2\cos^2\theta}\right) \tag{1.5}$$

Artmann was mainly interested in the behaviour of the GH shift in close proximity of critical angles. In the stationary phase approximation treatment, the fundamental principle is the decomposition of the light beam with finite transverse extent into a group of plane wave components. A plane wave has a definite *k* vector. But, for a finite light beam (having finite transverse width), the electromagnetic field consists of a group of plane wave components.

These plane wave components form an envelope in the momentum space. Each of these components suffers reflection discretely according to the laws of specular reflection. Hence, for total internal reflections at any point in the reflecting interface, the phase relationships in the reflected ensemble of plane waves are not the same as those in the incident ensemble. By adding up each of these plane wave components of the ensemble gives rise to the reflected beam centroid.

Mathematically, the theoretical expressions of the GH shift for the incident linearly S and P polarized beam can be derived:

$$d_S = \left(\frac{\lambda}{\pi}\right)\left(\frac{\sin\theta}{\sqrt{\sin^2\theta - n^2}}\right) \tag{1.6}$$

$$d_P = \left(\frac{\lambda}{\pi}\right)\left(\frac{\sin\theta}{\sqrt{\sin^2\theta - n^2}}\right)\left(\frac{n^2}{\sin^2\theta - n^2\cos^2\theta}\right) \tag{1.7}$$

1.3.2 Cause of IF shift

Fedorov first pointed out [4] that the time-averaged Poynting vector in the evanescent wave in the lower index medium has a nonzero component perpendicular to the plane of incidence that contributes to the transverse shift of the light beam. Imbert applied the above-mentioned energy flux conservation approach to theoretically [3] determine this transverse shift for total internal reflection of the circularly polarized light.

$$y_T = \pm\left(\frac{\lambda}{\pi}\right)\left(\frac{1}{1-n^2}\right)\left(\frac{\sin^3\theta\cos\theta}{\sin^2\theta - n^2\cos^2\theta}\right) \tag{1.8}$$

Following Artmann's stationary phase approach Schilling [16] and later many others derived the expression IF shift for the circularly polarized light.

$$y_T = \pm\left(\frac{\lambda}{\pi}\right)\left(\frac{\sin^3\theta\cos\theta}{\sin^2\theta - n^2\cos^2\theta}\right) \tag{1.9}$$

But both of these approaches suffer from several inconsistencies when one deals with the transverse shift of the light beam. In the standard procedure of the energy flux conservation, in the overlapped region of the incident and reflected beam (as shown in Figure 1.3), the Poynting vector is supposed to be the superposition of the incident and reflected beam taken separately. But, in Maxwell's theory, there is no superposition principle in effect for the Poynting vectors.

In the case of stationary phase approximation, there are no drastic assumptions, only the boundary conditions of the electric and magnetic fields and linearity of the wave equations are taken into account. But, this method could not explain the features below the critical angle of incidence. Hence, the study of IF shift encircles a lot of controversies in the research community. Fedoseyev and Player first introduced the concept of IF shift originating due to the balance and conservation of the angular momentum of light [19,20]. But soon with the evidence of spin-orbit interaction of light by Liberman & Zel'dovich [21], the concept of angular momentum of light takes a whole new direction. Onoda (2004) established the role of the spin Hall effect of light related to the Berry phase in governing the transverse shift of the beam [17]. A complete theoretical treatment of IF shift based on total angular momentum conservation of light by Bliokh & Bliokh (2006-07) produces the most-accepted explanation and precise expression of the IF shift [22-26].

1.4 Dependence of optical beam shift

Several parameters are related to the phenomena of reflection or refraction of the optical beam from a surface. Below we have listed different parameters that can influence the Goos-Hänchen & Imbert-Fedorov shifts.

(a) *Surface of interaction*:

The properties of the reflecting and refractive surface greatly influence the behaviour of the GH & IF shifts. Already a lot of studies have been carried out on different materials with changing their intrinsic and extrinsic properties such as thin film and bulk form of the material, thickness variation of a particular sample, application of external magnetic field, and artificial creation of different metamaterials, etc. In later chapters, we will also demonstrate how the properties of the reflecting surface affect the nature of the optical beam shifts.

(b) *Wavelength of the incident light*:

It is also a major contributing factor in the optical beam shift. It is already well-known that the magnitude of optical beam shift is approximately of the order of the incident wavelength of the light beam. In this thesis, we will also prove that by selecting a particular wavelength to work with, GH & IF shifts can be maximized or minimized.

(c) *Special angles*:

We know that there are two peculiar angles of incidence as the beam undergoes reflection from a plane dielectric interface: the *critical angle* and the *Brewster angle* of incidence. The critical angle appears only in total internal reflection from a denser medium. According to recent studies, in close proximity of these angles the GH & IF shifts behave in an unusual manner with large enhancement in most of the cases (sometimes diverges). A more important point is that this behaviour is not universal, depending upon the reflecting surface the nature of the GH & IF shifts can be completely different at these special angles. In this thesis, we have deeply addressed this particular issue.

(d) *Spin and Orbital angular momentum of light*:

As we have already discussed the conservation of total angular momentum (spin and orbital angular momentum) is the principal reason for the generation of the IF shift. But, in general, both of the GH & IF shifts are dependent upon the angular momentum of light [21,24,25,27]. Till now, we have not been given any idea about the angular momentum of light but, in future, we want to study the effect of orbital angular momentum in the GH & IF shifts.

(e) *Higher-order modes of light*:

The optical beam shifts are mainly first-order deformations of the light beam. Nevertheless, higher-order deformations can also take place during reflection and refraction. To incorporate these higher-order effects, the orbital angular momentum vortex eigenmodes should be considered and superposed about the geometrical optics axis. Of late a lot of studies are trying to explore these higher-order contributions [118].

(f) *Complex beam modes*:

The beam shape is also a significant factor in GH and IF shift. Most common are the Gaussian and Laguerre-Gaussian beams for optical beam shift investigation. Recently, several studies are being performed for different beam structures such as paraxial Bessel [28], non-paraxial Bessel [29], Laguerre-Gaussian with higher radial order [30], Hermite-Gaussian [31], and dipole radiation [32]. General aspects of the beam shape have been discussed in the reference [33]. But, regarding this beam shape dependence, a lot of controversies are there over time [34-37].

1.5 Applications

In this decade, the Goos-Hänchen & Imbert-Fedorov shifts have received special attention in technological developments. The optical beam shifts explicitly influence the optical waveguide modes and microcavities [38,39]. The GH shift has also been applied in the areas of biosensors [40], optical heterodyne sensors [41], measurement of beam angle, refractive index detector, temperature sensors, and film thickness measurement device [42]. Additionally, the GH shift is also utilized in characterizing the permittivity and permeability of different materials in optical microscopy study and lithography [43,44]. Recently, It has also been applied in image edge detection [45], optical differential application, chemical rate detection purposes [46]. Thus, the study of GH & IF shifts have become indispensable in the advancement of the modern research industry.

1.6 2D Materials

1.6.1 Nature of the Materials at Nanoscale

The foundation of material science technology starts first with the understanding of material systems. Specific applications require specific properties of the materials. To show a few examples, building circuits requires knowledge of the electrical conductivity of copper, creating skyscrapers needs the compressive strength of the concrete, and making car tires requires the robustness and flexibility of rubber. More understanding of the properties of a material is required for the progress of the technology further.

Generally, we consider that the constituents of the material determine its properties. Like, electricity is conducted by the metal due to the metallic bonding of atoms, which permits electrons to drift freely throughout the external field acting upon it.

1.6.2 What exactly are the 2D materials?

One can broadly classify nanomaterials and layered structures in the following way:

(a) When the three dimensions become comparable to the nano form, we call the material *zero dimensional* (0-D). They are conventionally termed nanoparticles.

(b) If only two dimensions become comparable to nano form, and another extending longer, we call the material *one dimensional* (1-D) material. They are commonly termed as ‘nanotube or nanowire’.

(c) When only one dimension becomes comparable to nano form, with both of the other two dimensions extending larger, we call them *two dimensional* (2-D) material.

(d) Lastly, when all the material dimensions extend longer and are beyond the nano limit, then we do not call it a nanomaterial. In such a case, we call it a *bulk* (3-D) material. In our day-to-day life, we mainly deal with these bulk materials.

TABLE 1.1

Nanoscopic Dimension	**Short Name**	**Classification**	**Example**
0	3-D	Bulk	Materials visible to the eye
1	2-D	Nano-sheet	Graphene, TMDCs, h-BN
2	1-D	Nano-tube or Nano-wire	Carbon nano-tube
3	0-D	Nano-particle	Quantum dot

It is possible to reach the single atom limit by reducing thickness of two-dimensional materials which gives rise to the most intriguing phenomena in these materials.

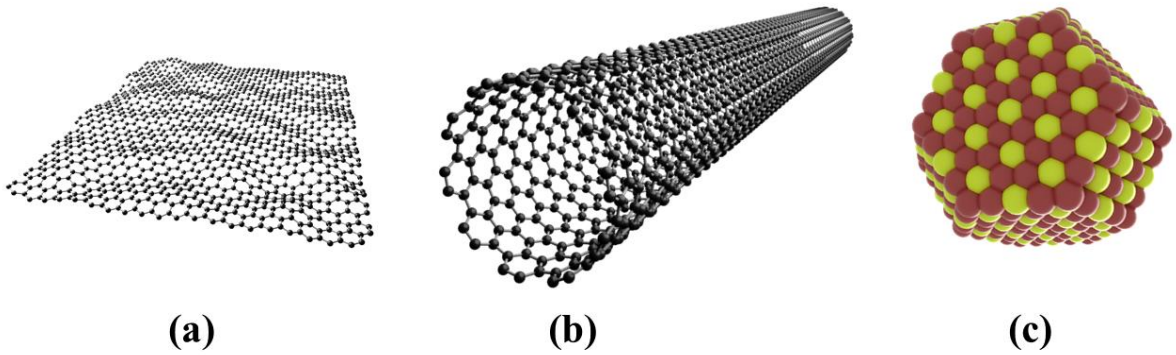

Figure 1.4. Characterization of nano-materials: **(a)** Graphene sheet, **(b)** Carbon nano-tube, and **(c)** Quantum dot (**Source: Internet**)

1.6.3 Well-known 2D Materials

The journey of 2D material started with the isolation of graphene long back around 2004 [47]. After its discovery, there have been a plethora of new 2D materials till date [48], with various intriguing electrical and optical properties. Here, we provide a few well-known 2D materials.

(a) *Graphene*:

A renaissance occurred in the field of material science with the invention of graphene. Graphene possesses a hexagonal lattice with covalent bonding of carbon atoms. Its thickness is down to almost a single atom (of the order of 1.4 micron). The conduction band touches with the valence band making graphene semimetal in nature. The special band structure permits its electrons to roam with tremendous velocity. This linear dispersion in graphene gives rise to various novel properties like room temperature anomalous quantum Hall effect. A minor quantity, of the order of 2% of visible light is absorbed by graphene. It possesses high tensile strength in comparison to others [49]. Hence it finds promising applications in high-speed optoelectronics devices, energy storing and processing devices, sensor industry, and several other proofs of concept devices.

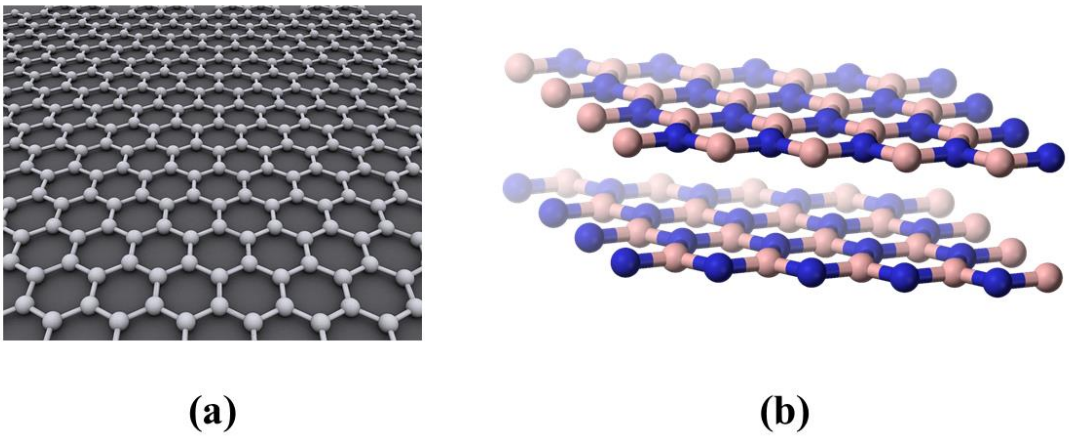

Figure 1.5. (a) Graphene and **(b)** hexagonal boron nitride both belong to the 2D materials category (**Source: Wikipedia**)

(b) *Hexagonal boron nitride*:

Hexagonal boron nitride, popularly known as hBN, has a crystal structure similar to graphene. Here, the presence of B and N atoms in place of C atoms makes it a wide-bandgap insulator considerably different from graphene. Although they have close similarities in structure, graphene is a very good conductor but hBN is an insulator.

(c) *Transition Metal Di-chalcogenides* (*TMDCs*)*:*

The overwhelming success of graphene shifted the attention of the researchers to look for the other layered structures and 2D materials in search of novel physical phenomena and potential device applications.

Transition metal di-chalcogenides (widely termed as TMDC) show the chemical structure MX_2 (X-M-X). Here, M is any transition metal (e.g. molybdenum, tungsten, etc.) and X is any chalcogen (e.g. sulfur, selenium, Tellurium, etc.). In each layer of this van der Waals material, the metallic layer is inserted between the two chalcogenides layers (hence di-chalcogenides). TMDCs display layered structures with tight covalent bonding along with 2D (intralayer) and weak van der Walls bonding along the third dimension (interlayer) which permits easy exfoliation into monolayers. That is why they are obtainable in single layer, bilayer, few-layer, and bulk limit.

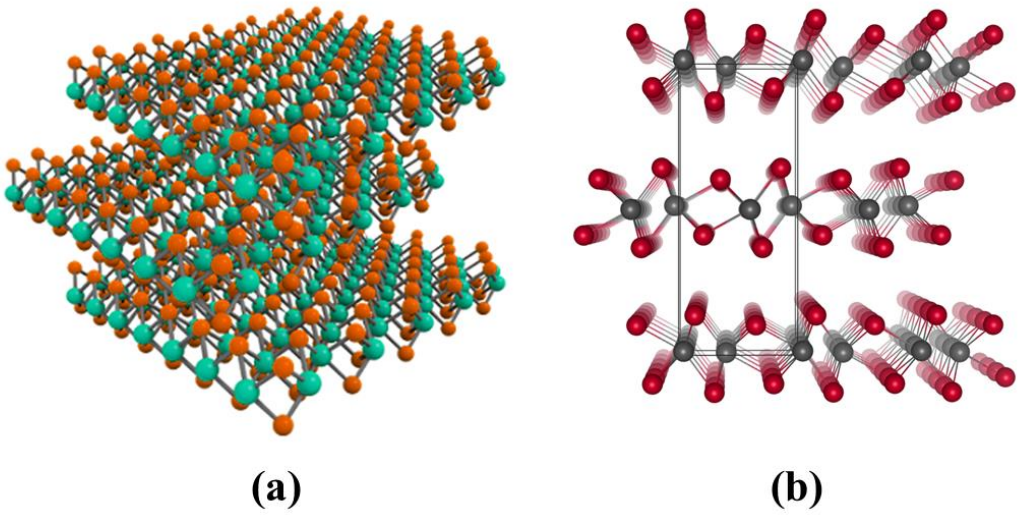

Figure 1.6. (a) Molybdenum di-sulphide (MoS_2) common in 2H phase and **(b)** Tungsten di-telluride (WTe_2) common in 1T phase (**Source: Internet**)

TDMCs can yield several structures - 2H phase and 1T phase. The 2H-phase belongs to the trigonal symmetry class and is the most common. This gives rise to the semiconducting characteristics as observed in MoS_2, WS_2, WSe_2, and $MoSe_2$. TMDCs possess an indirect bandgap in the bulk form. In the monolayer limit, the bandgap dramatically changes to direct that too in the visible region of the spectrum. External factors like temperature, pressure, field, strain, etc. greatly influence TMDCs' electronic properties. This band gap engineering makes TMDCs so significant for optoelectronics applications. Moreover, impurities, boundaries, vacancies generated in the material give rise to intriguing features. We also got our primary interest in TMDCs at the first sight due to these special optical signatures. TMDCs have strong spin-orbit coupling along with their spin and valley degrees of freedom providing them a greater edge over others in their technological applications. Their high charge mobility makes them a significant candidate for transistors application.

(*d*) *Phosphorene*:

Phosphorene is nothing but a monolayer black phosphorus that is a stable allotrope of phosphorus. Phosphorene possesses a puckered honeycomb structure. It also depicts a direct bandgap, highly dependent on the layer numbers. Its charge mobility (of the order of 1000 $cm^2V^{-1}s^{-1}$) is also high. Hence, it is also a popular candidate for transistors, optoelectronic, and the device industry. Phosphorene has a corrugated structure causing its properties to differ considerably according to the direction of measurement.

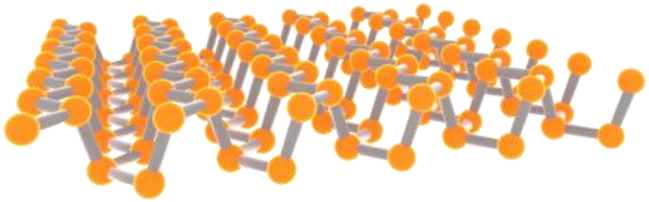

Figure 1.7. Structure of Phosphorene (**Source: Internet**)

(e) *Xenes*:

Single layers of silicon, germanium, and tin are popularly termed Xenes. They all possess a hexagonal structure. It is similar to graphene in structure. But it cannot be exfoliated into monolayers quite different from graphene. They are primarily grown on a specific substrate

epitaxially. These materials are still not studied in detail and are under constant investigation till date. They have potential applications in the field of field-effect transistors and topological insulators.

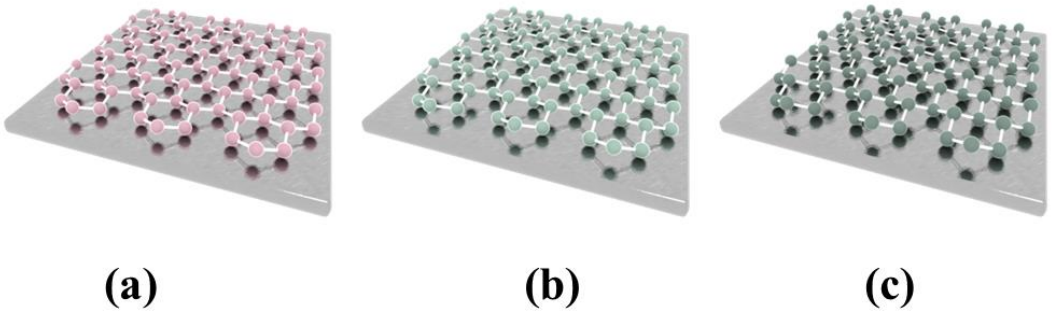

Figure 1.8. The structure of **(a)** Silicene, **(b)** Germanene, and **(c)** Stanene: with buckled hexagonal structure (**Source: Internet**)

Recently, several other 2D analogs such as antimomene and bismuthine are also been discovered [50] which display magneto-electronic applications in future [51].

1.6.4 How do we make 2D materials?

Any bulk material can be taken and thinned down nearly about the thickness of a few atoms to produce two-dimensional materials. Nonetheless, not all the materials are layered in nature and several materials retain their three-dimensional form. Hence, thinning down any material involves cutting the out of plane bonds causing 'dangling' bonds to arise. Following such a procedure, if we thin down a material to generate a 2D material, it may have a high density of dangling bonds making it energetically and chemically unstable. Moreover, the structure of the material can be rearranged to lower its surface energy due to this instability.

The 2D materials are mostly originated from a broader class of layered materials. In two conventional ways 2D materials can be prepared:

(a) *Top-down*: Here one starts with bulk material and thin it down to 2D form.

(b) *Bottom-up*: Here, one starts with the atomic ingredients and begins assembling them to generate 2D form.

(a) Top-down approach

(I) *Mechanical exfoliation* – It is nothing but the method of '*Scotch-tape'*. Single-layer of graphene was first generated by this method. One first attaches a sticky tape to the layered material. Next, after peeling off, few layers get attached to the tape. Then we press the tape on top of a substrate. In this way, few layers of the 2D materials are transferred to the substrate. Producing an exact monolayer is very difficult using this method as the process involves no monitoring of the size and shapes. Nevertheless, it can produce good quality monolayer having almost no defects.

(II) *Liquid exfoliation* – In this method, organic solvents are utilized for transferring mechanical force to the powdered material in the liquid. By sonication, one applies tensile stress to the layers formed causing them to move away from each other. The quality of the monolayer produced is not good and generally possesses many defect states.

(b) Bottom-up approach

(I) *Chemical vapour deposition* (CVD) - In this method, depending upon the 2D materials to be deposited, precursor gases are passed through the furnace that is heated at a definite temperature. In the chamber, interaction occurs between the sample and the substrate, and a thin layer is subsequently deposited over the surface. The quality of the deposited layer, thickness, layer number, composition, defects, etc. can be monitored by externally controllable parameters like the temperature of the chamber, chamber pressure, reaction time, etc. This technique produces high-quality samples with minimum defects but is quite expensive to conduct.

(II) *Chemical synthesis* – By this chemical synthesis method based on chemical solution, many techniques were proposed by time for the synthesis of layered structures. Many different procedures are available depending upon specific type of material to be synthesized such as:

(*i*) Chemical reactions at high or low temperatures

(*ii*) Nanoparticles fusion to form larger structures, and so on.

This technique is very much versatile and of low cost and highly scalable. Hence, it is used by a lot of researchers for 2D materials preparation. It has similar disadvantages to the liquid exfoliation method.

1.6.5 Difference of 2D materials from the bulk samples

(a) *Van der Waals interactions exclusion*:

In these layered structures, different planes (which are formed by strong 2-D covalent bonding) are connected by the weak out of plane Van der Wall's interaction. Since these Van der Walls bonds are weak in nature, they can be broken by applying an external force that causes the generation of separate layers. But the in-plane covalent bonds are very strong, hence even a single layer generation is possible.

(b) *Surface area to volume ratio*:

This is a very important factor that controls the amount of exposure in the atmosphere which in turn is a governing factor of the rate of a reaction. This ratio causes 2D materials to have a higher surface-to-volume ratio. Hence they react much more than the bulk samples. Moreover, 2D materials show larger sensitivity to the neighbouring environment making them suitable for sensor application.

(c) *Electron confinement in a plane*:

The band structure of a material is the principal governing factor behind its electronic properties and optical response. The movement of electrons and the corresponding band structure for material are dependent upon the periodicity of the lattice. In comparison to bulk samples, 2D materials do not possess the periodicity in the out-of-plane direction causing subtle changes in the band structure of the material. That is why 2D materials show considerably different properties than bulk samples.

Due to this electron confinement dielectric screening occurs in semiconductors. Due to the smaller number of electrons in 2D materials, the Coulomb force is stronger causing the generation of the strongly bound exciton. These are stronger than the bulk sample, hence increasing their stability. The quantum confinement found in 2D materials causes an increase in energy. Hence, the absorption and emission spectrum change appreciably in comparison to the bulk samples. The number of layers thus controls the absorbed or emitted energy from the sample.

1.6.6 2D materials Application areas

Due to the dimensional difference, the 2D materials depict special properties that are not found in the corresponding bulk samples. Hence, it finds a lot of promising applications in the modern-day optoelectronics and device industry.

Transistors Industry:

Field-effect transistors (FETs) have been fabricated from a variety of semiconducting 2D materials such as TMDCs [52] and black phosphorus [53]. They are widely used in fabricating FET devices using their high mobility and bandgap in the visible region. The hBN is applied in the transistor gate-making purpose. Using external field, doping, edge state modulation, etc. graphene is also being used for device-making purposes.

Flexible Electronics:

2D materials are largely used in recent Flextronics applications due to their flexibility property over conventional semiconductors [54].

Sensor application:

TMDCs are currently applied in making sensors based on FETs. Detecting chemicals up to *ppm* range, that includes detection of triethylamine [55], NO, NO_2, NH_3, etc. [56] with high precision.

Photodetectors:

The bandgap of most of the TMDCs (MoS_2, $MoSe_2$, WS_2, WSe_2, Black phosphorus) lies in the optical region or NIR region of the spectrum. In parallel, TMDCs also show high absorbance in the visible domain [57]. This property makes the TMDCs suitable for optical detection applications, subsequently the production of high-efficiency photodetectors [58]. Different hetero-structures (such as graphene/MoS_2, MoS_2/WS_2, etc.) are also in wide use for producing high-efficiency detectors [59].

Battery electrodes:

Because of their high mobility, flexibility, strong in-plane bonding, the surface to mass ratio graphene and TMDCs (especially MoS_2) are currently used in electrode production [60] that lead to [61] fast charging, lighter weight, low consumption devices.

Topological insulators (*TI*):

Topological insulators behave as an insulator in bulk but conducting in edge states. Opposite spin electrons can pass through the edges in opposite directions. They have also great potential in low consumption, power-efficient devices. One of the TMDCs, Xenes work as topological insulator [62]. Switching between a TI and superconductor by applying external field [63,64] are also realized in WTe_2.

Valleytronics:

The extra valley degree of freedom gives rise to a new direction in modern technology, the 'Valleytronics'. Special behaviour of the spin and angular momentum of the electrons in TMDCs provides them this additional degree of freedom for movement. This degree of freedom allows TMDCs special properties to be used for data processing and storage [65] devices.

1.7 Transition metal di-chalcogenides (TMDCs)

A lot of studies have been carried out regarding TMDCs. Countless review papers are available on this subject [66-71]. There are around 60 TMDCs available with many of them showing layered structures. MoS_2 is well-known and most studied material among them due to its abundant availability along with the special properties that it shows with reducing dimensionality.

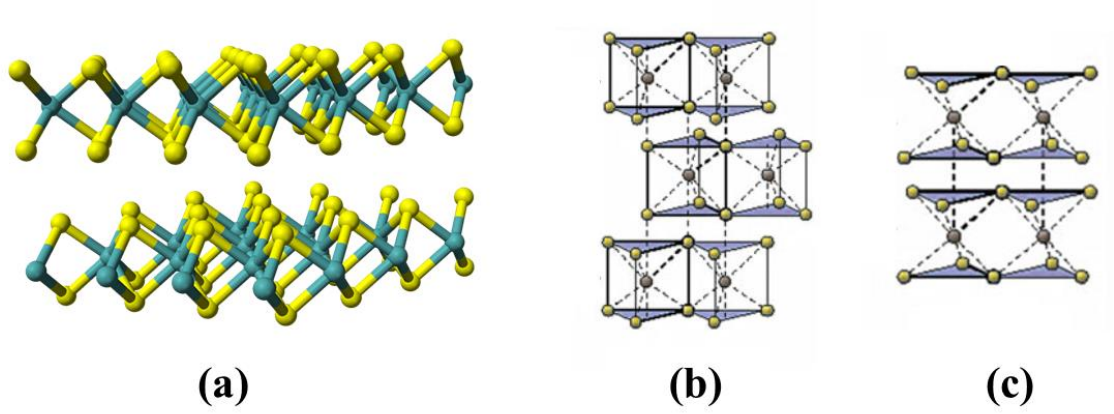

Figure 1.9. (a) General structure of TMDCs: top view of a typical MX_2 (X-M-X) form, **(b)** Schematics of the structural polytypes: 2H (hexagonal symmetry), and **(c)** 1T (tetragonal symmetry) (**Source: Internet**)

1.7.1 Chemistry of TMDCs

TMDCs have the renowned chemical structure of MX_2, with M layer sandwiched between the two X layers (M = Group IV, V, VI transition metals, and X = Chalcogens). As shown in Figure 1.9, the atoms exhibit hexagonal packing with weak Van der Walls force acting between adjacent (out of plane) layers.

In this thesis, we have mainly focussed on molybdenum di-sulfide. There are varieties of applications of this material (MoS_2) like phototransistor, photodiode, photovoltaic cell, photo-catalyst, nanotribology, battery production, and lubrication industry, etc. MoS_2 is semiconducting having an indirect bandgap of 1.25 eV in its bulk form. But it changes to a direct bandgap of 1.88 eV in its monolayer limit. Their physical, electrical, optical, as well as chemical properties, can precisely be predicted from the first-principles DFT calculations.

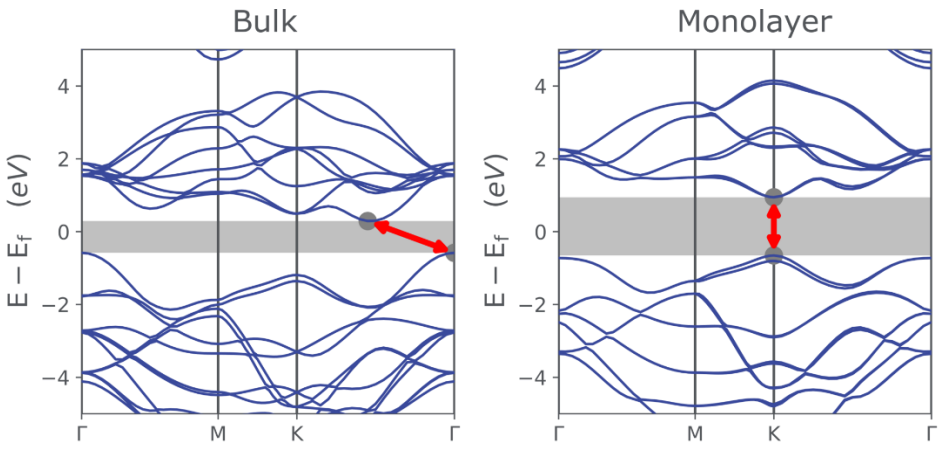

Figure 1.10. Electronic band structure of MoS_2 **(a)** in the bulk form (Indirect gap) and **(b)** in the monolayer form (Direct gap). (**Source: Internet**)

1.7.2 Electronic properties of MoS_2

For the applications of MoS_2 in optoelectronic devices and the sensor industry, information about its electronic and optical properties, like the electronic band structure, optical conductivity, the density of states permittivity and permeability are necessary. Using first-principles calculations, the band structure of bulk MoS_2 can be determined [72]. From the band structure, it is evident that MoS_2 is a semiconductor showing an indirect bandgap of 1.25 eV in the bulk (3D) limit. The origin of this indirect bandgap is due to a transition from the top of

the valence band at Γ point to the bottom of the conduction band midway between Γ point and K point. But, the direct (optical) bandgap is positioned at the K point. With the decrease in layer numbers, the indirect bandgap starts increasing. In the limit of a single layer, the material is reduced to the 2D form. This monolayer 2D MoS_2 yields a direct bandgap with a gap of 1.88 eV displaying semiconducting nature [73,74]. However, at the K point, the direct (optical) bandgap stays nearly unaffected and is independent of layer number or thickness variation.

1.7.3 Optical properties of MoS_2

There had been a lot of experimental studies to investigate the optical properties of bulk MoS_2 [75,76]. From the calculated absorption spectrum of bulk MoS_2, we can find two peaks, one at 1.88, another at 2.06 eV [77]. Among the material parameters, the absorption coefficients and refractive indices greatly influence the optical properties of the material.

MoS_2 depicts large absorbance in the visible and near-infrared wavelength range. Its bandgap can be monitored by external factors such as electric field, pressure, temperature, etc. As the bandgap can be tuned by controlling external parameters, the bandgap engineering provides an extra advantage of using MoS_2 in optoelectronics and device application over others. Tunable bandgaps give rise to higher photo-responsivity, detectivity, and response time [78] which is most required in device application. The bandgap and chemical structure also affect photoluminescence (PL) spectra. TMDCs generally have a low quantum yield for photoluminescence [79]. Monolayer MoS_2 shows a single exciton peak. MoS_2 is also highly effective in solar cells due to its carrier lifetime.

1.7.4 Electronic Spin Hall Effect

It is often experienced in crystalline semiconductors that conduction band bottom and the valence band top are located at degenerate valleys in *k*-space [80,81]. They have a specific valley degree of freedom for low-energy carriers because of the huge valley separation in *k*-space. These valley degrees of freedom are related to orbital magnetic moment and Berry curvature [82]. The phenomena of inversion symmetry breaking generates the 'Valley Hall Effect' in TMDCs [82]. These valley degrees of freedom make TMDCs suitable for device making.

1.7.5 Lattice Dynamics

Raman spectroscopy is an important and multipurpose technique for the characterization of the material and investigation of electronic as well as its vibrational characteristics.

There are two characteristic peaks in the Raman spectrum of MoS_2, E^1_{2g} and A_{1g} peaks. Figure 1.11 shows the Raman study of one of the samples (monolayer MoS_2) that we have used for the study. The difference between the E^1_{2g} and A_{1g} peak was 24 cm^{-1}. Here, the ratio $A_{1g}/E^1_{2g} = 1.06 \approx 1$, which establishes that the MoS_2 sample is a monolayer [74,83,84].

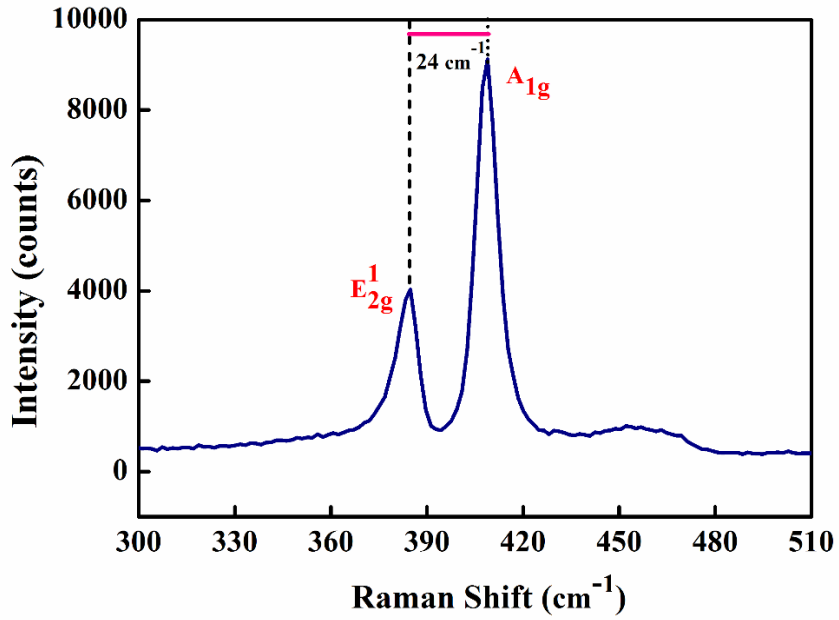

Figure 1.11. Room temperature Raman spectroscopy measurements performed on CVD grown full-area coverage MoS_2 monolayer on SiO_2 (**courtesy: 2D Semiconductors, USA**)

1.8 Motivation and Objective of the Thesis

As discussed in the previous sections, owing to their distinctive and intriguing electrical, optical, and chemical properties, 2D materials have attracted immense research interest both in fundamental domain and application in technology. Due to their high potential in the upcoming optoelectronics industry, we have shifted our attention to TMDCs. The study of the optical beam shifts in 2D materials can reveal new directions not only in the improvement of optoelectronics and the device industry but also towards the development of new devices based on solely the effect of the optical beam shift.

In this thesis, we have theoretically examined the nature of the GH and IF shifts, their principal, and controlling parameters. A general theoretical model is developed such that GH and IF shifts can be predicted in any layered structure. A detailed theoretical calculation is

prescribed for monolayer TMDCs (WS_2, WSe_2, MoS_2, and $MoSe_2$) and graphene-coated surfaces. The observation of non-zero GH & IF shift in case of partial reflection, the occurrence of giant beam shift, and unusual behaviour in the neighbourhood of critical angle and Brewster's angle of incidence are some of the significant results that will be drawn in the following *Chapters*.

In this *Chapter*, it is also pointed out that due to the tiny wavelength-scale magnitude of the optical beam shifts it is really tough to detect. Therefore, we have set our goals in the development of an experimental setup for the precise detection of the optical beam shifts. In the following Chapters, we have shown two different techniques by which one can effectively measure the GH and IF shifts along with the photonic spin Hall effect phenomena. We have generalized the measurement technique such that the method can be applied to other materials too for the detection of the corresponding shifts.

This thesis is divided into two sections – (A) Theoretical Work and (B) Experimental Measurement. The *Theoretical* section consists of three Chapters discussing the theoretical determination of GH & IF shifts in different 2D materials.

In *Chapter* 2, a theoretical method is proposed for the detection of GH shift in monolayer MoS_2 for partial as well as the total internal reflection of the light beam. The unusual features near the special angles are explained. A comparison is also done between different 2D materials, different substrates, and the difference of the monolayer sample from the corresponding bulk material. *Chapter* 3 deals with both GH and IF shifts in different TMDCs (WS_2, WSe_2, MoS_2, and $MoSe_2$) for a fundamental Gaussian mode beam. A general theoretical model is suggested that is applicable to other 2D materials, layered structures, and also valid in the vicinity of the critical angle and Brewster's angle of incidence. Tuning of the GH and IF shifts in the TMDCs with the wavelength of the incident beam is also discussed. In *Chapter* 4, we discuss GH and IF shifts and their controlling parameters for graphene-coated surfaces. The explicit dependence of the chemical potential of graphene and the wavelength of the incident beam is well-explained. This gives us freedom in controlling the magnitude of the GH and IF shifts to the desired magnitude.

The *Experimental section* constitutes six *Chapters*. In Chapter 5, we discuss the available techniques for the optical beam shift measurement, their advantages, and disadvantages, working principle, application areas, etc. *Chapter* 6 consists of the experimental development of the quantum weak measurement setup for the detection of the GH shift for the

total internal reflection of the light beam from a prism surface. In *Chapter* 7, we generalize the quantum weak measurement technique for the GH shift measurement in any layered structure and apply it to detect the GH shift in monolayer MoS_2. *Chapter* 8 describes the modification of weak measurement techniques for detection of IF shift in monolayer MoS_2. Again, the technique is generalized such that it can be applicable to other surfaces as well. Next, we have developed a different indirect technique for the measurement of the GH and IF shifts. Though precise, weak measurement is a difficult and time taking experiment to carry out. But, this Polarimetric method of beam shift measurement is simple and easy to conduct. *Chapter* 9 explains the results of GH and IF shift measurement in monolayer MoS_2 using this indirect Polarimetric technique. In *Chapter* 10 we have discussed a new phenomenon of the *Photonic spin Hall effect*. This effect is imminent in monolayer MoS_2 and has a close connection with the geometric phases of the light. Finally, in *Chapter* 11, we give a detailed conclusion of our findings and suggested future works that can be explored in subsequent time.

References

[1] M. Born and E. Wolf, *Principles of Optics: Electromagnetic Theory of Propagation, Interference and Diffraction of Light* (Elsevier Science, 2013).

[2] F. Goos and H. Hänchen, Annalen der Physik **436**, 333 (1947).

[3] C. Imbert, Physical Review D **5**, 787 (1972).

[4] F. I. Fedorov, Dokl. Akad. Nauk SSSR **105**, 465 (1955).

[5] K. Y. Bliokh and A. Aiello, Journal of Optics **15**, 014001 (2013).

[6] O. Hosten and P. Kwiat, Science **319**, 787 (2008).

[7] K. Artmann, Annalen der Physik **437**, 87 (1948).

[8] R. H. Renard, J. Opt. Soc. Am. **54**, 1190 (1964).

[9] O. C. de Beauregard and C. Imbert, Physical Review D **7**, 3555 (1973).

[10] O. C. de Beauregard, C. Imbert, and Y. Levy, Physical Review D **15**, 3553 (1977).

[11] Y. M. Antar and W. M. Boerner, Canadian Journal of Physics **52**, 962 (1974).

[12] J. W. Ra, H. L. Bertoni, and L. B. Felsen, SIAM Journal on Applied Mathematics **24**, 396 (1973).

[13] C. C. Chan and T. Tamir, Opt. Lett. **10**, 378 (1985).

[14] M. Merano, A. Aiello, M. P. van Exter, and J. P. Woerdman, Nature Photonics **3**, 337 (2009).

[15] C. V. Fragstein, Annalen der Physik **439**, 271 (1949).

[16] H. Schilling, Annalen der Physik **471**, 122 (1965).

[17] M. Onoda, S. Murakami, and N. Nagaosa, Physical Review Letters **93**, 083901 (2004).

[18] K. Yasumoto and Y. Ōishi, Journal of Applied Physics **54**, 2170 (1983).

[19] M. A. Player, Journal of Physics A: Mathematical and General **20**, 3667 (1987).

[20] V. G. Fedoseyev, Journal of Physics A: Mathematical and General **21**, 2045 (1988).

[21] V. S. Liberman and B. Y. Zel'dovich, Physical Review A **46**, 5199 (1992).

[22] K. Y. Bliokh and Y. P. Bliokh, Physical Review Letters **96**, 073903 (2006).

[23] K. Y. Bliokh and Y. P. Bliokh, Physical Review E **75**, 066609 (2007).

[24] K. Y. Bliokh, A. Niv, V. Kleiner, and E. Hasman, Nature Photonics **2**, 748 (2008).

[25] K. Y. Bliokh, F. J. Rodríguez-Fortuño, F. Nori, and A. V. Zayats, Nature Photonics **9**, 796 (2015).

[26] K. Y. Bliokh, D. Smirnova, and F. Nori, Science **348**, 1448 (2015).

[27] K. Y. Bliokh, E. A. Ostrovskaya, M. A. Alonso, O. G. Rodríguez-Herrera, D. Lara, and C. Dainty, Opt. Express **19**, 26132 (2011).

[28] A. Aiello and J. P. Woerdman, Opt. Lett. **36**, 543 (2011).

[29] E. Nordblad, Physical Review A **85**, 013847 (2012).

[30] N. Hermosa, A. Aiello, and J. P. Woerdman, Opt. Lett. **37**, 1044 (2012).

[31] C. Prajapati and D. Ranganathan, J. Opt. Soc. Am. A **29**, 1377 (2012).

[32] M. V. Berry, Proceedings of the Royal Society A: Mathematical, Physical and Engineering Science **467**, 2500 (2011).

[33] A. Aiello, New Journal of Physics **14**, 013058 (2012).

[34] A. Aiello and J. P. Woerdman, Opt. Lett. **37**, 1057 (2012).

[35] R. Simon and T. Tamir, J. Opt. Soc. Am. A **6**, 18 (1989).

[36] W. Löffler, A. Aiello, and J. P. Woerdman, Physical Review Letters **109**, 213901 (2012).

[37] M. Merano, G. Umbriaco, and G. Mistura, Physical Review A **86**, 033842 (2012).

[38] D. H. Foster, A. K. Cook, and J. U. Nöckel, Opt. Lett. **32**, 1764 (2007).

[39] J. Unterhinninghofen, J. Wiersig, and M. Hentschel, Physical Review E **78**, 016201 (2008).

[40] X. Yin and L. Hesselink, Applied Physics Letters **89** (2006).

[41] T. Hashimoto and T. Yoshino, Optics Letters **14**, 913 (1989).

[42] Z. Qin, Q. Liu, C. Yue, Y. Lang, and X. Zhou, Review of Scientific Instruments **91**, 123111 (2020).

[43] X. Hu, Y. Huang, W. Zhang, D.-K. Qing, and J. Peng, Opt. Lett. **30**, 899 (2005).

[44] F. de Fornel, *Evanescent Waves: From Newtonian Optics to Atomic Optics* (Springer, 2001).

[45] D. Xu, S. He, J. Zhou, S. Chen, S. Wen, and H. Luo, Applied Physics Letters **116**, 211103 (2020).

[46] R. Wang, J. Zhou, K. Zeng, S. Chen, X. Ling, W. Shu, H. Luo, and S. Wen, APL Photonics **5**, 016105 (2020).

[47] K. S. Novoselov, A. K. Geim, S. V. Morozov, D. Jiang, Y. Zhang, S. V. Dubonos, I. V. Grigorieva, and A. A. Firsov, Science **306**, 666 (2004).

[48] N. Mounet *et al.*, Nature Nanotechnology **13**, 246 (2018).

[49] C. Lee, X. Wei, J. W. Kysar, and J. Hone, Science **321**, 385 (2008).

[50] F. Reis, G. Li, L. Dudy, M. Bauernfeind, S. Glass, W. Hanke, R. Thomale, J. Schäfer, and R. Claessen, Science **357**, 287 (2017).

[51] S.-C. Chen, J.-Y. Wu, and M.-F. Lin, New Journal of Physics **20**, 062001 (2018).

[52] B. Radisavljevic, A. Radenovic, J. Brivio, V. Giacometti, and A. Kis, Nature Nanotechnology **6**, 147 (2011).

[53] L. Li, Y. Yu, G. J. Ye, Q. Ge, X. Ou, H. Wu, D. Feng, X. H. Chen, and Y. Zhang, Nature Nanotechnology **9**, 372 (2014).

[54] W. Zhu, M. N. Yogeesh, S. Yang, S. H. Aldave, J.-S. Kim, S. Sonde, L. Tao, N. Lu, and D. Akinwande, Nano Letters **15**, 1883 (2015).

[55] F. K. Perkins, A. L. Friedman, E. Cobas, P. M. Campbell, G. G. Jernigan, and B. T. Jonker, Nano Letters **13**, 668 (2013).

[56] D. J. Late *et al.*, ACS Nano **7**, 4879 (2013).

[57] M. Bernardi, M. Palummo, and J. C. Grossman, Nano Letters **13**, 3664 (2013).

[58] O. Lopez-Sanchez, D. Lembke, M. Kayci, A. Radenovic, and A. Kis, Nature Nanotechnology **8**, 497 (2013).

[59] W. Zhang *et al.*, Scientific Reports **4**, 3826 (2014).

[60] X. Yang, C. Cheng, Y. Wang, L. Qiu, and D. Li, Science **341**, 534 (2013).

[61] J. Hassoun *et al.*, Nano Letters **14**, 4901 (2014).

[62] A. Molle, J. Goldberger, M. Houssa, Y. Xu, S.-C. Zhang, and D. Akinwande, Nature Materials **16**, 163 (2017).

[63] E. Sajadi *et al.*, Science **362**, 922 (2018).

[64] V. Fatemi, S. Wu, Y. Cao, L. Bretheau, Q. D. Gibson, K. Watanabe, T. Taniguchi, R. J. Cava, and P. Jarillo-Herrero, Science **362**, 926 (2018).

[65] D. Xiao, G.-B. Liu, W. Feng, X. Xu, and W. Yao, Physical Review Letters **108**, 196802 (2012).

[66] M. Xu, T. Liang, M. Shi, and H. Chen, Chemical Reviews **113**, 3766 (2013).

[67] S. Z. Butler *et al.*, ACS Nano **7**, 2898 (2013).

[68] D. Jariwala, V. K. Sangwan, L. J. Lauhon, T. J. Marks, and M. C. Hersam, ACS Nano **8**, 1102 (2014).

[69] W. Zhao, R. M. Ribeiro, and G. Eda, Accounts of Chemical Research **48**, 91 (2015).

[70] D. Lembke, S. Bertolazzi, and A. Kis, Accounts of Chemical Research **48**, 100 (2015).

[71] D. Voiry, A. Mohite, and M. Chhowalla, Chemical Society Reviews **44**, 2702 (2015).

[72] J. K. Ellis, M. J. Lucero, and G. E. Scuseria, Applied Physics Letters **99**, 261908 (2011).

[73] K. F. Mak, C. Lee, J. Hone, J. Shan, and T. F. Heinz, Physical Review Letters **105**, 136805 (2010).

[74] Y. P. Venkata Subbaiah, K. J. Saji, and A. Tiwari, Advanced Functional Materials **26**, 2046 (2016).

[75] R. F. Frindt, A. D. Yoffe, and F. P. Bowden, Proceedings of the Royal Society of London. Series A. Mathematical and Physical Sciences **273**, 69 (1963).

[76] Z. M. Wang, *MoS_2: Materials, Physics, and Devices* (Springer, 2013).

[77] R. Coehoorn, C. Haas, and R. A. de Groot, Physical Review B **35**, 6203 (1987).

[78] H. S. Nalwa, RSC Advances **10**, 30529 (2020).

[79] M. Amani *et al.*, Science **350**, 1065 (2015).

[80] X. Cui *et al.*, Nature Communications **9**, 1301 (2018).

[81] S. K. C, R. C. Longo, R. Addou, R. M. Wallace, and K. Cho, Scientific Reports **6**, 33562 (2016).

[82] C. Choi *et al.*, Nature Communications **11**, 5934 (2020).

[83] T. Han, H. Liu, S. Wang, S. Chen, W. Li, X. Yang, M. Cai, and K. Yang, Nanomaterials (Basel) **9**, 740 (2019).

[84] J. Wang, L. Chen, W. Lu, M. Zeng, L. Tan, F. Ren, C. Jiang, and L. Fu, RSC Advances **5**, 4364 (2015).

Section A: Theoretical Study

"Deep in the sea
all molecules repeat
the patterns of one another
till complex new ones are formed.
They make others like themselves
and a new dance starts."

-From a poem by Richard Feynman

Chapter 2 Goos-Hänchen Shift in MoS_2

We discuss here a general theoretical model for the study of the GH shifts in layered structures. The unusual features of the GH shift at the special angles, the importance of optical conductivities in the GH shift, as well as the dependence on the incident angle, wavelength, polarization, and layer numbers are demonstrated.

Content of this chapter has been published in: **A. Das** and M. Pradhan, "*Goos-Hänchen shift for Gaussian beams impinging on monolayer-MoS_2-coated surfaces*," **Journal of the Optical Society of America B** 35 (8), 1956-1962 (2018).

2 Goos-Hänchen Shift in MoS_2

2.1 Introduction

The familiar Fresnel reflection formulae and Snell's law are enough to precisely demonstrate the nature of the plane wave in geometrical optics [1,2]. As we already know, finite light beams show a contrasting behaviour in comparison to the plane waves and suffer longitudinal (in the plane of incidence) and transverse (perpendicular to the plane of incidence) shifts, which are known as Goos-Hänchen (GH) and Imbert-Fedorov (IF) shifts, respectively [3-10]. GH shift is extensively applied in the field of photonics, plasmonics, chiral materials, metamaterials, dielectrics, and numerous quantum systems [11-25]. On top of that, the GH shift has also displayed great potential in sensors and device industry e.g. refractive index sensor, optical heterodyne sensors, biosensors, temperature sensor, thickness detector, beam angle measurement [11,26], and optical microscopy, and lithography too [27,28].

In modern-day research, there has been tremendous research interest in layered structures [29] like graphene, TMDCs, and topological insulators [30-32]. We already know that graphene is a semimetal with a zero band gap [33]. In contrast, MoS_2 depicts semiconducting behaviour with indirect (1.29 eV) band gap in the bulk form and direct (1.9 eV) band gap in the monolayer form [34-36]. This direct band gap being in the visible region makes monolayer MoS_2 striking for optoelectronics device applications. There are several recent reports that have concentrated on graphene [37-40] as an area of optical beam shift investigation. Being a 2D material, the response of light interacting with MoS_2 surface and whether giving rise to any lateral or longitudinal shift is an important topic of research.

Our main goal in this study is to develop a theoretical model for studying Goos-Hänchen shift as a Gaussian light beam is reflected from MoS_2 coated surfaces. Two different scenarios of reflection are taken into account for this study (a) partial reflection (PR) and (b) total internal reflection (TIR). The optical beam shift can manifest in both spatial and angular forms. All of these GH shifts for MoS_2 are investigated in detail. Previous studies mainly concentrated on incident light of definite wavelength interacting with definite surface [39]. In the present study, the dependence on wavelength (450-785 nm) and different surfaces (on which MoS_2 is deposited) is thoroughly explained.

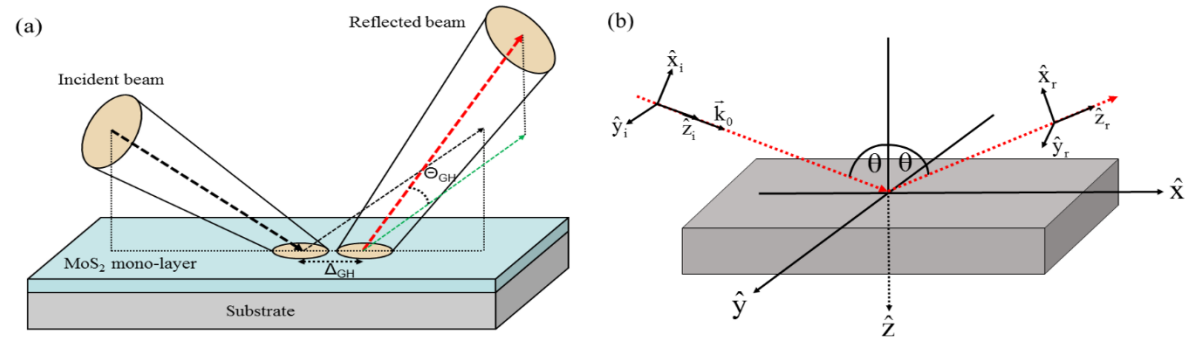

Figure 2.1. The observation of GH shift: **(a)** Pictorial representation of GH shift generation as light is reflected from MoS_2 surface and **(b)** The coordinate system that are used in the theoretical calculation for studying GH shift in layered structures.

2.2 Theory

2.2.1 Introduction of Transfer Matrix Method

The transfer matrix method is mainly applied in the study of light propagation through layered media [41-43]. In this method, the electric and magnetic fields in one position can be linked with those in a different position via a transfer matrix. In this formulation, we use two kinds of matrices:

(a) *Transmission matrix* connecting the fields across an interface,

(b) *Propagation matrix* connecting the fields propagating over a distance within a medium.

We first consider the propagation of light across an interface designed by a layer (placed at $z=0$) of optical conductivity σ separating two dielectrics with dielectric constants ε_1 and ε_2, as shown in Figure 2.2. We consider that the light is polarized along $\hat{y}$ and propagates along $\hat{z}$ direction. For the above-mentioned structures, the S and P polarizations can be decoupled. As a result, we can proceed separately with the S and P polarization components.

The magnetic field for P polarization can be written as:

$$H_{1y} = \left(a_1 e^{ik_{1z}z} + b_1 e^{-ik_{1z}z}\right) e^{ik_{1x}x}, z < 0 \tag{2.1a}$$

$$H_{2y} = \left(a_2 e^{ik_{2z}z} + b_2 e^{-ik_{2z}z}\right) e^{ik_{2x}x}, z > 0 \tag{2.1b}$$

Here, a_i and b_i are the coefficients of the field ($i = 1,2$), $k_i = \left(\omega\sqrt{\varepsilon_i}/c\right)$ is the wave vector in the respective media.

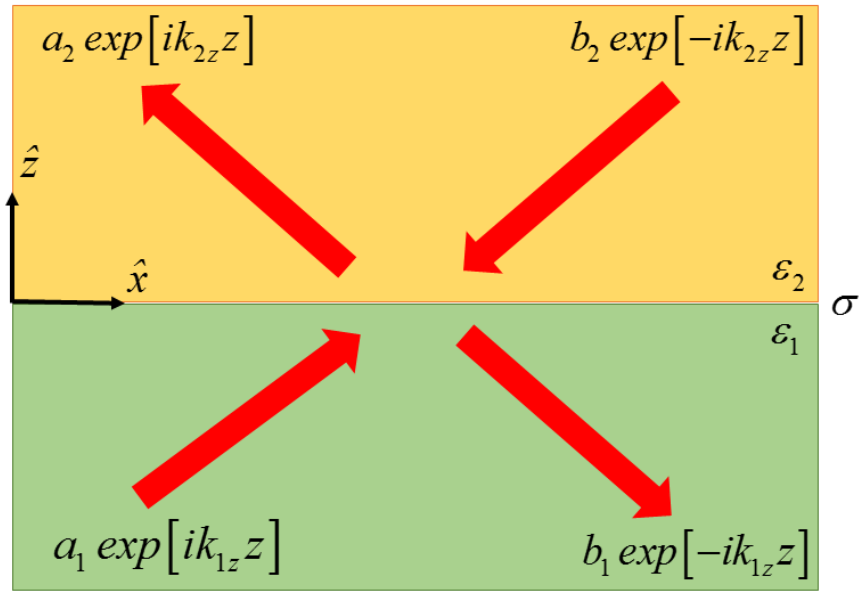

Figure 2.2. An interface characterized by surface conductivity σ is placed in between two media of dielectric constants ε_1 and ε_2.

The boundary conditions across the interface will be:

$$\hat{n}\times\left(\vec{E}_2 - \vec{E}_1\right)\Big|_{z=0} = 0 \tag{2.2a}$$

$$\hat{n}\times\left(\vec{H}_2 - \vec{H}_1\right)\Big|_{z=0} = \vec{J} \tag{2.2b}$$

where, $\hat{n}$ is the unit vector normal to the surface and $\vec{J}$ denotes surface current density of the separating layer. The above boundary condition yields:

$$\frac{k_{1z}}{\varepsilon_1}\left(a_1 - b_1\right) - \frac{k_{2z}}{\varepsilon_2}\left(a_2 - b_2\right) = 0 \tag{2.3a}$$

$$\left(a_1 + b_1\right) - \left(a_2 + b_2\right) = J_x \tag{2.3b}$$

The current density can be determined from the Ohm's Law:

$$J_x = \sigma E_x(z=0) = \frac{\sigma k_{2z}}{\varepsilon_0 \varepsilon_2 \omega}(a_2 - b_2) \tag{2.4}$$

From the above equations, we can obtain:

$$\begin{pmatrix} a_1 \\ b_1 \end{pmatrix} = D_{12} \begin{pmatrix} a_2 \\ b_2 \end{pmatrix} \tag{2.5}$$

where,

$$D_{12}^{p} = \frac{1}{2}\begin{pmatrix} 1+\eta_p+\xi_p & 1-\eta_p-\xi_p \\ 1-\eta_p+\xi_p & 1+\eta_p-\xi_p \end{pmatrix} \tag{2.6}$$

$$\eta_p = \frac{\varepsilon_1 k_{2z}}{\varepsilon_2 k_{1z}}, \xi_p = \frac{\sigma k_{2z}}{\varepsilon_0 \varepsilon_2 \omega}$$

Similar type of relation, we can derive for S polarized component:

$$D_{12}^{s} = \frac{1}{2}\begin{pmatrix} 1+\eta_s+\xi_s & 1-\eta_s+\xi_s \\ 1-\eta_s-\xi_s & 1+\eta_p-\xi_s \end{pmatrix} \tag{2.7}$$

$$\eta_s = \frac{k_{2z}}{k_{1z}}, \xi_s = \frac{\sigma \mu_0 \omega}{k_{1z}}$$

Considering both polarization components, the transmission matrix can be written as:

$$D_{12,m} = \frac{1}{2}\begin{pmatrix} 1+\eta_m+\xi_m & 1-\eta_m-\zeta_m\xi_m \\ 1-\eta_m+\zeta_m\xi_m & 1+\eta_m-\xi_m \end{pmatrix} \tag{2.8}$$

where, $m = s, p$ and $\zeta_p = 1, \zeta_s = -1$.

Next, let us consider the propagation of light through a homogeneous medium. It can be proved [35] that the electric or magnetic at two different points z and $z+\delta z$ are connected by the following propagation matrix:

$$P(\delta z) = \begin{pmatrix} e^{-ik_z \delta z} & 0 \\ 0 & e^{ik_z \delta z} \end{pmatrix} \tag{2.9}$$

If we consider successive N layers of separating media, the transfer matrix (M) is nothing but continuous multiplication of transmission (D) and propagation (P) matrices like:

$$\begin{pmatrix} a_1 \\ b_1 \end{pmatrix} = \mathrm{M} \begin{pmatrix} a_{N+1} \\ b_{N+1} \end{pmatrix} \tag{2.10}$$

where $M = D_{12}P(d_{12})D_{23}P(d_{23}).....P(d_{N-1,N})D_{N,N+1}$ is the transfer matrix.

For any multi-layered sample, the Fresnel reflection and refraction coefficients can easily be calculated if we know the transfer matrix for the structure. With a little bit of algebra, it can be proved that the coefficients are related to the transfer matrix by the following relation:

$$r = \frac{M_{21}}{M_{11}} \tag{2.11a}$$

$$t = \frac{1}{M_{11}} \tag{2.11b}$$

From this, the reflectance and transmittance can easily be calculated:

$$R_{s,p} = \left| r_{s,p} \right|^2 \tag{2.12a}$$

$$T_{s,p} = \eta_{s,p} \left| t_{s,p} \right|^2 \tag{2.12b}$$

where, $\eta_s = \frac{k_{(N+1)z}}{k_{1z}}$ and $\eta_p = \frac{\varepsilon_1 k_{(N+1)z}}{\varepsilon_{N+1} k_{1z}}$.

After some algebra, we can obtain:

$$R_s = \left| \frac{\sqrt{\varepsilon_1}\cos\theta_1 - \sqrt{\varepsilon_2}\cos\theta_2 - \tilde{\sigma}}{\sqrt{\varepsilon_1}\cos\theta_1 + \sqrt{\varepsilon_2}\cos\theta_2 + \tilde{\sigma}} \right|^2 \tag{2.13a}$$

$$R_p = \left| \frac{\sqrt{\varepsilon_2}/\cos\theta_2 - \sqrt{\varepsilon_1}/\cos\theta_1 + \tilde{\sigma}}{\sqrt{\varepsilon_2}/\cos\theta_2 + \sqrt{\varepsilon_1}/\cos\theta_1 + \tilde{\sigma}} \right|^2 \tag{2.13b}$$

$$T_s = \frac{4\sqrt{\varepsilon_1\varepsilon_2}\cos\theta_1\cos\theta_2}{\left| \sqrt{\varepsilon_1}\cos\theta_1 + \sqrt{\varepsilon_2}\cos\theta_2 + \tilde{\sigma} \right|^2} \tag{2.14a}$$

$$T_p = \frac{4\sqrt{\varepsilon_1\varepsilon_2}/\cos\theta_1\cos\theta_2}{\left| \sqrt{\varepsilon_2}/\cos\theta_2 + \sqrt{\varepsilon_1}/\cos\theta_1 + \tilde{\sigma} \right|^2} \tag{2.14b}$$

These reflection and refraction coefficients are the most significant parameters in governing the GH and IF shifts. It will be more prominent in the next section.

2.2.2 Theoretical calculation of the GH shift

Consider a monochromatic collimated Gaussian beam (having wave vector $\vec{k}$) is incident on a dielectric surface (refractive index *n*) coated with monolayer MoS_2 [Figure 2.1(a)]. Figure 2.1(b) has shown the full geometry taken for this calculation. The $\hat{z}$ axis of the laboratory frame $K=(O,x,y,z)$ is taken normal to the interface. We choose the origin in a manner that the reflecting interface has an equation $z=0$. In addition to the laboratory frame, we use a Cartesian frame $K_i=(O,x_i,y_i,z_i)$ attached to the incident beam and another one, $K_r=(O,x_r,y_r,z_r)$ attached to the reflected beam [10]. Let $\vec{k}_0=k_0\hat{z}_i$ and $\vec{k}$ denote the central and non-central wave vectors of the incident beam, respectively with $|\vec{k}|=|\vec{k}_0|=k_0$. The electric field of the incident beam at the air side ($z < 0$) of the interface can be expressed in the angular spectrum representation as [44]:

$$E_i(r)=\sum_{\lambda=1}^{2}\int_{-\infty}^{+\infty} e_\lambda(U,V,\theta)E_\lambda(U,V,\theta)e^{i(UX_i+VY_i+WZ_i)}dUdV \tag{2.15}$$

where, $U=\vec{k}.\hat{x}_i/|\vec{k}_0|, V=\vec{k}.\hat{y}_i/|\vec{k}_0|$

$W=(1-U^2-V^2)^{1/2}$.

We have also defined $X_\alpha=k_0x_\alpha$, $Y_\alpha=k_0y_\alpha$ and $Z_\alpha=k_0z_\alpha$, with $\alpha\in\{i,r\}$. The polarization unit basis vectors $\{e_\lambda\}$ have been chosen as: $\hat{e}_1=\hat{e}_2\times\vec{k}/|\hat{e}_2\times\vec{k}|$ and $\hat{e}_2=\hat{z}\times\vec{k}/|\hat{z}\times\vec{k}|$, where the '×' symbol denotes standard vector cross product in $\mathbb{R}_3$.

By definition, $\vec{k}=k_0(Ux_i+Vy_i+Wz_i)=\hat{x}k_x+\hat{y}k_y+\hat{z}(k_0^2-k_x^2-k_y^2)^{1/2}$ and both $\hat{e}_1$ and $\hat{e}_2$ are orthogonal to $\vec{k}$.

In Equation (2.15), $E_\lambda(U,V)$ is given by:

$$E_\lambda(U,V)=A(U,V)\alpha_\lambda(U,V)$$

where $\alpha_\lambda(U,V,\theta)=e_\lambda(U,V,\theta).\hat{f}$

$\hat{f} = f_p\hat{x} + f_s\hat{y}$ is polarization vector that obeys $|f_p|^2 + |f_s|^2 = 1$.

For a monochromatic Gaussian beam,

$$A(U,V) = exp\left(-w_0^2\left(U^2+V^2\right)\right) \tag{2.16}$$

If we consider the paraxial domain i.e. $U^2+V^2 << 1$, the reflected electric field can be written:

$$E_r(r) = \sum_{\lambda=1}^{2}\int_{-\infty}^{+\infty}\hat{e}_\lambda(-U,V,\pi-\theta)\tilde{A}_\lambda(U,V,\theta)e^{i(-UX_r+VY_r)}dUdV \tag{2.17}$$

where, $\tilde{A}_\lambda(U,V,\theta) = r_\lambda(U,V,\theta)A_\lambda(U,V,\theta)$

$r_\lambda(U,V,\theta)$ are the Fresnel reflection coefficient associated with the plane wave components of the electric field.

Monolayer MoS_2 affects the Fresnel reflection coefficients. Applying Transfer Matrix Method [43], we obtain:

$$r_s(\theta) = \frac{\cos\theta - \sqrt{n^2-\sin^2\theta} - \sigma(\Omega)}{\cos\theta + \sqrt{n^2-\sin^2\theta} + \sigma(\Omega)} \tag{2.18a}$$

$$r_p(\theta) = \frac{n^2\cos\theta - \sqrt{n^2-\sin^2\theta}\left[1-\sigma(\Omega)\cos\theta\right]}{n^2\cos\theta + \sqrt{n^2-\sin^2\theta}\left[1+\sigma(\Omega)\cos\theta\right]} \tag{2.18b}$$

where, θ is the incident angle and σ is the surface conductivity of MoS_2. The Fresnel reflection coefficient can be represented in a general complex form:

$$r_\lambda = R_\lambda\, exp(i\phi_\lambda) \tag{2.19}$$

where, R_λ is the amplitude and ϕ_λ is the phase of the reflection coefficient ($\lambda \in \{p,s\}$). To evaluate the GH shift, we first calculate the centre of mass of the intensity distribution in the reflected frame [45]:

$$\langle R\rangle = \iint dX_r dY_r |E_r|^2 R \Big/ \iint dX_r dY_r |E_r|^2 = \langle X\rangle X_r + \langle Y\rangle Y_r \tag{2.20}$$

The spatial (Δ_{GH}) and angular (Θ_{GH}) GH shift can be calculated.

$$k_0\Delta_{GH} = \langle X_r\rangle_{z=0} \tag{2.21a}$$

$$\Theta_{GH} = \partial\langle X_r \rangle / \partial z \tag{2.21b}$$

Now, in case of a Gaussian light beam [45] :

$$k_0 \Delta_{GH} = w_p \frac{\partial \phi_p}{\partial \theta} + w_s \frac{\partial \phi_s}{\partial \theta} \tag{2.22a}$$

$$\Theta_{GH} = -\left(w_p \frac{\partial \ln R_p}{\partial \theta} + w_s \frac{\partial \ln R_s}{\partial \theta} \right) \tag{2.22b}$$

The GH shift for total internal reflection can also be determined. Consequently, TMM method can be applied to calculate the modified coefficients [43]:

$$r_s(\theta) = \frac{n\cos\theta - \sqrt{1 - n^2 \sin^2\theta} - n\sigma(\Omega)}{n\cos\theta + \sqrt{1 - n^2 \sin^2\theta} + n\sigma(\Omega)} \tag{2.23a}$$

$$r_p(\theta) = \frac{\cos\theta - n\sqrt{1 - n^2 \sin^2\theta}\left[1 - \sigma(\Omega)\cos\theta\right]}{\cos\theta + n\sqrt{1 - n^2 \sin^2\theta}\left[1 + \sigma(\Omega)\cos\theta\right]} \tag{2.23b}$$

The calculation of the GH shift for total internal reflection [45] yields identical Equation (2.22).

MoS_2 layer is categorized by the optical conductivity (σ) which has a significant effect in the GH shift [37-39,46,47] as obvious from the Equations (2.22). For the first time, such a theoretical model has been developed in the analysis of GH shift in 2D materials.

2.3 Results & Discussions

2.3.1 GH shift for partial reflection

Equation (2.22) shows that the spatial and angular GH shifts are influenced by the phase and amplitude parts of the reflection coefficients. Thus we have to first study the complex reflection coefficient of the reflecting surface. Figures 2.3 and 2.4 display the angular dependence of the amplitude and phase of the complex reflection coefficients for P and S-polarization states of the light beam incident upon monolayer MoS_2 coated glass and silicon surfaces, respectively. We have found interesting changes for the surfaces when they are coated with monolayer MoS_2. The amplitude R_p possesses a non-zero value at the pseudo Brewster's angle (θ_B) and also changes with the wavelength of the incident light for MoS_2 coated surfaces. In contrast, the amplitude R_p goes to exactly zero value at θ_B for the uncoated surfaces (when MoS_2 is

absent). Likewise, the phase part ϕ_p undergoes a steady jump to $-\pi$ around θ_B for monolayer MoS_2 coated surfaces whereas it suffers a sharper jump for the uncoated surfaces. The behaviour of R_s and ϕ_s are also wavelength dependent and show dissimilar characteristics when monolayer MoS_2 is present. Also, $R_{p,s}$ has a greater value for monolayer MoS_2 coated silicon surface due to the higher index of refraction of silicon in comparison to the glass surface as seen from Figures 2.3 and 2.4.

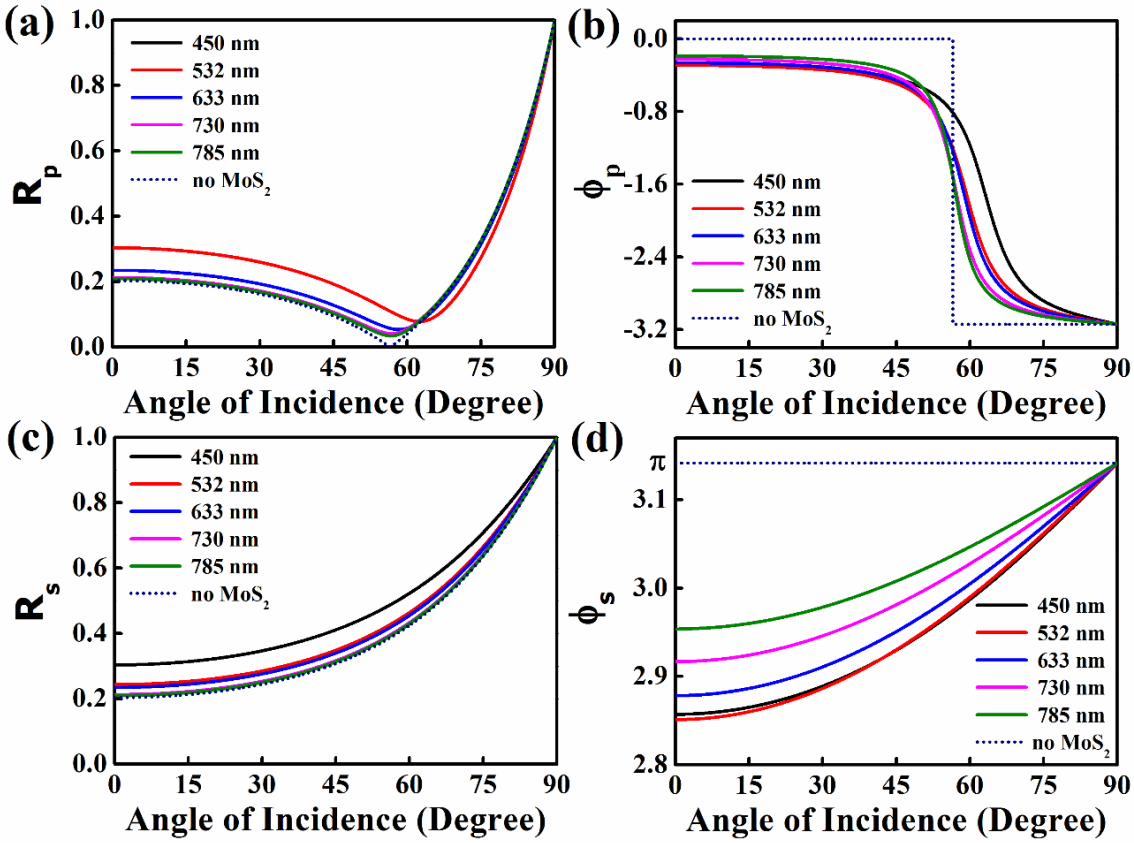

Figure 2.3. Modulus (R) and phase (ϕ) of reflection coefficients for **(a, b)** P-polarized and **(c, d)** S-polarized light beam incident on monolayer MoS_2 coated glass surface for partial reflection.

It is well-established that (in the absence of monolayer MoS_2 coating) for an air-dielectric interface, $\partial\phi_\lambda/\partial\theta = 0$ and therefore, the spatial GH shift, $\Delta_{GH} = 0$. The revolutionary experiment by Goos and Hänchen proved that $\Delta_{GH} \neq 0$ occurs for total internal reflection of

light, where $R_\lambda = 1 \text{and} \partial\phi_\lambda / \partial\theta \neq 0$ (λ = P, S). Contrastingly, for both partial and total internal reflection of light from monolayer MoS_2 coated surfaces, R_λ and ϕ_λ change with θ and λ.

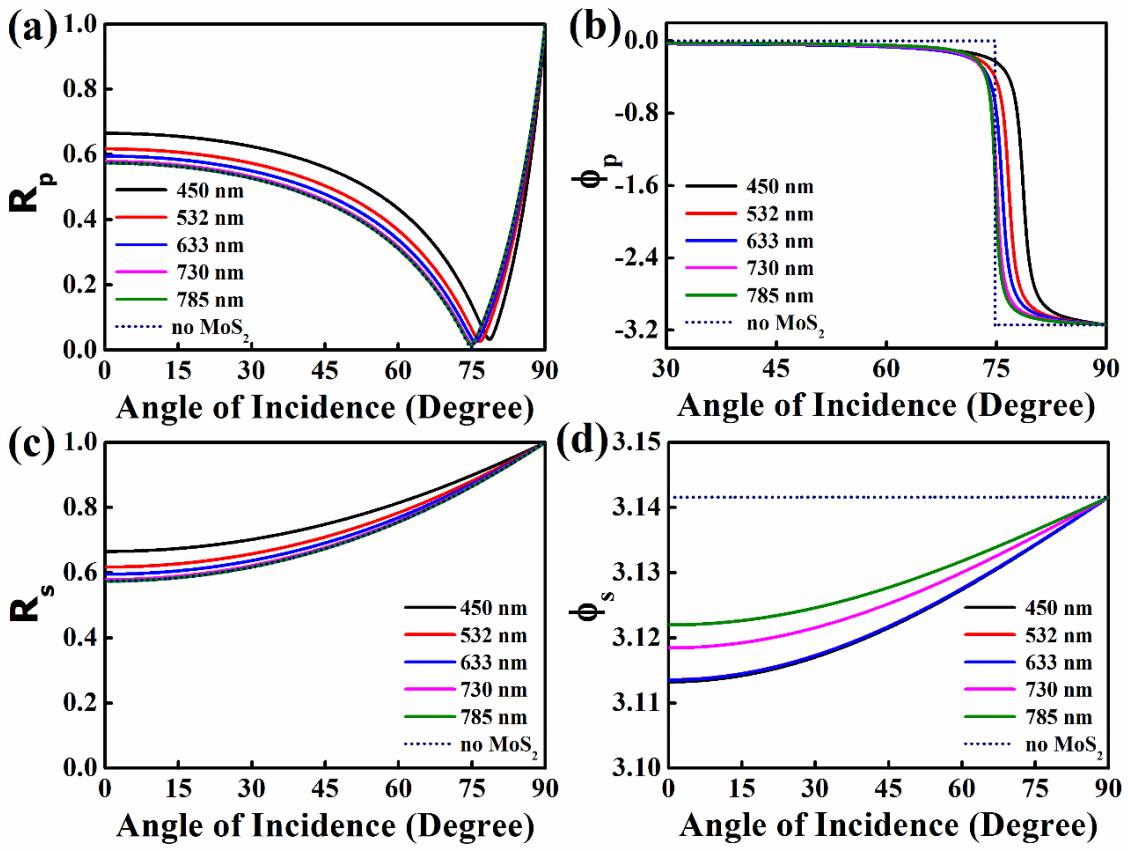

Figure 2.4. Modulus (R) and phase (ϕ) of reflection coefficient for: **(a, b)** P-polarized and **(c, d)** S-polarized light beam incident on monolayer MoS_2 coated silicon surface for partial reflection.

Subsequently, we observed spatial and angular GH shifts even without the total internal reflection domain for the monolayer MoS_2-coated surfaces, which is an outstanding observation of this *Chapter*. Monolayer MoS_2 is one of the few cases [48,49] where non-zero GH shift exists also for partial reflection of light. The adimensional spatial GH shift ($k_0\Delta_{GH}$) and the angular GH shift (Θ_{GH}) for partial reflection of light are displayed in Figure 2.5 and Figure 2.6, respectively. The nature of spatial shift (Figure 2.5) and angular shift (Figure 2.6) are different for incident P and S-polarization states of the beam.

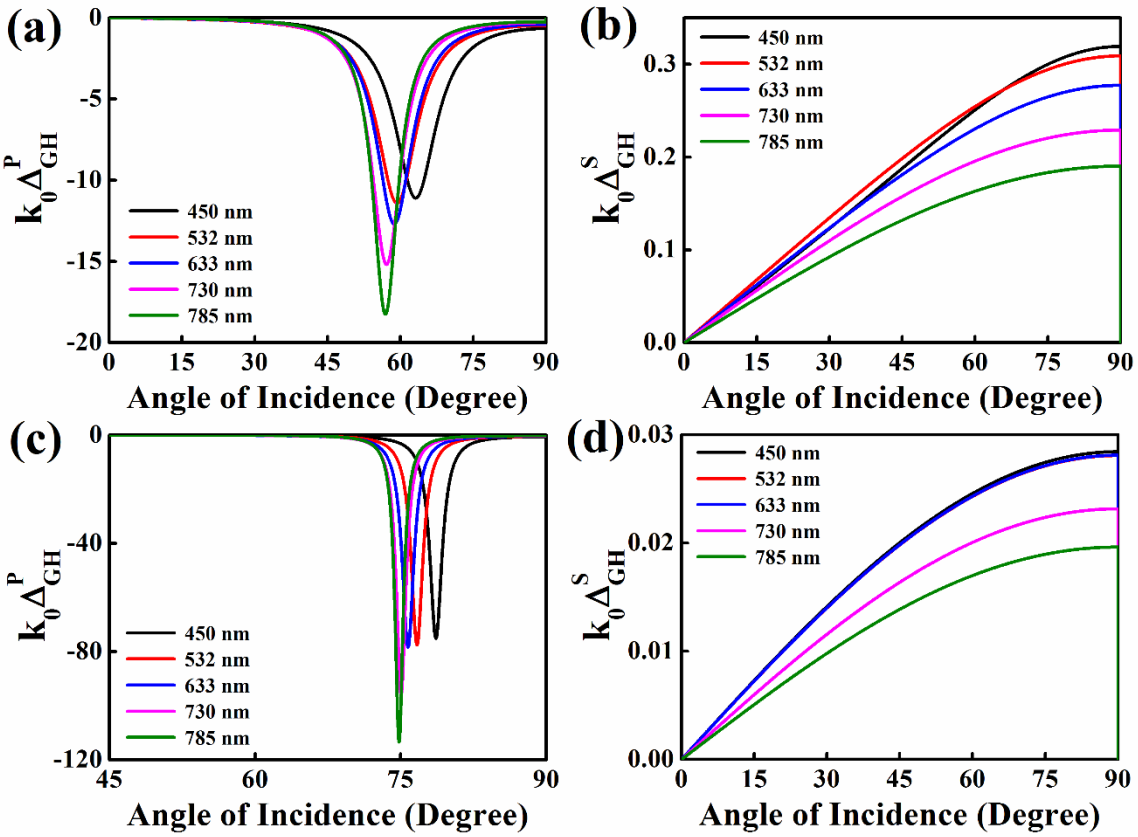

Figure 2.5. Spatial GH shift in monolayer MoS_2-coated glass for **(a)** P-polarized and **(b)** S-polarized light. Spatial GH shift in monolayer MoS_2-coated silicon for **(c)** P-polarized and **(d)** S-polarized light (**Partial reflection**).

Remarkably, the spatial shift for P-polarization ($k_0\Delta_{GH}^P$) shows a negative peak at the pseudo Brewster's angle because of the sharp variation of ϕ_p from 0 to -π in the vicinity of the pseudo Brewster's angle. Nevertheless, the existence of a giant negative shift was predicted for the graphene-coated surfaces [36]. Though monolayer MoS_2 coated surface yields a negative shift, but it is not as high as graphene coated surfaces. The spatial shift for S-polarization ($k_0\Delta_{GH}^S$) is, however, smoothly increasing with incident angle. For the monolayer MoS_2 coated silicon surface, the spatial shift for P-polarization is greater than the glass surface whereas it is found to be reversed for the S-polarization. Furthermore, the spatial shifts are also wavelength dependent being greater for longer wavelength light for P-polarization. In contrast, the S-polarized light behaves in a different manner where $k_0\Delta_{GH}^S$ becomes greater for the shorter wavelength side. We also found that spatial shift for S-polarization state is 10^2 orders of

magnitude smaller than P-polarization states of the light beam and larger in magnitude than the graphene-coated surfaces [36].

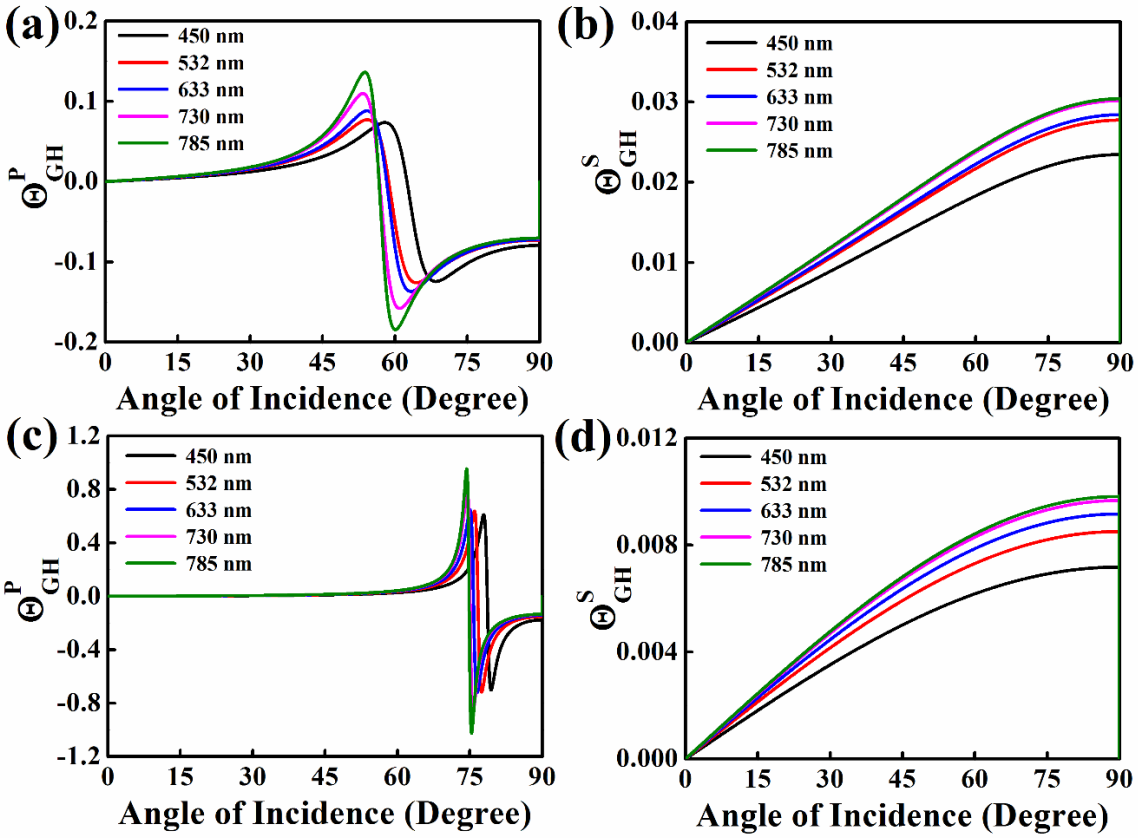

Figure 2.6. Angular GH shift in monolayer MoS_2 coated glass for **(a)** P-polarized and **(b)** S-polarized light. Angular GH shift in monolayer MoS_2 coated silicon for **(c)** P-polarized and **(d)** S-polarized light (**Partial reflection**)

Afterward, we have observed angular GH shifts for partial reflection as shown in Figure 2.6. The change in R_λ caused by the presence of the monolayer MoS_2 is quite small, although the change increases with decreasing wavelength. Hence, we have observed a non-zero but small angular GH shift when monolayer MoS_2-coating is present. This is a noteworthy observation for the MoS_2-coated surface compared to a graphene-coated surface as the angular shifts were not present for graphene [39].

2.3.2 GH shift for total internal reflection

We have then concentrated on the GH shift for the total internal reflection of the light. In both Figure 2.7 and Figure 2.8, we have explained the behaviour of amplitude and phase of the complex reflection coefficients for S and P-polarization states of light incident on MoS_2-coated glass and silicon surfaces, respectively. The amplitude R_p dips down to zero at the pseudo Brewster's angle and acquires its peak of unity at the critical angle of incidence in absence of MoS_2 coating.

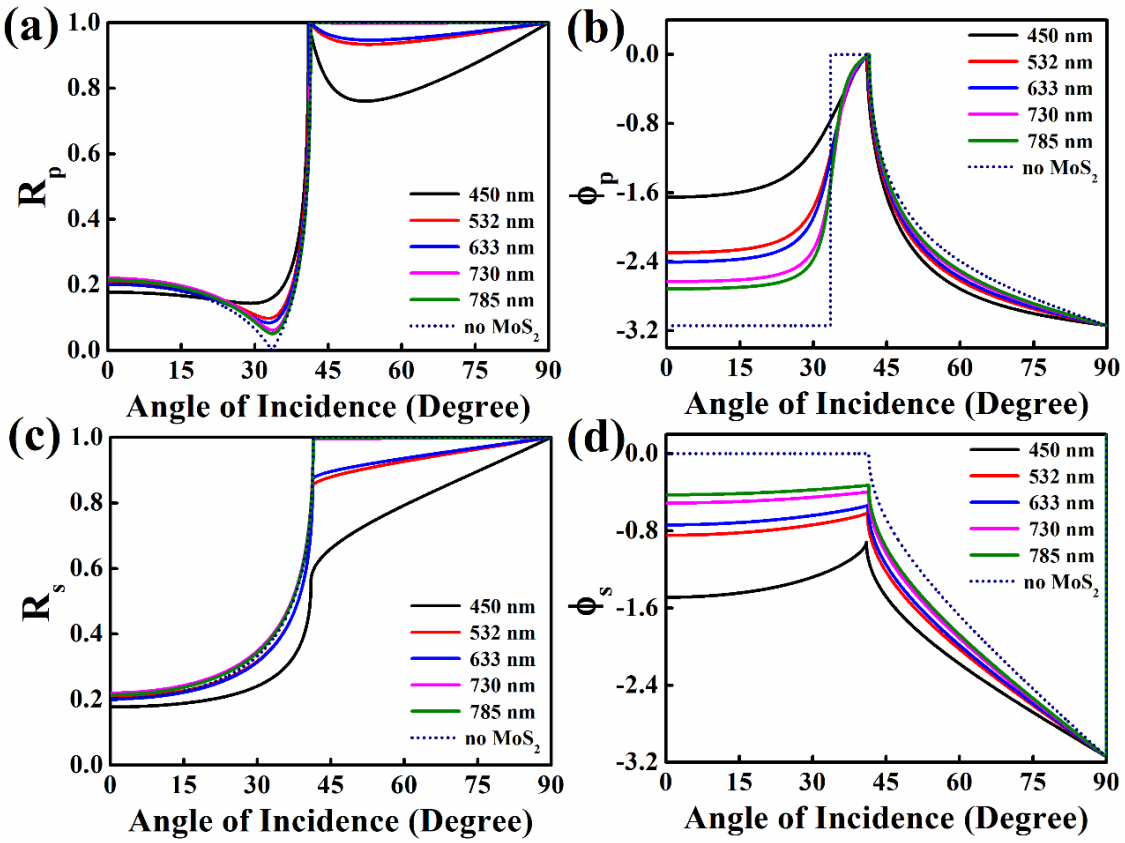

Figure 2.7. Modulus (R) and phase (ϕ) of reflection coefficient for: **(a, b)** P-polarized and **(c, d)** S-polarized light incident on monolayer MoS_2-coated glass surface for total internal reflection.

The phase ϕ_p also jumps from $-\pi$ to 0 at θ_B followed by a continuous jump from 0 to $-\pi$ at the critical angle (θ_C) when there is no MoS_2 coating. But, when the monolayer MoS_2 is present, deviations are observed for different wavelengths as demonstrated in Figures 2.7 & 2.8. Greater deviations are seen for longer wavelengths in monolayer MoS_2 coated surfaces. Likewise, for

S-polarized light beam, R_s smoothly increases to unity and ϕ_s smoothly decreases from 0 to - π near θ_C for uncoated surfaces. Noteworthy deviations are observed for monolayer MoS_2 coated surfaces for different wavelengths with larger deviations occurring at smaller wavelengths. Nevertheless, the variation of ϕ_λ with incident angle as well as wavelength directly affects the spatial GH shift. The spatial GH shift ($k_0\Delta_{GH}^{P}$) for the P-polarization state of light shows a peak at θ_B and a dip at θ_C [Figure 2.9].

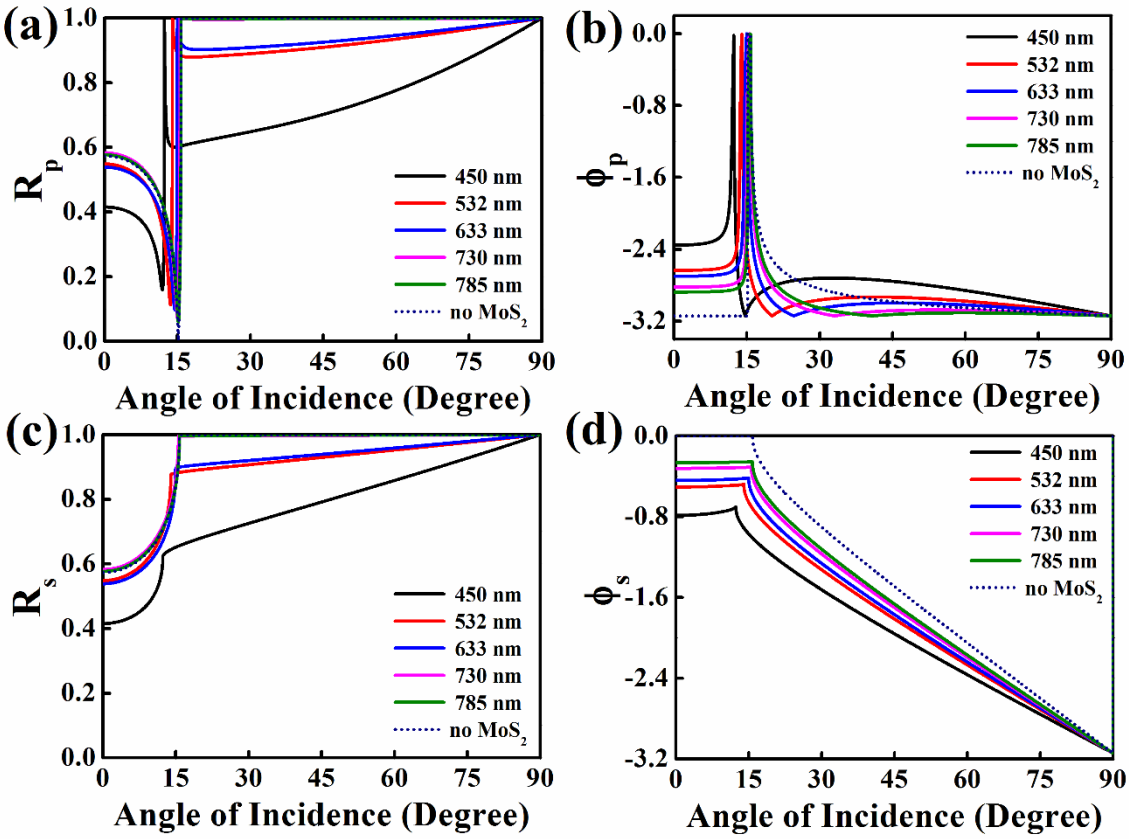

Figure 2.8. Modulus (R) and phase (ϕ) of reflection coefficient for: **(a, b)** P-polarized **(c, d)** S-polarized light beam incident on monolayer MoS_2-coated silicon surface for total internal reflection.

Its magnitude is greater in comparison to the case of the graphene-coated surface as stated previously [36]. Moreover, the spatial shift ($k_0\Delta_{GH}^{S}$) for the S-polarization state of light displays a negative to positive change near the critical angle which was not seen for the graphene-coated

surface. The behaviour of spatial GH shifts is similar for both types of surfaces except the magnitudes of shifts are greater for monolayer MoS_2 coated silicon than the glass surface. With decreasing wavelength, R_λ shows a larger deviation in comparison to the surfaces without monolayer MoS_2 coating. Hence, we presume greater angular GH shift for smaller wavelengths which is straightforward from Figure 2.10.

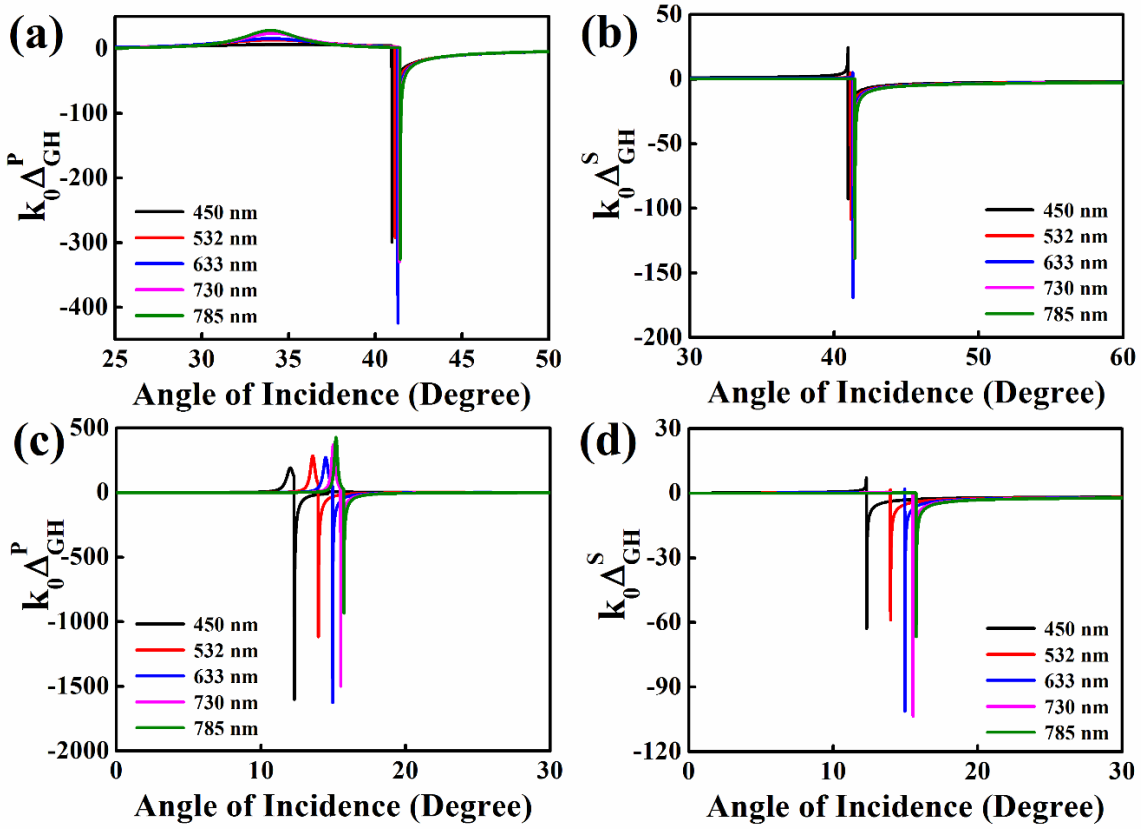

Figure 2.9. Spatial GH shift in monolayer MoS_2-coated glass for **(a)** P-polarized and **(b)** S-polarized light. Spatial GH shift in monolayer MoS_2-coated silicon for **(c)** P-polarized and **(d)** S-polarized light. (**Total internal reflection**)

We have previously found that the GH shifts in monolayer MoS_2 coated surfaces depend upon the mode of polarization, the wavelength of incident light, and the characteristics of the reflecting surfaces. For the P-polarization state of light beam, the GH shift unveils peak (for partial reflection) or dip (for total internal reflection) in the neighbourhood of the pseudo Brewster's angle and also exhibits a peak adjacent to the critical angle. In contrast, the S-

polarization state of light does not resemble the similar dependence on these special angles. These observations give insight into the non-trivial features of the GH shifts adjacent to the pseudo Brewster's angle and the critical angle which agrees well with the preceding reports [50].

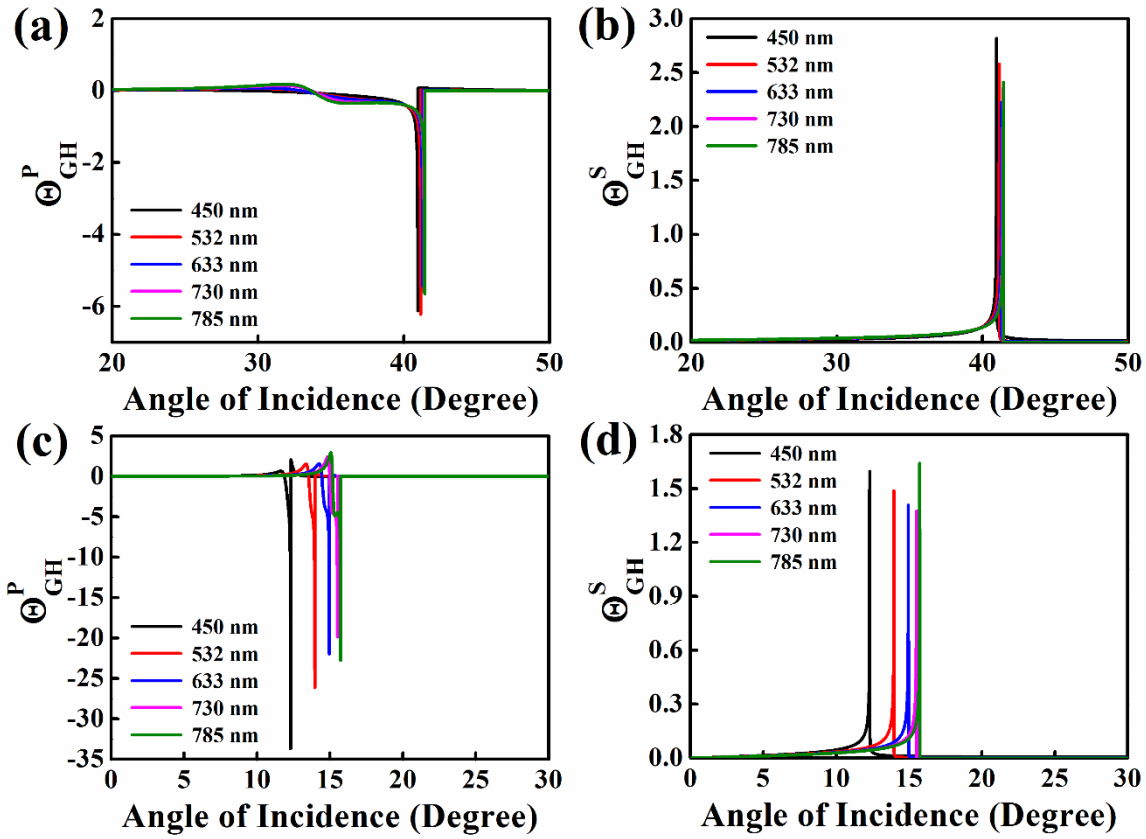

Figure 2.10. Angular GH shift in monolayer MoS_2-coated glass for **(a)** P-polarized and **(b)** S-polarized light. Spatial GH shift in monolayer MoS_2-coated silicon for **(c)** P-polarized and **(d)** S-polarized light. (**Total internal reflection**)

2.3.3 Variation of GH shift with the thickness

We have also concentrated on the thickness dependence of the GH shift. It is already proven that the thickness of monolayer MoS_2 is about 0.65 nm [51]. The characteristics of monolayer MoS_2 is reasonably different from its multilayered form as already discussed in the last *Chapter*. In this section, we have performed a comparison of the nature of spatial GH shifts for monolayer MoS_2 with the bulk material. As seen from Figure 2.11, for partial reflection of the S-polarized light, $k_0\Delta_{GH}^S$ is larger for monolayer MoS_2 than the bulk counterpart. But, for the

P-polarization state, the shift $k_0\Delta_{GH}^{P}$ has a lesser magnitude for monolayer MoS_2 coated surface. For the total internal reflection of both P and S-polarized incident light, a giant negative shift is found, but the maximum shift value is dominated by the bulk MoS_2 material. The reason may be due to the surface optical conductivity of the material. The optical conductivity of bulk MoS_2 is different than its monolayer [47] form which evidently gives rise to the differing effects on the reflection coefficients. Considering this, GH shift obviously relies upon the layer thickness of MoS_2 and can be an effective way to differentiate a monolayer MoS_2 from a multi-layered material.

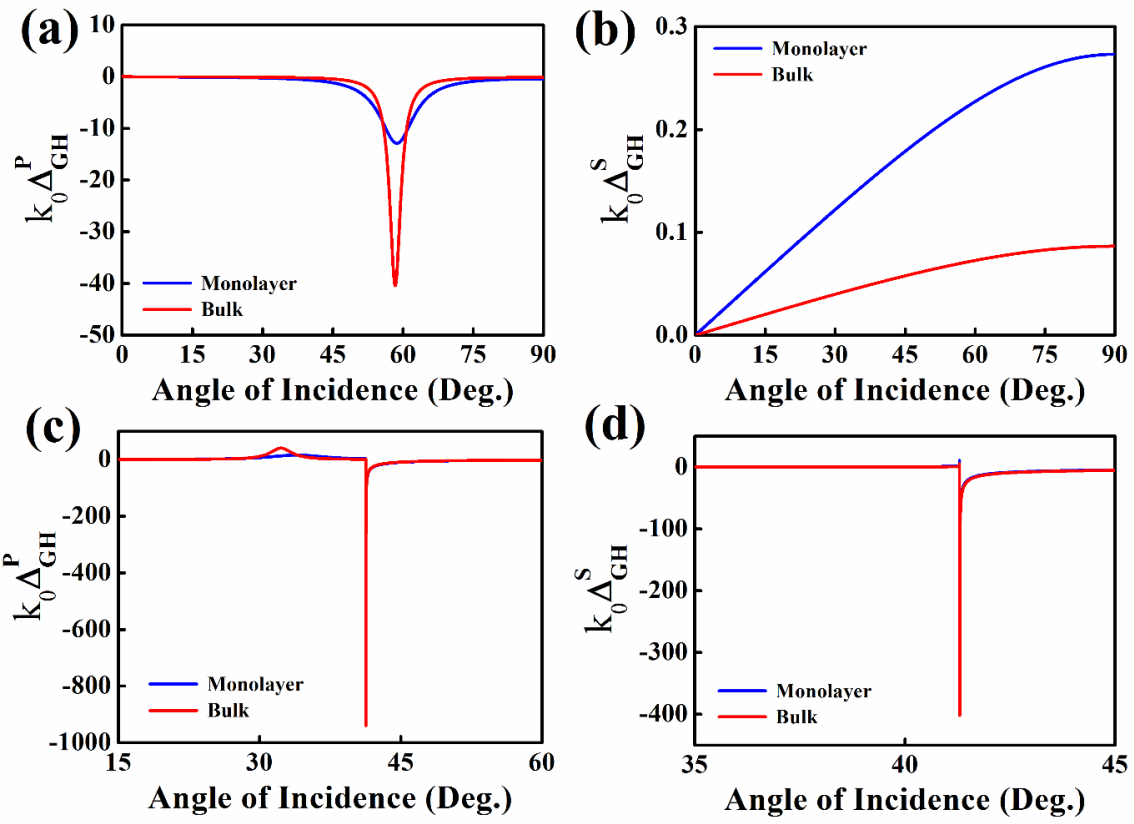

Figure 2.11. Spatial GH shift for P-polarized and S-polarized light incident on monolayer MoS_2 coated glass surface for partial reflection **(a, b)** and total internal reflection **(c, d)**.

2.3.4 Shift comparison between different 2D materials

We have also investigated the GH shift for different types of 2D materials like graphene, monolayer boron nitride (BN), monolayer MoS_2. Although all of them belong to the 2D

materials class, they have several different features from each other [52], as discussed in *Chapter* 1. Hence, we presume dissimilar behavior in their optical properties. We can find from Figure 2.12 that $k_0\Delta_{GH}^{S}$ has a large magnitude for partial reflection of the S-polarized light in monolayer MoS_2. But, for the P-polarized light, the shift $k_0\Delta_{GH}^{P}$ is sufficiently suppressed. The giant negative spatial shift is found for total internal reflection of both P and S-polarization states of light. Though the nature of GH shift, in this case, is similar for all three materials, the maximum shift is obtained for BN which is marginally greater in magnitude than monolayer MoS_2 but significantly greater than graphene coated surfaces.

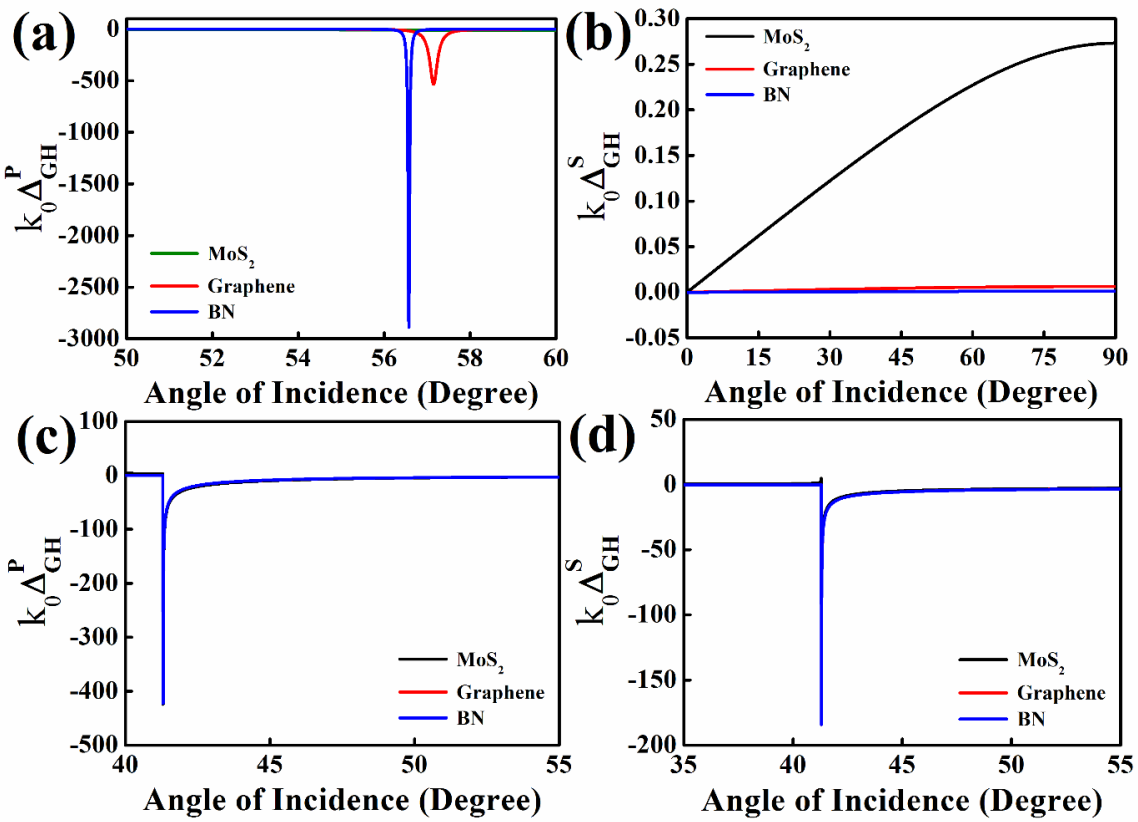

Figure 2.12. Spatial GH shift for P-polarized and S-polarized light incident on monolayer MoS_2, graphene, monolayer BN coated glass surface for partial reflection **(a, b)** and total internal reflection **(c, d)**.

Again, the optical properties of these materials rely on the surface optical conductivities. The reflection coefficients are well-affected by the optical conductivities of these materials that

result differing GH shifts. On that account, we can infer that the nature of different 2D materials is not so distinct from each other for total internally reflected light. But for partial reflection of light, we notice significant dissimilarities in their response of GH shifts. The GH shift for monolayer MoS_2 greatly dominates for S-polarization states, but is significantly suppressed for P-polarization states of light in comparison to graphene and monolayer boron nitride. Hence, the observation of spatial GH shifts for partial reflection of light provides us the opportunity to distinguish different 2D materials from their individual characteristics.

2.4 Outlook & Summary

We have a comprehensive theoretical analysis of the GH shift in monolayer MoS_2-coated surfaces for a fundamental Gaussian beam and consequently discovered the characteristics of GH shift like their dependence on different wavelengths, different surfaces, polarization states, incident angles, etc. The GH shift, in general, depends upon the amplitude and phase of reflection coefficients of the incident beam. From the analysis, it is quite obvious that the reflection coefficients are greatly affected by the presence of monolayer MoS_2, which causes non-zero GH shift even for partial reflection of light. The effect on the reflection coefficients increases with decreasing wavelength, which ultimately causes greater shifts. Additionally, we have thoroughly investigated how the GH shift in presence of monolayer MoS_2 coating depends upon the substrate properties. We find that the silicon substrate (having a larger index of refraction than the glass) generates greater GH shifts. In addition, we have demonstrated the thickness dependence of GH shift for MoS_2 coated surfaces which offers a scope to distinguish monolayers from bulk MoS_2 by observing the beam shift characteristics. Consequently, we have compared the GH shift behaviour for different 2D materials (graphene, monolayer MoS_2, monolayer BN). The vast contribution of optical conductivity on the Fresnel reflection coefficients which in effect governs the characteristics of GH shifts has been discussed throughout. Our theoretical model can also be applied to predict the nature of beam shifts for other 2D TMDCs, layered structures as well as topological insulators with different modes of the light beam (e.g. Laguerre-Gauss, Hermite-Gauss, and Bessel, etc.) other than Gaussian. These theoretical findings may open new possibilities for further understanding of GH shift for TMDCs which may lead to several new applications of these materials.

References

[1] M. Born and E. Wolf, *Principles of Optics: Electromagnetic Theory of Propagation, Interference and Diffraction of Light* (Elsevier Science, 2013).

[2] J. D. Jackson, *Classical electrodynamics* (Wiley, 1975).

[3] K. Y. Bliokh and A. Aiello, Journal of Optics **15**, 014001 (2013).

[4] A. Aiello, New Journal of Physics **14**, 013058 (2012).

[5] F. Goos and H. Hänchen, Annalen der Physik **436**, 333 (1947).

[6] C. Imbert, Physical Review D **5**, 787 (1972).

[7] K. Artmann, Annalen der Physik **437**, 87 (1948).

[8] F. I. Fedorov, Dokl. Akad. Nauk SSSR **105**, 465 (1955).

[9] H. Schilling, Annalen der Physik **471**, 122 (1965).

[10] A. Aiello, M. Merano, and J. P. Woerdman, Physical Review A **80**, 061801 (2009).

[11] X. Yin and L. Hesselink, Applied Physics Letters **89** (2006).

[12] L. Salasnich, Physical Review A **86**, 055801 (2012).

[13] J. He, J. Yi, and S. He, Opt. Express **14**, 3024 (2006).

[14] I. V. Soboleva, V. V. Moskalenko, and A. A. Fedyanin, Physical Review Letters **108**, 123901 (2012).

[15] S. Longhi, G. Della Valle, and K. Staliunas, Physical Review A **84**, 042119 (2011).

[16] S. Grosche, A. Szameit, and M. Ornigotti, Physical Review A **94**, 063831 (2016).

[17] C. Xu, J. Xu, G. Song, C. Zhu, Y. Yang, and G. S. Agarwal, Opt. Express **24**, 21767 (2016).

[18] H. M. Lai and S. W. Chan, Opt. Lett. **27**, 680 (2002).

[19] Y. Huang, Z. Yu, C. Zhong, J. Fang, and Z. Dong, Opt. Mater. Express **7**, 1473 (2017).

[20] Y. Y. Huang, W. T. Dong, L. Gao, and C. W. Qiu, Opt. Express **19**, 1310 (2011).

[21] W. Dong, L. Gao, and C. W. Qiu, Progress In Electromagnetics Research **90**, 255 (2009).

[22] C. W. J. Beenakker, R. A. Sepkhanov, A. R. Akhmerov, and J. Tworzydło, Physical Review Letters **102**, 146804 (2009).

[23] S.-Y. Lee, J. Le Deunff, M. Choi, and R. Ketzmerick, Physical Review A **89**, 022120 (2014).

[24] D. H. Foster, A. K. Cook, and J. U. Nöckel, Opt. Lett. **32**, 1764 (2007).

[25] J. Unterhinninghofen, J. Wiersig, and M. Hentschel, Physical Review E **78**, 016201 (2008).

[26] T. Hashimoto and T. Yoshino, Optics Letters **14**, 913 (1989).

[27] X. Hu, Y. Huang, W. Zhang, D.-K. Qing, and J. Peng, Opt. Lett. **30**, 899 (2005).

[28] F. de Fornel, *Evanescent Waves: From Newtonian Optics to Atomic Optics* (Springer, 2001).

[29] K. S. Novoselov, D. Jiang, F. Schedin, T. J. Booth, V. V. Khotkevich, S. V. Morozov, and A. K. Geim, Proceedings of the National Academy of Sciences of the United States of America **102**, 10451 (2005).

[30] A. D. Yoffe, Solid State Ionics **39**, 1 (1990).

[31] A. H. Castro Neto, Physical Review Letters **86**, 4382 (2001).

[32] K. F. Mak, C. Lee, J. Hone, J. Shan, and T. F. Heinz, Physical Review Letters **105**, 136805 (2010).

[33] K. S. Novoselov, V. I. Fal′ko, L. Colombo, P. R. Gellert, M. G. Schwab, and K. Kim, Nature **490**, 192 (2012).

[34] C. Ataca, H. Şahin, and S. Ciraci, The Journal of Physical Chemistry C **116**, 8983 (2012).

[35] A. Splendiani, L. Sun, Y. Zhang, T. Li, J. Kim, C.-Y. Chim, G. Galli, and F. Wang, Nano Letters **10**, 1271 (2010).

[36] J. K. Ellis, M. J. Lucero, and G. E. Scuseria, Applied Physics Letters **99** (2011).

[37] X. Li, P. Wang, F. Xing, X.-D. Chen, Z.-B. Liu, and J.-G. Tian, Opt. Lett. **39**, 5574 (2014).

[38] S. Chen, C. Mi, L. Cai, M. Liu, H. Luo, and S. Wen, Applied Physics Letters **110**, 031105 (2017).

[39] S. Grosche, M. Ornigotti, and A. Szameit, Opt. Express **23**, 30195 (2015).

[40] W. Wu, S. Chen, C. Mi, W. Zhang, H. Luo, and S. Wen, Physical Review A **96**, 043814 (2017).

[41] P. Yeh, *Optical Waves in Layered Media* (Wiley, 2005).

[42] J. Zi, J. Wan, and C. Zhang, Applied Physics Letters **73**, 2084 (1998).

[43] T. Zhan, X. Shi, Y. Dai, X. Liu, and J. Zi, Journal of Physics: Condensed Matter **25**, 215301 (2013).

[44] L. Mandel and E. Wolf, *Optical Coherence and Quantum Optics* (Cambridge University Press, Cambridge, 1995).

[45] M. Ornigotti and A. Aiello, Journal of Optics **15**, 014004 (2013).

[46] A. Rohatgi, WebPlotDigitizer.

[47] Y. V. Morozov and M. Kuno, Applied Physics Letters **107** (2015).

[48] P. Ma and L. Gao, Opt. Express **25**, 9676 (2017).

[49] L.-G. Wang, H. Chen, and S.-Y. Zhu, Opt. Lett. **30**, 2936 (2005).

[50] A. Aiello and J. P. Woerdman, arxiv **0903** (2009).

[51] H. Rydberg, M. Dion, N. Jacobson, E. Schröder, P. Hyldgaard, S. I. Simak, D. C. Langreth, and B. I. Lundqvist, Physical Review Letters **91**, 126402 (2003).

[52] J.-W. Jiang, Frontiers of Physics **10**, 287 (2015).

Chapter 3 Optical Beam Shifts in TMDCs

Using the Transfer Matrix Method, we theoretically studied GH and IF shifts for different TMDCs (WS_2, WSe_2, MoS_2, $MoSe_2$). We have done a detailed comparative analysis of optical beam shifts along with their explicit dependence on the wavelength, angle of incidence, and wavelength of incident light.

Content of this chapter has been published in: **A. Das** and M. Pradhan, "*Exploring the optical beam shifts in monolayers of transition metal dichalcogenides using Gaussian beams*," **Optics Communications** 437, 312-320 (2019).

3 Optical Beam Shifts in TMDCs

3.1 Introduction

We have already discussed in the last *Chapter* the inability of the conventional laws of reflection and refraction [1,2] in real optical beams. The electromagnetic field of a real optical beam can be disintegrated into an assembly of plane wave components each having a definite wave vector (developing an envelope in momentum space). Each of these plane waves suffers reflection independently according to the laws of reflection. The summation of all of these components generates the resultant beam. This reflected beam can manifest both the GH and IF shifts [3-14] depending upon the external and internal conditions (that will be explained in this *Chapter*). As indicated in *Chapter* 1, the detection of these beam shifts is a challenging job due to its wavelength scale magnitude [8,15-20]. However, if detected precisely, these transverse or longitudinal shifts can be applied at a large scale in the modern device industry depending upon the field of application [21-23].

In the last *Chapter*, we have discussed GH shift in monolayer MoS_2 extensively. Hence, we now concentrate on other TMDCs that have close similarities with it. It is expected that all of these TMDCs [24-26] due to their distinctive band structure and optoelectrical properties can be interesting candidates for both GH and IF shifts study [27-30]. Similar to the other quantum systems [15,31-40], we expect non-trivial features of optical beam shifts in TMDCs.

In this *Chapter*, four TMDCs are considered (a) WS_2, (b) WSe_2, (c) MoS_2, and (d) $MoSe_2$. Like the last *Chapter*, the optical beam shifts for partially reflected as well as total internally reflected light are explained. Non-trivial nature around the special angles [41,42] is observed for all the TMDCs. The presence of the Giant GH shift can be stimulating in sensors and device applications. The dependence of GH and IF shifts on the external factors such as the wavelength (400-1200 nm) and polarization states of the incident light beam, angle of incidence, thickness dependence (comparison with the bulk sample) are well-explained in this *Chapter*.

Furthermore, surface optical conductivity of the 2D materials is a major factor in governing the optical response of the materials [43,44]. Accordingly, the influence of the optical conductivity in the nature of GH and IF shifts are explained in later sections.

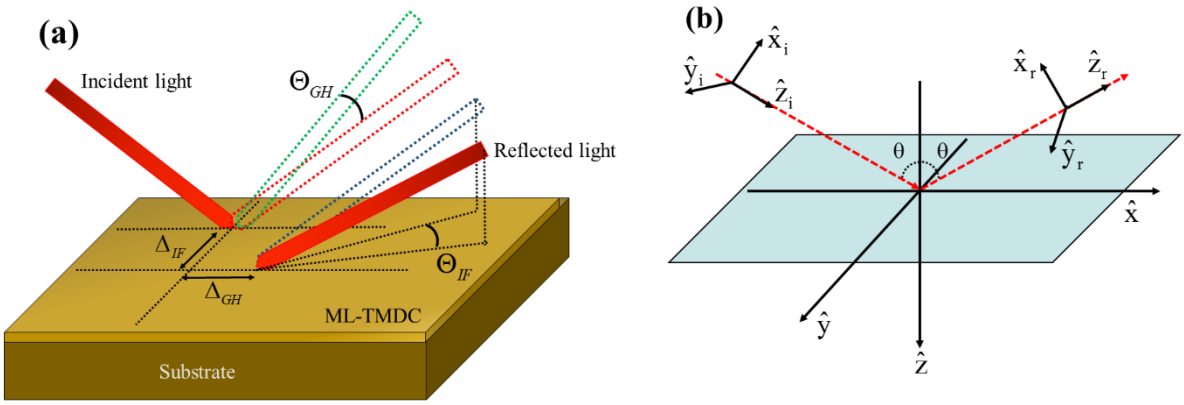

Figure 3.1. GH and IF shifts: **(a)** Pictorial representation of the phenomena and **(b)** Construction of the coordinate system for the theoretical calculation of the optical beam shifts.

3.2 Theory

Following the schematic representation of Figure 3.1, let us consider a monochromatic Gaussian light beam reflected from a monolayer (ML) TMDC coated surface. Here, the TMDC monolayer is modelled as an infinitesimally thin, local two-sided surface characterized by a complex surface conductivity $\sigma(\omega)$ following the previous works for graphene [45,46].

For convenience, we can define three coordinate systems: the laboratory frame $\{\hat{x},\hat{y},\hat{z}\}$ attached to the dielectric interface, and two auxiliary frames $\{\hat{x}_k,\hat{y}_k,\hat{z}_k\}$ attached to the incident ($k=i$) and the reflected ($k=r$) field, respectively [11,14,31,41,47]. In the angular spectrum representation, the electric field of the incident beam at the air side of the interface ($z<0$) can be written as [48]:

$$E_i(r)=\sum_{\lambda=1}^{2}\int_{-\infty}^{+\infty} e_\lambda(U,V,\theta)E_\lambda(U,V,\theta)e^{i(UX_i+VY_i+WZ_i)}dUdV \tag{3.1}$$

where, λ is the polarization index ($\lambda=1,2$ corresponds to P and S-polarization, respectively). Also, $U=\vec{k}.\hat{x}_i/|\vec{k}_0|$, $V=\vec{k}.\hat{y}_i/|\vec{k}_0|$ and $W=\sqrt{1-U^2-V^2}$ are the dimensionless components of the wave vector $\vec{k}$ in the incident frame, connected to the wave vector in the laboratory frame by:

$$\vec{k} = k_0\left(Ux_i + Vy_i + Wz_i\right) = \hat{x}k_x + \hat{y}k_y + \hat{z}\sqrt{k_0^2 - k_x^2 - k_y^2} \tag{3.2}$$

Moreover, in Equation (3.1), $E_\lambda(U,V)$ is the vector spectral amplitude which determines the shape and polarization of the beam and can be written as:

$$E_\lambda\left(U,V\right) = A\left(U,V\right)\alpha_\lambda\left(U,V\right)$$

Here, $A\left(U,V\right)$ being the angular spectrum of the incident field and $\alpha_\lambda\left(U,V\right)$ the polarization function given by $\alpha_\lambda\left(U,V,\theta\right) = \hat{e}_\lambda\left(\vec{k}\right).\hat{f}$, with $\hat{e}_\lambda\left(\vec{k}\right)$ representing the polarisation vectors attached to the single plane wave components of the incident beam. The polarization unit basis vectors $\left\{e_\lambda\right\}$ have been chosen as: $\hat{e}_1 = \dfrac{\hat{e}_2 \times \vec{k}}{\left|\hat{e}_2 \times \vec{k}\right|}$ and $\hat{e}_2 = \dfrac{\hat{z} \times \vec{k}}{\left|\hat{z} \times \vec{k}\right|}$, where the '×' symbol denotes the standard vector cross product in $\mathbb{R}_3$.

Thus $\left\{\hat{e}_1, \hat{e}_2, \hat{k}\right\}$ forms a complete orthogonal basis set in $\mathbb{R}_3$. Conventionally, a plane wave whose electric field is parallel to either $\hat{e}_1$ or $\hat{e}_2$ is referred to as either TM (p-polarization) or TE wave (s-polarization), respectively.

The unit vector $\hat{f} = a_p\hat{x}_i + a_s\, exp\left(i\eta\right)\hat{y}_i$ (with $a_p, a_s, \eta \in \mathbb{R}$) fixes the polarization state.

After reflection, each plane wave component of the Fourier spectrum (Equation (3.1)) undergoes modification by Fresnel's law.

Therefore, $\hat{e}_\lambda\left(\vec{k}\right)e^{i\vec{k}.\vec{r}} \rightarrow r_\lambda\left(\vec{k}\right)\hat{e}_\lambda\left(\tilde{k}\right)e^{i\tilde{k}.\vec{r}}$

where, $r_\lambda\left(\vec{k}\right)$ is the Fresnel reflection coefficient and $\tilde{k} = \vec{k} - 2\hat{z}\left(\hat{z}.\vec{k}\right)$

Thus, the electric field in the reflected frame can be expressed as:

$$E_r\left(r\right) = \sum_{\lambda=1}^{2}\int_{-\infty}^{+\infty}\tilde{A}_\lambda\left(U,V,\theta\right)e^{i\left(-UX_r + VY_r + WZ_r\right)}dUdV \tag{3.3}$$

where, $\tilde{A}_\lambda\left(U,V,\theta\right) = \hat{e}_\lambda\left(-U,V,\pi-\theta\right)r_\lambda\left(U,V\right)\alpha_\lambda\left(U,V,\theta\right)A\left(U,V\right)$

When a 2D material is deposited upon a dielectric surface, the Fresnel's reflection coefficients are modified, and by applying the Transfer Matrix Method (TMM) for layered media [49], these reflection coefficients can be obtained as:

$$r_s(\theta)=\frac{\cos\theta-\sqrt{n^2-\sin^2\theta}-\tilde{\sigma}(\Omega)}{\cos\theta+\sqrt{n^2-\sin^2\theta}+\tilde{\sigma}(\Omega)} \tag{3.4a}$$

$$r_p(\theta)=\frac{n^2\cos\theta-\sqrt{n^2-\sin^2\theta}\left[1-\tilde{\sigma}(\Omega)\cos\theta\right]}{n^2\cos\theta+\sqrt{n^2-\sin^2\theta}\left[1+\tilde{\sigma}(\Omega)\cos\theta\right]} \tag{3.4b}$$

where, θ is the angle of incidence, n is the refractive index of the substrate,

$\tilde{\sigma}=\frac{\sigma}{c\varepsilon_0}$, σ is the complex surface conductivity of the TMDC under consideration and $\left(\frac{1}{c\varepsilon_0}\right)$ is the impedance of vacuum.

The Fresnel reflection coefficients can be expressed as:

$$r_\lambda = R_\lambda\, exp\left(i\phi_\lambda\right) \tag{3.5}$$

where R_λ is the amplitude and ϕ_λ is the phase of the reflection coefficient (with $\lambda\in\{p,s\}$).

After some mathematical steps [14,31,41,47], we can arrive at dimensionless spatial (Δ) and angular (Θ) GH and IF shifts which can be specified by the following expressions:

$$k_0\Delta_{GH}=w_p\frac{\partial\phi_p}{\partial\theta}+w_s\frac{\partial\phi_s}{\partial\theta} \tag{3.6a}$$

$$k_0\Delta_{IF}=-\cot\theta\left[\frac{w_p a_s^2+w_s a_p^2}{a_p a_s}\sin\eta+2\sqrt{w_p w_s}\,\sin\left(\eta-\phi_p+\phi_s\right)\right] \tag{3.6b}$$

$$\Theta_{GH}=-\left(w_p\frac{\partial\ln R_p}{\partial\theta}+w_s\frac{\partial\ln R_s}{\partial\theta}\right) \tag{3.7a}$$

$$\Theta_{IF}=\frac{w_p a_s^2-w_s a_p^2}{a_p a_s}\cos\eta\cot\theta \tag{3.7b}$$

where, $w_\lambda=\frac{a_\lambda^2R_\lambda^2}{a_P^2R_P^2+a_S^2R_S^2}$ is the fractional energy contained in each polarization state.

Similarly, we can also calculate the GH and IF shifts for total internal reflection (TIR) from the interface. In this case, the reflection coefficients are modified as prescribed before and can be calculated by the Transfer Matrix Method [49]:

$$r_s(\theta)=\frac{n\cos\theta-\sqrt{1-n^2\sin^2\theta}-n\tilde{\sigma}(\Omega)}{n\cos\theta+\sqrt{1-n^2\sin^2\theta}+n\tilde{\sigma}(\Omega)} \tag{3.8a}$$

$$r_p(\theta)=\frac{\cos\theta-n\sqrt{1-n^2\sin^2\theta}\left[1-\tilde{\sigma}(\Omega)\cos\theta\right]}{\cos\theta+n\sqrt{1-n^2\sin^2\theta}\left[1+\tilde{\sigma}(\Omega)\cos\theta\right]} \tag{3.8b}$$

Further calculations [31] provide adimensional spatial and angular GH & IF shifts for total internal reflection case which gives identical expressions (Equation (3.6) and (3.7)).

3.3 Results & Discussion

Let us first discuss the parameters having a substantial influence on GH and IF shifts. It is clear from the expressions of the reflection coefficients that the presence of TMDC largely affects the reflection coefficients via the introduction of the surface optical conductivity $\left(\sigma(\omega)\right)$ term. The knowledge of the optical conductivity of the TMDCs is absolutely necessary to start further analysis. For this, we have to know about the dielectric permittivity of TMDCs. Among the available methods, most commonly used for TMDCs are the Lorentz model, the Hybrid Lorentz-Drude-Gaussian model, the self-consistent method, the surface current model, the variational Kramers-Kronig function based on Lorentz [43,44,50-52], etc. Here we have taken Lorentz model results generating reliable fittings [44,53,54].

The relative permittivity for monolayer TMDCs can be stated as:

$$\varepsilon_R(\omega)=\frac{\varepsilon(\omega)}{\varepsilon_0}=1+\sum_{j=1}^{N}\frac{f_j}{\omega_j^2-\omega^2-i\omega\gamma_j}=1+\sum_{j=1}^{N}\frac{f_j^E}{E_j^2-E^2-iE\gamma_j^E} \tag{3.9}$$

where f_j = oscillator strength, ω_j = resonant frequency, and γ_j = spectral width of the j^{th} oscillator. The model parameters used in this study can be obtained from the reference [55]. The surface optical conductivity of the TMDC monolayers will be given by [43,44]:

$$\sigma_S(E)=\sigma_r(E)+i\sigma_i(E)=i\varepsilon_0\omega h_{eff}\left(1-\varepsilon_r(E)\right) \tag{3.10a}$$

$$\frac{\sigma_S}{\sigma_0}=\frac{i\omega h_{eff}}{\pi\alpha c}\left(1-\varepsilon_r(E)\right) \tag{3.10b}$$

where $\sigma_0 = \frac{e^2}{4\hbar}$, $\alpha = \frac{1}{137}$, $c = 3\times10^8 m/s$, and h_{eff} = the effective thicknesses of TMDC monolayers.

Optical conductivity is highly influenced by wavelength. Hence, for future studies, we will use a specific wavelength of 633 nm unless mentioned otherwise.

3.3.1 GH & IF shifts for partial reflection

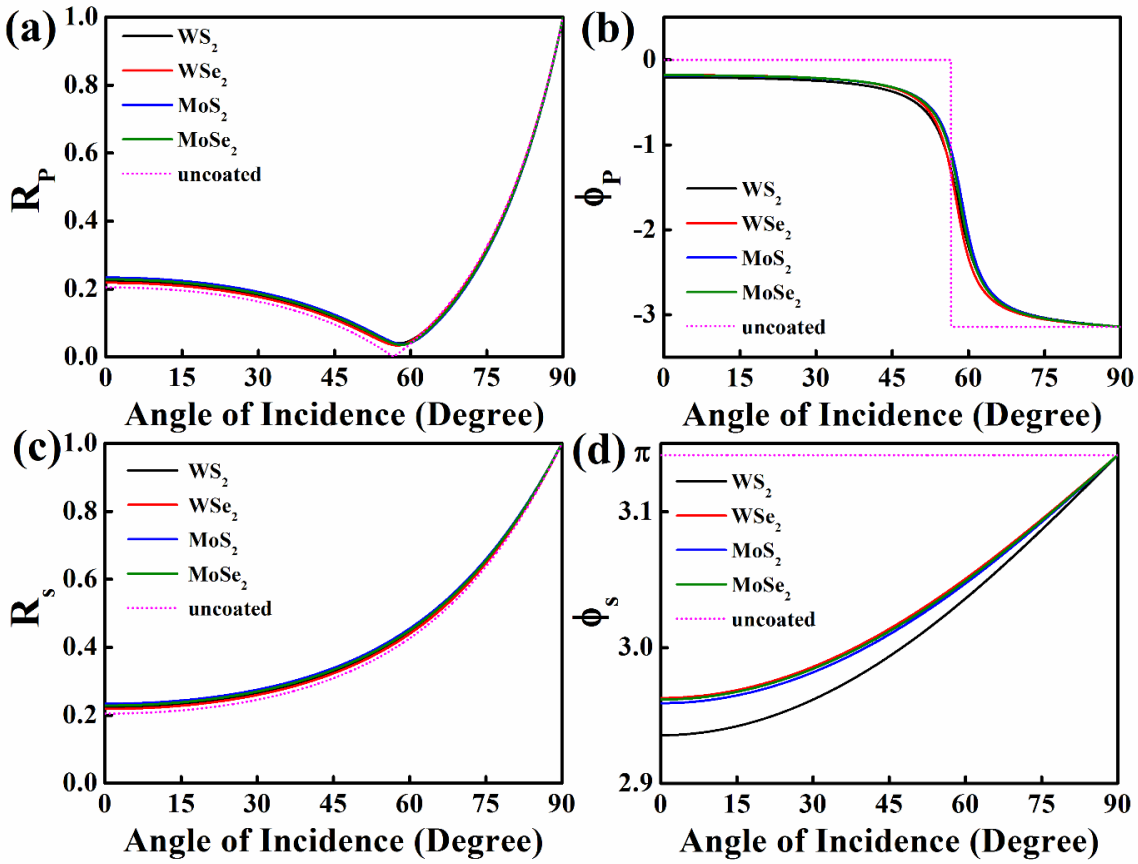

Figure 3.2. Modulus (R) and phase (ϕ) of reflection coefficient for: **(a, b)** p-polarized and **(c, d)** s-polarized light incident on monolayer TMDC coated glass surface for partial reflection.

We already know that the reflection coefficients have a significant role to play in the existence of the GH and IF shift. Therefore, we have plotted the modulus (R) and phase (ϕ) of the reflection coefficients for four monolayer TMDC-coated (WS_2, WSe_2, MoS_2, and $MoSe_2$) surfaces in Figure 3.2. The monolayers of TMDC affect the modulus and phase part of

reflection coefficients. A relative comparison of the modulus and phases are shown between the monolayers of TMDCs (solid curve) and the uncoated surface (dotted curve) in Figure 3.2. In case of the four different TMDCs, we observe no significant changes in the response of *R* and ϕ, hence, a close behaviour is expected in the GH and IF shifts of the four TMDCs.

The modulus (R_S) and phase part (ϕ_S) of the S-component reflection coefficient increase smoothly with the incident angle (θ) though ϕ_S does not change appreciably from the π value. In the other case of P-polarization, R_P reaches a minimum at pseudo-Brewster's angle (θ_{PB}). However, in absence of TMDCs, we get the conventional result, $R_P(\theta = \theta_{PB}) = 0$. Similarly, ϕ_P suffers a discontinuous jump from 0 to $-\pi$ in the neighbourhood of the pseudo-Brewster's angle. This Brewster's angle is a special angle in the partial reflection scenario where the P-polarized component of the reflected light vanishes. These typical characteristics of *R* and ϕ, influence the angular variation of the spatial GH and F shifts (following Equation 3.6) as presented in Figure 3.3.

Looking at Equation 3.6, the slope of ϕ - θ plot is an influential parameter for the spatial GH shift. Consequently, dimensionless spatial GH shift ($k_0\Delta_{GH}$) which is precisely zero for partial reflection for uncoated surfaces (absence of TMDCs), as was firstly invented by Goos and Hänchen [3,56,57], now becomes non-zero in presence of monolayer TMDCs. It is quite an extraordinary observation in our investigation. Due to a negligible change in the slope of ϕ_S - θ plot, we notice a finite but small spatial GH shift for S-polarization ($k_0\Delta_{GH}^S$) [Figure 3.3(b)]. However, $k_0\Delta_{GH}^S$ increases monotonically with increasing incident angle. But, for P-polarization, the sharp jump of ϕ_P in the vicinity of θ_{PB}, gives rise to a large value of the spatial GH shift ($k_0\Delta_{GH}^P$) as presented in Figure 3.3(a). Therefore, we reckon finite spatial GH shifts even for partial reflection of S and P-polarized incident light.

Similarly, to figure out the IF shift, the information of $(\phi_P - \phi_S)$ is essential as seen from Equation (3.6b). A judicious look at Figure 3.3(b), (d) tells us that $(\phi_P - \phi_S)$ changes from $-\pi$ to -2π in the vicinity of Pseudo Brewster's angle (θ_{PB}). Therefore, we presume a nonzero spatial IF shift that exactly is shown in Figure 3.3(c), (d) for 45^0 linear polarization (LP) and circular polarization (CP) states, respectively. In contrast, spatial IF shift is absent for partial reflection in the uncoated surface (absence of TMDCs).

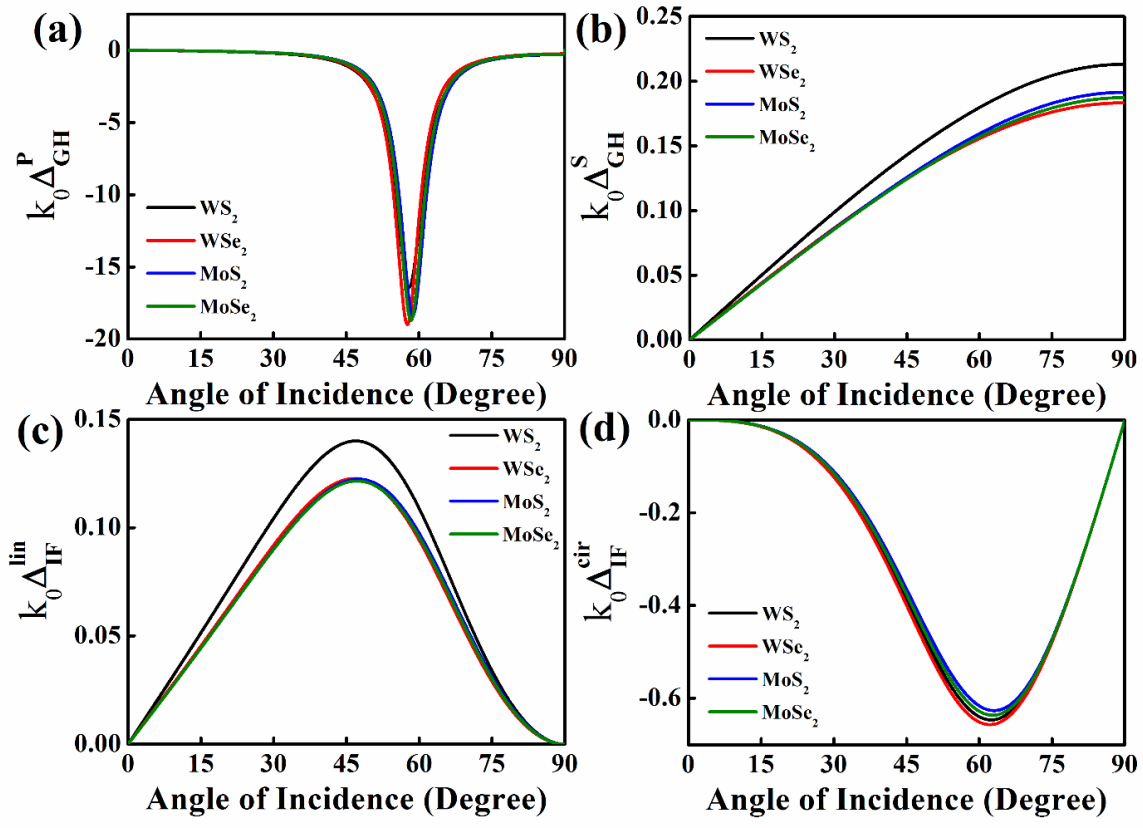

Figure 3.3. Spatial GH shift for **(a)** p-polarized and **(b)** s-polarized light. Spatial IF shift for **(c)** p-polarized and **(d)** s-polarized light **(Partial reflection)**.

In addition, all the four monolayers of TMDCs on dielectric surfaces produce similar effects. The minor changes in the respective angular variation of the GH and IF shifts can be ascribed to the surface optical conductivity of the individual TMDC monolayers. Their surface optical conductivity is a function of wavelength. The values of the optical conductivity at 633 nm for the above-stated four TMDC monolayers are adjacent to one another. On that note, the reflection coefficients are almost similarly influenced by the different TMDCs. This, in turn, causes spatial shifts not to differ considerably for the four different TMDC monolayers. Due to this wavelength dependency of the optical conductivity of TMDC monolayers, we expect changes in the GH and IF shift response as we modify the wavelength of the incident light. This will be clearer in the latter part of this section.

The optical response of the GH and IF shifts for the TMDCs can be compared to the graphene response [31]. A giant negative GH shift was witnessed for graphene coated

dielectric, but the presence of TMDC gives rise to finite GH shifts which are smaller in magnitude than the former.

3.3.2 GH & IF shifts for total internal reflection

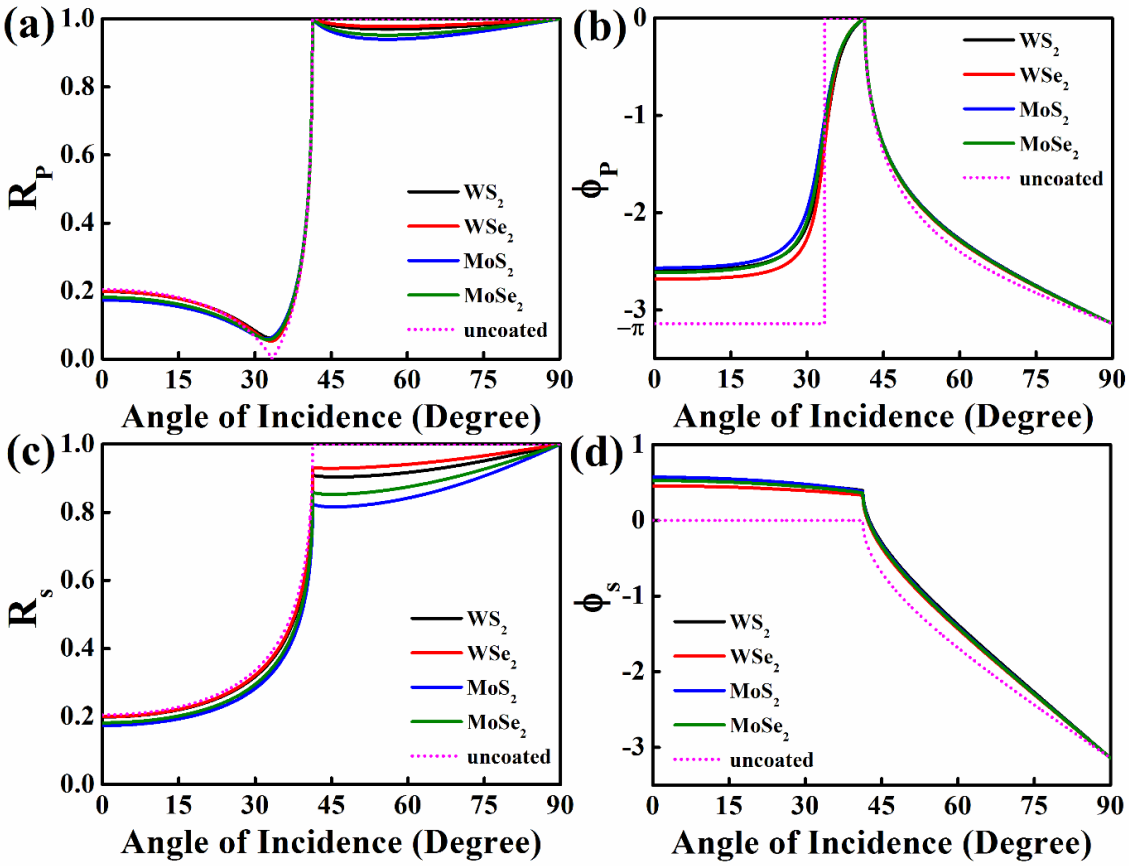

Figure 3.4. Modulus (R) and phase (ϕ) of reflection coefficient for: **(a, b)** p-polarized and **(c, d)** s-polarized light incident on monolayer TMDC coated glass surface for total internal reflection

We shall now emphasize on total internal reflection case where light is passed through the dielectric side of the interface. The angular variation of amplitude (R) and phase (ϕ) of the reflection coefficients in case of total internal reflection is portrayed in Figure 3.4 where the effects of TMDCs are explicitly observed. For incident angles greater than the critical angle ($\theta > \theta_C$), both ϕ_S and ϕ_P abruptly reduce from 0 to $-\pi$. This finite negative slope of ϕ-θ graph gives rise to finite negative spatial GH shifts for both S and P-polarizations of the light beam as shown in Figure 3.5.

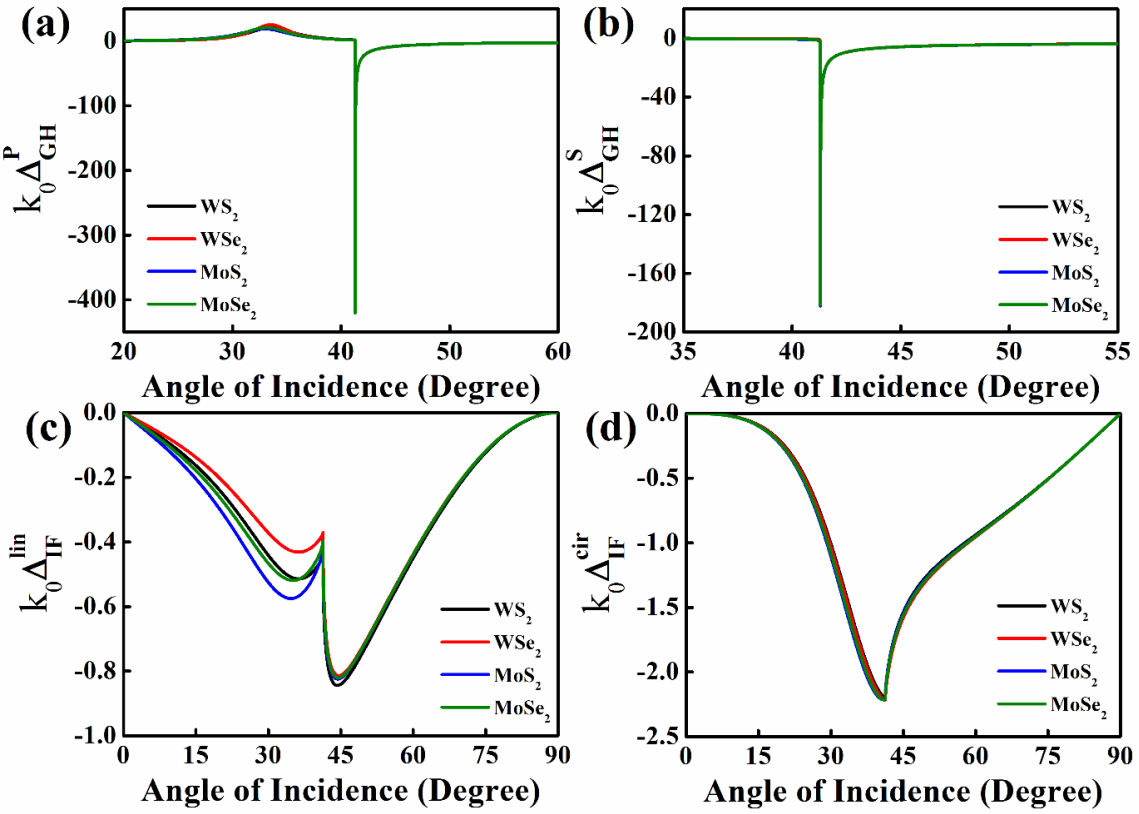

Figure 3.5. Spatial GH shift for **(a)** p-polarized and **(b)** s-polarized light. Spatial IF shift for **(c)** p-polarized and **(d)** s-polarized light **(Total internal reflection)**.

On that ground, the spatial GH shifts, $k_0\Delta^S_{GH}$ and $k_0\Delta^P_{GH}$ achieve huge negative values. But, we also find a minor positive peak of $k_0\Delta^P_{GH}$ at the Pseudo Brewster's angle because of the positive slope of ϕ_P - θ graph around pseudo-Brewster's angle θ_{PB}. Nevertheless, the existence of giant negative spatial GH shift is a significant finding in our study.

Next, to explain the IF shift we estimate the nature of $(\phi_P - \phi_S)$. It is clear from Figure 3.3 that $(\phi_P - \phi_S)$ value increases from a value adjacent to $(-\pi)$ to a value close to zero in the neighbourhood of the critical angle (θ_C). On that note, we expect a negative spatial IF shift for monolayer TMDCs in the case of diagonal linear polarization $(\eta = 0^0)$(LP) and circular polarization $(\eta = 90^0)$ (CP) [Figure 3.5] states of the light. Furthermore, the response of the four different TMDCs does not change significantly from each other because of the close

similarity of the optical conductivities of the monolayer TMDCs at the wavelength 633 nm. As a result, the spatial shift for the total internal reflection of light may be considerably enhanced by selecting a suitable wavelength. The dependency of the maximum spatial shift on the wavelength is also discussed in the latter part of this *Chapter*.

We can also make a comparison of our theoretical findings to the graphene-coated surfaces [31]. Giant spatial shifts are detected in both cases, though the positive peak in the neighbourhood of the pseudo-Brewster's angle was not detected for graphene-coated surfaces. Furthermore, the dip of the $k_0\Delta_{IF}^{lin}$ vs θ graph in the neighbourhood of the pseudo-Brewster's angle θ_{PB} is a noteworthy difference from graphene.

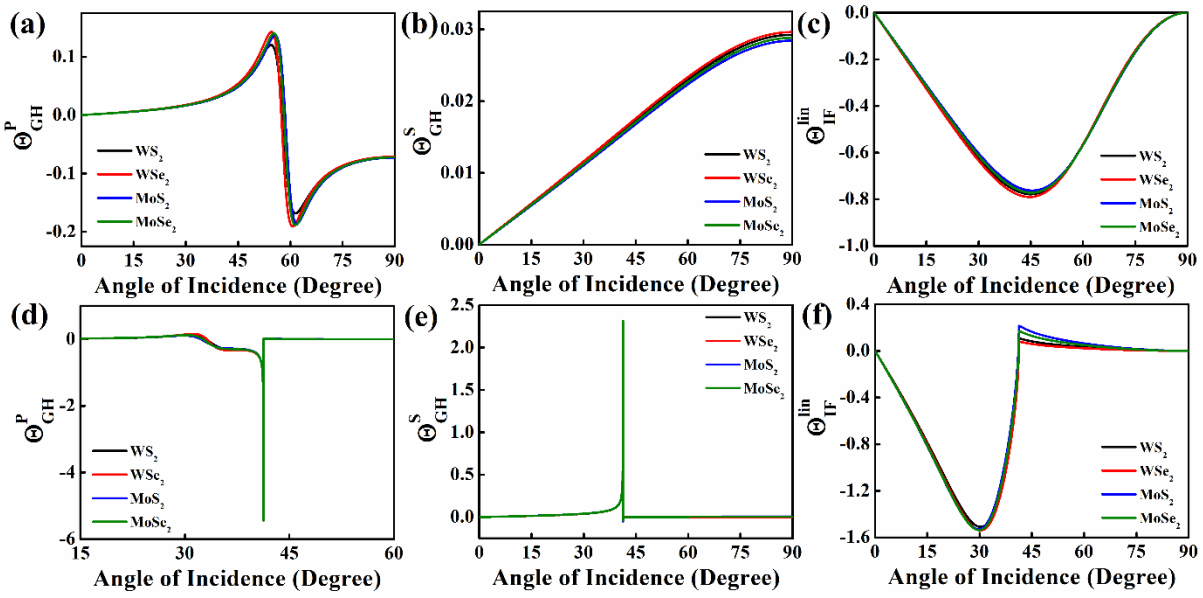

Figure 3.6. (a, b, c) Angular GH & IF shifts **(a, b, c)** for partial reflection and **(d, e, f)** for total internal reflection.

At the same time, we can also observe the angular GH and IF shifts which are in turn governed by the angular dependence of the amplitude of reflection coefficients. As displayed in Figure 3.6, the changes of R_λ in presence of TMDC are quite insignificant. Hence, we presume non-zero angular GH shifts, but noticeably smaller in magnitude in comparison to the spatial GH shifts. In addition, since $\eta = 0$, the angular GH shift is zero for circular polarization

states of light. Nonetheless, small angular IF shifts are detected for diagonal linear polarization states of light in both partial reflection and total internal reflection conditions.

Before proceeding further, we want to emphasize about the unusual nature of the spatial [Figure 3.5(a), (b)] and angular GH [Figure 3.6(d), (e)] shifts in case of total internal reflection. We can observe that there is a sudden spike near the critical angle of incidence. It may be due to the model-dependent divergence of the theory. While deriving the expressions of the optical beam shifts, the analysis has been approximated at the first order (in the Taylor series expansion) for the spatial shift and the second order for the angular part. Yet, to know the real cause of these spikes in the optical beam shifts, it will be necessary to take into account the higher-order terms in the theoretical calculations which is beyond the scope of the present work.

3.3.3 Dependence on the layer thickness

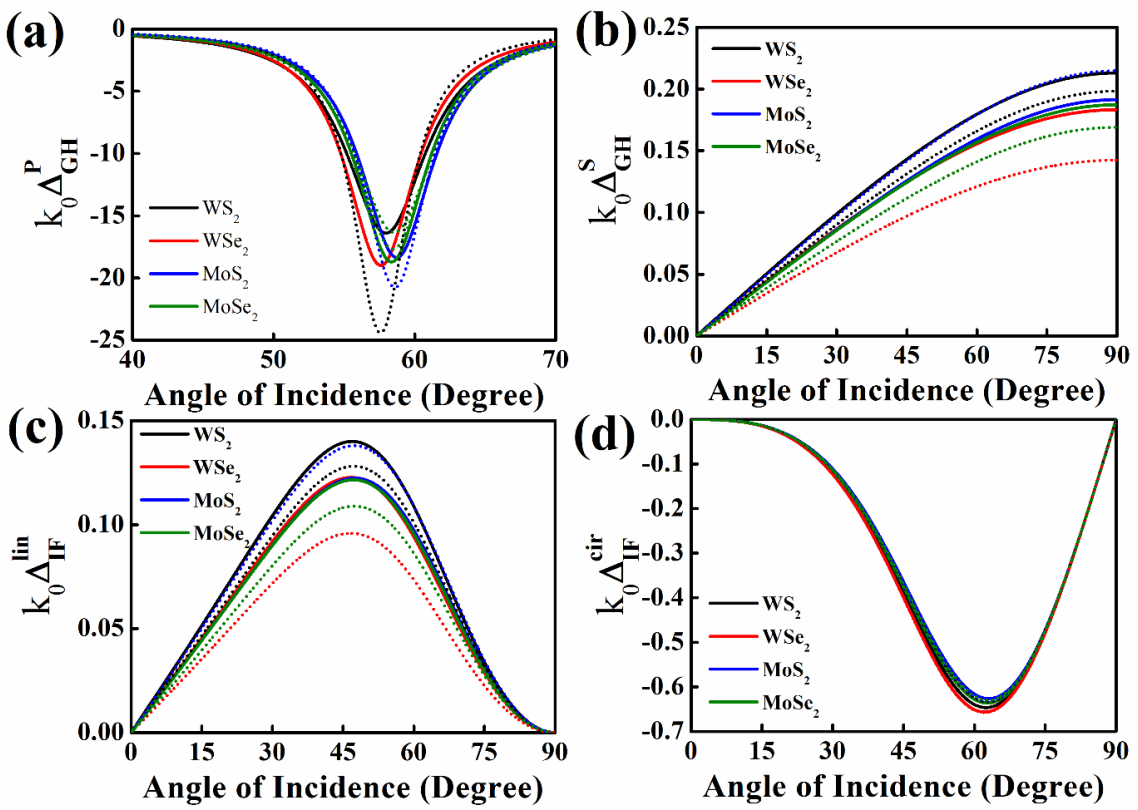

Figure 3.7. Study of layer dependence for partial reflection: **(a, b)** Spatial GH shift and **(c, d)** Spatial IF shift. (Monolayer: solid lines, Multilayer: dotted lines)

We have also investigated how the GH and IF shifts depend on sample thickness. Hence, we have made a comparison of the GH and IF shifts for the monolayer TMDC-coated surfaces with the corresponding bulk TMDCs. From Figure 3.7, we find that GH shifts are influenced significantly by layer thickness variation. For the S-polarization state of the incident light, GH shift is greater for monolayer TMDC coating than the bulk. But for the P-polarization state of the light, the result is reversed i.e. the GH shift is superior for bulk than the monolayer case. Additionally, for the IF shift in the linear polarization state of the light, maximum shifts occur for monolayer TMDCs in comparison to the bulk. But, IF shift for circular polarization state of the light remains nearly unaffected by the layer thicknesses.

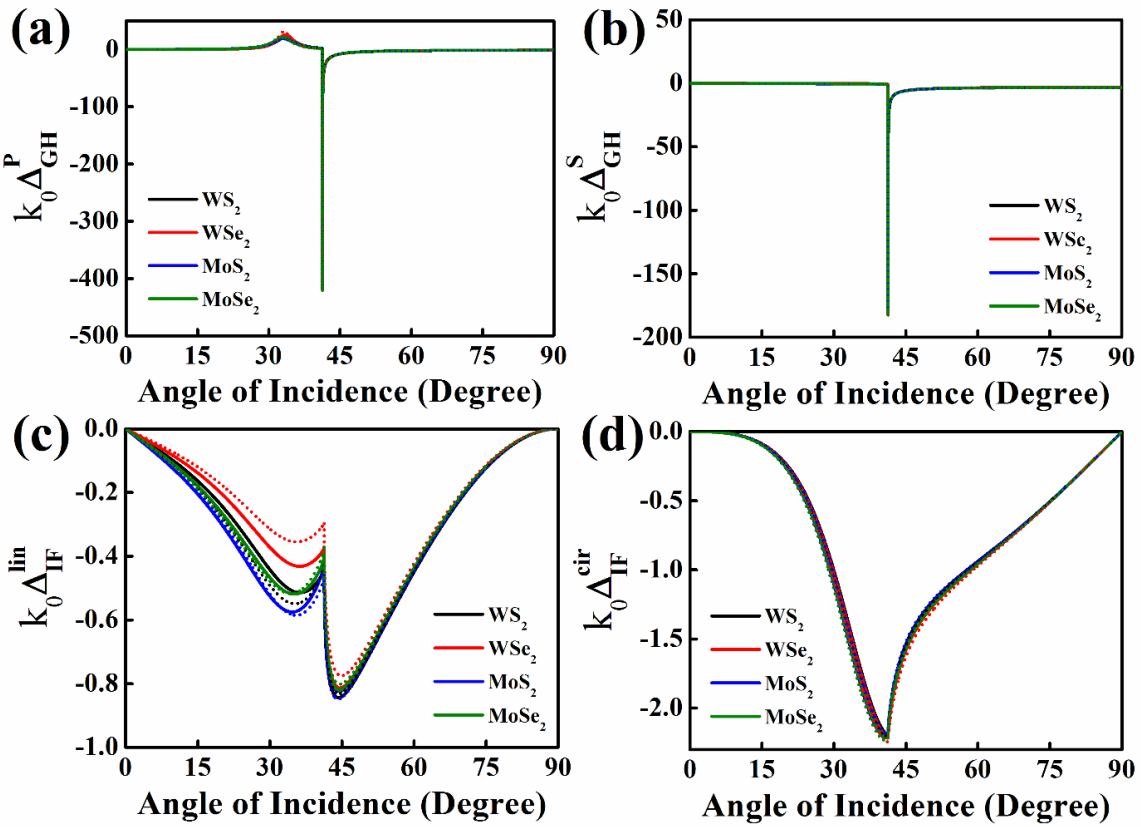

Figure 3.8. Study of layer dependence for total internal reflection: **(a, b)** Spatial GH shift and **(c, d)** Spatial IF shift. (Monolayer: solid lines, Multilayer: dotted lines)

Likewise, we can investigate the thickness dependence of the GH and IF shifts for total internally reflected light beam. Here, GH shifts stay almost unaffected by the thickness variation of the reflecting surface as demonstrated in Figure 3.8 (a, b). However, IF shift for

linear polarization state of the light is greater for monolayer TMDC-coated surfaces than the bulk. But, IF shift for circular polarization state of the light is independent of layer thicknesses similar to the case of partial reflection.

Taken together, the above theoretical results suggest that the difference in the optical beam shifts between the monolayer and bulk materials can be readily observed in the case of partial reflection, but not so in case of total internal reflection of light. This thickness dependence of the GH and IF shifts is because of the specific optical conductivity characteristics of the material at the particular wavelength under consideration. The optical conductivity of the monolayer TMDC is significantly different from its bulk counterpart [43,44]. The above findings signify that one can discriminate between the monolayer and the corresponding bulk TMDCs by looking at their optical beam shift response, particularly for partial reflection of the light beam from the reflecting surface.

3.3.4 Dependence on wavelength

Finally, we have studied how the optical beam shifts depend on the wavelengths of incident light ranging from ultraviolet-visible to infrared region of the spectrum. To better understand this nature, we have plotted the maximum of the absolute value of GH and IF shifts with the wavelength in Figure 3.9. In case of the P-polarization state of light, the value of maximum GH shift for WS_2 shows two comparatively larger peaks around 0.403 μm and 0.613 μm.

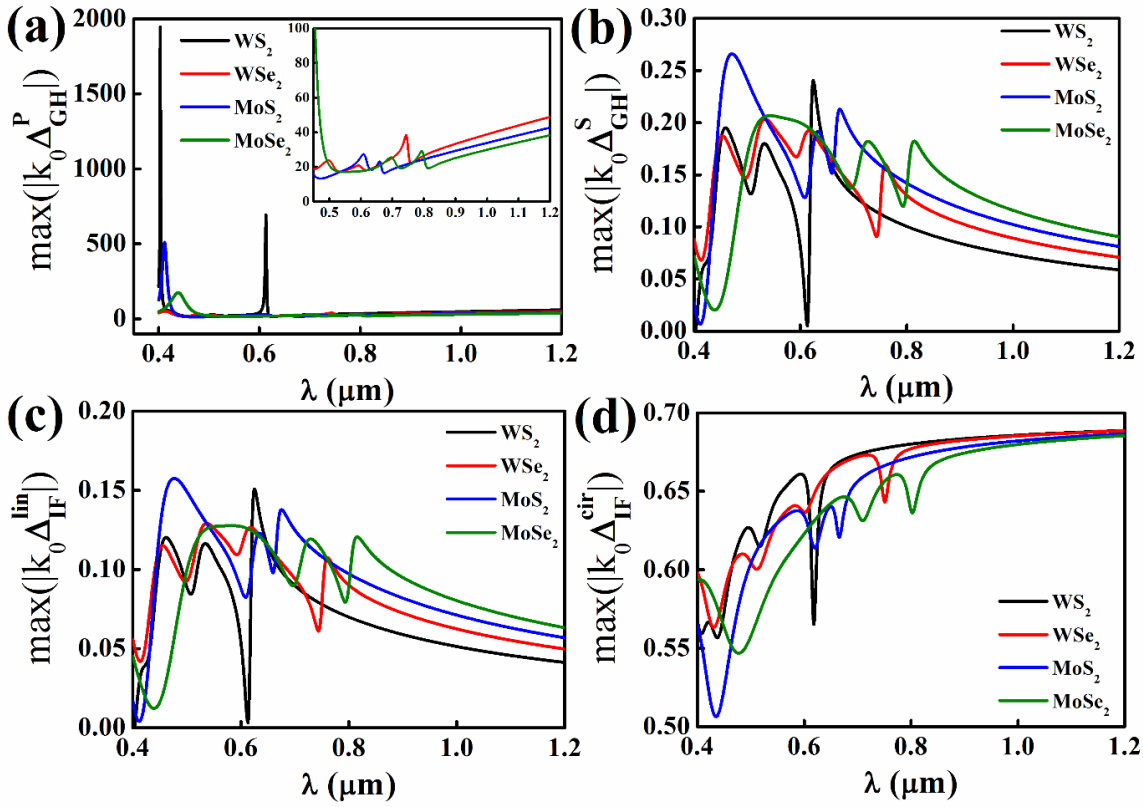

Figure 3.9. Study of wavelength dependence for partial reflection: **(a, b)** Maximum GH shift and **(c, d)** Maximum IF shift.

The most probable cause for the existence of these two large peaks of the maximum GH shifts for WS_2 is the imaginary part of the optical conductivity of WS_2 at these wavelengths under consideration. However, the variation of maximum GH shifts for the other three materials WSe_2, MoS_2, and $MoSe_2$ are quite identical to each other (inset of Figure 3.9(a)). But, for both P and S-polarization states of the incident light, the maximum GH shifts attain constant values as we go from visible to the infrared region. Hence, we should concentrate on the ultraviolet and visible regions of the spectrum to investigate the GH shifts experimentally for partial reflection of light. Furthermore, the maximum IF shifts for the diagonal linear polarization and circular polarization states of the light beam also differ substantially for all the materials under consideration. Nevertheless, the maximum of the IF shifts increases as we go to the infrared region, which is opposite in nature in comparison to the nature of the GH shifts.

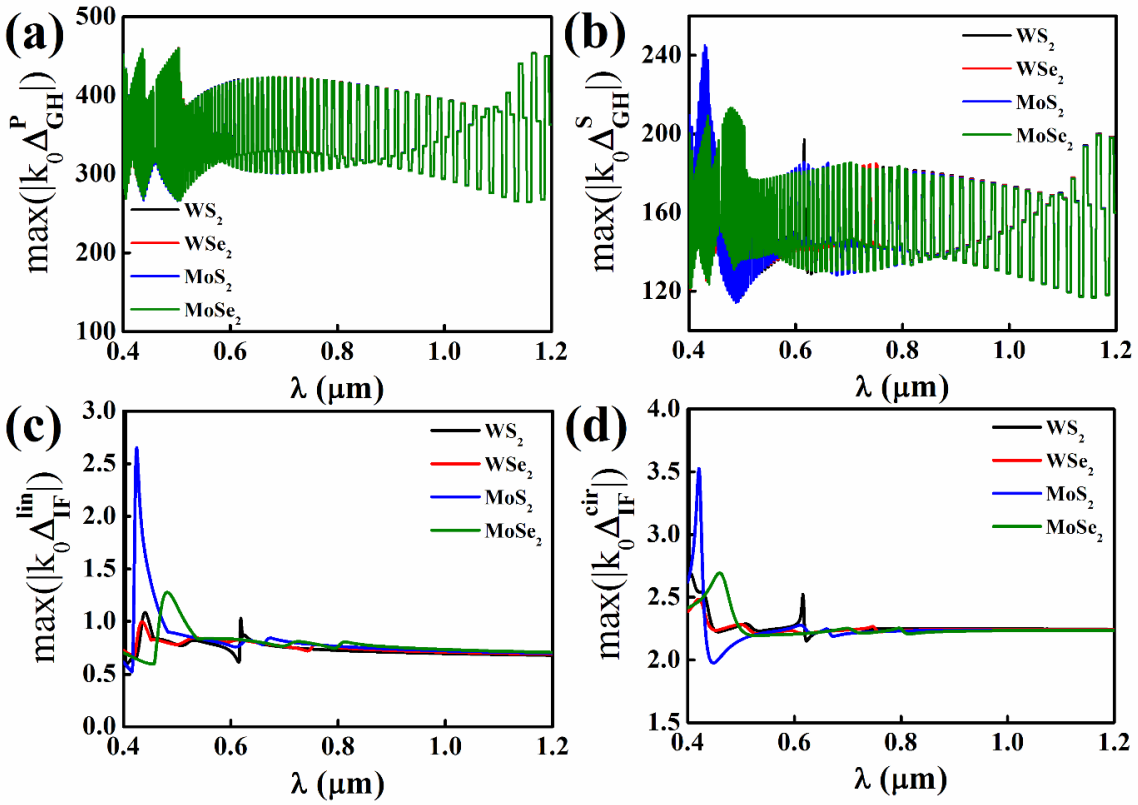

Figure 3.10. Study of wavelength dependence for total internal reflection: **(a, b)** Maximum GH shift and **(c, d)** Maximum IF shift.

In a similar fashion, we have studied the wavelength dependence of maximum GH and IF shifts for the total internal reflection of the light beam in monolayers of TMDC. The maximum GH shifts illustrate an interesting nature as shown in Figure 3.10 (upper panel). Also, the maximum shift for both GH and IF shifts reduce to a constant value in moving from the visible to the infrared region of the spectrum. Hence, it is better to work in the smaller wavelength region, i.e. visible and ultraviolet range of the spectrum to find greater optical beam shifts in the total internal reflection case.

On that ground, we can conclude that the maximum value of the GH and IF shifts essentially depend upon the surface optical conductivity of the materials. The dependence of the optical conductivity of the TMDCs on the wavelength is clear from Equation (3.9). $Re(\sigma_S/\sigma_0)$ sharply reduces to zero for all the TMDCs under consideration and $Im(\sigma_S/\sigma_0)$ increases to a constant negative value that approaches towards zero. Since optical conductivities for all the TMDCs approaches a constant value in moving from visible to

infrared region, the nature of the GH and IF shifts becomes identical for all the TMDCs in the infrared region of the spectrum.

3.4 Outlook and Summary

In summary, a comprehensive theoretical study of the optical beam shifts for a fundamental Gaussian beam reflected from TMDC (WS_2, WSe_2, MoS_2, and $MoSe_2$) coated surface is discussed. The explicit dependence of the optical beam shifts on the external parameters like incident angle, wavelength, polarization state, sample thickness is broadly explained. In general GH & IF shifts are mainly observed for total internal reflection of light. Conversely, in monolayer TMDCs, finite optical beam shifts are found even outside the domain of total internal reflection. Hence, TMDCs belongs to a special class of optical materials that exhibit contrasting response of GH & IF shifts in comparison to other materials. The difference in response of beam shifts for different TMDCs is due to a separate behaviour of the optical conductivity of different TMDCs. This also affects the response of beam shift over different wavelengths as the surface optical conductivity is an explicit function of the wavelength of incident light. Thus modulating the wavelength affects the optical conductivity of the sample that has a direct influence on the GH and IF shifts. Hence, we get additional freedom of controlling the optical beam shifts externally by choosing appropriate wavelengths for investigation. The thickness is also an important factor that can also greatly influence the optical beam shift as shown in the present study. Nevertheless, our theoretical model based on stationary phase approximation coupled with the transfer matrix method can also be applied for investigating the nature of the optical beam shifts in other layered structures as well as higher-order optical beams (e.g. Bessel, Laguerre-Gauss, and Hermite-Gauss).

References

[1] M. Born and E. Wolf, *Principles of Optics: Electromagnetic Theory of Propagation, Interference and Diffraction of Light* (Elsevier Science, 2013).

[2] J. D. Jackson, *Classical electrodynamics* (Wiley, 1975).

[3] F. Goos and H. Hänchen, Annalen der Physik **436**, 333 (1947).

[4] F. Bretenaker, A. Le Floch, and L. Dutriaux, Physical Review Letters **68**, 931 (1992).

[5] M. Peccianti, A. Dyadyusha, M. Kaczmarek, and G. Assanto, Nature Physics **2**, 737 (2006).

[6] F. I. Fedorov, Dokl. Akad. Nauk SSSR **105**, 465 (1955).

[7] C. Imbert, Physical Review D **5**, 787 (1972).

[8] O. Hosten and P. Kwiat, Science **319**, 787 (2008).

[9] K. Y. Bliokh and Y. P. Bliokh, Physical Review Letters **96**, 073903 (2006).

[10] K. Y. Bliokh and A. Aiello, Journal of Optics **15**, 014001 (2013).

[11] A. Aiello, New Journal of Physics **14**, 013058 (2012).

[12] F. Töppel, M. Ornigotti, and A. Aiello, New Journal of Physics **15**, 113059 (2013).

[13] J. B. Götte and M. R. Dennis, New Journal of Physics **14**, 073016 (2012).

[14] M. Ornigotti and A. Aiello, Journal of Optics **15**, 014004 (2013).

[15] S. Chen, C. Mi, L. Cai, M. Liu, H. Luo, and S. Wen, Applied Physics Letters **110**, 031105 (2017).

[16] M. R. Dennis and J. B. Götte, New Journal of Physics **14**, 073013 (2012).

[17] K. Y. Bliokh, C. T. Samlan, C. Prajapati, G. Puentes, N. K. Viswanathan, and F. Nori, Optica **3**, 1039 (2016).

[18] C. Prajapati and N. K. Viswanathan, Journal of Optics **19**, 105611 (2017).

[19] C. Prajapati, S. Pidishety, and N. K. Viswanathan, Opt. Lett. **39**, 4388 (2014).

[20] S. Goswami, M. Pal, A. Nandi, P. K. Panigrahi, and N. Ghosh, Opt. Lett. **39**, 6229 (2014).

[21] D. H. Foster, A. K. Cook, and J. U. Nöckel, Opt. Lett. **32**, 1764 (2007).

[22] J. Unterhinninghofen, J. Wiersig, and M. Hentschel, Physical Review E **78**, 016201 (2008).

[23] F. de Fornel, *Evanescent Waves: From Newtonian Optics to Atomic Optics* (Springer, 2001).

[24] K. S. Novoselov, D. Jiang, F. Schedin, T. J. Booth, V. V. Khotkevich, S. V. Morozov, and A. K. Geim, Proceedings of the National Academy of Sciences of the United States of America **102**, 10451 (2005).

[25] A. H. Castro Neto, Physical Review Letters **86**, 4382 (2001).

[26] A. Das and M. Pradhan, J. Opt. Soc. Am. B **35**, 1956 (2018).

[27] J. K. Ellis, M. J. Lucero, and G. E. Scuseria, Applied Physics Letters **99** (2011).

[28] C. Ataca, H. Şahin, and S. Ciraci, The Journal of Physical Chemistry C **116**, 8983 (2012).

[29] B. Yang *et al.*, Physical Review B **96**, 041409 (2017).

[30] J. R. Schaibley, H. Yu, G. Clark, P. Rivera, J. S. Ross, K. L. Seyler, W. Yao, and X. Xu, Nature Reviews Materials **1**, 16055 (2016).

[31] S. Grosche, M. Ornigotti, and A. Szameit, Opt. Express **23**, 30195 (2015).

[32] W. Wu, S. Chen, C. Mi, W. Zhang, H. Luo, and S. Wen, Physical Review A **96**, 043814 (2017).

[33] X. Li, P. Wang, F. Xing, X.-D. Chen, Z.-B. Liu, and J.-G. Tian, Opt. Lett. **39**, 5574 (2014).

[34] J. C. Martinez and M. B. A. Jalil, EPL (Europhysics Letters) **96**, 27008 (2011).

[35] M. Merano, Opt. Lett. **41**, 2668 (2016).

[36] M. Cheng, P. Fu, X. Chen, X. Zeng, S. Feng, and R. Chen, J. Opt. Soc. Am. B **31**, 2325 (2014).

[37] N. A. F. Zambale, J. L. B. Sagisi, and N. P. Hermosa, in *ArXiv e-prints*2018).

[38] I. V. Soboleva, V. V. Moskalenko, and A. A. Fedyanin, Physical Review Letters **108**, 123901 (2012).

[39] Ziauddin, Y.-L. Chuang, S. Qamar, and R.-K. Lee, Scientific Reports **6**, 26504 (2016).

[40] S. N. Kurilkina, N. S. Petrov, A. B. Zimin, and V. N. Belyi, Journal of Optics **19**, 125102 (2017).

[41] A. Aiello and J. P. Woerdman, arxiv **0903** (2009).

[42] M. M. Aiello A., and Woerdman J.P., Opt. Lett. **34**, 1207 (2009).

[43] M. Weismann and N. C. Panoiu, Physical Review B **94**, 035435 (2016).

[44] Y. Li *et al.*, Physical Review B **90**, 205422 (2014).

[45] G. W. Hanson, Journal of Applied Physics **103**, 064302 (2008).

[46] L. A. Falkovsky and S. S. Pershoguba, Physical Review B **76**, 153410 (2007).

[47] M. Merano, N. Hermosa, J. P. Woerdman, and A. Aiello, Physical Review A **82**, 023817 (2010).

[48] L. Mandel and E. Wolf, *Optical Coherence and Quantum Optics* (Cambridge University Press, Cambridge, 1995).

[49] T. Zhan, X. Shi, Y. Dai, X. Liu, and J. Zi, Journal of Physics: Condensed Matter **25**, 215301 (2013).

[50] B. Mukherjee, F. Tseng, D. Gunlycke, K. K. Amara, G. Eda, and E. Simsek, Opt. Mater. Express **5**, 447 (2015).

[51] Y. V. Morozov and M. Kuno, Applied Physics Letters **107** (2015).

[52] G. Jayaswal, Z. Dai, X. Zhang, M. Bagnarol, A. Martucci, and M. Merano, Opt. Lett. **43**, 703 (2018).

[53] L. Yilei and F. H. Tony, 2D Materials **5**, 025021 (2018).

[54] H.-L. Liu, C.-C. Shen, S.-H. Su, C.-L. Hsu, M.-Y. Li, and L.-J. Li, Applied Physics Letters **105**, 201905 (2014).

[55] Y. Li *et al.*, Physical Review B **90**, 205422 (2014).

[56] K. Artmann, Annalen der Physik **437**, 87 (1948).

[57] V. G. Fedoseyev, Journal of Physics A: Mathematical and General **21**, 2045 (1988).

Chapter 4 Optical Beam shifts in Graphene

An extensive investigation of the GH and IF shifts in graphene for a Gaussian beam is presented. The explicit dependence of the optical beam shifts on the chemical potential of graphene is revealed that permits modulation of beam shifts by tuning the chemical potential. The influence of the wavelength has also been discussed in this Chapter.

Content of this chapter has been published in: **A. Das** and M. Pradhan, "*Wavelength and chemical potential dependence of optical beam shifts in graphene*," **Journal of Modern Optics** 68 (3), 146-152 (2021).

4 Optical Beam shifts in Graphene

4.1 Introduction

Geometrical optics can accurately describe the reflection and transmission of a plane wave [1,2], but real optical beams with finite transverse extent experience diffractive corrections [3-12] depending upon wavelength, angle of incidence, polarization mode, and the surface of interaction. In this *Chapter,* we have described the existence of finite longitudinal (Goos-Hänchen) and transverse (Imbert-Fedorov) shifts [9,10] and their characteristics for Gaussian light incident upon the graphene interface.

Over the past few years, several theoretical models and special measurement techniques have been discovered to accurately measure these tiny optical beam shifts [11,13-15]. Here, we propose one theoretical model based on stationary phase approximation method coupled with 'Transfer Matrix Method' for the optical beam shift detection. After its emergence, optical beam shifts have been examined in several materials and surfaces [3,16-20]. These beam shifts are also relevant for other particles like a system of electrons, neutrons, atoms, etc. [21,22] due to their wave-particle duality. Especially, for the massless Dirac fermions in graphene systems, a giant beam shift is observed [23] and can be tuned by controlling the electric field [24]. The 2D materials are suitable candidates to study optical beam shifts because of their peculiar electrical, chemical, structural and mechanical properties [25-27]. Graphene, a monolayer of carbon atoms possessing honeycomb lattice symmetry and a band structure consisting of six Dirac cones [26], has become a promising material by the time for optoelectronics, remote sensing, and various other applications [28,29]. Graphene depicts a non-trivial band structure showing the existence of Dirac cones (conduction band bottom touches with the valence band top) and the occurrence of intriguing properties like anomalous quantum Hall effect, Klein tunneling [25,30,31], etc.

In this *Chapter*, we have concentrated on the optical response of graphene. Nevertheless, optical conductivity holds massive importance in the analysis of optical beam shift. According to previous observations, graphene possesses a universal optical conductivity given by $e^2/4\hbar$, at half-filling condition [32-34]. But, the optical conductivity can behave in a very complex manner [35]. In the present article, we have shown the variations of the complex

optical conductivity of graphene with wavelength and chemical potential. Additionally, we have explained the significance of the optical conductivity in controlling the nature of the optical beam shifts.

However, chemical potential (μ) is an important statistical property of a system that controls the fillings of the energy levels i.e. Fermi level position in the band structure of that material [35]. It is well-known that the chemical potential of graphene is of great significance as it can be tuned easily by controlling the electric field or applied gate voltage [35] and other parameters as well. Besides, the optical conductivity of graphene is explicitly reliant on its chemical potential. The chemical potential of the graphene sample can swiftly be tuned to monitor the band structure and hence, other outcomes related to the band structure of the material. For this reason, we have concentrated our attention on the chemical potential of graphene, a subject of massive research interest in recent years. In this study, we have varied the chemical potential of graphene over a broad range (0.4-1.4 eV) and explored its potential importance in the spatial and angular optical beam shifts accordingly. We have also explored the reliance of GH and IF shifts of graphene-coated surfaces for the laser beam of varying wavelengths covering a wide range (400-1300 nm), which has not been explored before. Here, we have concentrated on the fundamental Gaussian mode of the beam. Our study, thus, helps in exploring the maximum GH and IF shifts by suitable selection of chemical potential. It also enables one to choose the laser beam accordingly to observe maximum beam shift. Therefore, the present work signifies the importance of chemical potential in controlling the GH and IF shifts for graphene in response to the varying wavelengths of the light beam in the UV-VIS to infrared region.

4.2 Theoretical calculation of beam shifts

For reflection of a well-collimated Gaussian light beam from a graphene-coated dielectric surface. This Gaussian beam can be characterized by a monochromatic paraxial electric field. According to the zero thickness model, this graphene layer can be modelled as a thin layer having surface conductivity $\sigma(\omega)$ [36].

The reflection coefficients can be obtained by the Transfer Matrix Method (TMM) [37]. They behave differently for partial reflection [Equation (4.1)] and total internal reflection [Equation (4.2)] of light and are given by:

$$r_s(\theta) = \frac{\cos\theta - \sqrt{n^2 - \sin^2\theta} - \tilde{\sigma}(\Omega)}{\cos\theta + \sqrt{n^2 - \sin^2\theta} + \tilde{\sigma}(\Omega)} \tag{4.1a}$$

$$r_p(\theta)=\frac{n^2\cos\theta-\sqrt{n^2-\sin^2\theta}\left[1-\tilde{\sigma}(\Omega)\cos\theta\right]}{n^2\cos\theta+\sqrt{n^2-\sin^2\theta}\left[1+\tilde{\sigma}(\Omega)\cos\theta\right]} \tag{4.1b}$$

$$r_s(\theta)=\frac{n\cos\theta-\sqrt{1-n^2\sin^2\theta}-n\tilde{\sigma}(\Omega)}{n\cos\theta+\sqrt{1-n^2\sin^2\theta}+n\tilde{\sigma}(\Omega)} \tag{4.2a}$$

$$r_p(\theta)=\frac{\cos\theta-n\sqrt{1-n^2\sin^2\theta}\left[1-\tilde{\sigma}(\Omega)\cos\theta\right]}{\cos\theta+n\sqrt{1-n^2\sin^2\theta}\left[1+\tilde{\sigma}(\Omega)\cos\theta\right]} \tag{4.2b}$$

Here, θ = incident angle, n = refractive index of the substrate, and $\tilde{\sigma}=\sigma/c\varepsilon_0$, σ is the complex surface conductivity of graphene under consideration. The Fresnel reflection coefficients ar stated in the complex form:

$r_\lambda = R_\lambda\, exp\left(i\phi_\lambda\right)$

where R_λ is the amplitude and ϕ_λ represents phase (with $\lambda\in\{p,s\}$). Following the calculations of the previous works [9,18,23], the spatial (Δ) and angular (Θ) GH and IF shifts are stated as:

$$k_0\Delta_{GH}=w_p\frac{\partial\phi_p}{\partial\theta}+w_s\frac{\partial\phi_s}{\partial\theta} \tag{4.3a}$$

$$k_0\Delta_{IF}=-\cot\theta\left[\frac{w_p a_s^2+w_s a_p^2}{a_p a_s}\sin\eta+2\sqrt{w_p w_s}\,\sin\left(\eta-\phi_p+\phi_s\right)\right] \tag{4.3b}$$

$$\Theta_{GH}=-\left(w_p\frac{\partial \ln R_p}{\partial\theta}+w_s\frac{\partial \ln R_s}{\partial\theta}\right) \tag{4.4a}$$

$$\Theta_{IF}=\frac{w_p a_s^2-w_s a_p^2}{a_p a_s}\cos\eta\cot\theta \tag{4.4b}$$

Here, $w_\lambda=a_\lambda^2R_\lambda^2/(a_P^2R_P^2+a_S^2R_S^2)$.

The GH and IF shifts for total internal reflection (TIR) from the layered structure can similarly be calculated and yield the same set of Equations [Equations (4.3) & (4.4)].

On the other hand, a lot of theoretical investigations have been accomplished till now regarding electrodynamic properties of graphene [38] such as the frequency-dependent conductivity of graphene [33,34], collective excitations (plasmons), thermo-plasma polaritons, etc. Using Kubo formalism [39] or random phase approximation [40], one can obtain intra and interband optical conductivity of graphene layer, which can be expressed as [33]:

$$\sigma_{intra}(\omega)=\frac{e^2 g_s g_v}{16\hbar}\left(\frac{4i}{\pi\Omega}\right) \tag{4.5}$$

$$\sigma_{inter}(\omega) = \frac{e^2 g_s g_v}{16\hbar}\left[\Theta(|\Omega|-2) - \frac{i}{\pi} ln\left|\frac{\Omega+2}{\Omega-2}\right|\right] \tag{4.6}$$

Here, $\Omega = \hbar\omega/\mu$, μ is the chemical potential, g_s and g_v are the spin and valley degeneracy of graphene, Θ = Heaviside step function.

In the visible region of the spectrum, the interband contributions dominate the transition. Hence, the optical conductivity of graphene is monitored by it. But, as the frequency decreases, the intraband scattering comes into action and starts dominating the conductivity [33]. Furthermore, the temperature and chemical potential also come into the picture. By tuning chemical potential, the fillings of the energy level can be monitored. Thus, it has a considerable effect on the optical conductivity of the graphene monolayer. Bearing this in mind, the optical conductivity characterizing a graphene layer can be written in the following dimensionless form [33]:

$$\frac{\sigma(\Omega)}{\sigma(0)} = \Theta(|\Omega|-2) + i\left[\frac{4}{\pi\Omega} - \frac{1}{\pi} ln\left|\frac{\Omega+2}{\Omega-2}\right|\right] \tag{4.7}$$

Here, $\sigma(0) = e^2/4\hbar = \pi\alpha c\varepsilon_0 = 6.0853x10^{-5} AV^{-1}$ represents the universal dynamical conductivity of graphene.

4.3 Results & Discussion

4.3.1 Optical conductivity of graphene

At first, we concentrate on the variation of the optical conductivity of graphene. The behaviour of the complex optical conductivity of graphene can be easily predicted from Equation (4.7). Its real and imaginary parts has been shown in Figure 4.1, which clearly shows its dependence on wavelengths and chemical potential. We have not considered any variation in temperature in this study.

The real part of the conductivity, $Re(\sigma)$ decreases sharply from 1 to 0 with an increase in wavelength. At the same definite wavelength at which $Re(\sigma)$ undergoes jump, the imaginary part of the conductivity, $Im(\sigma)$ shows a sharp dip. As the chemical potential is increased, the discrete jump of $Re(\sigma)$ as well as the cusp of $Im(\sigma)$ occurs at a larger wavelength. It is obvious from the figure that for a particular wavelength (λ), there exists one definite chemical potential (μ) value at which the critical behaviour of the conductivity is prominent. Hence, a definite set of values of μ and λ exists over the operating region where we have found a critical

behaviour of the optical conductivity of graphene. We can define them as transition wavelength and chemical potential for the present study.

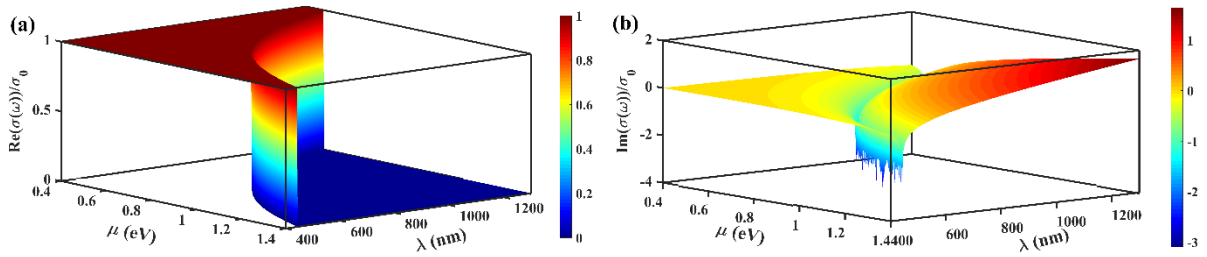

Figure 4.1. Surface optical conductivity (σ) of graphene: **(a)** Real part and **(b)** Imaginary part.

Naturally, the question arises that whether the optical conductivity has any role to play in the nature of beam shift. The optical beam shift arises for the reflection/refraction of a finite light beam which consists of a group of plane waves producing an envelope in the momentum space. Each of these components interacts differently with the interface depending upon Fresnel's reflection coefficients. These coefficients vary for different surfaces and depend on the optical conductivity of the surface [see Equations (4.1) and (4.2)]. This explains the importance of optical conductivity in the present study.

4.3.2 Spatial GH & IF shifts in graphene

We have fixed the incident angle at 45^0 for the rest of our study. Before going to the results, we should keep in mind that the eigen polarization states for the GH shifts are the S and P-polarized light beam and for the IF shifts are the circularly polarized (CP) & 45^0 linearly polarized (LP) light beam [41]. We have selected the polarization states of the incident light consequently.

Figure 4.2 represents spatial GH shifts for the case of partial reflection (upper panel) & total internal reflection (lower panel) of the light from graphene. The spatial GH shift in case of S-polarization states (Δ_{GH}^{S}) at first rises sharply up to a peak, subsequently declines to zero, and again increases monotonically with an increase in wavelength of the incident beam. The peak of Δ_{GH}^{S} shifts to a larger wavelength value with a decrease in the value of the chemical potential of graphene. Spatial GH shift for the P-polarization (Δ_{GH}^{P}) is opposite and an order

of magnitude greater than Δ_{GH}^{S} . But, the nature of variation of the GH shift is similar in both these cases. We already know that at higher wavelengths, the intraband transition dominates the optical conductivity. Also, an increase in chemical potential causes a larger filling of the bands. It has a combined consequence in modifying the Fresnel reflection coefficients in such a way that GH shift increases with increasing wavelength and chemical potential.

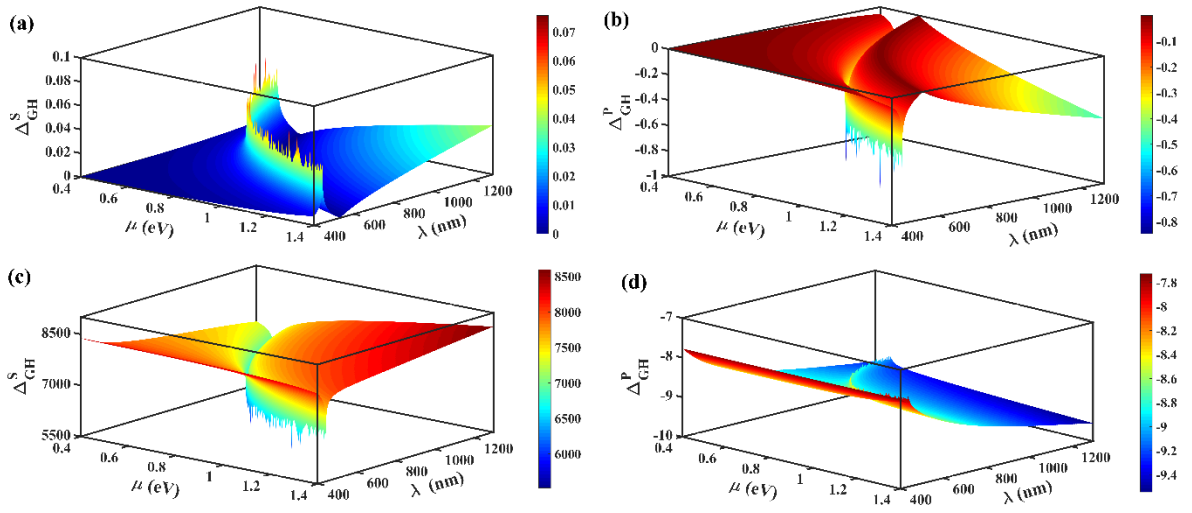

Figure 4.2. Variation of the spatial GH shift: **(a, b)** partial reflection and **(c, d)** total internal reflection.

However, for the spatial shift for TIR of the light, we observe a giant (much large than the general value of GH shift) GH shift for S-polarization states [Figure 4.2 (c)]. The observed shift, Δ_{GH}^{S} at first decreases with increasing wavelength and shows a dip at the specific wavelength (transition wavelength, as defined), then again increases to a larger value. In contrast, Δ_{GH}^{P} is opposite in magnitude and much smaller compared to Δ_{GH}^{S} i.e. it does not show any giant value. The shift, Δ_{GH}^{P} increases continuously to a higher negative magnitude with small peaks at specific wavelengths depending upon the chemical potential value. The peaks of the GH shift, in all the discussed cases, occur at the same transition wavelengths and chemical potentials as mentioned previously. It is noteworthy that the GH shift increases in magnitude as the intraband transition starts dominating the conductivity. But, the GH shift does

not change appreciably and remains almost constant within the range of chemical potential chosen.

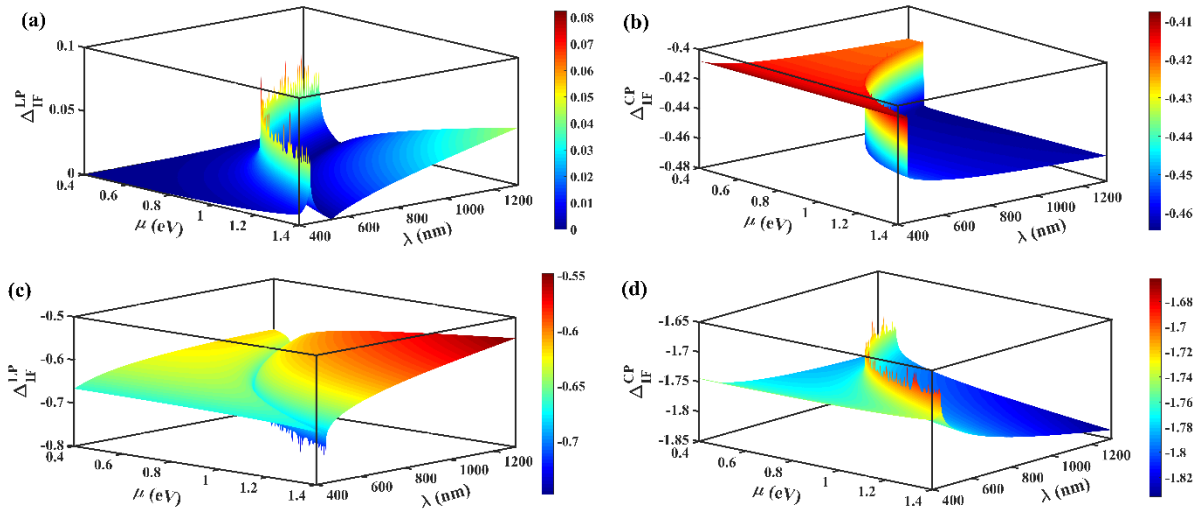

Figure 4.3. Variation of the spatial IF shift: **(a, b)** partial reflection and **(c, d)** total internal reflection.

Thereafter, we have studied the spatial IF shift that has been presented in Figure 4.3. We, at first, discuss the PR case [upper panel of Figure 4.3]. The spatial IF shift for LP (Δ_{IF}^{LP}) has a sharp peak at the transition point. At a higher wavelength, Δ_{IF}^{LP} goes on increasing to a larger value and is more sensitive to the chemical potential compared to the lower wavelength region. The spatial IF shift for the circularly polarized (CP) light (Δ_{IF}^{CP}) is completely different in nature and carries similarity with the real part of the optical conductivity. With varying wavelength and chemical potential, Δ_{IF}^{CP} produces a sharp jump at the transition point towards higher IF shift. At lower wavelength, Δ_{IF}^{CP} is independent of change in chemical potential, although the dependence comes at a higher wavelength value.

In the case of TIR [lower panel of Figure 4.3], the IF shift for 45^0 LP (Δ_{IF}^{LP}) decreases continuously with increasing wavelength, shows a dip, and again starts increasing. However, for circularly polarized light Δ_{IF}^{CP} remains almost constant for smaller wavelengths. Afterward, it shows a peak and monotonically decreases to a smaller magnitude. It is clear that the IF shift remains almost constant with a change in chemical potential. Though at higher wavelengths,

small peaks of IF shift are observed. Similar to the aforementioned cases, the jumps of IF shifts occur at the same transition wavelength and chemical potential. But, IF shifts for total internal reflection is an order of magnitude higher compared to partial reflection case.

4.3.3 Angular GH & IF shifts in graphene

For partial reflection, the angular GH shift for S-polarization (Θ_{GH}^{S}) and P-polarization states of light (Θ_{GH}^{P}) are similar in nature as shown in Figure 4.4 (upper panel). With increasing wavelength, Θ_{GH}^{S} increases as well as Θ_{GH}^{P} showing a sharp jump at the transition wavelength and chemical potential. At smaller wavelength (UV region), no effect of chemical potential is observed. But at large wavelength, a sudden increase is observed at the transition value of chemical potential. Though nature is identical for both Θ_{GH}^{S} and Θ_{GH}^{P}, Θ_{GH}^{P} is larger in magnitude than Θ_{GH}^{S}, but are much smaller than the spatial GH shifts.

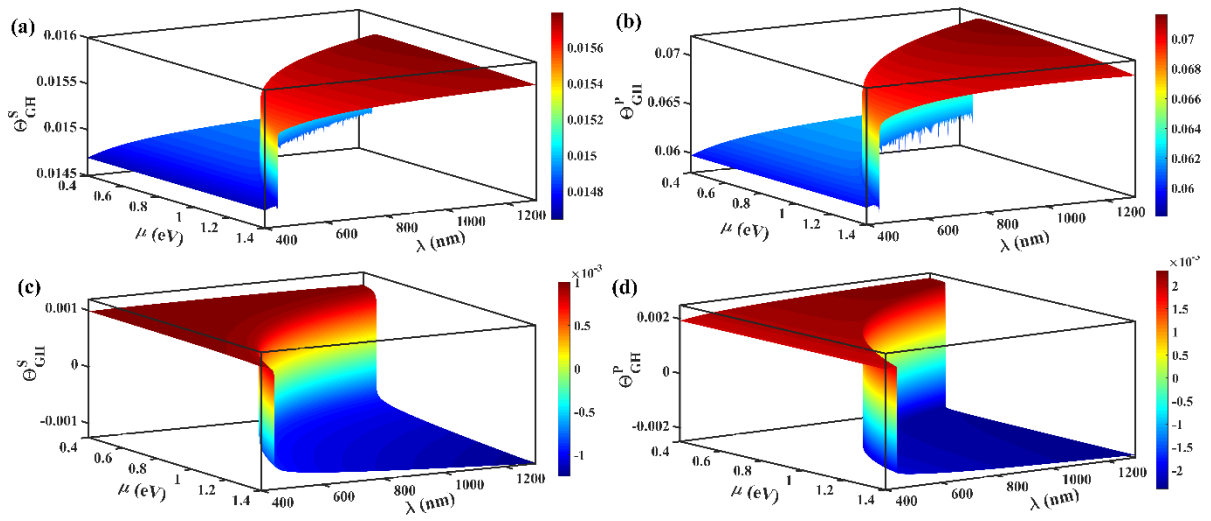

Figure 4.4. Variation of the angular GH shift: **(a, b)** partial reflection and **(c, d)** total internal reflection.

On the other hand, the angular shift for TIR is almost negligible in magnitude. We have decided to show their behavior also. In this case, both Θ_{GH}^{S} and Θ_{GH}^{P} sharply decrease in magnitude with increasing wavelength exhibiting a sharp dip at a definite wavelength and chemical potential [lower panel of Figure 4.4] which agrees with the previously mentioned values of the transition

region. Hence, the angular shift is much larger for smaller wavelengths (UV region) and is practically independent of chemical potential. But, at the longer wavelength infrared region, the angular shift is much smaller and shows a jump from a higher to lower value with an increase in chemical potential.

Furthermore, we have also investigated the behavior of the angular IF shift [Figure 4.5]. As we know already, for circularly polarized light, $\eta = 0$ (where $\hat{f} = a_p \hat{x}_i + a_s \, exp(i\eta)\hat{y}_i$ controls the polarization state of the beam [18]). Therefore, no angular IF shift exists for circularly polarized light. But, there exists non-zero angular IF shift for the graphene-coated surface for 45^0 linearly polarized light (LP) in both PR and TIR cases. Angular IF shift is also order of magnitude higher than angular GH shift. For partial reflection of the light beam, Θ_{IF}^{LP} is negative valued and increases in magnitude with an increase in wavelength. Again, at a smaller wavelength (UV) region, the angular IF shift is practically independent of the chemical potential. But, at the longer wavelength region, we have observed a sharp jump to a higher negative magnitude. For total internal reflection, the angular IF shift, Θ_{IF}^{LP} depicts identical nature in comparison to that of the partial reflection case. But, Θ_{IF}^{LP} for total internal reflection is order of magnitude lesser than that of partial reflection condition. The point of transition remained the same as predicted before.

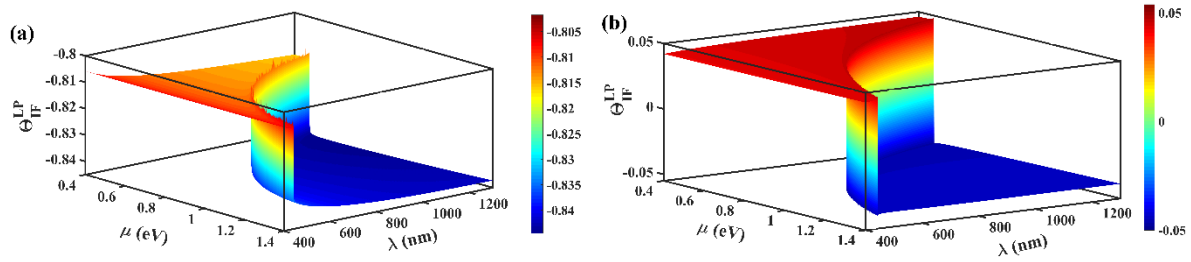

Figure 4.5. Variation of the angular IF shift: **(a)** partial reflection and **(b)** total internal reflection

4.4 Outlook & Summary

In this work, we have studied the behavior of spatial as well as angular optical beam shifts for the graphene-coated surface in both partial and total internal reflection cases. We have shown the variation of the GH & IF shifts and emphasized on their typical characteristics over a wide

wavelength range, starting from ultraviolet up to the infrared region of the electromagnetic spectrum. The study is important as it provides the experimentalists a broad overview of the region of wavelength over which the GH & IF shifts are appreciable. Moreover, the nature of GH & IF shifts for a range of chemical potential of graphene samples has been discussed. Hence, the present study also helps in tuning a specific value of the chemical potential to maximize optical beam shift. The present study can be extended for multilayer samples and higher-order modes of the light beam as well.

References

[1] M. Born and E. Wolf, *Principles of Optics: Electromagnetic Theory of Propagation, Interference and Diffraction of Light* (Elsevier Science, 2013).

[2] J. D. Jackson, *Classical electrodynamics* (Wiley, 1975).

[3] K. Y. Bliokh and A. Aiello, Journal of Optics **15**, 014001 (2013).

[4] F. Goos and H. Hänchen, Annalen der Physik **436**, 333 (1947).

[5] K. Artmann, Annalen der Physik **437**, 87 (1948).

[6] C. Imbert, Physical Review D **5**, 787 (1972).

[7] F. I. Fedorov, Dokl. Akad. Nauk SSSR **105**, 465 (1955).

[8] A. Aiello, New Journal of Physics **14**, 013058 (2012).

[9] M. Ornigotti and A. Aiello, Journal of Optics **15**, 014004 (2013).

[10] F. Töppel, M. Ornigotti, and A. Aiello, New Journal of Physics **15**, 113059 (2013).

[11] O. Hosten and P. Kwiat, Science **319**, 787 (2008).

[12] A. Aiello, M. Merano, and J. P. Woerdman, Physical Review A **80**, 061801 (2009).

[13] S. Chen, C. Mi, L. Cai, M. Liu, H. Luo, and S. Wen, Applied Physics Letters **110**, 031105 (2017).

[14] P. W. Xin Li, Fei Xing, Xu-Dong Chen, Zhi-Bo Liu, and Jian-Guo Tian, Opt. Lett. **39**, 5574 (2014).

[15] A. Das and M. Pradhan, Laser Physics Letters **17**, 066001 (2020).

[16] M. Merano, A. Aiello, G. W. 't Hooft, M. P. van Exter, E. R. Eliel, and J. P. Woerdman, Opt. Express **15**, 15928 (2007).

[17] Y. Huang, Z. Yu, C. Zhong, J. Fang, and Z. Dong, Opt. Mater. Express **7**, 1473 (2017).

[18] A. Das and M. Pradhan, Optics Communications **437**, 312 (2019).

[19] A. Das and M. Pradhan, J. Opt. Soc. Am. B **35**, 1956 (2018).

[20] A. Farmani, M. Miri, and M. H. Sheikhi, J. Opt. Soc. Am. B **34**, 1097 (2017).

[21] X. Chen, X.-J. Lu, Y. Ban, and C.-F. Li, Journal of Optics **15**, 033001 (2013).

[22] V.-O. de Haan, J. Plomp, T. M. Rekveldt, W. H. Kraan, A. A. van Well, R. M. Dalgliesh, and S. Langridge, Physical Review Letters **104**, 010401 (2010).

[23] S. Grosche, M. Ornigotti, and A. Szameit, Opt. Express **23**, 30195 (2015).

[24] C. W. J. Beenakker, R. A. Sepkhanov, A. R. Akhmerov, and J. Tworzydło, Physical Review Letters **102**, 146804 (2009).

[25] M. I. Katsnelson, *Graphene: Carbon in Two Dimensions* (Cambridge University Press, Cambridge, 2012).

[26] K. S. Novoselov, A. K. Geim, S. V. Morozov, D. Jiang, M. I. Katsnelson, I. V. Grigorieva, S. V. Dubonos, and A. A. Firsov, Nature **438**, 197 (2005).

[27] A. H. Castro Neto, F. Guinea, N. M. R. Peres, K. S. Novoselov, and A. K. Geim, Reviews of Modern Physics **81**, 109 (2009).

[28] F. Bonaccorso, Z. Sun, T. Hasan, and A. C. Ferrari, Nature Photonics **4**, 611 (2010).

[29] K. S. Novoselov, A. K. Geim, S. V. Morozov, D. Jiang, Y. Zhang, S. V. Dubonos, I. V. Grigorieva, and A. A. Firsov, Science **306**, 666 (2004).

[30] A. K. Geim and K. S. Novoselov, Nature Materials **6**, 183 (2007).

[31] M. I. Katsnelson, Materials Today **10**, 20 (2007).

[32] M. Merano, Opt. Lett. **41**, 5780 (2016).

[33] S. A. Mikhailov and K. Ziegler, Physical Review Letters **99**, 016803 (2007).

[34] K. F. Mak, M. Y. Sfeir, Y. Wu, C. H. Lui, J. A. Misewich, and T. F. Heinz, Physical Review Letters **101**, 196405 (2008).

[35] E. M. Hajaj, O. Shtempluk, V. Kochetkov, A. Razin, and Y. E. Yaish, Physical Review B **88**, 045128 (2013).

[36] G. W. Hanson, Journal of Applied Physics **103**, 064302 (2008).

[37] T. Zhan, X. Shi, Y. Dai, X. Liu, and J. Zi, Journal of Physics: Condensed Matter **25**, 215301 (2013).

[38] V. P. Gusynin, S. G. Sharapov, and J. P. Carbotte, Physical Review Letters **96**, 256802 (2006).

[39] K. Ziegler, Physical Review Letters **97**, 266802 (2006).

[40] P. M. Platzman, P. M. Platzman, and P. A. Wolff, *Waves and Interactions in Solid State Plasmas* (Academic Press, 1973).

[41] J. B. Götte, W. Löffler, and M. R. Dennis, Physical Review Letters **112**, 233901 (2014).

Section B: Experimental Investigation

"The significant problems we have cannot be solved at the same level of thinking with which we created them."

- Albert Einstein

Chapter 5 Experimental Measurement of the Optical Beam Shifts

Here we discuss the different experimental techniques for the measurement of the Goos-Hänchen and Imbert-Fedorov shifts. The advantages and disadvantages of the different techniques have also been demonstrated.

5 Experimental Measurement of the Optical Beam Shifts

5.1 Introduction

In this second part of this thesis, the principal objective is to develop appropriate experimental methods for the measurement of the optical beam shifts. As stated in *Chapter* 1, numerous studies were carried out to experimentally measure the Goos-Hänchen (GH) and Imbert-Fedorov (IF) shifts [1-6]. Several upgradations have been done to increase the detection efficiency and accuracy. But, the first major breakthrough in this experimental field was the renowned experiment of Paul Kwiat & his graduate student Onur Hosten at the University of Illinois (2008). They first experimentally demonstrated how to apply quantum weak measurement to measure the optical spin Hall shift [7]. Later, a lot of modifications were introduced for better amplification and a few other techniques were also proposed to ease the complexity of the measurement process [8-13]. In this *Chapter*, we discuss different techniques for the measurement of optical beam shifts. We have specifically elaborated the two techniques (a) *Quantum weak measurement* and (b) *Stokes Polarimetric* Technique. The advantages of the above techniques over others are also discussed in the respective sections.

5.2 Difficulty in the measurement process

We already know that typical amplitudes of the optical beam shift go in the order of $(1/k)$ (where k is the wave vector). This means optical beam shifts are in the range of a fraction of wavelengths. In general GH shift is the dominant one, IF and spin Hall shifts are order of magnitude lesser than the former. Therefore, the measurements of such tiny optical beam shift is not an easy task. The experiments performed in the earlier days were unable to study the beam shifts for varying parameters, such as the change in angle of incidence, change in wavelength, etc. The earlier experiments were focussed on studying these optical shifts in the neighbourhood of critical angle of incidence where the shift, in general, depicts larger values.

Over time, several new experimental techniques were proposed and developed subsequently. The principal challenges and objectives for the measurement of the optical beam shifts are listed below:

(a) Measurement with high precision.

(b) Increase the measurement efficiency.

(c) Reduce the source of noise and unwanted fluctuations.

(d) Greater amplification of the beam shift.

(e) Study over a large range of incident angles.

(f) The correct determination of GH and IF shifts in the neighbourhood of critical angle of incidence.

(h) Accurate definition & determination of the optical beam shift at Brewster's angle.

(i) A generalized method that is applicable to measure the optical beam shift in case of any materials.

In this thesis, we have logically answered these questions. The experimental methods developed by us are in accordance with all the above questions and is very fundamental and general that can be applied in future fundamental research as well as application purpose.

5.3 Different measurement techniques

Starting from the 1950s, numerous studies have been ongoing focussing upon removing the difficulties associated with the measurement process (as discussed in the previous section) and introducing a general method for the measurement. Over time, only a few of the several proposed techniques have been approved by the research community.

(a) Quantum Weak Measurement (QWM),

(b) Stokes Polarimetric technique (SP),

(c) Beam Splitter Scanning method (BSS),

(d) Interferometric Weak Value amplification (IWV).

In the following, we discuss the basic formalism of these techniques.

5.3.1 Quantum Weak Measurement (QWM)

The technique of *weak measurement* is gradually recognized as one of the most encouraging tools in modern advanced quantum mechanical research. Aharonov, Albert & Vaidman first announced the concept of *weak measurement* (1989) [14-16]. This method can disclose important information about a quantum state's amplitude without being collapsed into the

eigenvectors. In this method, a weak coupling between the system and the measuring device is performed. Due to such weak coupling, the state vector is not collapsed in a specific eigenstate, but it is only biased by a small angle i.e. we get a superposition of unresolved eigenvalues instead of a specific one. Finally, post-selection of the output to a specific quantum state (by coherent interference) is performed to get a 'weak value' that can stay well outside the range of eigenvalues. It has many advantages which will be addressed in detail in *Chapters* 6 & 7.

Aharonov, Albert & Vaidman (AAV) first performed the breakthrough experiment where they applied a beam of spin 1/2 electrons for illustration. The initial state ($|\psi_i\rangle$) and the final state ($|\psi_f\rangle$) were set as spin up directions by using the Stern-Gerlach magnets which made $|\psi_i\rangle \& |\psi_f\rangle$ 'almost orthogonal' to each other [15,17]. The weak measurement of the spin in a direction perpendicular to the post-selection direction was performed in between the pre-selection and post-selection units. This was done by another weak Stern-Gerlach magnet that deflected the two spin directions by a small angle (less than the divergence angle of the electron beam). The detailed experimental method and theoretical treatment can be found out in the references [14,15].

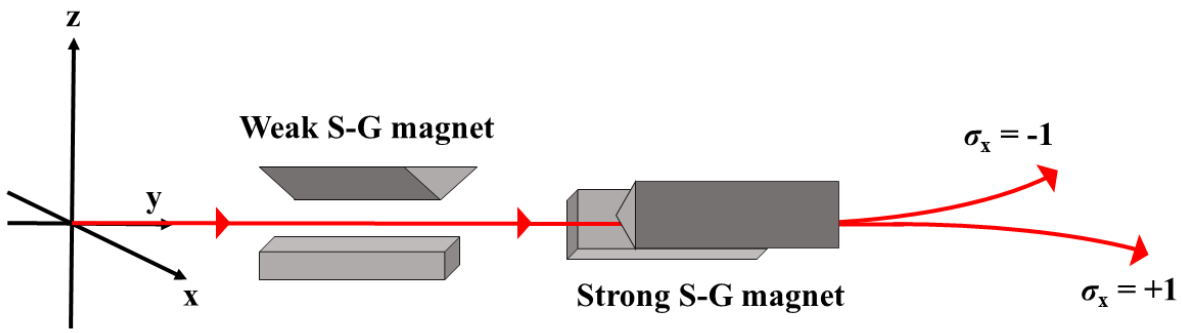

Figure 5.1. Stern Gerlach experimental setup as proposed by AAV to observe the weak value of electron spin.

The above methodology is the well-known *weak measurement* of a quantum mechanical spin half particle. An optical analogue of this weak measurement technique was first formulated by Duck, Stevenson & Sudarshan (1989) [18]. Later, Ritchie, Story & Hulet [19] removed the inconsistencies and developed a modified model that can be applied for the

optical measurement purpose. This is the very basic formalism of the optical weak measurement technique which will be described below.

Instead of a spin-1/2 electron beam, a fundamental Gaussian beam is considered. The weak and strong Stern-Gerlach magnets are substituted with the polarizers. Polarizers act as the pre-selection and post-selection units. Weak measurement is accomplished by a birefringent crystalline quartz plate. It separates the two perpendicular (P and S) polarization states of the light beam by a separation distance much less than the beam waist.

The electric field vector representing the incident light is:

$$E_i = E_0 \, exp\left[-\frac{\left(x^2 + y^2\right)}{w_0^2} \right] \left[\hat{i} \cos\alpha + \hat{j} \sin\alpha \right] \tag{5.1}$$

where, the incident beam is assumed to be along the $\hat{z}$ direction, w_0 denotes beam waist.

The light is incident on a uniaxial birefringent plate normally whose optic axis is aligned with the $\hat{x}$ direction (the $\hat{x}$ axis rests in the plane of the plate). The plane is rotated about the $\hat{y}$ axis by an angle θ. The weak measurement is performed by the uniaxial birefringent plate by spatially separating the two orthogonal linear polarization components (the ordinary and extraordinary rays) of the incident light field, by a separation distance (δa) which is small compared to the beam waist. Additionally, a phase difference ϕ between the two rays is introduced by the birefringence plate due to a difference in optical path length traversed inside. After emergence, the output electric field (neglecting the displacement caused by refraction present in both polarization components) is described by:

$$E_w = E_0 \, exp\left[-\frac{x^2}{w_0^2} \right] \left[\hat{i} e^{i\phi} \cos\alpha \, exp\left[-\frac{\left(y + \delta a\right)^2}{w_0^2} \right] + \hat{j} \sin\alpha \, exp\left[-\frac{y^2}{w_0^2} \right] \right] \tag{5.2}$$

The polarizer is applied to post-select the output field at angle β (w. r. t. $\hat{x}$). Therefore, the post-selected electric field becomes:

$$E_f = E_0 \, exp\left[-\frac{x^2}{w_0^2} \right] \left[e^{i\phi} \cos\alpha \cos\beta \, exp\left[-\frac{\left(y + \delta a\right)^2}{w_0^2} \right] + \sin\alpha \sin\beta \, exp\left[-\frac{y^2}{w_0^2} \right] \right] \left[\hat{i} \cos\beta + \hat{j} \sin\beta \right] \tag{5.3}$$

Now, the finally transmitted light intensity can be found out from the electric field by $\left|E_f\left(x=0\right)\right|^2$. Therefore, the final transmitted light intensity $I\left(y\right)$ detected along $\hat{y}$ can be expressed as:

$$I\left(y\right)=I_0\left[\begin{array}{l} cos^2\alpha\, cos^2\beta\, exp\left[-\frac{2\left(y+\delta a\right)^2}{w_0^2}\right]+sin^2\alpha\, sin^2\beta\, exp\left[-\frac{2y^2}{w_0^2}\right] \\ +2\cos\phi\cos\alpha\cos\beta\sin\alpha\sin\beta\, exp\left[-\frac{\left(y+\delta a\right)^2+y^2}{w_0^2}\right] \end{array}\right] \tag{5.4}$$

where, I_0 is the maximum light intensity.

In weak measurement, we assume the beam displacement, $\delta a \ll w_0$. To get maximum displacement, $\alpha=\pi/4$ is chosen.

If we set $\beta=\alpha$, resultant intensity $I\left(y\right)$ is generated by the constructive superposition of two Gaussian distributions separated by a distance small compared to the respective Gaussian widths. Hence, $I\left(y\right)$ is nearly a single, un-shifted Gaussian. When the second polarizer is rotated by the post-selection angle, $\beta=\left(\alpha+\pi/2\right)+\varepsilon$, with $\varepsilon\ll1$, the initial and final states are not exactly orthogonal but in the close neighbourhood of the orthogonal condition. In this case, the two Gaussians destructively interfere. If $\delta a/2w_0 \ll \varepsilon \ll 1$, the interference would yield a single Gaussian that is shifted from the original position. The centroid is shifted by an amount equal to the weak value:

$$A_w \approx \frac{1}{2}\delta a \times cot\left(\varepsilon\right) \tag{5.5}$$

This weak value can attain larger value than δa .

As ε approaches zero, the approximations made by AAV break down. For $\varepsilon=0$, rather than a single shifted Gaussian, the intensity profile depicts two peaks separated by approximately $\sqrt{2}w_0$, with maximum intensity given by:

$$I \approx \frac{1}{2e}\left(\frac{\delta a}{w_0}\right)^2 I_0 \tag{5.6}$$

Therefore, the birefringence-induced separation δa is magnified in the resulting intensity distribution, but at the expense of reduced intensity. This is the celebrated phenomenon of *Weak Value Amplification*.

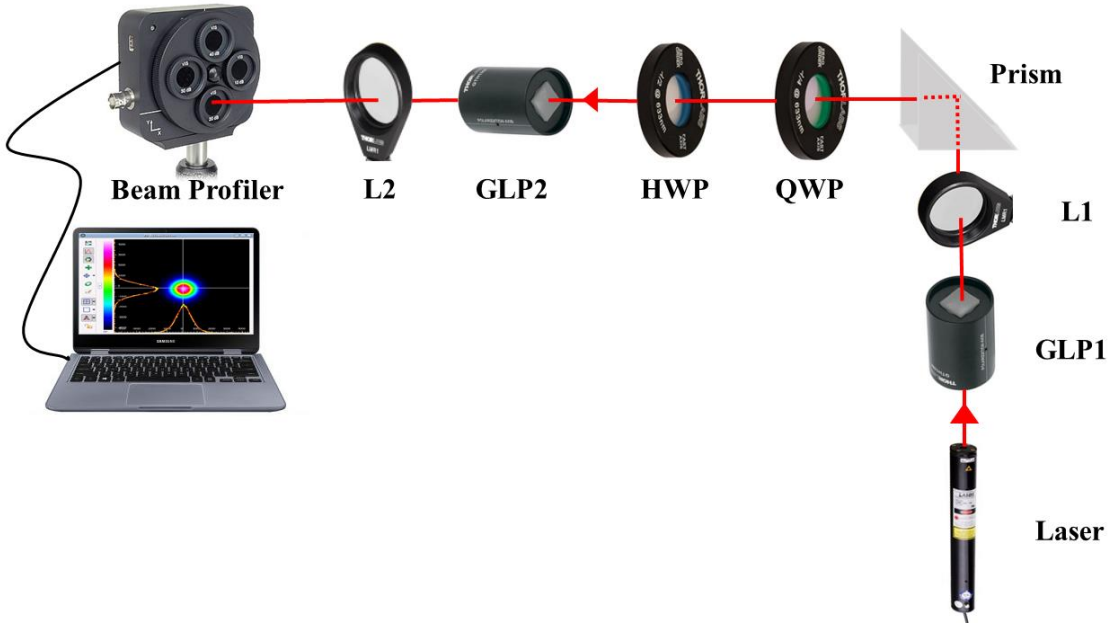

Figure 5.2. Quantum weak measurement setup for the precise measurement of the optical beam shift (working principle explained in *Chapter* 6).

5.3.2 Stokes Polarimetric technique (SP)

The measurement of optical beam shift using the Stokes Polarimetric technique is an indirect but quicker one. In this method, the GH and IF shifts are determined mainly from the Fresnel reflection coefficients. The reflection coefficients can be calculated from the experimentally measured values of the Stokes parameters.

Irish Physicists Sir George Gabriel Stokes first revealed that the polarization state of light can be categorized by four intensity parameters [20,21]. The Stokes polarization parameters are extensively used to label the polarization nature of the light beam. The polarization ellipse is an amplitude description of the polarized beam that is not directly measurable.

The Stokes parameters define different polarization states of light like plane polarization, elliptical polarization, and circular polarization along with the unpolarized, and partially polarized light. Polarization arises when the optical beam consists of two independent orthogonal components $E_x(z,t)$ & $E_y(z,t)$. It may possesses different amplitudes and phases.

$$E_x(z,t) = E_{0x}\cos(\omega t - \kappa z + \delta_x) \tag{5.7a}$$

$$E_y(z,t) = E_{0y}\cos(\omega t - \kappa z + \delta_y) \tag{5.7b}$$

Eliminating the propagator from the above equations provides the equation of the polarization ellipse.

$$\frac{E_x^2(z,t)}{E_{0x}^2} + \frac{E_y^2(z,t)}{E_{0y}^2} - \frac{2E_x(z,t)E_y(z,t)}{E_{0x}E_{0y}}\cos\delta = \sin^2\delta \tag{5.8}$$

where, $\delta = \delta_y - \delta_x$ is the phase difference.

By taking the time average of the polarization ellipse we reach to the following equation:

$$S_0^2 = S_1^2 + S_2^2 + S_3^2 \tag{5.9}$$

where, the Stokes parameters are defined as:

$$S_0 = E_{0x}^2 + E_{0y}^2 \tag{5.10a}$$

$$S_1 = E_{0x}^2 - E_{0y}^2 \tag{5.10b}$$

$$S_2 = 2E_{0x}E_{0y}\cos\delta \tag{5.10c}$$

$$S_3 = 2E_{0x}E_{0y}\sin\delta \tag{5.10d}$$

The conventional measurement of the Stokes parameters is performed by passing the polarized light successively through a quarter-wave plate and a linear polarizer. A wave plate is characterized by the fast and slow axes that yield a phase difference among the orthogonal components. The quarter-wave plate introduces a phase shift of $\lambda/4$ between the orthogonal components. In a linear polarizer, no transmission happens along one direction and complete transmission appears along its perpendicular direction. A linear polarizer can also transform any other polarization state to a linear polarization state.

During the measurement, the wave plate is kept immovable with its fast axis along $\hat{x}$ and the transmission axis (linear polarizer) is rotated by an angle θ. The intensity of the optical beam entering the detector will be:

$$I(\theta,\phi)=\frac{1}{2}\left[S_0+S_1\cos 2\theta+S_2\sin 2\theta\cos\phi-S_3\sin 2\theta\sin\phi\right] \tag{5.11}$$

where, θ is the linear polarization angle and ϕ is the phase generated by the quarter-wave plate.

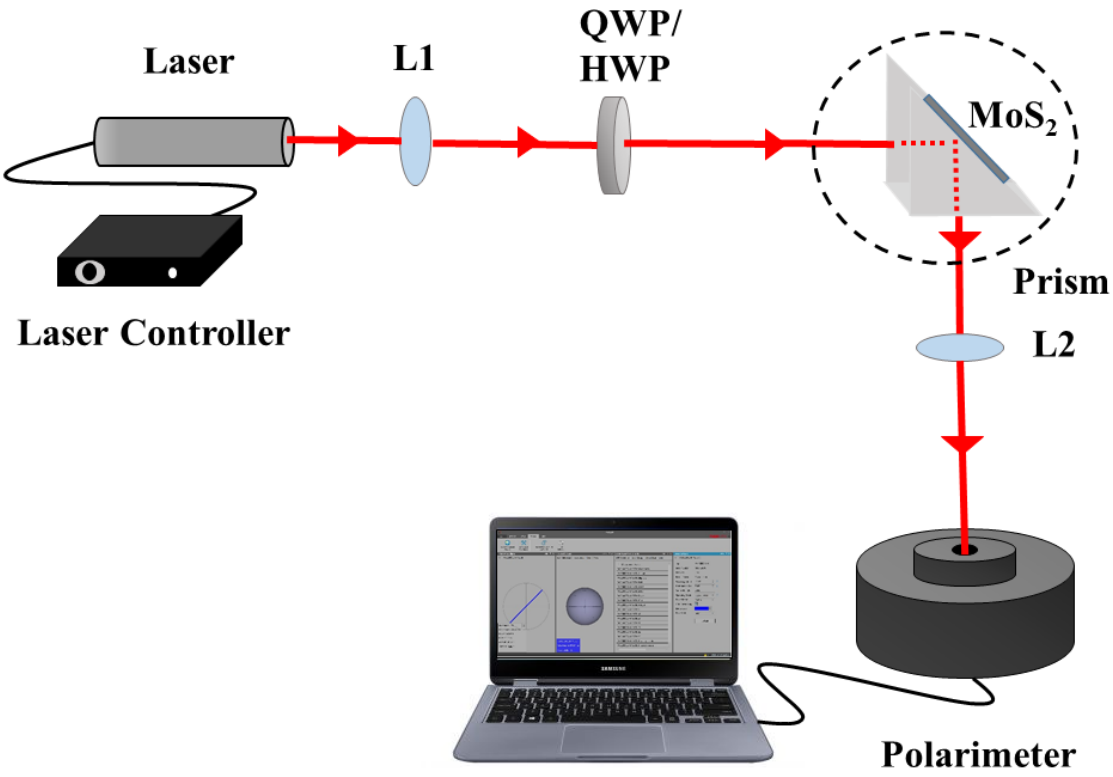

Figure 5.3. Schematic representation of the Polarimetric measurement of the GH & IF shift.

The Stokes parameters can be measured by first moving away from the wave plate and then measuring consecutively the intensity of the optical beam with the linear polarizer positioned at incident angles, θ = 0°, 45°, and 90°, respectively. The final (fourth) measurement is performed by introducing a quarter-wave plate ($\phi = 90^0$) in the optical path with the linear polarizer set at $\theta = 45^0$. The four Stokes parameters can be calculated by using the following:

$$S_0 = I(0,0) + I(\pi/2,0) \tag{5.12a}$$

$$S_1 = I(0,0) - I(\pi/2,0) \tag{5.12b}$$

$$S_2 = 2I(\pi/4,0) - S_0 \tag{5.12c}$$

$$S_3 = S_0 - I(\pi/4,\pi/2) \tag{5.12d}$$

The calculation of amplitudes of the reflection coefficients are easier now [22]:

$$|r_S| = \sqrt{S_0 + S_1/2E_{0x}^2} \tag{5.13a}$$

$$|r_P| = \sqrt{S_0 - S_1/2E_{0y}^2} \tag{5.13b}$$

The magnitudes and relative phases of the reflection coefficients produce GH and IF shifts for both partial and total internally reflected light [5,23].

$$\Delta_{GH} = \left(\frac{\lambda}{2\pi}\right)\frac{|r_S|^2 a_S^2 Im\left(\frac{\partial \ln r_S}{\partial \theta_i}\right) + |r_P|^2 a_P^2 Im\left(\frac{\partial \ln r_P}{\partial \theta_i}\right)}{|r_S|^2 a_S^2 + |r_P|^2 a_P^2} \tag{5.14a}$$

$$\Theta_{GH} = \left(\frac{Z_r}{k^2 L^2}\right)\frac{|r_S|^2 a_S^2 Re\left(\frac{\partial \ln r_S}{\partial \theta_i}\right) + |r_P|^2 a_P^2 Re\left(\frac{\partial \ln r_P}{\partial \theta_i}\right)}{|r_S|^2 a_S^2 + |r_P|^2 a_P^2} \tag{5.14b}$$

$$\Delta_{IF} = \left(-\frac{\lambda}{2\pi}\right)\left(\frac{a_P a_S \cot\theta_i}{|r_S|^2 a_S^2 + |r_P|^2 a_P^2}\right).\left[\left(|r_S|^2 + |r_P|^2\right)\sin\eta + 2r_S r_P \sin\left(\eta + \phi_S - \phi_P\right)\right] \tag{5.15a}$$

$$\Theta_{IF} = \left(-\frac{Z_r}{k^2 L^2}\right)\left(\frac{a_P a_S \left(|r_S|^2 - |r_P|^2\right)\cot\theta_i}{|r_S|^2 a_S^2 + |r_P|^2 a_P^2}\right)\cos\eta \tag{5.15b}$$

Here, $a_s\left(E_{0x}\right)$ and $a_p\left(E_{0y}\right)$ signifies the S and P-polarization components of the light, θ_i denotes incident angle; $Z_r = kz_r$, where z_r is the distance of propagation; $L = kw_0^2/2$, and $k = 2\pi n/\lambda_0$ is the corresponding wave vector, η is the relative phase difference of the incident light (η=0 for S & P, η=0 or π for +45^0 LP & -45^0 LP, η=+π/2 or –π/2 for RCP & LCP).

5.3.3 Beam Splitter Scanning method (BSS)

This method is also used to enhance the optical beam shift in a simplified way.

The Goos-Hänchen shift is determined by the application of the stationary phase approximation method. The GH shift can be written as [24]:

$$\Delta(\theta_i,x)=-\frac{1}{k_g}\frac{d\phi_r(\theta_i,x)}{d\theta_i}=-\frac{\lambda}{2\pi n_g}\frac{1}{|r|^2}\left[Re(r)\frac{d\,Im(r)}{d\theta_i}-Im(r)\frac{d\,Re(r)}{d\theta_i}\right] \tag{5.16}$$

where, x denotes the thickness of the material.

The reflection coefficient can be represented as:

$$r=\frac{r_{12}+r_{23}\,exp(2ik_2x)}{1+r_{12}r_{23}\,exp(2ik_2x)} \tag{5.17}$$

where r_{12} is the reflection coefficient in the prism/film interface, r_{23} is the reflection coefficient in the film/air interface, and k_2 is the x-component of wave vector k. They can be written in complex notation:

$$r(\theta_i,x)=|r(\theta_i,x)|exp[i\phi(\theta_i,x)] \tag{5.18}$$

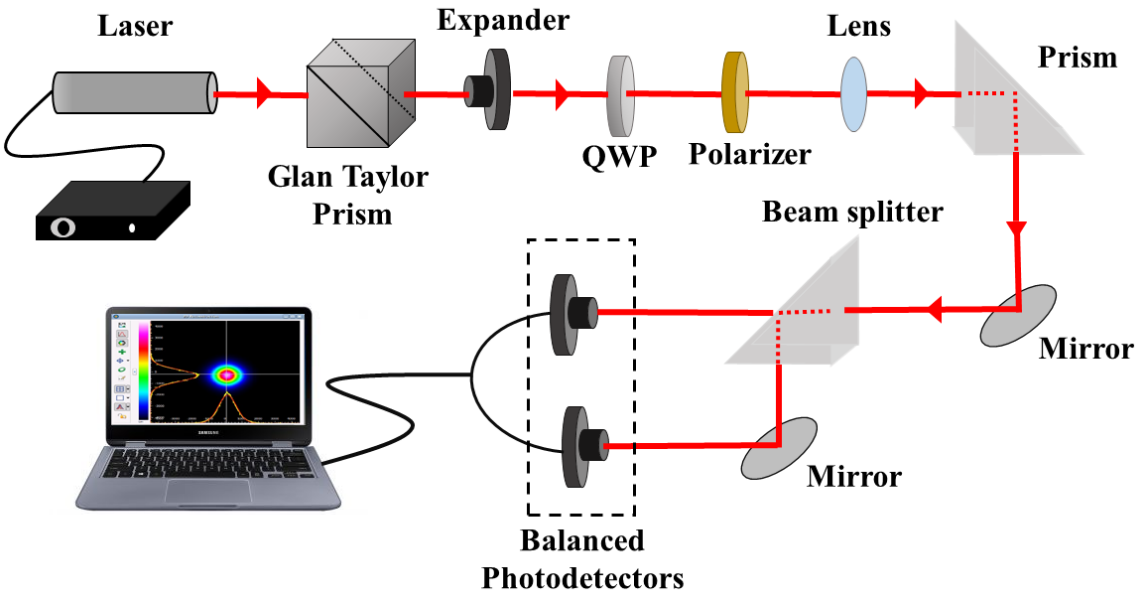

Figure 5.4. Schematic presentation of the Beam Splitter Scanning technique.

In conducting the experiments, the sensitivity of the GH shift for both TM and TE polarized modes is first verified. After that, the beam splitter prism is placed onto a piezo nano-positioning stage to split and scan the light beam. The balanced amplified photodetector records the voltage changes at the time of scanning. The beam splitter prism distributed the light beam into two alike parts. The photocurrents in the two photodiodes were measured to be identical. Subsequently, the voltage of the balanced photodetector was recorded and calibrated as zero-point. By using this process under different conditions of incident polarization states, the separation between the two zero points of the TM and TE polarization modes can be measured. This difference is nothing but the difference in GH shift of the TM mode relative to the TE polarization mode, ($\Delta_{TM} - \Delta_{TE}$).

5.3.4 Interferometric Weak Value amplification (IWV)

This technique is another example of the weak value amplification scheme but realized in a different way. As already stated, the weak value is the average of measurement results over a subset of data that correspond to a specific outcome of a projective measurement (discussed before).

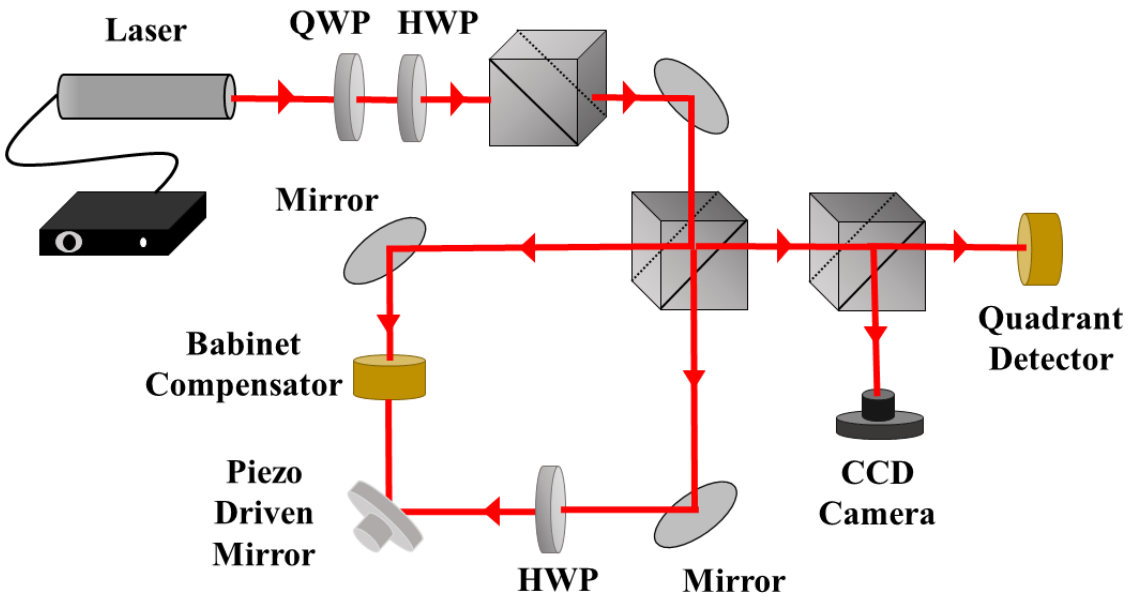

Figure 5.5. Interferometric measurement setup to measure the GH shift.

To realize the measurement technique, first, consider the pictorial representation of the weak value amplification concept as described in Figure 5.5. The light beam arrives at the Sagnac interferometer consisting of a 50/50 beam splitter and mirrors to send the beam in one of two paths. In ideal case, all of the light leaves the input terminal (called a bright port) and the other terminal is called the dark port. There is constructive interference observed at the entrance terminal (two $\pi/2$ phase differences). This symmetry is broken with the presence of a half-wave plate and a Soleil-Babinet compensator (SBC) by introducing a relative phase ϕ in the tracks, permitting one to constantly alternate the dark port to a bright port. This experiment is nothing but the modified classical optics interferometry. The beam traverses through the interferometer. Subsequently, the spatial shift of light departing the dark port is examined. The transverse position degree of freedom of the beam, labelled by $|x\rangle$ is denoted as the detection meter. The mirror is tilted a little at the symmetric point in the interferometer. Such a tilt resembles a transverse momentum shift of the beam, breaking the symmetry of the interferometer. As a result, one propagation direction is bent to the left of the optic axis, and the other to the right.

The final shift can be expressed as the position expectation:

$$\langle x\rangle = 2k|A_w|\frac{\sigma^2 l_{1m} + a\sigma l_{md}}{l_{1m} + l_{md}} \tag{5.19}$$

where, $\sigma = a(l_{im} + l_{md})/s_i$ is the beam size at the detector, l_{im} is the distance from the lens image to the moving mirror, l_{md} is the distance from the moving mirror to the detector, a is the initial collimated beam radius.

5.4 Outlook & Summary

To summarize, in this chapter we have discussed the different experimental techniques available now for the measurement of Goos-Hänchen & Imbert-Fedorov shifts. We have discussed the fundamental mechanisms of the four different experimental setups. Different experimental techniques have different advantages and disadvantages associated with them. But, depending on particular research objective, different techniques can be implemented keeping in mind the problems linked with the measurement process. In the next few chapters, we will discuss the first two measurement techniques and their advantages while applied in the measurement of optical beam shifts in material surfaces.

References

[1] K. Y. Bliokh and A. Aiello, Journal of Optics **15**, 014001 (2013).

[2] K. Y. Bliokh and Y. P. Bliokh, Physical Review E **75**, 066609 (2007).

[3] F. Töppel, M. Ornigotti, and A. Aiello, New Journal of Physics **15**, 113059 (2013).

[4] A. Aiello, New Journal of Physics **14**, 013058 (2012).

[5] M. Ornigotti and A. Aiello, Journal of Optics **15**, 014004 (2013).

[6] M. Merano, N. Hermosa, J. P. Woerdman, and A. Aiello, Physical Review A **82**, 023817 (2010).

[7] O. Hosten and P. Kwiat, Science **319**, 787 (2008).

[8] S. Chen, X. Zhou, X. Ling, W. Shu, H. Luo, and S. Wen, Applied Physics Letters **118**, 111104 (2021).

[9] D. Xu, S. He, J. Zhou, S. Chen, S. Wen, and H. Luo, Applied Physics Letters **116**, 211103 (2020).

[10] S. Chen, X. Ling, W. Shu, H. Luo, and S. Wen, Physical Review Applied **13**, 014057 (2020).

[11] L. Xiaohui, Z. Xinxing, H. Kun, L. Yachao, Q. Cheng-Wei, L. Hailu, and W. Shuangchun, Reports on Progress in Physics **80**, 066401 (2017).

[12] A. Das and M. Pradhan, J. Opt. Soc. Am. B **38**, 387 (2021).

[13] A. Das and M. Pradhan, Laser Physics Letters **17**, 066001 (2020).

[14] Y. Aharonov, D. Z. Albert, and L. Vaidman, Physical Review Letters **60**, 1351 (1988).

[15] Y. Aharonov and D. Rohrlich, *Quantum Paradoxes: Quantum Theory for the Perplexed* (Wiley, 2005).

[16] S. Wu and Y. Li, Physical Review A **83**, 052106 (2011).

[17] L. Vaidman, in *Compendium of Quantum Physics*, edited by D. Greenberger, K. Hentschel, and F. Weinert (Springer Berlin Heidelberg, Berlin, Heidelberg, 2009), pp. 840.

[18] I. M. Duck, P. M. Stevenson, and E. C. G. Sudarshan, Physical Review D **40**, 2112 (1989).

[19] N. W. M. Ritchie, J. G. Story, and R. G. Hulet, Physical Review Letters **66**, 1107 (1991).

[20] A. Das and M. Pradhan, Journal of Optics **22**, 105004 (2020).

[21] C. Prajapati, S. Pidishety, and N. K. Viswanathan, Opt. Lett. **39**, 4388 (2014).

[22] D. H. Goldstein, *Polarized Light* (CRC Press, 2017).

[23] A. Aiello and J. P. Woerdman, Opt. Lett. **33**, 1437 (2008).

[24] X. Li, P. Wang, F. Xing, X.-D. Chen, Z.-B. Liu, and J.-G. Tian, Opt. Lett. **39**, 5574 (2014).

Chapter 6 Development of Quantum Weak Measurement to measure Goos-Hänchen shift

In this chapter, we have demonstrated the experimental development of the Quantum Weak Measurement technique (QWM). The effective way of applying this QWM technique for the amplification and subsequent detection of the GH shift for Gaussian light. We have also examined the beam profiles and explained our findings.

Content of this chapter has been published in: **A. Das** and M. Pradhan, "*Quantum weak measurement of Goos-Hänchen effect of light in total internal reflection using a Gaussian-mode laser beam*," **Laser Physics Letters** 17 (6), 066001 (2020).

6 Development of Quantum Weak Measurement to measure Goos-Hänchen shift

6.1 Introduction

One of the most versatile techniques in the framework of quantum mechanics is the 'Quantum weak measurement' (QWM) that has found a vast area of application in precision measurement. It was invented and consequently described first by Aharonov, Albert, and Vaidman (AAV) [1-3]. The basic idea and perception of weak measurement based on weak value are already discussed in detail in a general context in *Chapter* 5 [2,4-7]. The optical counterpart of this weak measurement method was established by Duck et. al. [4,8]. Thereafter, Hosten and Kwiat applied the weak value amplification for measuring minute photonic spin Hall shift of the light [5].

Of late, optical beam shifts have generated a lot of interest in the modern research community [6,7,9-12] due to their possible applications in photonics, plasmonics, topological materials, metamaterials, and many other quantum systems [13-19]. Recently, a lot of modifications of this setup have been done to determine thickness, optical conductivity, rate of chemical reaction, ion concentration [20-25], etc. As we already know, the longitudinal (i.e. in the plane of incidence) shift of the light beam because of diffractive corrections is popularly termed as Goos-Hänchen shift (GH) [6,7,9,10,26]. Generally, the GH shift is very small (of the order of the wavelength) in magnitude. Hence, the accurate detection of the GH shifts is not an easy task [9]. As we have mentioned in the previous *Chapter*, several techniques were invented for the detection of the optical beam shift [27-30]. The quantum weak measurement technique [5,7,23,31-33] is an accurate and versatile method as it can amplify the tiny shifts by weak value amplification scheme, can detect them with very high precision, and is applicable to different conditions.

Here, we have described the development of the QWM technique for detecting the GH shift in the glass-air interface using a fundamental Gaussian beam. The beam first undergoes pre-selection in a linear polarization state and after reflection, the reflected beam undergoes post-selection to another linear polarization state that is almost orthogonal to the input state but not exactly orthogonal. We have taken a prism for our study that works as the glass-air interface

and serves as a weak measuring device. This QWM technique also performs amplification of the shift which helps in reducing the noise in the measurement and cancels the contributions arising from other angular or spin Hall type of shifts [5,9,34,35].

The profiles of the output beam are demonstrated explicitly along with the respective horizontal and vertical displacement. The domain of validity of the AAV approximations is also discussed. Besides, we have inspected the angular dependence of the GH shifts and, afterward, have made a comparison of our experimental findings with the theoretical results to verify the domain of applicability of the AAV method.

6.2 Formulation of Quantum Weak Measurement

The common perception is that the expectation values (quantum mechanical average) of the quantum mechanical operators must lie inside its eigenvalue range i.e. in between the maximum and minimum eigenvalue. But this concept was challenged by Aharonov, Albert, and Vaidman [1,2]. They first came with the idea of 'weak value', which is entirely different from the eigenvalue concept and can yield values well outside the range of eigenvalues of any observable. To digest this idea, let us first introduce the idea of common strong quantum mechanical measurement and the corresponding eigenvalue.

6.2.1 Strong Measurement & Eigenvalue

We start with a pure quantum mechanical state $|\psi\rangle$. In case of a strong measurement, we have to take into account three factors [36]:

(a) The outcome of the measurement '*g*',

(b) The probability for getting that particular measurement product *P*(*g*),

(c) The ultimate state after the measurement $|\psi_g\rangle$.

Let us consider a basic measurement phenomena where the physical observable is described by the operator $\hat{J}_g$. We further consider that they satisfy the relation:

$$\sum \hat{J}_g^{\dagger}\hat{J}_g = \hat{I} \tag{6.1}$$

The set will describe a quantum measurement with probability defined as:

$$P(g) = \langle\psi|\hat{J}_g^{\dagger}\hat{J}_g|\psi\rangle \tag{6.2}$$

And the final output state will be:

$$\left|\psi_g\right\rangle = \hat{J}_g \left|\psi\right\rangle \tag{6.3}$$

If $\hat{J}_g^{\dagger}\hat{J}_g = \hat{J}_g$, we call the operators projective operator and the measurement process as *projective measurement*.

In certain cases, it is sufficient to recognize the probabilities of the measurement outcome. In these situations it is sufficient to claim the presence of a set of positive operators ($\hat{M}_g$) so that:

$$\sum_g \hat{M}_g = \hat{I}$$

where the probability to get '*g'* is given by:

$$P(g) = \left\langle\psi\right| \hat{M}_g \left|\psi\right\rangle \tag{6.4}$$

This is called *Positive Operator Valued Measurement* (POVM). To implement this method, the system can be coupled with an ancilla representing the environment. Then, the whole system along with the ancilla cab evolved by using a unitary operator, and subsequent measurement can be recorded from the ancilla space applying a projective measurement. This generates a series of positive operators. The method is often used in quantum operations [2].

6.2.2 Weak Measurement

Generalizing this (projective measurement) into weak measurements can give rise to countless advantages, such as determination of the state of the system between two back to back strong measurements and finding non-trivial weak values.

Weak measurement can be described in terms of generalization of quantum strong measurement. The basic weak measurement involves two steps.

(a) Weak coupling of the measurement device to the quantum system.

(b) Strong measurement of the measurement device.

The collapsed state of the measurement device after the strong measurement is denoted as the consequence of the weak measurement. The standard deviation of the measured value ought to be higher than the difference between the eigenvalues of the system for a measurement to be in the weak measurement category.

For example, let $|\varphi_d\rangle$ symbolize the quantum mechanical state of the measurement device. It can be expanded in position basis:

$$|\varphi\rangle = |\varphi_d\rangle = \int_x \varphi(x)|x\rangle\, dx \tag{6.5}$$

$$\varphi(x) = \frac{1}{\sqrt[4]{2\pi\sigma^2}} exp\left(\frac{x^2}{4\sigma^2}\right) \tag{6.6}$$

where x denotes the position variable of the measuring needle. If $\hat{X}_d$ represents the position operator, then $\hat{X}_d|x\rangle = x|x\rangle$.

Let S indicate the system and $\hat{A}$ is a Hermitian operator acting in the system. Assume that $\hat{A}$ has N eigenvectors $|a_j\rangle$ such that $\hat{A}|a_j\rangle = a_j|a_j\rangle$

Take a state that can be expanded in the eigenbasis of $\hat{A}$ as follows:

$$|\psi\rangle = \sum \alpha_j |a_j\rangle \tag{6.7}$$

The conventional weak interaction Hamiltonian can be expressed in this case as [2]:

$$\hat{H} = \hat{H}_{int} = g(t)\hat{A} \otimes \hat{P}_d \tag{6.8}$$

where $g(t)$ is the coupling impulse function that obeys:

$$\int_0^T g(t)\, dt = 1$$

where T denotes coupling time and $\hat{P}_d$ is momentum operator which is conjugate to the position operator $\hat{X}_d$.

Considering the vector in the tensor space of the two systems:

$$|\psi\rangle \otimes |\varphi\rangle \tag{6.9}$$

After applying the Hamiltonian, we obtain:

$$exp\left(-\frac{i\hat{H}t}{\hbar}\right)|\psi\rangle \otimes |\varphi\rangle = \sum_j \alpha_j |a_j\rangle \otimes |\varphi(x - a_j)\rangle \tag{6.10}$$

Since the wave function φ has high variance, they overlap with each other causing a weaker measurement process. If the normal wave functions do not overlap the measurement becomes strong. Thus, variance is an important parameter.

6.2.3 Weak Measurements & Post-selection

Bringing together the post-selection mechanism with the theory of weak measurement results in many bizarre, fascinating, and sometimes puzzling phenomena such as massive, negative, and even complex weak values, amplification, super-oscillations, negative probabilities, etc.

Consider a Hermitian operator $\hat{A}$ acting on the system S, $|\psi_i\rangle$ and $|\psi_f\rangle$ are the two state vectors lying in the Hilbert space of S, $|\varphi(x)\rangle$ is the state vector of the measuring needle. Suppose, the system is prepared in an initial state $|\psi_i\rangle$. We perform a weak measurement on an ensemble of particles prepared in $|\psi_i\rangle$ by taking the Hamiltonian operator $\hat{H} = \hat{A} \otimes \hat{P}_d$. After the weak interaction, the system is finally post-selected in the state $|\psi_f\rangle$. The probability amplitude to obtain $|\psi_f\rangle$ will be given by:

$$\langle \psi_f | exp\left(-\frac{i\hat{H}t}{\hbar}\right) |\psi_i\rangle$$

The above steps physically imply that if we start the measurement with an ensemble of systems, all are weakly measured by the weak Hamiltonian $\hat{H}$. By post-selecting, we only select those that lie in the direction of $|\psi_f\rangle$. Basically, post-selection is one kind of strong measurement but in a state different from the initial state. We can define two operators:

$$\hat{P}_1 = |\psi_f\rangle\langle\psi_f| \otimes \hat{I}_d$$

$$\hat{P}_0 = \sum_{i\neq 0} |\psi_{f,j}\rangle\langle\psi_{f,j}| \otimes \hat{I}_d$$

After the weak coupling of the system, the state becomes:

$$|\psi_w\rangle = exp\left(-\frac{i\hat{H}t}{\hbar}\right)|\psi_i\rangle \otimes |\varphi(x)\rangle \tag{6.11}$$

After the post-selection, we get:

$$\left|\psi_f\right\rangle \otimes \left\langle \psi_f \middle| \psi_i \right\rangle exp\left(-\frac{i\left\langle \hat{A} \right\rangle_w \hat{P}_d T}{\hbar} \right) \otimes \left|\varphi(x)\right\rangle \tag{6.12}$$

where the weak value is [3]:

$$\left\langle \hat{A} \right\rangle_w = \frac{\left\langle \psi_f \middle| \hat{A} \middle| \psi_i \right\rangle}{\left\langle \psi_f \middle| \psi_i \right\rangle} \tag{6.13}$$

Here, the normal probability distribution is centred around $\left\langle \hat{A} \right\rangle_w$. If $\left|\psi_f\right\rangle$ and $\left|\psi_i\right\rangle$ are exactly orthogonal, $\left\langle \hat{A} \right\rangle_w$ blows up. If they are not exactly orthogonal, but slightly deviated from the orthogonal position $\left\langle \hat{A} \right\rangle_w$ diverges and yields a massive value well outside the range of the eigenvalues.

6.3 Theoretical background of QWM

Figure 6.1 illustrates the working principle of the experimental setup for the weak measurement of the GH shift. The incident beam of a definite polarization state suffers total internal reflection (TIR) at the glass-air interface. For the weak measurement of the shift, the incident beam at first undergoes pre-selection to a definite initial quantum state $\left|\Psi_1\right\rangle$. The beam then undergoes total internal reflection from the prism, where the weak interaction occurs. Afterward, the system undergoes post-selection to the final quantum state $\left|\Psi_2\right\rangle$, projected almost orthogonal to the pre-selection input state. According to Aharonov-Albert-Vaidman's (AAV) approach [1,2], the amplified (weak values) GH shifts are:

$$x_{GH}^{w} = \frac{\left\langle \Psi_2 \middle| \hat{X}_{GH} \middle| \Psi_1 \right\rangle}{\left\langle \Psi_2 \middle| \Psi_1 \right\rangle} \tag{6.14}$$

The real and imaginary parts of Equation (6.14) resemble spatial and angular GH shifts. The optic axis of the Glan-Thompson polarizer (GLP1) is fixed to an angle α for the pre-selection of the incident beam into a definite quantum state given by [8]:

$$e^{-\frac{x^2}{w^2}} \begin{pmatrix} cos(\alpha) \\ sin(\alpha) \end{pmatrix} \tag{6.15}$$

Afterward, the incoming beam suffers total internal reflection from the glass-air interface. The reflection generates a phase difference $\delta = \left(\delta_p - \delta_s\right)$. Finally, the post-selection is performed by the suitable combination of a half-wave plate (HWP), a quarter-wave plate (QWP), and a Glan-Thompson linear polarizer. Here, the combination of HWP and QWP is adjusted in such a way as to cancel out the relative phase difference generated. Then, the Glan-Thompson linear (GLP2) polarizer is rotated at an angle β to get the post-selected final state:

$$\begin{pmatrix} cos(\alpha)cos(\beta)exp\left(-\frac{\left(x-D_p\right)^2}{w^2}\right) \\ sin(\alpha)sin(\beta)exp\left(-\frac{\left(x-D_s\right)^2}{w^2}\right) \end{pmatrix} \tag{6.16}$$

where, $\beta = \left(\alpha + \frac{\pi}{2}\right) + \varepsilon$

The parameters D_p and D_s are nothing but the GH shift generated after total internal reflection of the light. Following Duck's method [8], this state could be written as:

$$\frac{1}{2}\left[(1+\varepsilon)exp\left[-\frac{\left(x-\frac{1}{2}\Delta_{GH}\right)^2}{w^2}\right] - (1-\varepsilon)exp\left[-\frac{\left(x+\frac{1}{2}\Delta_{GH}\right)^2}{w^2}\right]\right] \tag{6.17}$$

where we have considered $tan(\varepsilon) \simeq \varepsilon$ and $\Delta_{GH} = \left(D_p - D_s\right)$.

For $\varepsilon = 0$, the above wave function evidently comprises of two different Gaussians with centres located at: $x = \pm\Delta_{GH}/2$. Two Gaussians are roughly separated by $\sqrt{2}w_0$ [1,4,8]. Under the condition, $\Delta_{GH}/2w \ll \varepsilon \ll 1$, there will be constructive interference of the two separate Gaussians that yield a single Gaussian with centroid shifted by the weak value [2-4]:

$$A_w \approx \frac{1}{2}cot(\varepsilon)\Delta_{GH} \tag{6.18}$$

6.4 Experimental measurement setup for QWM

To arrange the experimental setup, a He-Ne laser (30991, Research Electro Optics Inc.) is used as the source. It yields good quality Gaussian beam with a power less than 5.0 mW. A plano-

convex lens, L1 (LA1433, Thorlabs) having a focal length of 150 mm collimates and focusses the light to a specific spot size of around 250 µm. We monitor the polarization state of the incident light with a Glan-Thompson Linear polarizer, GLP1 (GTH10M-A, Thorlabs). This polarizer is mounted on a high-precision (PRM1/M, Thorlabs) rotational mount. Afterward, the beam suffers total internal reflection from the 45^0-90^0-45^0 prism (N-BK7 RA, Thorlabs, refractive index, $n = 1.516$) which is mounted on a high-precision rotation stage (M-481-A, Newport). The post-selection unit is comprised of a combination of a quarter-wave plate (WPMQ10M-633, Thorlabs), a half-wave plate (WPMH10M-633, Thorlabs), and another Glan-Thompson linear polarizer, GLP2 (GTH10M-A, Thorlabs), all mounted on high precision Rotation Mounts (PRM1/M, Thorlabs). The resulting beam shift is consequently examined by a Beam Profiler, (LBP-4-USB, 6610d, Newport).

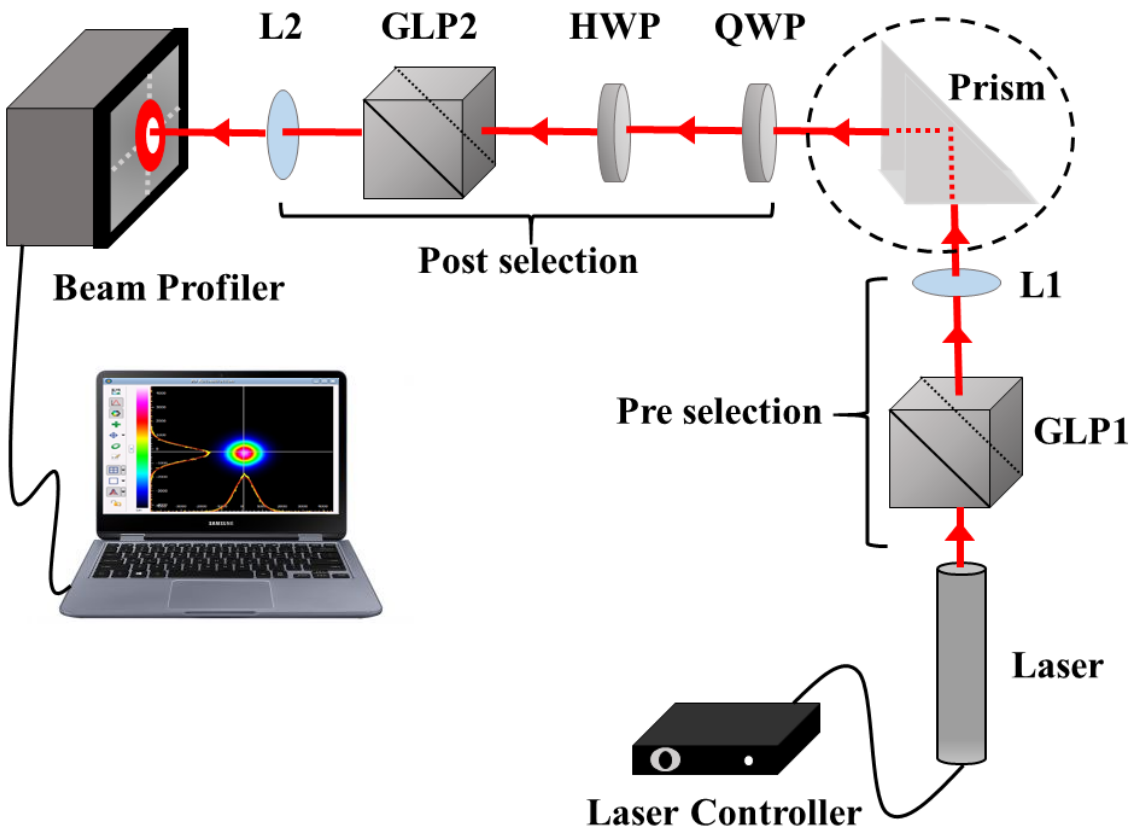

Figure 6.1. Experimental weak measurement setup for measuring GH shift, where **GLP1, GLP2** denote Glan-Thompson Polarizer; **L1**, **L2** denote Plano-convex lenses; **HWP** denotes Half-wave plate; **QWP** denotes Quarter-wave plate**.**

For the weak measurement, we have first reviewed the characteristics of the light beam, its Gaussian nature, width, and power, etc. Next, the light is pre-selected to 45^0 linear polarization state by proper rotation of the optic axis of GLP1. After the reflection of this pre-selected beam, the combination of QWP, HWP and GLP2 is used for the post-selection. As stated earlier, we suitably fix the QWP and HWP combination first to a particular angle to cancel out the relative phase difference (δ). We have fixed the input polarization state $\alpha = \pi/4$ using GLP1. Hence, we now regulate the output light beam using GLP2 with its location at: $\beta = (\alpha + \pi/2) + \varepsilon, (\varepsilon \ll 1)$. This scenario helps to attain the almost-orthogonal necessary for the weak measurement. The final beam, coming out of the GLP2, is shifted by an amount $\left(\frac{1}{2}\Delta_{GH}\, cot(\varepsilon)\right)$. Next, we determine the separation of the beam centroids $\left(\Delta_{GH}\, cot(\varepsilon)\right)$ corresponding to two different polarization settings of:

(1) $\alpha = \pi/4$ (Pre-selection) and $\beta = (\alpha + \pi/2) + \varepsilon$ (Post-selection),

(2) $\alpha = \pi/4$ (Pre-selection) and $\beta = (\alpha + \pi/2) - \varepsilon$ (Post-selection).

6.5 Results & Discussions

At first, the polarizer at the input, GLP1 is set at $\alpha = \pi/4$, and the polarizer at the output, GLP2 is set at a nearly orthogonal position, $\beta = (\alpha + \pi/2) - \varepsilon$. Thereafter, we rotate the 2nd polarizer GKLP2 in small steps of ε (0^0-3^0).

The final output is demonstrated in Figure 6.2. Column (a) of Figure 6.2 exhibits the final output beam profiles that are observed in the beam profiler. Column (b) and column (c) of Figure 6.2 describe the horizontal and vertical patterns of the resultant beam, respectively. Figure 6.2(a5, b5, c5) displays the resultant beam profiles for angle of deviation, $\varepsilon \approx 0$ i.e. the condition of exact orthogonality, where the AAV condition breaks down [1,8]. It is evident from Figure 6.2 that the output beam dissociates into two different Gaussian profiles separated by $\sqrt{2}w$ [4] as stated earlier in the theory section.

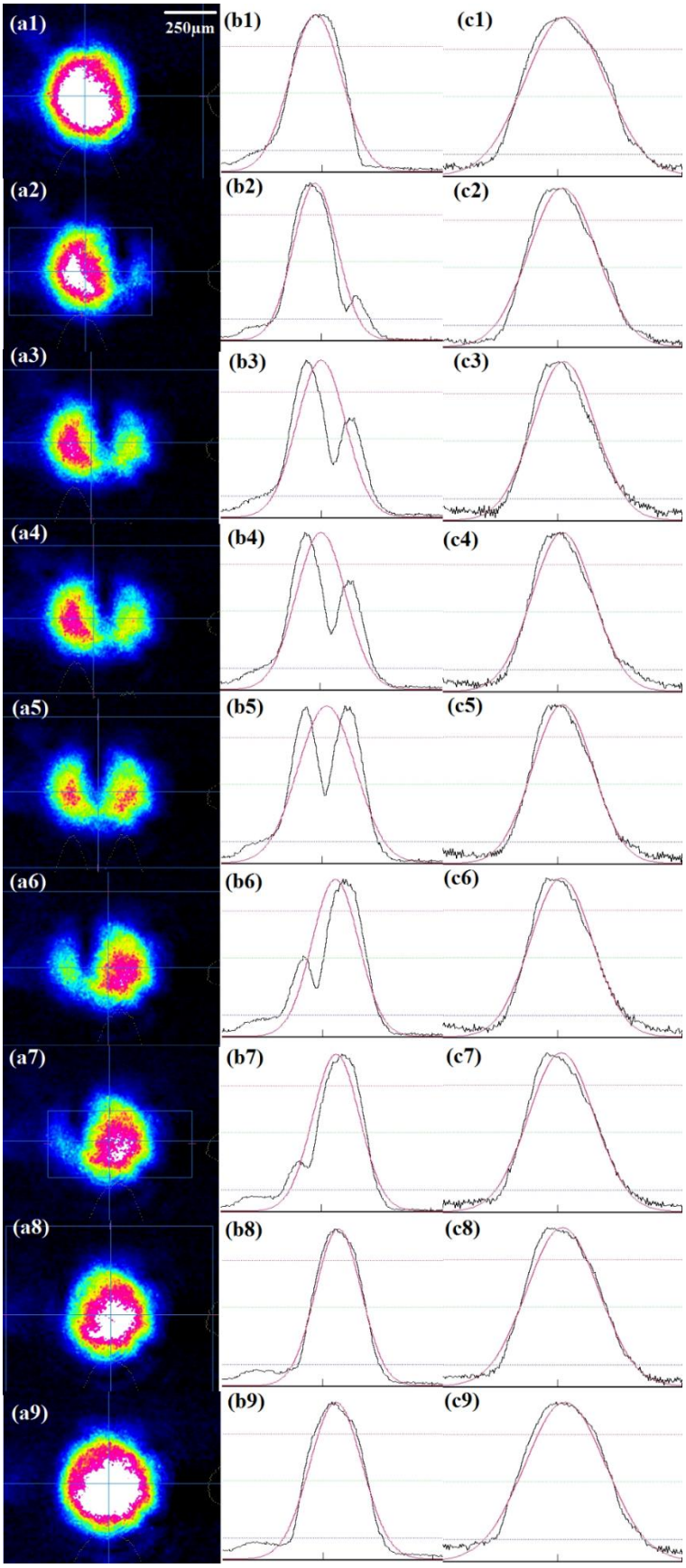

Figure 6.2. Beam intensity profiles: **(a)** Centroid intensity, **(b)** Horizontal profile, and **(c)** Vertical profile.

Figure 6.2 [upper panel (a4-a1)] describes the nature of the output beam when ε is negatively increasing. In this situation, the 2nd polarizer GLP2 is rotated in a clockwise direction from the orthogonal position. Consequently, in Figure 6.2, the lower panel (a6-a9) describes the same when ε is positively increasing i.e. the GLP2 is rotated anticlockwise from the orthogonal position. As we go on increasing ε (increasing angular separation from the orthogonal position), one of the Gaussians dominates, overwhelming the other. Our experimental findings are in good agreement with the weak measurement concepts suggested by AAV [1,8].

We have studied the nature of the horizontal and vertical shifts of the centroid of the output light beam as we travel away from the orthogonal position (by changing ε in clockwise and anti-clockwise direction). We have plotted the same in Figure 6.3(a) and (b).

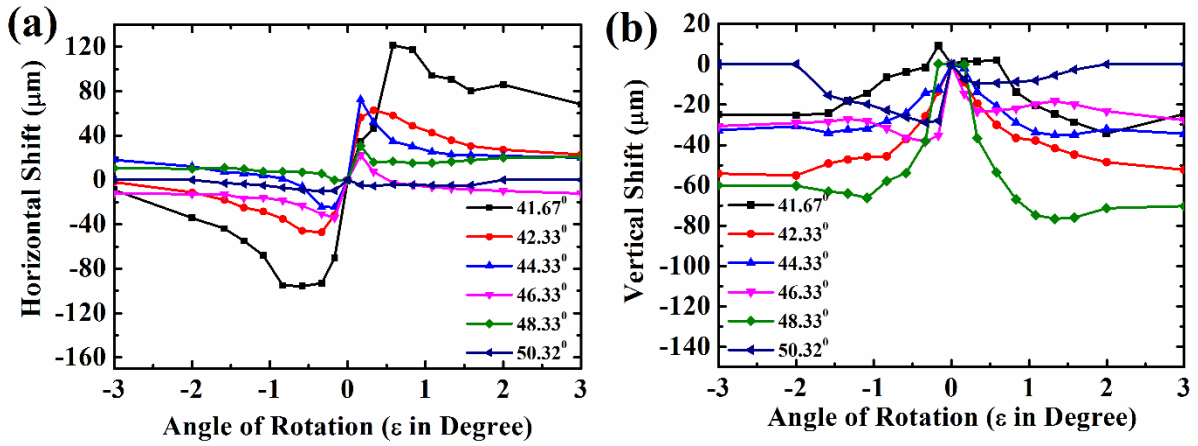

Figure 6.3. Dependence of shift on the angle of rotation (ε) of GLP2 from exact orthogonal condition: **(a)** Horizontal shift and **(b)** Vertical shift of the beam centroid.

It is evident that as ε starts increasing, but is adjacent to zero, the shifts gain a very large value (Figure 6.3(a)). The breakdown of AAV approximation in close neighbourhood of the orthogonal position, where $\langle \Psi_2 | \Psi_1 \rangle = 0$, blows up Equation (6.14). As we recede away from the orthogonal location, the horizontal shift starts to reduce continuously, which agrees with AAV suggestion [1,4,8]. Also, one exciting fact is that the horizontal shift for positive ε is in the opposite sense in comparison to that for negative ε. It is apparent from the column (a, b) of Figure 6.2. We can also conclude from Figure 6.2, that for negative ε, the left-sided peak is

dominating and for positive ε, the right-sided peak is dominating which are in agreement with our earlier comments. Additionally, we have inspected the horizontal shift for different incident angles in proximity of the critical angle ($\theta_C = 41.6^0$ for glass surface in air medium). The horizontal shift attains a greater value in the vicinity of the critical angle. Nevertheless, as we go away from the critical angle, the horizontal shift reduces sharply, which agrees with the earlier theoretical findings [4,8]. In the meantime, as displayed in Figure 6.3(b), the vertical shift grows with ε, in opposite to the nature of the horizontal shift. But, the increase in the vertical shift for positive ε and negative ε is in the same direction.

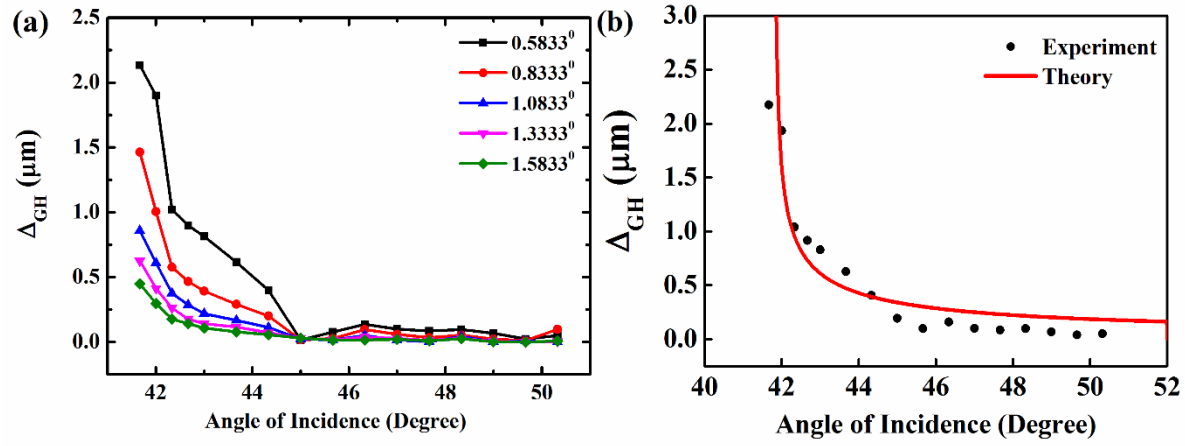

Figure 6.4. Angular variation of GH shift for glass-air interface: **(a)** for different ε, **(b)** comparison with the theoretical results.

Now, the behaviour of the Goos-Hänchen shift for different incident angles of the incoming light beam on the prism is plotted in Figure 6.4. The GH shift is not observed below the critical angle. But, a finite GH shift is observed above it as we enter the domain of total internal reflection of light in glass-air interface. In the neighbourhood of the critical angle, the GH shift acquires giant value which is in good agreement with the earlier theoretical results [37]. But as we recede away from θ_C, the GH shift monotonically reduces and with increasing incident angle, GH shift reaches zero level even inside total internal reflection domain (but away from the critical region).

Furthermore, we have also explored the characteristics of GH shift for different values of angle of deviation from the exact orthogonal position (ε) (Figure 6.4(a)). As ε is increased

(moving away from orthogonality), the GH shift largely declines for all incident angles. Lastly, we have made a comparison of the experimental findings to the theoretical results. We have considered the theoretical model of Aiello and Woerdman that is well established [38]. As depicted in Figure 6.4(b), experimental GH shift agrees well with the theoretical predictions for a particular ε value of $0.5833^0/7' \approx 10^{-2}$ radian. That specific ε value gives a reasonable amplification of the GH shift to be detected in accordance with the theoretical prediction without violating AAV theory [1] of weak measurement.

6.6 Outlook & Summary

We have developed a quantum weak measurement setup for the accurate detection of the GH shift of a Gaussian light beam. We have applied the weak value amplification mechanism to amplify the wavelength scale shift in glass-air interface. The nature of the horizontal and vertical beam profiles are studied in detail. The dependence of the shift of the centroid with deviation from the orthogonal condition and the breakdown of the AAV approximation is well-explained. We have also explained the presence of the finite GH shift in the total internal reflection scenario which disappears beneath the critical angle. The comparison with the theoretical model also suggests good agreement with our findings. Our results validate the advantages of the present method and open new avenue for future applications in device industry and precision metrology.

References

[1] Y. Aharonov, D. Z. Albert, and L. Vaidman, Physical Review Letters **60**, 1351 (1988).

[2] Y. Aharonov and D. Rohrlich, *Quantum Paradoxes: Quantum Theory for the Perplexed* (Wiley, 2005).

[3] L. Vaidman, in *Compendium of Quantum Physics*, edited by D. Greenberger, K. Hentschel, and F. Weinert (Springer Berlin Heidelberg, Berlin, Heidelberg, 2009), pp. 840.

[4] N. W. M. Ritchie, J. G. Story, and R. G. Hulet, Physical Review Letters **66**, 1107 (1991).

[5] O. Hosten and P. Kwiat, Science **319**, 787 (2008).

[6] M. Ornigotti and A. Aiello, Journal of Optics **15**, 014004 (2013).

[7] F. Töppel, M. Ornigotti, and A. Aiello, New Journal of Physics **15**, 113059 (2013).

[8] I. M. Duck, P. M. Stevenson, and E. C. G. Sudarshan, Physical Review D **40**, 2112 (1989).

[9] K. Y. Bliokh and A. Aiello, Journal of Optics **15**, 014001 (2013).

[10] A. Aiello, New Journal of Physics **14**, 013058 (2012).

[11] A. Aiello and J. P. Woerdman, arxiv **0903** (2009).

[12] A. Aiello, M. Merano, and J. P. Woerdman, Physical Review A **80**, 061801 (2009).

[13] X. Yin, L. Hesselink, Z. Liu, N. Fang, and X. Zhang, Applied Physics Letters **85** (2004).

[14] C. W. J. Beenakker, R. A. Sepkhanov, A. R. Akhmerov, and J. Tworzydło, Physical Review Letters **102**, 146804 (2009).

[15] W. Zhang, W. Wu, S. Chen, J. Zhang, X. Ling, W. Shu, H. Luo, and S. Wen, Photon. Res. **6**, 511 (2018).

[16] L. Salasnich, Physical Review A **86**, 055801 (2012).

[17] W. Dong, L. Gao, and C. W. Qiu, Progress In Electromagnetics Research **90**, 255 (2009).

[18] Y. Huang, Z. Yu, C. Zhong, J. Fang, and Z. Dong, Opt. Mater. Express **7**, 1473 (2017).

[19] C. Xu, J. Xu, G. Song, C. Zhu, Y. Yang, and G. S. Agarwal, Opt. Express **24**, 21767 (2016).

[20] X. Zhou, X. Ling, H. Luo, and S. Wen, Applied Physics Letters **101**, 251602 (2012).

[21] S. Chen, X. Ling, W. Shu, H. Luo, and S. Wen, Physical Review Applied **13**, 014057 (2020).

[22] C. Mi, S. Chen, W. Wu, W. Zhang, X. Zhou, X. Ling, W. Shu, H. Luo, and S. Wen, Opt. Lett. **42**, 4135 (2017).

[23] S. Chen, C. Mi, L. Cai, M. Liu, H. Luo, and S. Wen, Applied Physics Letters **110**, 031105 (2017).

[24] R. Wang, J. Zhou, K. Zeng, S. Chen, X. Ling, W. Shu, H. Luo, and S. Wen, APL Photonics **5**, 016105 (2020).

[25] J. Liu, K. Zeng, W. Xu, S. Chen, H. Luo, and S. Wen, Applied Physics Letters **115**, 251102 (2019).

[26] A. Das and M. Pradhan, J. Opt. Soc. Am. B **35**, 1956 (2018).

[27] P. W. Xin Li, Fei Xing, Xu-Dong Chen, Zhi-Bo Liu, and Jian-Guo Tian, Opt. Lett. **39**, 5574 (2014).

[28] P. B. Dixon, D. J. Starling, A. N. Jordan, and J. C. Howell, Physical Review Letters **102**, 173601 (2009).

[29] N. Brunner and C. Simon, Physical Review Letters **105**, 010405 (2010).

[30] A. Das and M. Pradhan, Journal of Optics **22**, 105004 (2020).

[31] M. R. Dennis and J. B. Götte, New Journal of Physics **14**, 073013 (2012).

[32] G. Jayaswal, G. Mistura, and M. Merano, Opt. Lett. **38**, 1232 (2013).

[33] G. Jayaswal, G. Mistura, and M. Merano, Opt. Lett. **39**, 2266 (2014).

[34] J. B. Götte and M. R. Dennis, New Journal of Physics **14**, 073016 (2012).

[35] Y. Qin, Y. Li, X. Feng, Y.-F. Xiao, H. Yang, and Q. Gong, Opt. Express **19**, 9636 (2011).

[36] J. Von Neumann, R. T. Beyer, and N. A. Wheeler, *Mathematical foundations of quantum mechanics* 2018).

[37] A. Das and M. Pradhan, Optics Communications **437**, 312 (2019).

[38] A. Aiello and J. P. Woerdman, Opt. Lett. **33**, 1437 (2008).

Chapter 7 Weak measurement of Goos-Hänchen shift in monolayer MoS_2

In this chapter, we have proved the existence of finite (longitudinal) Goos-Hänchen shift in monolayer MoS_2. We have modified the basic QWM technique for applying it in GH shift measurement. We have also discussed the dependence of the GH shift on the incident angle including the non-trivial nature around the critical angle.

Content of this chapter has been published in: **A. Das** and M. Pradhan, "Quantum weak measurement of Goos-Hänchen shift in monolayer MoS_2," **Journal of the Optical Society of America B** 38 (2), 387-391 (2021).

7 Weak measurement of Goos-Hänchen shift in monolayer MoS_2

7.1 Introduction

The phenomena of the Goos-Hänchen (GH) effect, invented long back in 1947 [1], can be defined as the longitudinal (in the plane of incidence) displacement of a finite light-beam that can arise as it undergoes reflection from a surface [2-5]. Although the GH shift was first reported in total internal reflection of light [6] depending upon the characteristics of the reflecting surface, the wavelength and polarization states of the light, there has been some recent reports in a few systems where non-zero GH shifts can also be observed under partial reflection conditions [7,8]. Over the years, the GH shift has created special interest in different optical surfaces and various quantum systems [2,9-12]. The inherent reason behind this phenomenon has already been well-explained in previous *Chapters*. However, as a wave-optical phenomenon, the scale of the GH shift is significantly small [2], thus making its detection one of the most fundamental and toughest tasks. As mentioned before, several theoretical suggestions have been proposed [4,5,13] and a lot of experiments have been performed [14-20] for the precision measurement of the tiny GH shifts.

In this *Chapter*, we have employed the *Quantum Weak Measurement* (QWM) scheme [14-17,20-24] for the investigation of the optical GH shift for plane glass-air interface. The available techniques [25-27] for the measurement of the GH shifts suffer from inaccuracy due to intensity fluctuations and noise. But, QWM is an accurate and promising method to determine the GH shift with high precision. From the postulates of quantum mechanics [28], we already know that when a measurement is performed on a physical system, the result has to be one of the eigenvalues of the Hermitian operator. But, Aharonov, Albert & Vaidman (AAV), working on electron spin measurement [29], first invented a scheme of measurement that can yield outcome well outside the eigenvalue spectrum. Subsequently, Duck et. al. in their seminal paper [30], upgraded the measurement technique, simplified the inherent physics and proposed an optical analogue of the scheme [31]. The weak measurement technique has been applied in several areas of optics such as beam detection, GH & IF shifts, Spin Hall Effect (SHE), birefringence, angular rotation, optical differential operation [32-34].

Here, we have concentrated our attention on the GH shift for monolayer (ML) of MoS_2, a promising 2D material with massive opportunities in the present optoelectronics and sensor industry [35]. Similar to other TMDCs, MoS_2 exhibits a layered structure with tight covalent bonding along with 2D (intralayer) and weak van der Walls bonding along the third dimension (interlayer) which enables easy exfoliation into monolayers [36]. These materials have subtle differences from their bulk phase in terms of their electronic and phonon structure [37,38]. As we have stated in *Chapter* 1, MoS_2 possesses a layer-dependent bandgap with a crossover from indirect (1.25 eV) to direct (1.88 eV) as it is exfoliated to individual monolayers from the bulk phase. In addition, its direct bandgap corresponds to the visible region of the spectrum, making this a promising material for efficient electronic, and optoelectronic devices [36,37,39-41].

Based on Duck's formalism and subsequent up-gradation of the works by other groups [14,20,30], we have developed a more advanced experimental QWM setup to measure the GH shift of monolayer MoS_2 using a fundamental Gaussian beam. In general, the GH shifts are largest for the incident angle in the neighbourhood of the critical angle [7,42] in the total internal reflection (TIR) scenario, due to the special behavior of the Fresnel coefficients. Hence, we have studied the GH shift over a wide range of incident angles (15^0-60^0). Besides, we have made a detailed comparison of GH shifts for monolayer MoS_2 with the previous works on graphene and plane air-glass interface.

7.2 Formulation of GH shift measurement

Let us consider a system as described in Figure 7.1. A polarized Gaussian light beam incident at a specific angle upon a prism-MoS_2-air system to undergo reflection. Due to the interaction of light with MoS_2, GH shift is produced but is too small to be detected precisely. The suitable pre-selection and post-selection arrangements are monitored to attain amplified GH shift. The incident beam is pre-selected by using a polarizer to the desired state $|\Psi_1\rangle$. The beam then undergoes interaction with a 'weak measuring device' (prism-MoS_2-air system). The resultant beam is lastly post-selected to another specific state $|\Psi_2\rangle$. The post-selected state is projected not exactly orthogonal but slightly deviated from the exact orthogonal position to the preselected state $|\Psi_1\rangle$.

According to the AAV formalism, the final amplified GH shift will be [5,19]:

$$x_{GH}^{w} = \frac{\langle \Psi_2 | \hat{X}_{GH} | \Psi_1 \rangle}{\langle \Psi_2 | \Psi_1 \rangle} \tag{7.1}$$

The real part of the above equation represents a spatial shift, whereas the imaginary part corresponds to the angular shift. It is noteworthy to remark that a well-collimated ($\frac{Z_r}{kL}$) beam, where $Z_r = kz_r, L = kw_0^2/2, z_r$ is the propagation distance and w_0 is the beam waist) produces greater amplification in the spatial shift. Whereas a focussed beam generates greater amplification in angular shift [25]. To obtain substantial amplification in spatial GH shift in our experiment, we have used a well-collimated light beam with $Z_r/kL = 0.6$. We can also mathematically explain the nature of the beam profiles after it passes through the optical elements and undergoes interaction with monolayer MoS_2.

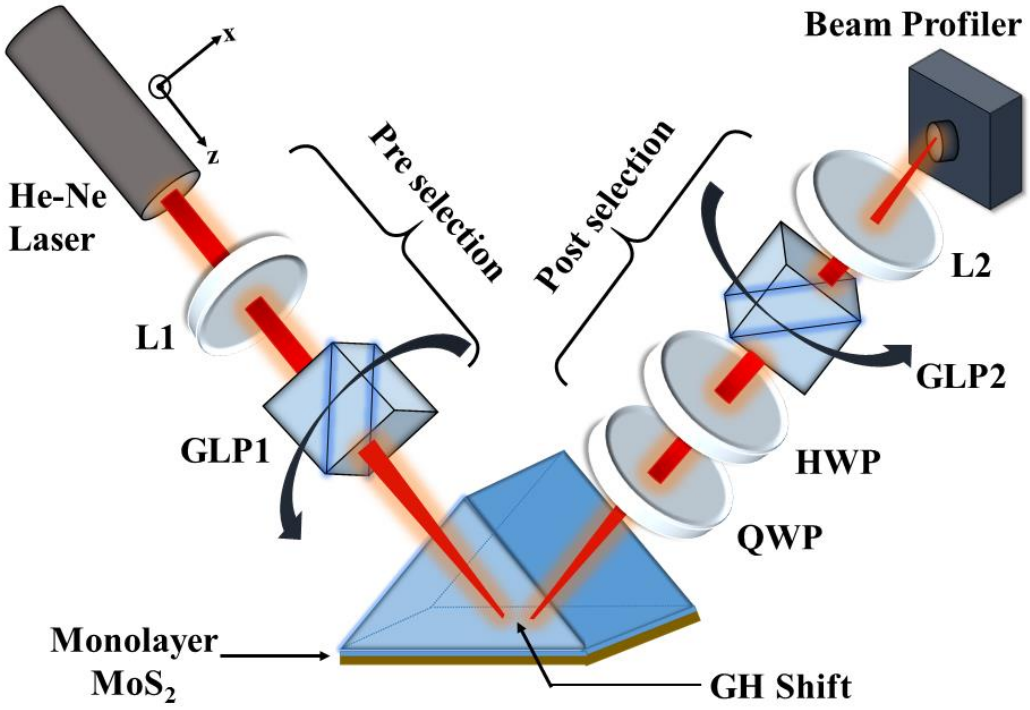

Figure 7.1. Experimental setup for detecting the GH shift, where **L1, L2** denote plano-convex lenses, **GLP** denotes Glan-Thompson polarizer, **HWP** denotes half-wave plate, **QWP** denotes quarter-wave plate.

7.3 Experimental setup

The experimental set-up is demonstrated in Figure 7.1 for detecting the GH shift in monolayer MoS_2. The spatial GH shift (Δ_{GH}) is characterized by the displacement of *x* coordinates in the vertical *x-y* plane. After the pre-selection of the incident beam by the Glan-Thompson polarizer to an angle α, the pre-selected quantum state can be expressed as [30]:

$$e^{-\frac{x^2}{w^2}}\begin{pmatrix} cos(\alpha) \\ sin(\alpha) \end{pmatrix} \tag{7.2}$$

Then, the light is reflected from the prism-MoS_2 system introducing additional phase difference (δ). The quantum state now becomes:

$$\begin{pmatrix} cos\alpha.e^{-\frac{(x-D_p)^2}{w^2}}.e^{-i\frac{\delta}{2}} \\ sin\alpha.e^{-\frac{(x-D_s)^2}{w^2}}.e^{+i\frac{\delta}{2}} \end{pmatrix} \tag{7.3}$$

where, D_λ indicate the GH shift generated by the interaction of light with the MoS_2 monolayer. Here, $\lambda = p,s$ denote two components.

Later, a combination of a half-wave plate (HWP) and a quarter-wave plate (QWP) is employed in the path of the light. This combination nullifies any relative phase difference (δ) generated. Lastly, the action of another Glan-Thompson polarizer (GLP2) set at an angle β compared to GLP1, produce the post-selected output quantum state:

$$\begin{pmatrix} cos\alpha.cos\beta.e^{-\frac{(x-D_p)^2}{w^2}} \\ sin\alpha.sin\beta.e^{-\frac{(x-D_s)^2}{w^2}} \end{pmatrix} \tag{7.4}$$

$$\text{Here, } \beta = \left(\alpha + \frac{\pi}{2}\right) + \varepsilon \tag{7.5}$$

Following the approach of Duck et. al. [30], Equation (7.4) can be written in a lucid form:

$$\frac{1}{2}\left[(1+\varepsilon).e^{-\frac{\left(x-\frac{1}{2}\Delta_{GH}\right)^2}{w^2}} - (1-\varepsilon).e^{-\frac{\left(x+\frac{1}{2}\Delta_{GH}\right)^2}{w^2}}\right] \tag{7.6}$$

where, $\Delta_{GH} = D_p - D_s$ [20,23].

If we set $\varepsilon = 0$, the quantum state presented by Equation (7.6) dissociates into two different Gaussian curves (Figure 7.2) with center at $x = \pm \Delta_{GH}/2$ and having a separation distance of approximately $\sqrt{2}w$ [43].

But, in a condition, $\frac{\Delta_{GH}}{2w} \ll \varepsilon \ll 1$, there is constructive interference of the two producing a solitary Gaussian peak with a shifted centroid. The separation distance is equal to the weak value [43]:

$$A_w \approx \frac{1}{2} cot(\varepsilon) \Delta_{GH} \tag{7.7}$$

However, throughout the experiment, we have selected and fixed the angle of deviation to a value given by, $\varepsilon = \pm 10^{-2}$ radian which produces substantial amplification (by a factor of 100).

The experimental setup for detecting GH shift in monolayer MoS_2 is presented in Figure 7.1. The experimental arrangement is exactly identical as prescribed in the previous *Chapter* 6. The only difference is in the physical system of reflection under consideration. A high-quality monolayer MoS_2 is taken (2D Semiconductors, USA) for the experimental study whose refractive index is (4.92+i1.06) [44] at 633 nm. The monolayer MoS_2 is placed on the surface of the prism to visualize the direct effect of the total internal reflection of the He-Ne laser beam (633 nm). The pre-selection and the post-selection units are the same as described in the previous *Chapter* 6.

The process of performing the experiment is also similar as explained in the previous *Chapter*. The incident beam should be pre-selected to 45^0 linear polarization state (by GLP1) before reflection. The pre-selected beam then suffers reflection from the prism-MoS_2 system. The combination of the half-wave and quarter-wave plate cancels out any relative phase difference that can be generated after reflection. The ultimate post-selection is finalized by the polarizer GLP2 set at an angle β with respect to GLP1. Hence, the actual position of the GLP2 can be denoted by: $\beta = \left(\alpha + \frac{\pi}{2}\right) + \varepsilon, \varepsilon \ll 1$ which is consistent with the almost orthogonal condition of the weak value amplification. The output beam is shifted by:

$\frac{1}{2}\Delta_{GH}\, cot\, \varepsilon$.

We also determine the separation distance of the centre of the output beam (which is given by $\Delta_{GH}.cot\,\varepsilon$) for different scenarios of the above-stated polarization settings. Let us consider:

(A) Pre-selection at: $\alpha = \frac{\pi}{4}$, while post-selection at: $\beta = \left(\alpha + \frac{\pi}{2}\right) + \varepsilon$

(B) Pre-selection at: $\alpha = \frac{\pi}{4}$, while post-selection at: $\beta = \left(\alpha + \frac{\pi}{2}\right) - \varepsilon$

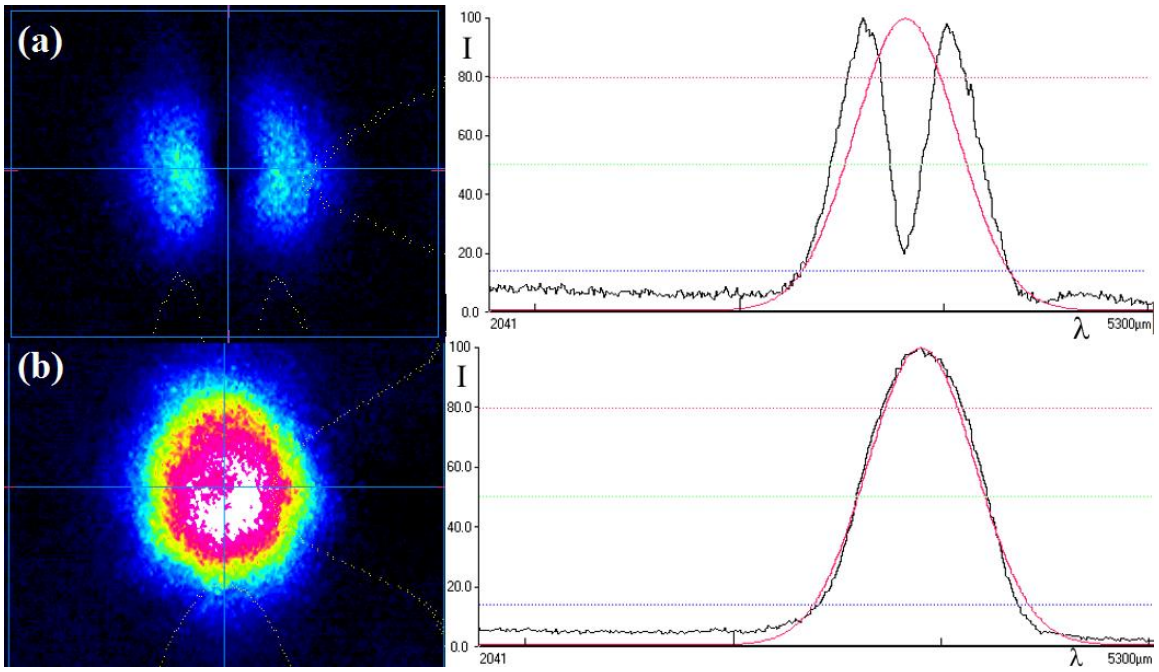

Figure 7.2. Intensity of the output beam (left column) and the horizontal beam profile (right column) **(a)** at exact orthogonal position ($\varepsilon = 0$ radian), **(b)** deviation from orthogonal position ($\varepsilon = \pm 10^{-2}$ radian)

As stated earlier, at first, we set GLP1 at $\alpha = \pi/4$ to get linearly polarized light, and GLP2 at the orthogonal position, $\beta = \left(\alpha + \frac{\pi}{2}\right)$. Subsequently, we deviate the GLP2 from the orthogonal position by a small angle ε first (both in a positive and negative sense) to achieve the AAV condition. The output profile of the resultant beam at exact orthogonal condition ($\varepsilon \approx 0$) is shown in Figure 7. 2, where the AAV condition breaks down. The final output beam separates

into two Gaussian peaks by approximately $\sqrt{2}w$. Further, if we go on increasing ε, one Gaussian peak dominates over the other in agreement with AAV and Duck's claims [17,29,30].

7.4 Results & Discussions

We have also performed an angular variation of the GH shift. For this, we have gradually rotated the high precision rotation stage on which our physical system (prism-monolayer MoS_2-air) is mounted and calculated the angle of incidence from the base reading. For each incident angle, the proper pre-selection and post-selection of the light beam are performed and the separation of the output beam centroid at $\pm\varepsilon$ position of GLP2 is noted.

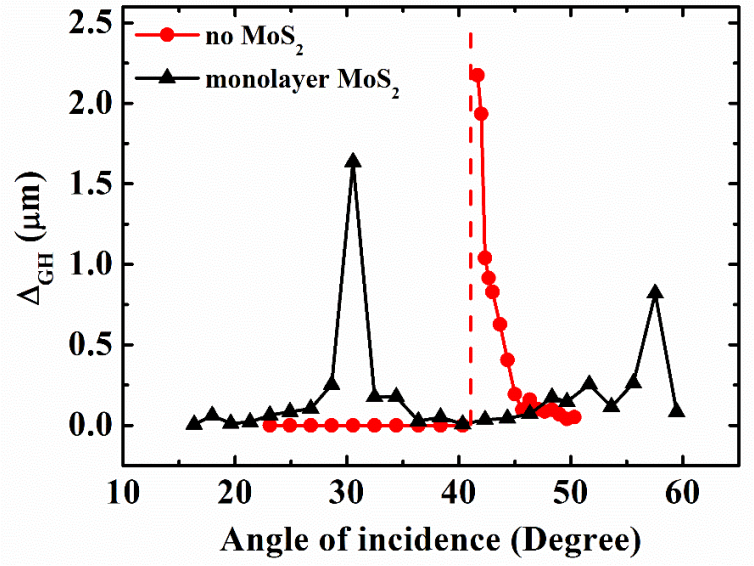

Figure 7.3. Spatial GH shift: in the presence (black) and in the absence (red) of monolayer MoS_2

In Figure 7.3, we have studied the GH shifts in monolayer MoS_2 for a wide range of incident angles (15^0-60^0), which has not been done in any previous works on the optical beam shift. We have also compared the GH shift for the MoS_2 sample (prism-MoS_2-air system) to that of the air-glass (prism-air system) interface [17]. There are subtle differences in both cases. Firstly, there exists no GH shift for the air-glass interface below the critical angle (41.3^0) (partial reflection case). But, in presence of the monolayer MoS_2 sample, finite non-zero (although small) GH shift is observed even beneath the critical angle. This is a significant result as it supports the theoretical claim of the existence of finite GH shift even beneath the critical angle

for monolayer TMDCs [8,45] and other 2D materials [7]. Secondly, a very large GH shift is observed for a glass-air interface near the critical angle of incidence which sharply decreases to zero with increasing incident angle [17]. But, when the monolayer MoS_2 is present, the critical angle is displaced (due to the refractive index of MoS_2) to a smaller angle. Finally, the maximum value of the GH shift for monolayer MoS_2 is also smaller in magnitude than the glass-air interface. This is likely because of the greater absorbance effect of monolayer MoS_2 in the visible region [46] and has been discussed later in detail.

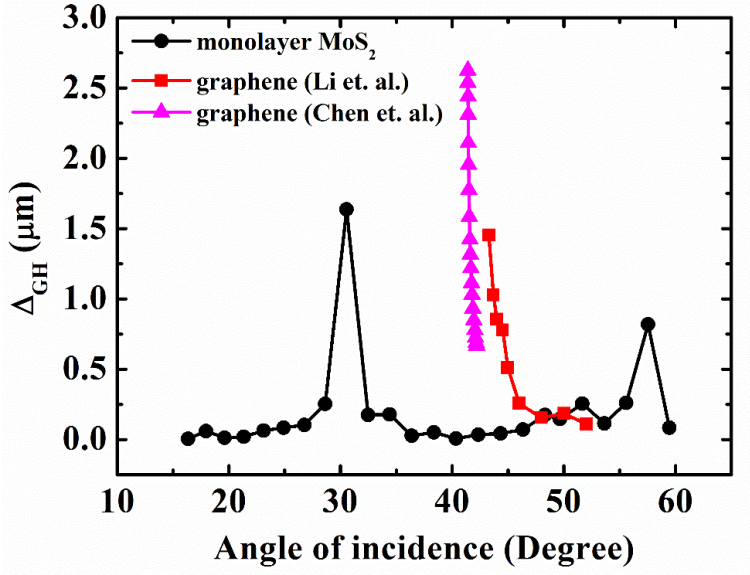

Figure 7.4. Angular variation of GH shift for different 2D materials (monolayer MoS_2 and graphene)

Additionally, we have compared our observations to the previous results of GH shifts observed in graphene [21,26] as graphene is a gapless material in comparison to the monolayer MoS_2 having a finite direct bandgap. Hence, it would be very interesting to observe their comparative response in the GH shifts as both of them are 2D in nature. Figure 7.4 shows the GH shift of graphene observed by *Chen et. al.* [21] and *Li et. al.* [26] along with our results of the GH shift for monolayer MoS_2. Clearly, the GH shift is smaller in magnitude compared to graphene. It is primarily due to the greater absorbance of monolayer MoS_2 than a single layer of graphene in the visible region. Figure 7.4 also shows a reduced critical angle of incidence, where we get a peak in the GH shift, in comparison to graphene. Also, the response of the GH shift is sharper in case of MoS_2 which makes it more suitable in sensor application. Another

small secondary peak is apparent at the far end of the angle of incidence. The reason of it is inherent in the position of beam spot at the time of reflection from the interface. As the angle of incidence is increased and goes well past the critical angle, the beam spot of incidence at the interface gradually shifts towards the edge of the sample. As the angle of incidence reaches closer to 58^0-59^0, the sample edge becomes dominant and gives rise to beam distortions which, in turn, produces a minor secondary peak in the spatial shift. Similar effect was also observed at the other edge (14^0) which has not been shown explicitly in Figure 7.4. It is striking that all the previous studies mainly focus on the critical angle and conducted GH shift measurement in the close neighbourhood of critical angle over a small region above it. But, we have performed the measurement over a large angle of incidence to show a detailed angular dependence of the GH shift.

Although previous theoretical works predict the presence of giant GH shift for monolayer MoS_2 [8,45], we do not observe the same in our QWM experiment. The reason is prominent in the approximations of the theoretical model [8,45,47]. Previous studies have already shown that absorbance has a significant effect in controlling the GH & IF shifts in presence of lossy or absorbing medium [48-50]. It is already proven that monolayer MoS_2 has large absorbance exceeding 10^7 m^{-1}. The enhanced light absorption by monolayer MoS_2 is due to the existence of strong Van-Hove singularities [46]. The previous theoretical calculations primarily depend upon the Transfer Matrix Method (TMM) [8,47]. This model does not incorporate such strong absorbance effects. Hence, we get some differences in comparison to the theoretical predictions due to these approximations [8,18]. In our experiment, we have also observed a major reduction in the reflected intensity due to the increased absorbance of monolayer MoS_2 and scattering losses associated with our system. Hence, the theoretical prediction of the giant GH shifts is not detected in the experiment.

7.5 Outlook & Summary

In summary, we have experimentally detected the GH shift for monolayer MoS_2 using a Gaussian beam and have applied the quantum weak measurement (QWM) technique as an effective way of measuring such precise shifts in monolayer MoS_2. Using such a weak value amplification (WVA) scheme, we have studied the GH shift over a wide range of incident angles that has not been explored in any previous experiments. Our observations on monolayer MoS_2 bears importance and this QWM method can also be prolonged for the study of the GH shifts for MoS_2 in bulk and few-layer cases as well to conduct a layer-dependent study in future.

References

[1] F. Goos and H. Hänchen, Annalen der Physik **436**, 333 (1947).

[2] K. Y. Bliokh and A. Aiello, Journal of Optics **15**, 014001 (2013).

[3] M. Ornigotti and A. Aiello, Journal of Optics **15**, 014004 (2013).

[4] F. Töppel, M. Ornigotti, and A. Aiello, New Journal of Physics **15**, 113059 (2013).

[5] J. B. Götte and M. R. Dennis, New Journal of Physics **14**, 073016 (2012).

[6] K. Artmann, Annalen der Physik **437**, 87 (1948).

[7] S. Grosche, M. Ornigotti, and A. Szameit, Opt. Express **23**, 30195 (2015).

[8] A. Das and M. Pradhan, J. Opt. Soc. Am. B **35**, 1956 (2018).

[9] A. Farmani, M. Miri, and M. H. Sheikhi, J. Opt. Soc. Am. B **34**, 1097 (2017).

[10] L. Salasnich, Physical Review A **86**, 055801 (2012).

[11] W. Xu, Q. Yang, G. Ye, W. Wu, W. Zhang, H. Luo, and S. Wen, Physical Review A **101**, 023826 (2020).

[12] S. Grosche, A. Szameit, and M. Ornigotti, Physical Review A **94**, 063831 (2016).

[13] M. R. Dennis and J. B. Götte, New Journal of Physics **14**, 073013 (2012).

[14] O. Hosten and P. Kwiat, Science **319**, 787 (2008).

[15] S. Goswami, S. Dhara, M. Pal, A. Nandi, P. K. Panigrahi, and N. Ghosh, Opt. Express **24**, 6041 (2016).

[16] G. Jayaswal, G. Mistura, and M. Merano, Opt. Lett. **38**, 1232 (2013).

[17] A. Das and M. Pradhan, Laser Physics Letters **17**, 066001 (2020).

[18] A. Das and M. Pradhan, Journal of Optics (2020).

[19] C. Prajapati and N. K. Viswanathan, Journal of Optics **19**, 105611 (2017).

[20] O. J. S. Santana, S. A. Carvalho, S. De Leo, and L. E. E. de Araujo, Opt. Lett. **41**, 3884 (2016).

[21] S. Chen, C. Mi, L. Cai, M. Liu, H. Luo, and S. Wen, Applied Physics Letters **110**, 031105 (2017).

[22] G. Jayaswal, G. Mistura, and M. Merano, **39**, 6260 (2014).

[23] M. P. Araújo, L. Stefano De, and G. M. Gabriel, Journal of Optics **17**, 035608 (2015).

[24] P. T. Leung, C. W. Chen, and H. P. Chiang, Optics Communications **276**, 206 (2007).

[25] C. Prajapati, S. Pidishety, and N. K. Viswanathan, Opt. Lett. **39**, 4388 (2014).

[26] X. Li, P. Wang, F. Xing, X.-D. Chen, Z.-B. Liu, and J.-G. Tian, Opt. Lett. **39**, 5574 (2014).

[27] P. B. Dixon, D. J. Starling, A. N. Jordan, and J. C. Howell, Physical Review Letters **102**, 173601 (2009).

[28] J. von Neumann and R. T. Beyer, *Mathematical Foundations of Quantum Mechanics* (Princeton University Press, 1955).

[29] Y. Aharonov, D. Z. Albert, and L. Vaidman, Physical Review Letters **60**, 1351 (1988).

[30] I. M. Duck, P. M. Stevenson, and E. C. G. Sudarshan, Physical Review D **40**, 2112 (1989).

[31] Y. Aharonov and D. Rohrlich, *Quantum Paradoxes: Quantum Theory for the Perplexed* (Wiley, 2005).

[32] S. He, J. Zhou, S. Chen, W. Shu, H. Luo, and S. Wen, APL Photonics **5**, 036105 (2020).

[33] D. Xu, S. He, J. Zhou, S. Chen, S. Wen, and H. Luo, Applied Physics Letters **116**, 211103 (2020).

[34] M. Pfeifer and P. Fischer, Opt. Express **19**, 16508 (2011).

[35] Z. M. Wang, *MoS_2: Materials, Physics, and Devices* (Springer, 2013).

[36] S. Manzeli, D. Ovchinnikov, D. Pasquier, O. V. Yazyev, and A. Kis, Nature Reviews Materials **2**, 17033 (2017).

[37] K. F. Mak, C. Lee, J. Hone, J. Shan, and T. F. Heinz, Physical Review Letters **105**, 136805 (2010).

[38] K. S. Novoselov, D. Jiang, F. Schedin, T. J. Booth, V. V. Khotkevich, S. V. Morozov, and A. K. Geim, Proceedings of the National Academy of Sciences of the United States of America **102**, 10451 (2005).

[39] J. K. Ellis, M. J. Lucero, and G. E. Scuseria, Applied Physics Letters **99**, 261908 (2011).

[40] C. Ataca, H. Şahin, and S. Ciraci, The Journal of Physical Chemistry C **116**, 8983 (2012).

[41] C. Lee, H. Yan, L. E. Brus, T. F. Heinz, J. Hone, and S. Ryu, ACS Nano **4**, 2695 (2010).

[42] A. Aiello and J. P. Woerdman, arxiv **0903** (2009).

[43] N. W. M. Ritchie, J. G. Story, and R. G. Hulet, Physical Review Letters **66**, 1107 (1991).

[44] C. Hsu, R. Frisenda, R. Schmidt, A. Arora, S. M. de Vasconcellos, R. Bratschitsch, H. S. J. van der Zant, and A. Castellanos-Gomez, Advanced Optical Materials **7**, 1900239 (2019).

[45] A. Das and M. Pradhan, Optics Communications **437**, 312 (2019).

[46] L. Britnell *et al.*, Science **340**, 1311 (2013).

[47] T. Zhan, X. Shi, Y. Dai, X. Liu, and J. Zi, Journal of Physics: Condensed Matter **25**, 215301 (2013).

[48] Q. Zhang, S. Zhou, S.-F. Fu, and X.-Z. Wang, J. Opt. Soc. Am. B **36**, 1429 (2019).

[49] A. Aiello, M. Merano, and J. P. Woerdman, Physical Review A **80**, 061801 (2009).

[50] L.-G. Wang, H. Chen, and S.-Y. Zhu, Opt. Lett. **30**, 2936 (2005).

Chapter 8 Weak measurement of Imbert-Fedorov shift in monolayer MoS_2

Here, we explain the experimental mechanism to detect the transverse IF shift for monolayer MoS_2. By effective application of Jones matrices, we have modified the arrangements of the basic quantum weak measurement setup and successfully applied it for the detection of such transverse shift. The non-trivial features of the IF shift near the special angles are prominent from the results. This technique is a general one and can be applied to other layered structures as well.

Content of this chapter has been published in: **A. Das**, S. Mandal, and M. Pradhan, "Observation of Imbert-Fedorov shift in monolayer MoS_2 via quantum weak measurement," **Optics Letters** 46 (23), 5826-5829 (2021).

8 Weak Measurement of Imbert-Fedorov shift in monolayer MoS_2

8.1 Introduction

Interaction of real light beam (having finite transverse width) with matter can yield longitudinal and transverse shifts [1-7]. In *Chapters* 6 and 7, we have discussed all the characteristics of the longitudinal GH shift. In this *Chapter*, we will concentrate on the transverse Imbert-Fedorov shift. The origin of the Imbert-Fedorov shift was debated over a long time and a number of views were offered previously [8-13]. This is discussed in detail in *Chapter* 1 of this thesis. It is now well-accepted that the IF effect primarily arises because of the conservation of the total angular momentum of the light. Hence, we have to take into account the orbital angular momentum of light along with its spin part [14-16].

Though originally invented in the total internal reflection [4,6,7,17-22], in previous Chapters we have proven that finite shift can be observed in TMDCs outside this region. Here, we examine the transverse IF shift in monolayer MoS_2 that exists both inside and outside the domain of total internal reflection. Being in the sub-wavelength scale [1], the measurement of such transverse shifts is a hard job. Among the available techniques for the optical beam shift measurement, quantum weak measurement (QWM) [23-25], interferometric method [26], beam splitter scanning technique [27], etc. are applied primarily for the GH shift measurement only. Although QWM is one of the best tools available for the precise optical beam shift [28-32] determination, only its application in the GH shift measurement is well-known to us. Hence, we have developed a new technique based on the weak measurement principle for the detection of the (transverse) IF shift.

In this *Chapter*, we have chosen the monolayer (ML) MoS_2 to investigate the presence of transverse (IF) shift. The special electronic and optical properties of MoS_2 have already been discussed in previous *Chapters*. The interested readers may also follow these references [33-37] for details. We have inspected the IF shift over a large range of incident angles for circular polarization (CP) and 45^0 linearly polarization states (LP). The proposed technique is universal and may be applied for other materials, thickness variation, optical constant measurement, detecting the existence of defects, etc. Furthermore, we have calculated the theoretical

predictions from the Aiello & Woerdman [38] model and compared with the experimental results with considerable similarity.

Before going into the experimental details, we will first introduce the concept of the Jones vector which will be necessary for the weak value amplification of the Imbert-Fedorov shift.

8.2 Jones Vector Formulation

For an arbitrarily polarized light wave the electric field component can be written as:

$$E(z,t) = E_x(z,t)\,\hat{x} + E_y(z,t)\,\hat{y} = \hat{x}a_x \cos(\omega t - kz + \delta_x) + \hat{y}a_y \cos(\omega t - kz + \delta_y) \tag{8.1}$$

From the Jones vector approach, we can write:

$$E(z,t) = \begin{pmatrix} E_x \\ E_y \end{pmatrix} = \begin{pmatrix} a_x \cos(\omega t - kz + \delta_x) \\ a_y \cos(\omega t - kz + \delta_y) \end{pmatrix} \tag{8.2}$$

Using the complex variable notations:

$$E(z,t) = \begin{pmatrix} a_x \exp\left[i(\omega t - kz + \delta_x)\right] \\ a_y \exp\left[i(\omega t - kz + \delta_y)\right] \end{pmatrix} = \exp\left[i(\omega t - kz + \delta_x)\right] \begin{pmatrix} a_x \\ a_y e^{i\delta} \end{pmatrix} \tag{8.3}$$

where, $\delta = \delta_y - \delta_x$ = the relative phase difference .

In a crisp form, the previous electric field $E(z,t)$ can be expressed as:

$$E(z,t) = \begin{pmatrix} a_x \\ a_y e^{i\delta} \end{pmatrix} \tag{8.4}$$

It is identified as the *Jones vector* of the field. The intensity of the wave is:

$$I = E^{\dagger}E = E_x^* E_x + E_y^* E_y = |a_x|^2 + |a_y|^2 \tag{8.5}$$

The Jones vector is usually written in the following normalized form:

$$E(z,t) = \frac{1}{\sqrt{a_x^2 + a_y^2}} \begin{pmatrix} a_x \\ a_y e^{i\delta} \end{pmatrix} \tag{8.6}$$

Normalized Jones vector for different polarization states can be written as:

(a) A *linear polarization* state of amplitude *a* making an angle θ with the *x*-axis is described by:

$$E_{LP} = \begin{pmatrix} \cos\theta \\ \sin\theta \end{pmatrix} \tag{8.7}$$

In the special case of a linear horizontal ($\theta = 0$) or vertical polarization ($\theta = \pi/2$), the Jones vectors will be:

Horizontal (P) polarization: $E_H = \begin{pmatrix} 1 \\ 0 \end{pmatrix}$ (8.8a)

Vertical (S) polarization: $E_V = \begin{pmatrix} 0 \\ 1 \end{pmatrix}$ (8.8b)

(b) A *left circular polarization* (LCP) state of amplitude a making an angle θ with the $\hat{x}$ axis is given by:

$$E_{LCP} = \frac{1}{\sqrt{2}} \begin{pmatrix} 1 \\ e^{-i\pi/2} \end{pmatrix} = \frac{1}{\sqrt{2}} \begin{pmatrix} 1 \\ -i \end{pmatrix} \tag{8.9}$$

(c) A *right circular polarization* (RCP) state of amplitude *a* making an angle θ with the *x*-axis is given by:

$$E_{RCP} = \frac{1}{\sqrt{2}} \begin{pmatrix} 1 \\ e^{+i\pi/2} \end{pmatrix} = \frac{1}{\sqrt{2}} \begin{pmatrix} 1 \\ i \end{pmatrix} \tag{8.10}$$

It is also clear that:

$$E_{LCP} = \frac{1}{\sqrt{2}} \left(E_H - iE_V \right) \& \; E_{RCP} = \frac{1}{\sqrt{2}} \left(E_H + iE_V \right) \tag{8.11}$$

(d) Now, in case of *elliptically polarized* (EP) wave, let us write the component fields first:

$$E_x = a\cos\left(wt - kz\right)$$

$$E_y = b\cos\left(wt - kz \pm \frac{\pi}{2} \right)$$

where (+) & (-) represent right & left elliptically polarized wave, respectively.

For *left elliptically polarized* (LEP) wave, normalized Jones vector will be:

$$E_{LEP} = \frac{1}{\sqrt{a^2 + b^2}} \begin{pmatrix} a \\ be^{-i\pi/2} \end{pmatrix} = \begin{pmatrix} \cos\varepsilon \\ -i\sin\varepsilon \end{pmatrix} \tag{8.12}$$

where, $\varepsilon = tan^{-1}(b/a)$ is a measure of the ellipticity.

Likewise, a *right elliptically polarized* (REP) wave will be given by:

$$E_{REP} = \frac{1}{\sqrt{a^2 + b^2}} \begin{pmatrix} a \\ be^{+i\pi/2} \end{pmatrix} = \begin{pmatrix} \cos\varepsilon \\ i\sin\varepsilon \end{pmatrix} \tag{8.13}$$

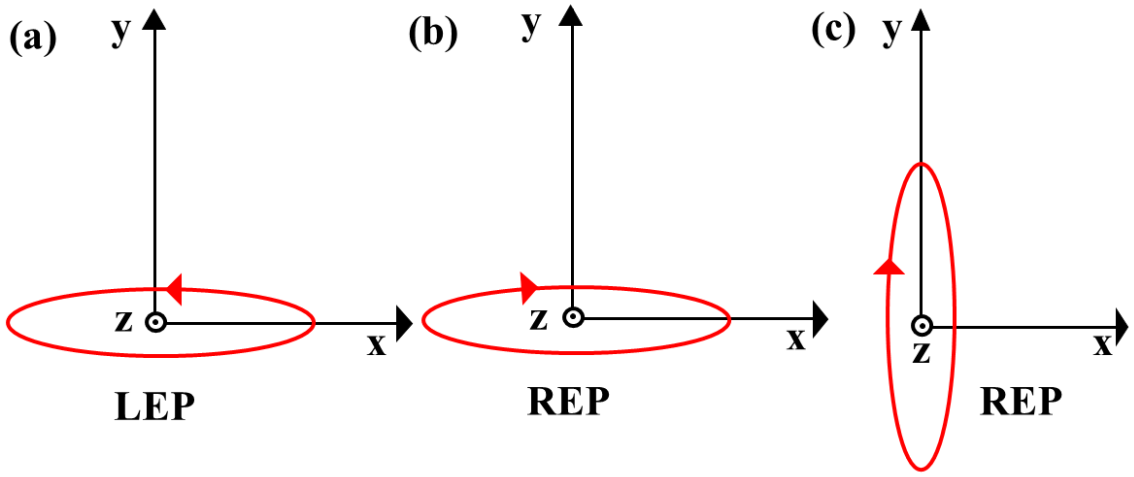

Figure 8.1. Schematic representation of **(a)** left elliptically and **(b)** right elliptically polarized beam with its major axis along the *x*-direction. **(c)** Right elliptical polarization state that is orthogonal to the one shown in **(a)**.

Both of these states are represented in Figure 8.1 above. But, if we check the orthogonality of the above two states, we find that E_{LEP} & E_{REP} are not orthogonal (except at $\varepsilon = \pi/4$) to each other.

$$E_{LEP}^{\dagger} E_{REP} = \cos 2\varepsilon \neq 0$$

The orthogonal state to E_{LEP} is depicted above (Figure 8.1(c)), whose Jones vector is given by:

$$\tilde{E}_{REP} = \frac{1}{\sqrt{a^2 + b^2}} \begin{pmatrix} b \\ ae^{+i\pi/2} \end{pmatrix} = \begin{pmatrix} \sin\varepsilon \\ i\cos\varepsilon \end{pmatrix} \tag{8.14}$$

We can also see that, $E_{LEP}^{\dagger}\tilde{E}_{REP}=0$ (establishing their relative orthogonal nature).

8.3 Jones Vectors for Optical Components

The light beam after passing through the optical components gets modified. The optical components can be represented by the Jones matrix. Consider an input polarization state *A***.** It is passed through an optical component (with Jones matrix is *J*). The output polarization state *B* is calculated as *B = JA*. If there are two Jones matrices *J1* and *J2* representing two optical components, the Jones matrix of the effective system can be calculated as ($J2\times J1$). Hence, the output polarization state is, *B = (J2.J1) A*. In Later Chapters, we require the information of Jones matrices for several optical components like half-wave plate, quarter-wave plate, polarizer, etc. Here, we have represented the Jones matrices representing the actions of these optical components.

(a) *Linear Polarizer*:

The action of a *linear polarizer* having a pass axis that makes an angle θ with the *x*-direction is represented as:

$$\begin{pmatrix} E_x^{'} \\ E_y^{'} \end{pmatrix}=\begin{pmatrix} cos^2\theta & sin\theta cos\theta \\ cos\theta sin\theta & sin^2\theta \end{pmatrix}\begin{pmatrix} E_x \\ E_y \end{pmatrix}=J_{LP}\begin{pmatrix} E_x \\ E_y \end{pmatrix}$$

The associated Jones matrix will be:

$$J_{LP}=\begin{pmatrix} cos^2\theta & sin\theta cos\theta \\ cos\theta sin\theta & sin^2\theta \end{pmatrix} \tag{8.15}$$

(b) *Linear Retarder*:

The action of a *linear retarder* having a fast axis that makes an angle θ with the *x*-direction and generates a certain phase difference δ between the components can be represented as:

$$\begin{pmatrix} E_x^{'} \\ E_y^{'} \end{pmatrix}=J_{LR}(\theta)\begin{pmatrix} E_x \\ E_y \end{pmatrix}$$

$$J_{LR}(\theta)=\begin{pmatrix} cos\theta & -sin\theta \\ sin\theta & cos\theta \end{pmatrix}\begin{pmatrix} e^{i\delta} & 0 \\ 0 & 1 \end{pmatrix}\begin{pmatrix} cos\theta & sin\theta \\ -sin\theta & cos\theta \end{pmatrix}$$

$$J_{LR} = \begin{pmatrix} sin^2\theta + e^{i\delta} cos^2\theta & (e^{i\delta} - 1) sin\theta cos\theta \\ (e^{i\delta} - 1) sin\theta cos\theta & cos^2\theta + e^{i\delta} sin^2\theta \end{pmatrix} = J_{LR}(\theta, \delta) \tag{8.16}$$

$J_{LR}(\theta, \delta)$ is the Jones matrix of the linear retarder.

The most frequently used retarders are the *half-wave plate* and the *quarter-wave plate*, whose Jones matrices can be attained from the earlier equations by substituting $\delta = \pi$ and $\pi/2$. Thus, the corresponding Jones matrices will be:

$$J_{QWP}\left(\theta, \frac{\pi}{2}\right) = \begin{pmatrix} -cos 2\theta & -sin 2\theta \\ -sin 2\theta & cos 2\theta \end{pmatrix} \tag{8.17}$$

$$J_{HWP}(\theta, \pi) = \begin{pmatrix} i cos^2\theta + sin^2\theta & (i-1) sin\theta cos\theta \\ (i-1) sin\theta cos\theta & i sin^2\theta + cos^2\theta \end{pmatrix} \tag{8.18}$$

8.4 Calculation of IF shift by Jones Vectors

We can represent the electric field of a paraxial monochromatic light using Jones matrices:

$$\vec{E} = a_1 \hat{e}_1 + a_2 \hat{e}_2$$

where, $|a_1|^2 + |a_2|^2 = 1$,

$\hat{e}_1 = \begin{pmatrix} 1 \\ 0 \end{pmatrix}$ & $\hat{e}_2 = \begin{pmatrix} 0 \\ 1 \end{pmatrix}$ serve as the polarization basis.

We already know that there is a one to one correspondence between the Schrodinger wave equation and the paraxial wave equation. Hence, the electric field constituting the light can also be defined formally in terms of a quantum mechanical wave function. Therefore, we can represent the quantum mechanical IF shift operator [39] by:

$$\hat{\Delta} = \begin{pmatrix} 0 & i\left\{1 + \left(r_p / r_s\right) cot\theta\right\} \\ -i\left\{1 + \left(r_s / r_p\right) cot\theta\right\} & 0 \end{pmatrix} \tag{8.19}$$

Here, r_s & r_p denote Fresnel reflection coefficient components. In the complex notation, the reflection coefficients are written as:

$$r_s = R_s \, exp(i\delta_s) \tag{8.20a}$$

$$r_p = R_p \, exp\left(i\delta_p\right) \tag{8.20b}$$

We also introduce new functions for future use:

$$R = R_s / R_p \tag{8.21a}$$

$$\delta = \delta_p - \delta_s \tag{8.21b}$$

$$\tilde{R} = \begin{pmatrix} R & 0 \\ 0 & R^{-1} \end{pmatrix} \tag{8.21c}$$

The above mentioned Equation (8.19) can be reduced in a simpler form [39]:

$$\hat{\Delta} = -cot\,\theta.\hat{\sigma}_2.\left[\hat{I} + cos\,\delta.\tilde{R}\right] - sin\,\delta\,cot\,\theta.\hat{\sigma}_1.\tilde{R} \tag{8.22}$$

Here, θ = the angle of incidence, σ_1 and σ_2 = the Pauli spin matrices, **I** = the identity matrix.

Looking at previous Equation (8.22), we can easily verify that $\hat{\Delta}$ is a Hermitian operator and will produce physically measurable eigenvalues.

Also, from the definition of Pauli matrices:

$$\sigma_1 = \begin{pmatrix} 0 & 1 \\ 1 & 0 \end{pmatrix}$$

$$\sigma_2 = \begin{pmatrix} 0 & -i \\ i & 0 \end{pmatrix}$$

Hence, it is apparent that the eigenbasis for σ_1 is the linear polarization (LP) states $\begin{pmatrix} 1/\sqrt{2} \\ \pm 1/\sqrt{2} \end{pmatrix}$

and for σ_2 is the circular polarization (CP) states $\begin{pmatrix} 1/\sqrt{2} \\ \pm i/\sqrt{2} \end{pmatrix}$.

Now, let us consider a P-polarized incident light, i.e.

$$\left|\psi_{in}\right\rangle = \begin{pmatrix} 1 \\ 0 \end{pmatrix}$$

Then, after post-selection to a specific polarization state,

$$\left|\psi_{out}^{1}\right\rangle = \begin{pmatrix} \varepsilon \\ 1 \end{pmatrix}$$

In this situation, the weak IF values can be written as:

$$\frac{\left\langle \psi_{out}^{1} \left| \hat{\Delta} \right| \psi_{in} \right\rangle}{\left\langle \psi_{out}^{1} \middle| \psi_{in} \right\rangle} = -\frac{\cot\theta}{\varepsilon}\left[R\sin\delta + i(1+R\cos\delta)\right] \tag{8.23}$$

In the derivation of the above equation, we have used the following relations:

$$\left\langle \Psi_{out}^{1} \left| \hat{\sigma}_1 . \tilde{R} \right| \Psi_{in} \right\rangle = R$$

$$\left\langle \Psi_{out}^{1} \left| \hat{\sigma}_2 \right| \Psi_{in} \right\rangle = i$$

$$\left\langle \Psi_{out}^{1} \left| \hat{\sigma}_2 . \tilde{R} \right| \Psi_{in} \right\rangle = iR$$

Here (set as Case **A**), σ_1 contributes the real part and σ_2 contributes the imaginary part of the above expression. Therefore, the real part will signify the IF shift for the $\begin{pmatrix} 1/\sqrt{2} \\ \pm 1/\sqrt{2} \end{pmatrix}$ LP state, and the imaginary part will signify the IF shift for the $\begin{pmatrix} 1/\sqrt{2} \\ \pm i/\sqrt{2} \end{pmatrix}$ CP state of the light.

In a likewise manner, if the pre-selection of the incident light is fixed to a P-polarization state, but, the post-selection of the output beam is fixed to a different state represented by: $\left|\psi_{out}^{2}\right\rangle = \begin{pmatrix} \varepsilon \\ -i \end{pmatrix}$

Then the weak values (of $\hat{\Delta}$ matrix) can be expressed as:

$$\frac{\left\langle \psi_{out}^{2} \left| \hat{\Delta} \right| \psi_{in} \right\rangle}{\left\langle \psi_{out}^{2} \middle| \psi_{in} \right\rangle} = \frac{\cot\theta}{\varepsilon}\left[(1+R\cos\delta) - iR\sin\delta\right] \tag{8.24}$$

Here, we have applied the following relations for the derivation:

$$\left\langle \Psi_{out}^{2} \left| \hat{\sigma}_1 . \tilde{R} \right| \Psi_{in} \right\rangle = iR$$

$$\left\langle \Psi_{out}^{2} \left| \hat{\sigma}_2 \right| \Psi_{in} \right\rangle = -1$$

$$\left\langle \Psi_{out}^{2} \left| \hat{\sigma}_2 . \tilde{R} \right| \Psi_{in} \right\rangle = -R$$

In this condition (set as Case **B**), σ_1 makes way for the imaginary part, whereas σ_2 gives rise to for real part of the expression. The given weak values (shown by the Equations (8.23) & (8.24)) are dimensionless. The exact expression of Imbert-Fedorov shifts can be obtained from the Equations (8.23) & (8.24):

$$\Delta_1 = -\frac{\lambda}{2\pi}\frac{\cot\theta}{\varepsilon}\left[R\sin\delta + \frac{z}{z_0}(1+R\cos\delta) \right] \tag{8.25}$$

$$\Delta_2 = \frac{\lambda}{2\pi}\frac{\cot\theta}{\varepsilon}\left[(1+R\cos\delta) - \frac{z}{z_0}R\sin\delta \right] \tag{8.26}$$

If you look at the Equations above, the *propagation enhancement factor* ($\frac{z}{z_0}$) seems to be a significant controlling parameter for the shift calculation. The imaginary part of the weak shifts could be greatly enlarged compared to the real part's impact. Accurate measurement of the imaginary portion of the weak shifts allows one to find out the contributions from σ_1 and σ_2. From this, one can get the respective IF shifts for the 45^0 linearly polarized (LP) and circularly polarized (CP) light.

In Figure 8.2 the schematic diagram of the modified weak measurement setup is demonstrated for the IF shift measurement. The source of light is a He-Ne laser, as is used before. The plano-convex lens (L1) focusses the beam to the anticipated spot size (w ~200 μm). The reflection occurs from the prism-MoS_2 system after passing through the pre-selection unit. Subsequently, the output beam is post-selected to the anticipated state as stated earlier by the unit of a combination of a half-wave plate (HWP), quarter-wave plate (QWP), and polarizer (GLP2). Two lenses L1 and L2 organize a 4f system. The output beam state is monitored by a beam profiler.

As stated earlier, the pre-selection is performed on the beam to fix it in the p-polarized (1, 0) state before reflection. As the reflection occurs from the prism-MoS_2 configuration, the light is post-selected to specific post-selection states as mentioned previously. To realize the anticipated orthogonal condition for weak value amplification ($\varepsilon = 0$), we fix the GLP2 at the exact orthogonal spot with respect to GLP1. Thereafter, the collective rotation of QWP and HWP, the minimum light position can be achieved.

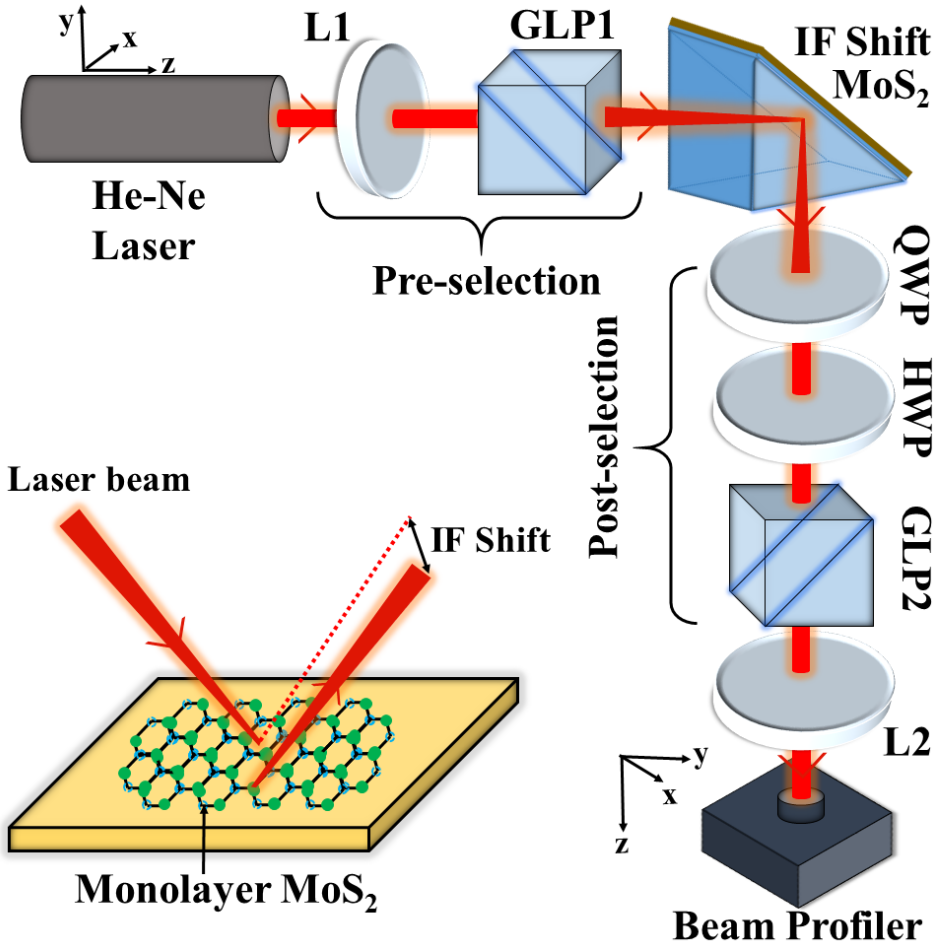

Figure 8.2. Experimental measurement setup for the IF shift, where **L1**, **L2** denote Plano-convex lenses, **GLP** denotes Glan-Thompson polarizer, **HWP** denotes half-wave plate, **QWP** denotes quarter-wave plate.

The beam centroid at the exact orthogonal position ($\varepsilon = 0$) of GLP1 and GLP2 is depicted in Figure 8.3(a). The '*I* vs *y*' graph displays the light intensity variation along the vertical direction ($\hat{y}$). From the figure, we observe that the output beam dissociates into two distinct Gaussians in the vertical direction ($\hat{y}$) separated by $\sqrt{2}w$ (at this orthogonal condition). Figure 8.3(b) exhibits the beam intensity when GLP2 is revolved by angle ε with respect to GLP1. The findings are in agreement with the formerly reported results which confirm the suitable working condition [20,40] of the experimental setup.

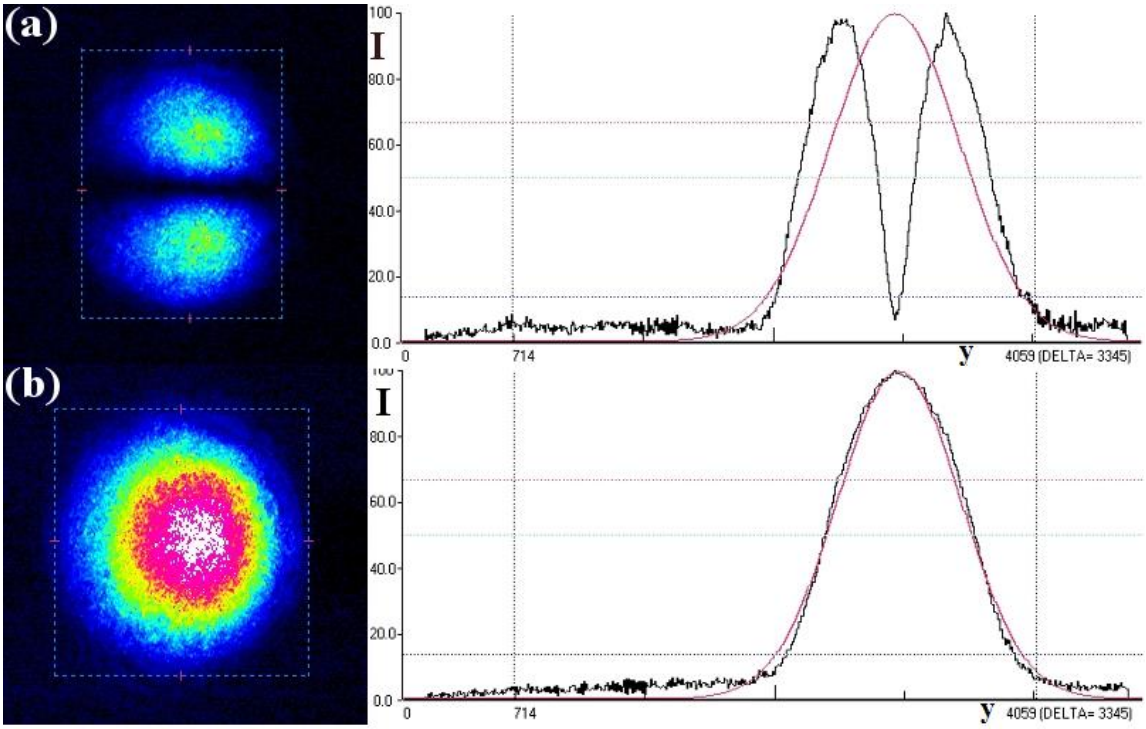

Figure 8.3. Beam profiles: **(a)** Strict orthogonal position ($\varepsilon = 0$ radian), **(b)** deviated from the exact orthogonal condition by angle ε (= 0.049 radians).

8.4.1 IF shift for diagonal (45^0) linearly polarized light

As proposed before, two separate mechanisms have to be followed during the experimental measurement. To realize Case **B** established by Equation (8.24), we go through a definite post-selection scheme to have the anticipated output $\left|\psi_{out}^{2}\right\rangle$. We keep the quarter-wave plate at the spot of minimum intensity, and rotate the half-wave plate by angle $+(\varepsilon/2)$ and at an angle $-(\varepsilon/2)$ ('+' for anticlockwise and '-' for clockwise rotation), successively and the corresponding positions of the centre of the beam spot are noted. It delivers the relative beam centroid locations for + 45^0 linearly polarized (LP) with respect to - 45^0 linearly polarized beam. We already know that the actions of linear retarders, in terms of Jones matrices, are denoted by:

$$J_{QWP}^{1} = \begin{pmatrix} i & 0 \\ 0 & 1 \end{pmatrix} \tag{8.27a}$$

$$J_{HWP}^{1}=\begin{pmatrix}-1 & \mp\varepsilon\\ \pm\varepsilon & 1\end{pmatrix} \tag{8.27b}$$

In case of this type of post-selection, the final output takes the following form:

$$\langle s|J_{HWP}^{1}.J_{QWP}^{1}\sim(\pm\varepsilon,i) \tag{8.28}$$

This is the anticipated output for Case **B** as stated earlier. The amplification and detection of the IF shift for the $\pm 45^0$ linear polarization state of the incident light are performed in this way.

In this case, the amplification factor is given by:

$$\left(\frac{1}{\varepsilon}\right)\left(\frac{z}{z_0}\right)$$

The experimental results in Figure 8.4 provide the relative IF shift for 45^0 linearly polarized beams. In Figure 8.4(a), we have shown the IF shifts for the glass surface (monolayer MoS_2 is absent) along with the results for the monolayer MoS_2 system. The results for the glass-air interface agree well with the earlier findings [20]. This proves the correct working condition of the present weak measurement setup for IF shift measurement. In Figure 8.4(a), we observe that there is no IF shift beneath the critical angle (θ_c) [20]. However, when the monolayer MoS_2 layer is present, non-zero IF shift even below the critical angle of incidence ($\theta<\theta_c$) is found out. Therefore, monolayer MoS_2 is one of the few materials that yield finite IF shift even below the critical angle. When the monolayer MoS_2 is present, the IF shift is lesser in magnitude and a minor dip is also observed in the shift value in the neighbourhood of the critical angle.

Furthermore, a comparative study is also presented showing the experimental data along with the theoretical model [38] predictions (Figure 8.4(b)). For this, we have considered the well-accepted model of Aiello & Woerdman [38] which is in accordance with the conservation of the total angular momentum of light. In this model, the IF shift is expressed in the following form:

$$\begin{aligned}\Delta_{IF}=&\left(-\frac{\lambda}{2\pi}\right)\left(\frac{a_P a_S\cot\theta_i}{|r_S|^2a_S^2+|r_P|^2a_P^2}\right)\left[\left(|r_S|^2+|r_P|^2\right)\sin\eta+2r_Sr_P\sin\left(\eta+\phi_S-\phi_P\right)\right]\\&+\left(-\frac{Z_r}{k^2L^2}\right)\left(\frac{a_Pa_S\left(|r_S|^2-|r_P|^2\right)\cot\theta_i}{|r_S|^2a_S^2+|r_P|^2a_P^2}\right)\cos\eta\end{aligned} \tag{8.29}$$

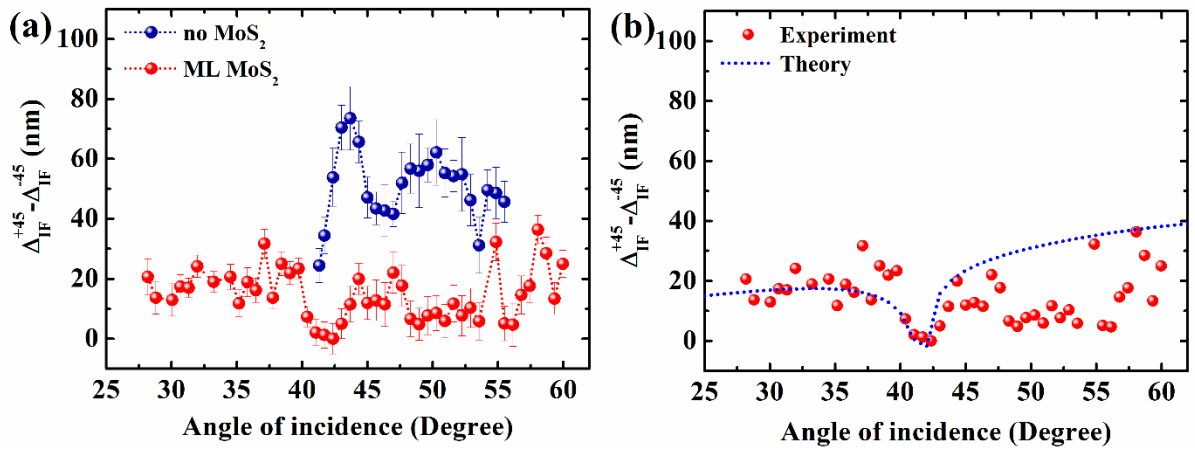

Figure 8.4. IF shift for 45^0 linearly polarized light: **(a)** comparison of IF shift in the presence and absence of monolayer MoS_2 and **(b)** comparison of experimental data with theoretical prediction.

In this theoretical model, η = relative phase difference of the incident light, $a_S\left(E_x\right)$ and $a_P\left(E_y\right)$ denote the S and P-polarization components; θ_i =incident angle; $Z_r = kz_r$, $L = kw^2/2$, (w is the beam waist). In the model, we have chosen the following values of the parameters:

$\eta = 0$

$\lambda = 633nm$

$z_r = 60cm$

$$\sigma_S\left(E\right) = \sigma_r\left(E\right) + i\sigma_i\left(E\right) = i\varepsilon_0\omega h_{eff}\left(1-\varepsilon_r\left(E\right)\right) \tag{8.30a}$$

$$\frac{\sigma_S}{\sigma_0} = \frac{i\omega h_{eff}}{\pi\alpha c}\left(1-\varepsilon_r\left(E\right)\right) \tag{8.30b}$$

$$\varepsilon_r\left(\omega\right) = \frac{\varepsilon\left(\omega\right)}{\varepsilon_0} = 1 + \sum_{k=1}^{N}\frac{f_k}{\omega_k^2 - \omega^2 - i\omega\gamma_k} = 1 + \sum_{k=1}^{N}\frac{f_k^E}{E_k^2 - E^2 - iE\gamma_k^E} \tag{8.30c}$$

The details of this oscillator model for the determination of the surface conductivity of monolayer TMDCS are explained in the reference [41]. The reflection coefficients are determined by the Transfer Matrix calculation [6].

It is apparent from Figure 8.4(b) that the experimental results are consistent with the theoretical prediction. The existence of the minor dip near the critical angle (θ_c) signifies the non-trivial behaviour of the Fresnel reflection coefficients in the close neighbourhood of the critical angle [6,42].

8.4.2 IF shift for circularly polarized light

To perform Case **A** (as given by Equation (8.23)), a separate post-selection scheme would be implemented. To achieve this, the half-wave plate, as well as the quarter-wave plate, are rotated from their location of minimum intensity at angles $\pm\varepsilon/2$ and $\pm\varepsilon$, respectively. To explain, the half-wave plate and the quarter-wave plate are rotated anticlockwise at $+\varepsilon/2$ & $+\varepsilon$ angles at first and note the respective beam centroid positions, afterwards, they are rotated at $-\varepsilon/2$ and $-\varepsilon$ angles, respectively, and note the same. After following these steps, the Jones matrices can be expressed as:

$$J_{QWP}^{2}=\begin{pmatrix} i & \pm(i-1)\varepsilon \\ \pm(i-1)\varepsilon & 1 \end{pmatrix} \tag{8.31a}$$

$$J_{HWP}^{2}=\begin{pmatrix} -1 & \mp\varepsilon \\ \pm\varepsilon & 1 \end{pmatrix} \tag{8.31b}$$

and the corresponding post-selected output would be given by:

$$\langle s|\, J_{HWP}^{2}.J_{QWP}^{2} \sim (\mp\varepsilon,1) \tag{8.32}$$

As before, this result agrees with the theoretically anticipated output for circular polarization input state [Equation (8.23)] of light. Thus, the IF shift for the circularly polarized (CP) light can be accurately determined with identical amplification (as stated earlier). We have presented the experimental data in Figure 8.5. In Figure 8.5(a), our findings of IF shift for the glass surface (when monolayer MoS_2 is absent) are compared with the IF shift for monolayer MoS_2. When MoS_2 monolayer is absent, the IF shift for circularly polarized light continuously declines with incident angles. Our experimental findings match well with the earlier findings [20]. However, when the monolayer MoS_2 is present, the behaviour of the IF shift alters considerably. IF shift starts growing with incident angles with a minor dip in the neighbourhood of the critical angle (θ_c). The IF shift is zero outside the domain of total internal reflection in absence of monolayer MoS_2. In our experiment, in monolayer MoS_2, we detect

finite IF shift below the critical angle ($\theta < \theta_c$) which is of utmost significance in both 45^0 linearly polarized and circularly polarized light. The cause is inherent in the surface optical conductivity of monolayer MoS_2 that yields an imaginary contribution giving rise to greater absorbance. The absorbance is dominating above the critical angle ($\theta > \theta_c$) triggering a sharp fall in the resultant intensity. It is in total contrast to the nature of the IF shift in the glass surface.

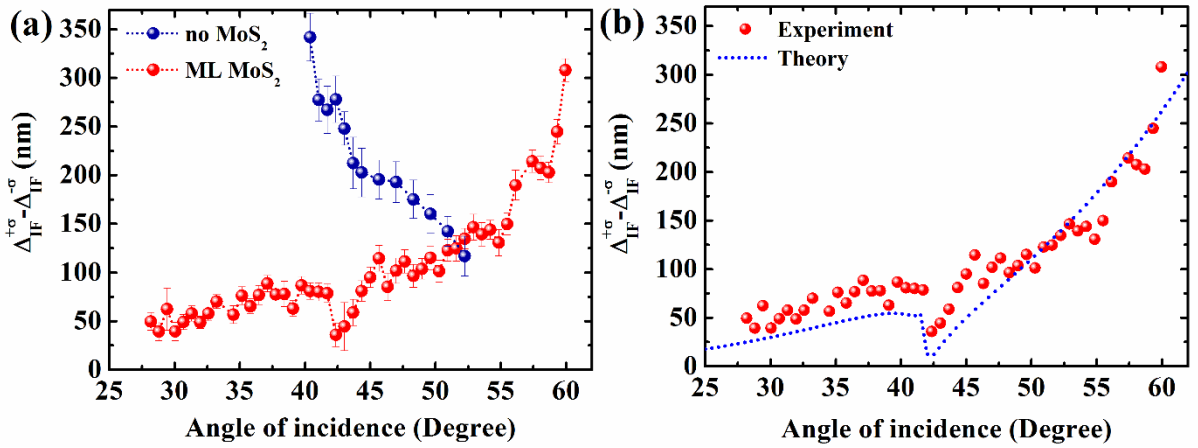

Figure 8.5. IF shift for circularly polarized light, **(a)** comparison of IF shift in the presence and absence of monolayer MoS_2 and **(b)** comparison of experimental data with the theoretical prediction.

Furthermore, we have also performed a relative comparison of the experimental findings with the theoretical model [38]. Excellent agreement was observed between the theoretical prediction and the experimental findings. The IF shift depicts fluctuations at larger incident angles because of the greater absorbance of monolayer MoS_2 in the visible region [43].

8.5 Outlook & Summary

In summary, we have accomplished a complete study of the Imbert-Fedorov shift in monolayer MoS_2. The experimental findings exhibit the sole effect of monolayer MoS_2 on the IF shift and compared the results with the results of the glass surface. All the non-trivial features of the IF shift in monolayer MoS_2 are explained in detail. The modification of the weak measurement

setup provides a novel way out to apply this technique in the transverse shift measurement for other materials.

References

[1] K. Y. Bliokh and A. Aiello, Journal of Optics **15**, 014001 (2013).

[2] M. Born and E. Wolf, *Principles of Optics: Electromagnetic Theory of Propagation, Interference and Diffraction of Light* (Elsevier Science, 2013).

[3] J. D. Jackson, *Classical electrodynamics* (Wiley, 1975).

[4] K. Artmann, Annalen der Physik **437**, 87 (1948).

[5] A. Aiello, New Journal of Physics **14**, 013058 (2012).

[6] A. Das and M. Pradhan, J. Opt. Soc. Am. B **35**, 1956 (2018).

[7] S. Goswami, M. Pal, A. Nandi, P. K. Panigrahi, and N. Ghosh, Opt. Lett. **39**, 6229 (2014).

[8] C. Imbert, Physical Review D **5**, 787 (1972).

[9] M. Onoda, S. Murakami, and N. Nagaosa, Physical Review Letters **93**, 083901 (2004).

[10] X. Chen, X.-J. Lu, P.-L. Zhao, and Q.-B. Zhu, Opt. Lett. **37**, 1526 (2012).

[11] K. Yasumoto and Y. Ōishi, Journal of Applied Physics **54**, 2170 (1983).

[12] R. H. Renard, J. Opt. Soc. Am. **54**, 1190 (1964).

[13] V. G. Fedoseyev, Journal of Physics A: Mathematical and General **21**, 2045 (1988).

[14] K. Y. Bliokh and Y. P. Bliokh, Physical Review Letters **96**, 073903 (2006).

[15] K. Y. Bliokh and Y. P. Bliokh, Physical Review E **75**, 066609 (2007).

[16] C.-F. Li, Physical Review A **76**, 013811 (2007).

[17] F. Goos and H. Hänchen, Annalen der Physik **436**, 333 (1947).

[18] S. Chen, C. Mi, L. Cai, M. Liu, H. Luo, and S. Wen, Applied Physics Letters **110**, 031105 (2017).

[19] L. Xie *et al.*, Opt. Express **26**, 22934 (2018).

[20] G. Jayaswal, G. Mistura, and M. Merano, Opt. Lett. **39**, 2266 (2014).

[21] S. Grosche, M. Ornigotti, and A. Szameit, Opt. Express **23**, 30195 (2015).

[22] S. Goswami, S. Dhara, M. Pal, A. Nandi, P. K. Panigrahi, and N. Ghosh, Opt. Express **24**, 6041 (2016).

[23] O. Hosten and P. Kwiat, Science **319**, 787 (2008).

[24] K. Y. Bliokh, C. T. Samlan, C. Prajapati, G. Puentes, N. K. Viswanathan, and F. Nori, Optica **3**, 1039 (2016).

[25] S. Chen, X. Zhou, X. Ling, W. Shu, H. Luo, and S. Wen, Applied Physics Letters **118**, 111104 (2021).

[26] C. Prajapati, D. Ranganathan, and J. Joseph, J. Opt. Soc. Am. A **30**, 741 (2013).

[27] X. Li, P. Wang, F. Xing, X.-D. Chen, Z.-B. Liu, and J.-G. Tian, Opt. Lett. **39**, 5574 (2014).

[28] A. Das and M. Pradhan, J. Opt. Soc. Am. B **38**, 387 (2021).

[29] N. W. M. Ritchie, J. G. Story, and R. G. Hulet, Physical Review Letters **66**, 1107 (1991).

[30] S. Wu and Y. Li, Physical Review A **83**, 052106 (2011).

[31] Y. Aharonov, D. Z. Albert, and L. Vaidman, Physical Review Letters **60**, 1351 (1988).

[32] I. M. Duck, P. M. Stevenson, and E. C. G. Sudarshan, Physical Review D **40**, 2112 (1989).

[33] A. D. Yoffe, Solid State Ionics **39**, 1 (1990).

[34] J. K. Ellis, M. J. Lucero, and G. E. Scuseria, Applied Physics Letters **99**, 261908 (2011).

[35] Y. Li *et al.*, Physical Review B **90**, 205422 (2014).

[36] S. Manzeli, D. Ovchinnikov, D. Pasquier, O. V. Yazyev, and A. Kis, Nature Reviews Materials **2**, 17033 (2017).

[37] A. V. Kolobov and J. Tominaga, *Two-Dimensional Transition-Metal Dichalcogenides* (Springer International Publishing, 2016).

[38] A. Aiello and J. P. Woerdman, Opt. Lett. **33**, 1437 (2008).

[39] F. Töppel, M. Ornigotti, and A. Aiello, New Journal of Physics **15**, 113059 (2013).

[40] G. Jayaswal, G. Mistura, and M. Merano, Opt. Lett. **38**, 1232 (2013).

[41] M. Weismann and N. C. Panoiu, Physical Review B **94**, 035435 (2016).

[42] M. V. Berry, Proceedings of the Royal Society A: Mathematical, Physical and Engineering Sciences **467**, 2500 (2011).

[43] L. Britnell *et al.*, Science **340**, 1311 (2013).

Chapter 9 Polarimetric measurement of the Optical Beam Shifts

In this Chapter, we have described another indirect but simpler technique, termed as 'Stokes Polarimetric method', for the easy detection of the GH and IF shift. We have successfully applied this method in monolayer MoS_2 for measuring the optical beam shift over different incident angles and polarization states. Moreover, the detection of the angular shift is also possible using this method as explained here.

Content of this chapter has been published in: **A. Das** and M. Pradhan, "Investigation of the optical beam shifts for monolayer MoS_2 using polarimetric technique," **Journal of Optics** 22 (10), 105004 (2020).

9 Polarimetric measurement of the Optical Beam Shifts

9.1 Introduction

We have already established the presence of finite longitudinal (GH) and transverse (IF) shifts [1-13] in most of the phenomena of light interaction with matter. The primary dependence of these shifts on the wavelength and polarization state of the incident light along with the characteristics of the reflecting surface [3,14-16] is also proved. Though initial observations of the GH and IF shifts strictly depend upon the condition of total internal reflection (TIR) of light [8,10,17]. But, this is not universal and finite shift can appear even beyond the total internal reflection domain [18,19] and we have proved that with 2D materials. In this Chapter, we will show this again, but, with a different experimental technique that is easier to perform. In addition, the angular shifts can also be found out by using the proposed technique. Since optical beam shifts are studied in various fields like plasmonics, photonics, metamaterials, and many quantum systems [2,20-27], the easier and time-saving methods for beam shift detection will be greatly advantageous while considering their practical applications. This experimental technique although indirect in principle, can be functional in these different fields because of its simplicity. We have again taken monolayer MoS_2 for our experiment due to their unique optical properties [28-35] and to better understand the technical differences in comparison to the weak measurement technique.

In this *Chapter*, we have described the detailed theoretical formalism of *Stokes Polarimetric* technique and subsequently demonstrated the experimental development of the setup and for the first time modified and used it to determine the GH and IF shifts in monolayer MoS_2. This polarimetric technique has found applications in different areas of the modern research community such as biomedical optics and engineering, imaging, remote sensing, electro-optical phenomena, astronomical investigations [36-38], etc. Other methods for optical beam shift detection like quantum weak measurement, beam splitter scanning, weak value interferometric techniques have other advantages but the experimental procedure is very much difficult, complex, and time taking [39-44]. The present method is easier than the others and the beam shift measurement can be performed in no time. The common source of noise like beam intensity fluctuations can be avoided in this method. Henceforth, the common sources of

errors are reduced in this technique. In this method, the polarization components have a great role to play. This method could also be effectively improved to detect GH and IF shifts in birefringent materials, liquid state, and angular rotation processes.

In this method, the Stokes parameters are experimentally measured which straight-forwardly provide reflection coefficient (r_p and r_s) values. The angular derivative of the imaginary part and real part of the reflection coefficients mainly govern the spatial and angular GH shifts. Conversely, the relative phase difference is the principal contributing factor in the spatial and angular IF shifts.

9.2 Stokes Vectors Formulation

This is a different way of representing the polarization states other than the Jones vector representation. In this representation, four observable parameters, known as *Stokes parameters*, are used. These are defined as:

$$S = I_0 \tag{9.1a}$$

$$S_1 = I_H - I_V \tag{9.1b}$$

$$S_2 = I_{+45} - I_{-45} \tag{9.1c}$$

$$S_3 = I_{RCP} - I_{LCP} \tag{9.1d}$$

I_0 represents the intensity of the given light beam, and I_H, I_V, I_{+45}, I_{-45}, $I_{RCP,}$ and I_{LCP} represent the transmitted intensities when the light beam is passed through a linear horizontal polarizer (LHP), a linear vertical polarizer (LVP), a linear $+45^0$ polarizer ($+45^0$ LP), a linear -45^0 polarizer (-45^0 LP), a right-circular polarizer, and left-circular polarizer, respectively. Physically, S_1 gives a notion of whether the SOP is nearer to linear horizontally polarized light ($S_1 > 0$) or to linear vertically polarized light ($S_1 < 0$) or to neither ($S_1 = 0$); S_2 gives an idea of whether the given SOP is closer to the linear + 45^0 ($S_2 > 0$), to linear - 45^0 ($S_2 < 0$), or to neither ($S_2 = 0$); similarly, S_3 gives an idea of whether the given SOP is closer to right-circular polarized light ($S_3 > 0$), to left-circular polarized light ($S_3 < 0$), or to neither ($S_3 = 0$).

Let us consider a plane monochromatic electromagnetic wave propagating along the *z*-direction that represents given light beam. The wave is considered to be a superposition of two electric field components given by:

$$E_x(t) = a_x \cos(\omega t - kz + \delta_x) \tag{9.2a}$$

$$E_y(t) = a_y \cos(\omega t - kz + \delta_y) \tag{9.2b}$$

where, $E_y / E_x = (a_y / a_x) exp[-i\delta]$, $\delta = \delta_y - \delta_x$ is the relative phase difference.

Then, the intensity of the light wave can be represented as:

$$I_0 = c\varepsilon_0 \left[\langle E_x^2(t) \rangle + \langle E_y^2(t) \rangle \right] = \frac{c\varepsilon_0}{2} \left[\langle a_x^2 \rangle + \langle a_y^2 \rangle \right] \tag{9.3}$$

The intensity passed through an LHP is clearly:

$$I_H = c\varepsilon_0 \left[\langle E_x^2(t) \rangle \right] = \frac{c\varepsilon_0}{2} \langle a_x^2 \rangle \tag{9.4}$$

The output intensity passed through a linear $+45^0$ polarizer:

$$I_{+45} = c\varepsilon_0 \left[\langle E_{+45}^2(t) \rangle + \langle E_y^2(t) \rangle \right] = \frac{c\varepsilon_0}{2} \frac{1}{2} \left[\langle a_x^2 \rangle + \langle a_y^2 \rangle + \langle 2a_x a_y \cos\delta \rangle \right] \tag{9.5}$$

Similarly, it can be shown that the intensity passed through a right-circular polarizer can be written as:

$$I_{RCP} = \frac{c\varepsilon_0}{2} \frac{1}{2} \left[\langle a_x^2 \rangle + \langle a_y^2 \rangle + \langle 2a_x a_y \sin\delta \rangle \right] \tag{9.6}$$

One obtains the following alternative definition of the Stokes parameters:

$$S_0 = \langle a_x^2 \rangle + \langle a_y^2 \rangle \tag{9.7a}$$

$$S_1 = \langle a_x^2 \rangle - \langle a_y^2 \rangle \tag{9.7b}$$

$$S_2 = \langle 2a_x a_y \cos\delta \rangle \tag{9.7c}$$

$$S_3 = \langle 2a_x a_y \sin\delta \rangle \tag{9.7d}$$

The Stokes parameters are conventionally written vertically in a column vector form or horizontally inside curly brackets. The way of representation is written below:

$$S = \begin{pmatrix} S_0 \\ S_1 \\ S_2 \\ S_3 \end{pmatrix} \tag{9.8a}$$

$$S = \{S_0, S_1, S_2, S_3\} \tag{9.8b}$$

S is known as the *Stokes vector* of the light beam. Generally, the Stokes vector is written in the normalized form, where all four parameters are divided by the first parameter S_0. Stokes parameters can be used to designate completely polarized, unpolarized, as well as partially polarized light. In the following sections, we discuss some important properties of the Stokes vectors for differently polarized light beams.

For a completely polarized beam, a_x, a_y, and δ are independent of time, and hence,

$$S_0 = a_x^2 + a_y^2 \tag{9.9a}$$

$$S_1 = a_x^2 - a_y^2 \tag{9.9b}$$

$$S_2 = 2a_x a_y \cos\delta \tag{9.9c}$$

$$S_3 = 2a_x a_y \sin\delta \tag{9.9d}$$

(a) *Linearly polarized*: For a linearly polarized beam with amplitude a, and orientation θ (with the *x*-axis). The Stokes vector of a linearly polarized wave oriented θ at with the x axis is given by ($a_x = a\cos\theta, a_y = a\sin\theta$):

$$S_{LP} = \begin{pmatrix} S_0 \\ S_0 \cos 2\theta \\ S_0 \sin 2\theta \\ 0 \end{pmatrix} \tag{9.10}$$

where, $S_0 = a_x^2 + a_y^2 = 2a^2$

In special cases of linear polarization, i.e. Horizontal (P) polarized ($\theta = 0^0$), Vertical (S) polarized ($\theta = 90^0$) and 45^0 diagonal linearly polarized states, the Stokes Vector takes the following form:

$$S_{HP} = \begin{pmatrix} S_0 \\ S_0 \\ 0 \\ 0 \end{pmatrix}, S_{VP} = \begin{pmatrix} S_0 \\ -S_0 \\ 0 \\ 0 \end{pmatrix}, S_{+45} = \begin{pmatrix} S_0 \\ 0 \\ S_0 \\ 0 \end{pmatrix} \;\&\; S_{-45} = \begin{pmatrix} S_0 \\ 0 \\ -S_0 \\ 0 \end{pmatrix} \tag{9.11}$$

(b) *Right Circularly polarized* light: ($a_x = a_y = a, \delta = +\frac{\pi}{2}$)

$$S_{RCP} = \begin{pmatrix} S_0 \\ 0 \\ 0 \\ S_0 \end{pmatrix} \tag{9.12}$$

where, $S_0 = a_x^2 + a_y^2 = 2a^2$

(c) *Left Circularly polarized* light: ($a_x = a_y = a, \delta = -\frac{\pi}{2}$)

$$S_{LCP} = \begin{pmatrix} S_0 \\ 0 \\ 0 \\ -S_0 \end{pmatrix} \tag{9.13}$$

where, $S_0 = a_x^2 + a_y^2 = 2a^2$

(d) *Elliptically polarized* light: ($a_x = a$ and $a_y = b$)

It can be proved that the orientation angle θ, ellipticity, and sense of rotation of the polarization ellipse are given by:

$$tan\,2\theta = \frac{2a_x a_y}{a_x^2 - a_y^2} \tag{9.14}$$

$$sin\,2\chi = \frac{2a_x a_y \, sin\,\delta}{a_x^2 + a_y^2} \tag{9.15}$$

where we have used,

$$tan\,\chi = \pm\frac{b}{a} \tag{9.16}$$

Here (-) & (+) signs correspond to the left and right sense of rotation of the electric field vector. Further, semi-major axis *a*, and semi-minor axis *b* of the polarization ellipse are given by:

$$a^2 = a_x^2 \cos^2\theta + a_y^2 \sin^2\theta + a_x a_y \sin 2\theta \cos\delta$$

$$b^2 = a_x^2 \cos^2\theta + a_y^2 \sin^2\theta - a_x a_y \sin 2\theta \cos\delta$$

Using these above Equations, we can derive the following relations:

$$\tan 2\theta = \frac{S_2}{S_1} \tag{9.17}$$

$$\sin 2\chi = \frac{S_3}{S_0} \tag{9.18}$$

Using the above Equations, we can derive:

$$S_1 = S_0 \cos 2\chi \cos 2\theta \tag{9.19a}$$

$$S_2 = S_0 \cos 2\chi \sin 2\theta \tag{9.19b}$$

$$S_3 = S_0 \sin 2\chi \tag{9.19c}$$

The preceding relations show that for completely polarized light, the four Stokes parameters are not independent and are related to each other through the following relation:

$$S_0^2 = S_1^2 + S_2^2 + S_3^2 \tag{9.20}$$

Thus, the normalized Stokes vector of a completely polarized beam is:

$$S = \begin{pmatrix} 1 \\ \cos 2\chi \cos 2\theta \\ \cos 2\chi \sin 2\theta \\ \sin 2\chi \end{pmatrix} \tag{9.21}$$

Conversely, if the Stokes parameters of a given polarized wave are known, the orientation θ and the ellipticity angle χ of its polarization ellipse can be obtained using the following relations:

$$2\theta = \tan^{-1}\left(\frac{S_2}{S_1}\right), 0 \le \theta \le \pi \tag{9.22a}$$

$$2\chi = sin^{-1}\left(\frac{S_3}{S_0}\right), -\frac{\pi}{4} \le \chi \le \frac{\pi}{4} \tag{9.22b}$$

9.3 Determination of Stokes Vectors

As suggested by Equation (9.23), the Stokes vector of a given light beam can be determined first by measuring its intensity directly and then measuring its intensity after passing it through three different polarizers, namely, a linear horizontal, a linear + 45^0, and a right-circular polarizer. The measured intensities will be I_0, I_H, $I_{+45,}$ and I_{RCP} respectively, from which the Stokes parameters S_0, S_1, S_2, and S_3 can easily be calculated using:

$$S_0 = I_0 \tag{9.23a}$$

$$S_1 = 2I_H - I_0 \tag{9.23b}$$

$$S_2 = 2I_{+45} - I_0 \tag{9.23c}$$

$$S_1 = 2I_{RCP} - I_0 \tag{9.23d}$$

9.4 Determination of the GH & IF shifts

The components of reflection coefficients can be determined from the Stokes parameters [45]:

$$|r_S| = \sqrt{S_0 + S_1/2E_{0x}^2} \tag{9.24a}$$

$$|r_P| = \sqrt{S_0 - S_1/2E_{0y}^2} \tag{9.24b}$$

The phase difference can also be determined from the Stokes parameters and the initial phase difference:

$$\phi_S - \phi_P = arctan\left(S_3/S_2\right) - \eta \tag{9.25}$$

Here, η = initial phase difference.

Consequently, the GH & IF shifts can be determined [4,46].

$$\Delta_{GH} = \left(\frac{\lambda}{2\pi}\right)\frac{|r_S|^2 a_S^2 Im\left(\frac{\partial ln\, r_S}{\partial \theta_i}\right) + |r_P|^2 a_P^2 Im\left(\frac{\partial ln\, r_P}{\partial \theta_i}\right)}{|r_S|^2 a_S^2 + |r_P|^2 a_P^2} \tag{9.26a}$$

$$\Theta_{GH} = \left(\frac{Z_r}{k^2 L^2}\right) \frac{|r_S|^2 a_S^2 \, Re\left(\frac{\partial \ln r_S}{\partial \theta_i}\right) + |r_P|^2 a_P^2 \, Re\left(\frac{\partial \ln r_P}{\partial \theta_i}\right)}{|r_S|^2 a_S^2 + |r_P|^2 a_P^2} \tag{9.26b}$$

$$\Delta_{IF} = \left(-\frac{\lambda}{2\pi}\right)\left(\frac{a_P a_S \cot\theta_i}{|r_S|^2 a_S^2 + |r_P|^2 a_P^2}\right).\left[\left(|r_S|^2 + |r_P|^2\right) sin\,\eta + 2 r_S r_P \, sin\left(\eta + \phi_S - \phi_P\right)\right] \tag{9.27a}$$

$$\Theta_{IF} = \left(-\frac{Z_r}{k^2 L^2}\right)\left(\frac{a_P a_S \left(|r_S|^2 - |r_P|^2\right) cot\,\theta_i}{|r_S|^2 a_S^2 + |r_P|^2 a_P^2}\right) cos\,\eta \tag{9.27b}$$

Here, $a_S\left(E_{0x}\right)$ and $a_P\left(E_{0y}\right)$ represents the S and P-polarization constituents, θ_i = angle of incidence; $Z_r = kz_r$, where z_r is the propagation distance; $L = kw_0^2/2$, where w_0 is the beam waist, and $k = 2\pi n/\lambda_0$ is the associated wave vector with n being the refractive index of the medium. In the above expressions, Δ represents spatial shift (in micrometers) and Θ represents angular shifts (in micro radians). However, greater spatial shifts are generated for a well-collimated beam ($Z_r/kL \ll 1$), while greater angular shifts are shown by a well-focussed beam. Nevertheless, a trade-off is needed to get the appreciable value of both. The beam has a waist (w_0) of 250 μm.

9.5 Experimental Measurement Process

Figure 9.1 represents the experimental setup for the polarimetric measurement. He-Ne laser, generating quality Gaussian beam, works as the source of light. The polarization state is monitored by linear polarizer or a grouping of a quarter-wave plate, and a half-wave plate available on rotation mounts. The actual reflection takes place at the surface of a 45^0-90^0-45^0 NBK-7 prism. On the rear side of the prism, the monolayer of MoS_2 (2dsemiconductors Inc.) is cautiously placed (as shown in Figure 9.1). The ultimate output state is cautiously examined by a Polarimeter.

We first perform the pre-selection of the incoming light to the physical system to the chosen state i.e. + 45^0 and - 45^0 linear polarized, right and left circularly polarized, S and P-polarized using the above-mentioned combination of the optical components. As the reflected light is emitted from the prism-MoS_2 system it is focussed directly on to a Polarimeter that yields Stokes parameters (S_0, S_1, S_2, and S_3). Lastly, we have changed the polarization states of

the incident light, subsequently measured the Stokes parameters for a large range of incident angles for each polarization state.

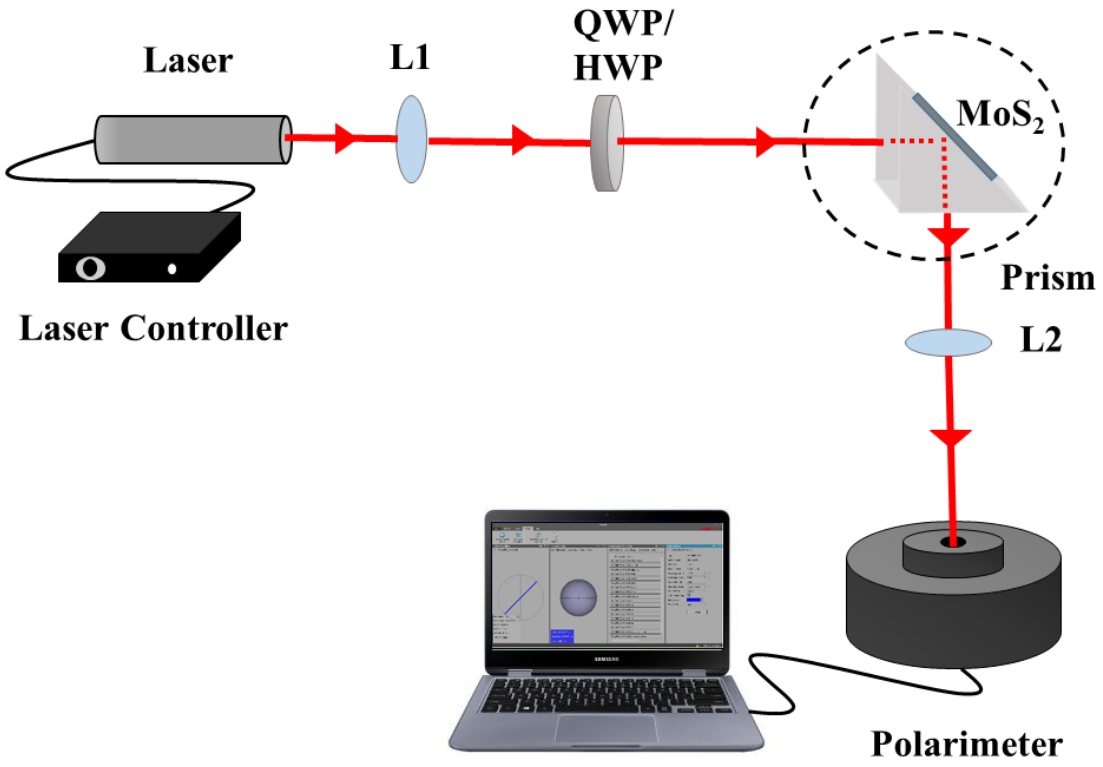

Figure 9.1. Experimental setup for the polarimetric measurement of the GH and IF shift, where HWP denotes half-wave plate, QWP denotes quarter-wave plate, and L1, L2 denote plano-convex lenses.

9.6 Results & Discussions

9.6.1 Polarimetric measurement of GH shift

The eigenstates of the GH are the S and P-polarized states [5], respectively. We already know that in general, the spatial GH shift appears in the total internal reflection regime (above the critical angle of incidence), the shift is exactly zero below this critical angle [14,18]. The results we obtained for the plane glass-air interface are in agreement with this concept. But, when monolayer MoS_2 is present, the spatial GH shift alters substantially. For P and S-polarization states of the incident light, the spatial GH shift is revealed in Figure 9.2. The spatial GH shift stays positive but its magnitude for MoS_2 is smaller than the glass interface.

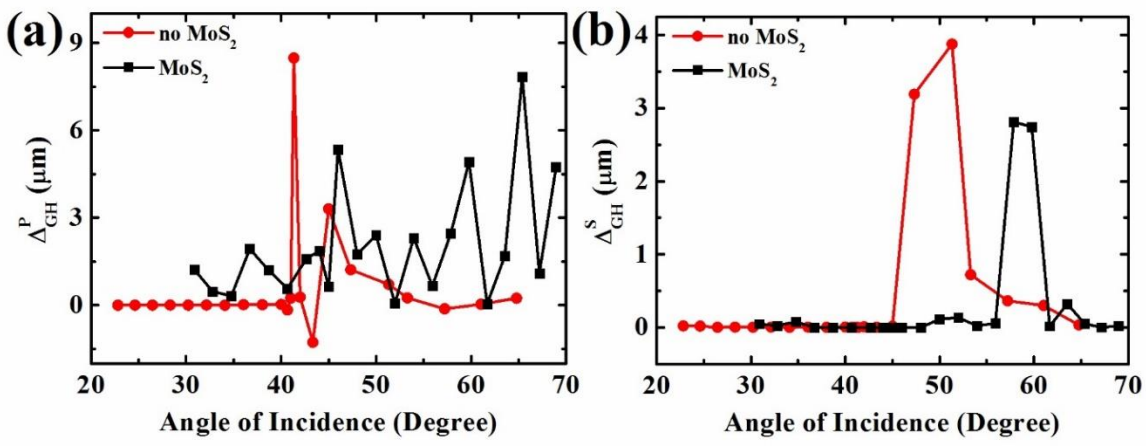

Figure 9.2. Spatial GH shift: **(a)** P-polarized and **(b)** S-polarized light.

For angular GH shift in the glass surface, P-polarization states depict non-zero value outside total internal reflection ($\theta < \theta_C$) having maxima at θ_C but the shift, $\Delta = 0$ for incident angles greater than the critical angle, consistent with the past findings. Nevertheless, when monolayer MoS_2 is present, the angular shift rises, getting maxima, and then severely declines (Figure 9.3). The shift again increases at higher incident angles. Likewise, the angular shift for S-polarized light abruptly rises to display maxima, then severely diminishes to zero at the total internal reflection. In the presence of MoS_2, the position of the maximum peak is found at 52^0.

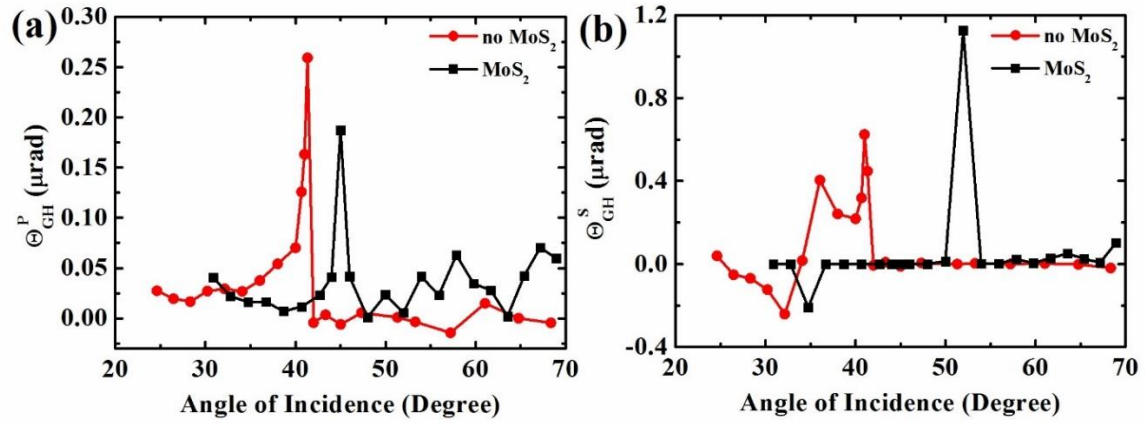

Figure 9.3. Angular GH shift: **(a)** P-polarized and **(b)** S-polarized light.

9.6.2 Polarimetric measurement of IF shift

The eigenstates for IF shifts are the 45^0 diagonally linear polarized and right circularly or left circularly polarized light beam states [5]. Henceforth, we have altered the polarization of the incident light accordingly.

For the air-glass interface, the spatial IF shifts totally agree with the former results [47]. For 45^0 linearly polarized light (Figure 9.4), we detected a sudden increase in shift value after overcoming the critical angle. But for circularly polarized light, no abnormal behaviour is perceived in the neighbourhood of the critical angle. The shift gradually declines with an increase in the incident angles and the rate of decline becomes quicker for $\theta < \theta_c$. When the monolayer MoS_2 is present, the spatial IF shift behaves contrarily and displays smaller values.

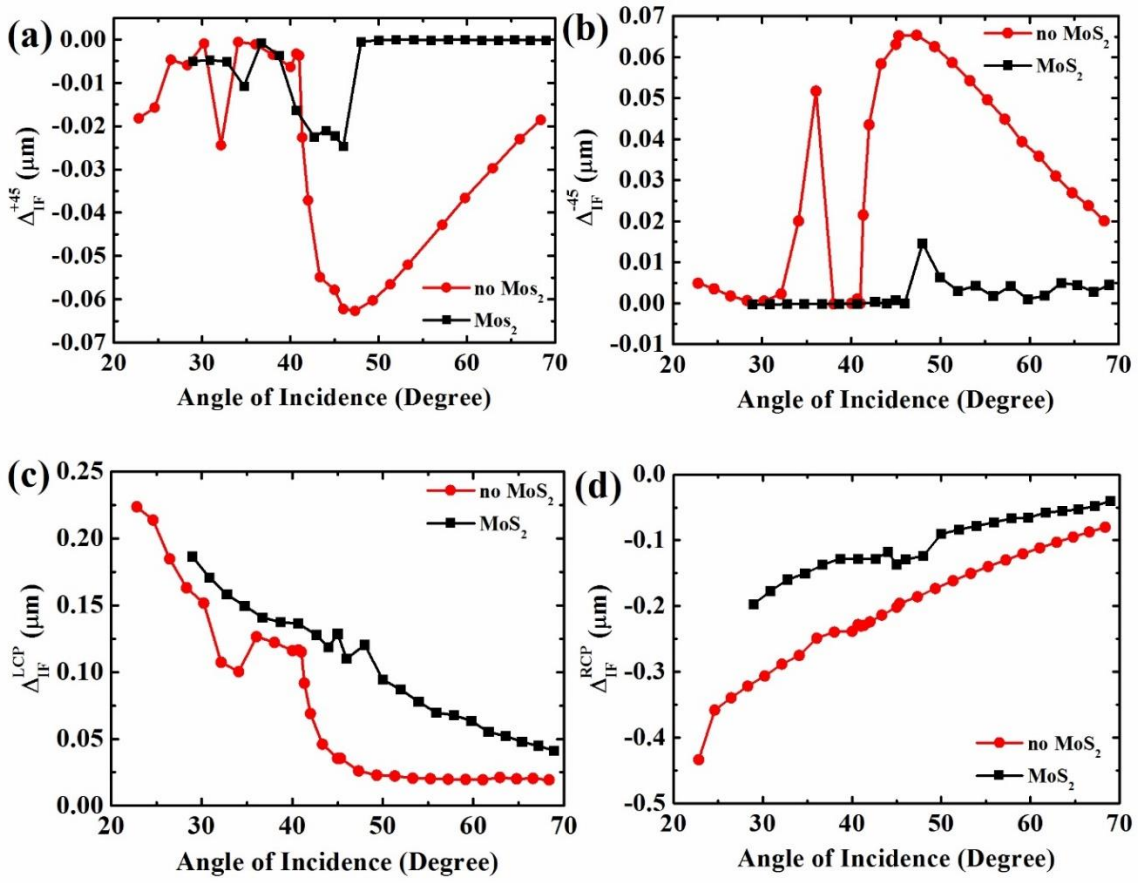

Figure 9.4. Spatial IF shift: **(a)** + 45^0 linearly polarized, **(b)** - 45^0 linearly polarized, **(c)** left circularly polarized, **(d)** right circularly polarized light.

The angular IF shift for 45^0 linear polarization state of light is non-zero for partial reflection, but abruptly reduces to zero at total internal reflection ($\theta > \theta_c$) scenario. When the monolayer MoS_2 is present, the angular IF shift gradually diminishes as we crossover the critical angle but never drops to zero shift which is a significant difference (Figure 9.5). The angular IF shift for left circularly or right circularly polarized light is zero theoretically as η=0 for the air-glass interface in the absence of any sample. But the same is not true in the case of monolayer MoS_2. As observed in Figure 9.5, negative IF shift occurs for both of the circularly polarized light which diminishes with growing incident angles.

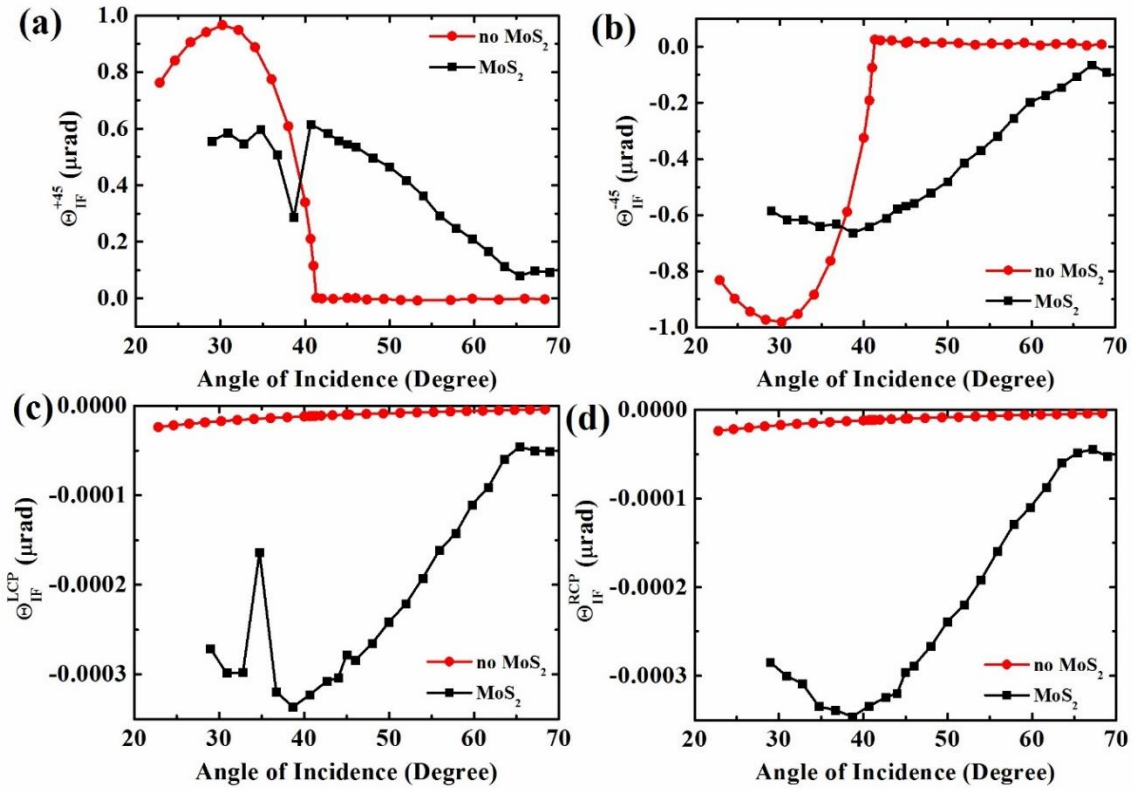

Figure 9.5. Angular IF shift: **(a)** + 45^0 linearly polarized, **(b)** - 45^0 linearly polarized, **(c)** left circularly polarized, **(d)** right circularly polarized light.

If we look at the sign of the shifts, we observe the spatial IF shifts to be positive for left circularly polarized and - 45^0 linear polarized states, whereas negative for right circularly and + 45^0 linearly polarized states of the input light. Likewise, the angular IF shifts appear positive for + 45^0 linearly polarized state, while, negative for - 45^0 linearly polarized, and both of the

circularly polarized (LCP & RCP) state of the incident light. The reflection coefficients along with the complex surface conductivity of the reflecting surface have a great influence on the nature and sign of the shifts for all the polarization states. The parameter ($\phi_S - \phi_P$) alters in an unusual manner in close proximity of the critical angle [14,18]. When the input state is + 45^0 & - 45^0 linear polarization state, ($\phi_S - \phi_P$) is the governing term that regulates the characteristics of the IF shift. Nevertheless, when the input state is circularly polarized (be it left or right), both terms of Δ_{IF} contest among themselves. The angular IF shift (as shown in Equation (9.27)) inclines to zero from the negative side for incident circular polarization state of the beam (as $cos(\eta) \to 0$). When we have + 45^0 and - 45^0 linear polarization input states, we find finite positive and negative shifts (as, $cos(\eta) \to \pm 1$), respectively.

Looking at the results, we infer that MoS_2 monolayer, in comparison to the glass surface, gives rise to lesser spatial shifts while greater angular shifts. Nevertheless, the theoretical prediction of the giant shift in monolayer MoS_2 [18] is absent in the experimental observation. The most probable cause is the greater absorption of monolayer MoS_2. Monolayer MoS_2 yields a high absorbance close to 10^7 m^{-1}. The occurrence of robust Van-Hove singularities in the density of states of monolayer MoS_2 boosts their light absorption [48] property. In the theoretical model based on stationary phase approximation, this high absorbance factor was not taken into account which leads to contradictions from our experimental findings although the conditions for the existence of the giant shift were severely followed.

9.7 Outlook & Summary

In summary, we have explained the principle and development of the 'Stokes Polarimetric' technique and applied it effectively for measuring the GH and IF shifts in monolayer MoS_2 for the first time. The greater absorbance of monolayer MoS_2 in the visible domain considerably affects the experimental findings and causes deviation from the theoretical predictions. The non-trivial nature of the GH and IF shifts in the neighbourhood of the critical angle is also confirmed.

References

[1] M. Born and E. Wolf, *Principles of Optics: Electromagnetic Theory of Propagation, Interference and Diffraction of Light* (Elsevier Science, 2013).

[2] K. Y. Bliokh and A. Aiello, Journal of Optics **15**, 014001 (2013).

[3] A. Aiello, New Journal of Physics **14**, 013058 (2012).

[4] M. Ornigotti and A. Aiello, Journal of Optics **15**, 014004 (2013).

[5] F. Töppel, M. Ornigotti, and A. Aiello, New Journal of Physics **15**, 113059 (2013).

[6] A. Aiello, M. Merano, and J. P. Woerdman, Physical Review A **80**, 061801 (2009).

[7] A. Aiello, M. Merano, and J. P. Woerdman, Opt. Lett. **34**, 1207 (2009).

[8] F. Goos and H. Hänchen, Annalen der Physik **436**, 333 (1947).

[9] M. McGuirk and C. K. Carniglia, J. Opt. Soc. Am. **67**, 103 (1977).

[10] C. Imbert, Physical Review D **5**, 787 (1972).

[11] S. I. V. Bliokh Konstantin Y., and Kivshar Yuri S. , Opt. Lett. **34**, 389 (2009).

[12] F. I. Fedorov, Dokl. Akad. Nauk SSSR **105**, 465 (1955).

[13] W. Löffler, A. Aiello, and J. P. Woerdman, Physical Review Letters **109**, 213901 (2012).

[14] A. Das and M. Pradhan, Optics Communications **437**, 312 (2019).

[15] M. Merano, A. Aiello, G. W. 't Hooft, M. P. van Exter, E. R. Eliel, and J. P. Woerdman, Opt. Express **15**, 15928 (2007).

[16] B. Aleksandr Ya, Journal of Optics **19**, 085602 (2017).

[17] K. Artmann, Annalen der Physik **437**, 87 (1948).

[18] A. Das and M. Pradhan, J. Opt. Soc. Am. B **35**, 1956 (2018).

[19] S. Grosche, M. Ornigotti, and A. Szameit, Opt. Express **23**, 30195 (2015).

[20] X. Yin, L. Hesselink, Z. Liu, N. Fang, and X. Zhang, Applied Physics Letters **85** (2004).

[21] M. Merano, Opt. Lett. **41**, 2668 (2016).

[22] I. V. Shadrivov, A. A. Zharov, and Y. S. Kivshar, Applied Physics Letters **83**, 2713 (2003).

[23] A. Szameit, H. Trompeter, M. Heinrich, F. Dreisow, U. Peschel, T. Pertsch, S. Nolte, F. Lederer, and A. Tünnermann, New Journal of Physics **10**, 103020 (2008).

[24] P. T. Leung, C. W. Chen, and H. P. Chiang, Optics Communications **276**, 206 (2007).

[25] R. Nasehi and M. Mahmoudi, Appl. Opt. **57**, 7714 (2018).

[26] X. Zhou, X. Lin, Z. Xiao, T. Low, A. Alù, B. Zhang, and H. Sun, Physical Review B **100**, 115429 (2019).

[27] Y. Wu, L. Sheng, L. Xie, S. Li, P. Nie, Y. Chen, X. Zhou, and X. Ling, Carbon **166**, 396 (2020).

[28] S. Manzeli, D. Ovchinnikov, D. Pasquier, O. V. Yazyev, and A. Kis, Nature Reviews Materials **2**, 17033 (2017).

[29] C. Schneider, M. M. Glazov, T. Korn, S. Höfling, and B. Urbaszek, Nature Communications **9**, 2695 (2018).

[30] C. Ataca, H. Şahin, and S. Ciraci, The Journal of Physical Chemistry C **116**, 8983 (2012).

[31] A. H. Castro Neto, Physical Review Letters **86**, 4382 (2001).

[32] A. V. Kolobov and J. Tominaga, *Two-Dimensional Transition-Metal Dichalcogenides* (Springer International Publishing, 2016).

[33] Y. Li *et al.*, Physical Review B **90**, 205422 (2014).

[34] K. F. Mak, C. Lee, J. Hone, J. Shan, and T. F. Heinz, Physical Review Letters **105**, 136805 (2010).

[35] K. S. Novoselov, D. Jiang, F. Schedin, T. J. Booth, V. V. Khotkevich, S. V. Morozov, and A. K. Geim, Proceedings of the National Academy of Sciences of the United States of America **102**, 10451 (2005).

[36] M. Izdebski, R. Ledzion, and W. Kucharczyk, J. Opt. Soc. Am. B **34**, 2281 (2017).

[37] D. Clarke, *Stellar Polarimetry* (Wiley, 2009).

[38] N. Ghosh and A. Vitkin, Journal of Biomedical Optics **16**, 110801 (2011).

[39] S. Chen, C. Mi, L. Cai, M. Liu, H. Luo, and S. Wen, Applied Physics Letters **110**, 031105 (2017).

[40] P. W. Xin Li, Fei Xing, Xu-Dong Chen, Zhi-Bo Liu, and Jian-Guo Tian, Opt. Lett. **39**, 5574 (2014).

[41] C. Prajapati, D. Ranganathan, and J. Joseph, J. Opt. Soc. Am. A **30**, 741 (2013).

[42] A. Das and M. Pradhan, Laser Physics Letters **17**, 066001 (2020).

[43] G. Jayaswal, G. Mistura, and M. Merano, Opt. Lett. **39**, 2266 (2014).

[44] G. Jayaswal, G. Mistura, and M. Merano, Opt. Lett. **38**, 1232 (2013).

[45] D. H. Goldstein, *Polarized Light* (CRC Press, 2017).

[46] A. Aiello and J. P. Woerdman, Opt. Lett. **33**, 1437 (2008).

[47] C. Prajapati, S. Pidishety, and N. K. Viswanathan, Opt. Lett. **39**, 4388 (2014).

[48] L. Britnell *et al.*, Science **340**, 1311 (2013).

Chapter 10 Photonic spin Hall effect in MoS_2

Here, we give experimental evidence of the photonic spin Hall shift (PSHS) in monolayer MoS_2 for a fundamental Gaussian beam via quantum weak measurement. It is observed that the PSHS is dependent on the angle of incidence, post-selection angles, as well as polarization states along with specific ways of interaction of the light with the MoS_2 surface. Our findings reveal a unique signature linking angular positions at which the spin Hall shifts change sign with the discontinuity in the phase difference further establishing the connection of PSHS to the geometric phases of the light.

Content of this chapter is currently submitted for publication: **A. Das**, S. Mandal and M. Pradhan, "*Photonic signature of spin Hall shift in monolayer MoS_2 via quantum weak measurement*" (**Under Review**)

10 Photonic spin Hall effect in MoS_2

10.1 Introduction

The photonic spin Hall effect (PSHE) of light is a spin-dependent out-of-plane shift of a finite width light beam which is nothing but the optical version of the electronic spin Hall effect with the electronic potential and the electron spin replaced by the refractive index of the medium and the spin of photons (circular polarization components), respectively [1-4]. When a light beam having a finite transverse profile is reflected from or refracted through an interface, the right and left circularly polarized components are found to be separated in the out of plane direction giving rise to this celebrated photonic spin Hall shift [1,5-11] as depicted in Figure 10.1. The origin of this shift is attributed to firstly, the spin-orbit interaction of light which couples the photonic spins to the trajectory of the light beam, and secondly, the conservation of total (both orbital and spin) angular momentum of the light beam [12-16]. PSHE has drawn special attention in several fields such as plasmonics [17], metamaterials [3], semiconductor physics [18], topological systems [19], high energy physics [20], etc. However, this spin Hall shift due to the spin-dependent splitting of the beam in the system is very weak in the sense that it is comparable only to a few sub-wavelengths of the incident light [10]. Hence, the direct application of this physical phenomenon to photonic and optoelectronics devices has several potential limitations although it can provide us useful information about the optical surface under consideration. If we can amplify and subsequently detect the precise amount of this photonic spin Hall shift, it can open up a new path for revealing information on optical surfaces. For this, the well-established technique of *weak value amplification* (WVA) proposed by Aharonov, Albert, and Vaidman is taken into account [21-23]. As discussed in the previous *Chapters*, by selecting a definite post-selected polarization state, which is almost (but not exact) orthogonal to the incident pre-selected polarization state, we can implement this weak value amplification to achieve largely amplified shift with ease (see Figure 10.2(a)) [24,25]. The effective way of applying this weak value amplification technique for any material surface to measure spin Hall shift is discussed later in this *Chapter*.

Photonic spin Hall shift (PSHS) is studied for a fundamental Gaussian mode laser beam employing the quantum weak measurement technique (QWM) [26]. We already know that

several attempts have already been made to analyze photonic spin Hall shifts in 2D materials, especially graphene [27-29]. Here, we have chosen monolayer MoS_2, a renowned member of the 2D family, to work with. As you already know, the atomically thin MoS_2 is a direct bandgap at monolayer thickness [30,31]. Its valley degree of freedom can also be accessed by the optical helicity due to the absence of the inversion symmetry and the large spin-orbit splitting [30,32].

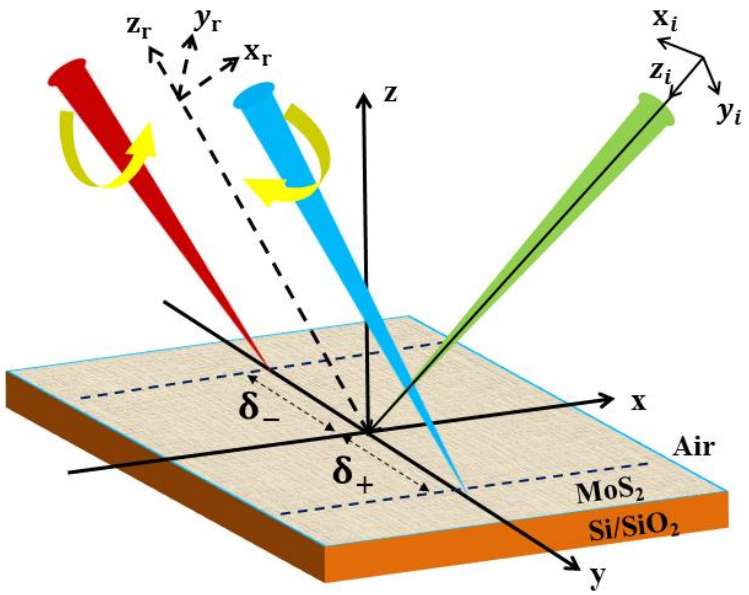

Figure 10.1. Schematic representation of the spin Hall shift in monolayer MoS_2 -coated surface. Linearly polarized beam (incident from the right side) undergoes spin-dependent splitting after reflection (external).

Motivated by these intriguing properties, we made an attempt to investigate the photonic spin Hall shift in MoS_2 in reflection mode. Two different configurations are thoroughly investigated (a) MoS_2/Si-SiO_2, & (b) Si-SiO_2/ MoS_2, where light is externally reflected from the MoS_2 side and the Si/SiO_2 substrate side, respectively, as demonstrated in Figure 10.2. We have elaborated on the dissimilarities in the respective results and explained their origin. The angles of incidence at which the zero-crossing of the spin Hall shifts are observed have a close analogy with the phase difference of the reflection coefficients. This helps in establishing a close connection of the spin Hall shifts with the geometric phases that arise due to reflections at physical surfaces [33]. Additionally, we have observed the

dependence of the spin Hall shifts on the angle of deviation (post-selection angle) from the orthogonality condition set for the quantum weak measurement. This helps one to select a particular post-selection angle to maximize the spin Hall shifts via weak value amplification. To validate the experimental findings, we have also presented an effective theoretical model for determining photonic spin Hall shifts primarily based upon Fresnel's slab model. Since monolayer MoS_2 is a strongly absorbing medium in the visible region of the spectrum [34], we have incorporated the loss factors in this model.

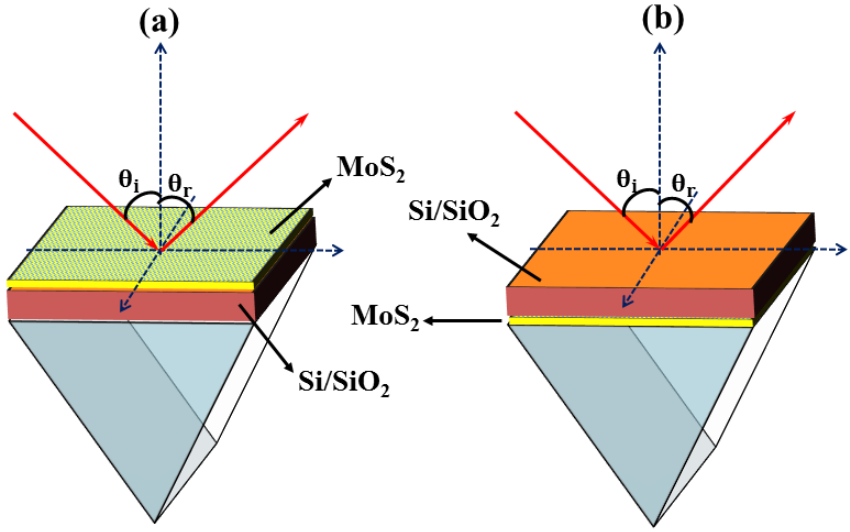

Figure 10.2. Two different configurations are used for the spin Hall shift measurement, **(a)** reflection from MoS_2 surface (configuration 1), and **(b)** reflection from Si/SiO_2 surface (configuration 2).

10.2 Theoretical calculation

We first consider an arbitrary polarized fundamental Gaussian beam. In angular spectrum representation, the corresponding electric field in the position space can be expressed as:

$$E_i = \begin{pmatrix} E_i^P \\ E_i^S \end{pmatrix} = \begin{pmatrix} f_P \\ f_S \end{pmatrix} \alpha \, exp\left[-\beta\left(x_i^2 + y_i^2\right)\right] \tag{10.1}$$

where, S and P represent the vertical (V) and horizontal (H) polarization components, respectively.

$\hat{f} = \dfrac{\left(f_P \hat{x}_i + f_S \hat{y}_i\right)}{\left(\left|f_P\right|^2 + \left|f_S\right|^2\right)}$ represents the polarization vector to characterize the polarization profile of the beam.

If we perform Fourier transform, the above representation takes the following form in the *k*-space:

$$\tilde{E}_i = \begin{pmatrix} \tilde{E}_i^P \\ \tilde{E}_i^S \end{pmatrix} = \begin{pmatrix} f_P \\ f_S \end{pmatrix} exp\left[-\frac{z_R}{2k_i}\left(k_{xi}^2 + k_{yi}^2\right) \right] \tag{10.2}$$

Application of proper boundary conditions yields the angular spectrum of the reflected field, given by:

$$\tilde{E}_r = \begin{pmatrix} \tilde{E}_r^P \\ \tilde{E}_r^S \end{pmatrix} = \begin{pmatrix} r_P + \dfrac{\left(r_P + r_S\right) k_{yi} \cot\theta}{k_i} \\ r_S - \dfrac{\left(r_P + r_S\right) k_{yi} \cot\theta}{k_i} \end{pmatrix} exp\left[-\frac{z_R}{2k_i}\left(k_{xi}^2 + k_{yi}^2\right) \right] \tag{10.3}$$

where, r_p & r_s denote the Fresnel's reflection coefficients for P and S-polarization components, respectively, and θ is the incident angle. The Fresnel reflection coefficients can be expanded in a Taylor series:

$$r_\lambda = r_{\lambda\theta} + \frac{k_{xi}}{k_i} \frac{\partial r_{\lambda\theta}}{\partial \theta} \tag{10.4}$$

The reflected field in the *x*-space can be achieved by inverse Fourier transform:

$$E_r = \int \tilde{E}_r(k_{xr}, k_{yr}) exp\left\{ i\left(x_r k_{xr} + y_r k_{yr} + z_r k_{zr}\right) \right\} dk_{xr} dk_{yr} \tag{10.5}$$

We can also incorporate the spin basis set in our formalism,

$$E_{r\sigma} = \frac{1}{\sqrt{2}}\left(E_r^P + E_r^V\right). \tag{10.6}$$

Finally, the spin Hall shift can be obtained by calculating the centroid position of the beam intensity:

$$\left\langle \delta_{y\sigma}^{P,S} \right\rangle = \frac{\iint y_r \left| E_{r\sigma}^{P,S} \right|^2 dx_r dy_r}{\iint \left| E_{r\sigma}^{P,S} \right|^2 dx_r dy_r} \tag{10.7}$$

Using the spin basis, the spin Hall shifts can finally be expressed for incident P & S polarized pre-selected state:

$$\left\langle \delta_{y\sigma}^{P} \right\rangle = -\frac{2\sigma \cot(\theta) R_P \left[R_P + R_S \cos(\phi_P - \phi_S) \right] z_R}{\cot^2\theta \left[2R_P R_S \cos(\phi_P - \phi_S) + R_P^2 + R_S^2 \right] + 2R_P^2 k_r z_R + \left(\rho_P^2 + \varphi_P^2 \right)} \tag{10.8}$$

$$\left\langle \delta_{y\sigma}^{S} \right\rangle = -\frac{2\sigma \cot(\theta) R_S \left[R_S + R_P \cos(\phi_P - \phi_S) \right] z_R}{\cot^2\theta \left[2R_P R_S \cos(\phi_P - \phi_S) + R_P^2 + R_S^2 \right] + 2R_S^2 k_r z_R + \left(\rho_S^2 + \varphi_S^2 \right)} \tag{10.9}$$

where, R and ϕ represent the magnitude and phase of the reflection coefficients, respectively. We have defined following parameters (where, $\lambda = p, s$):

$$\rho_\lambda = Re\left(\frac{\partial r_\lambda}{\partial \theta} \right) \tag{10.10a}$$

$$\varphi_\lambda = Im\left(\frac{\partial r_\lambda}{\partial \theta} \right) \tag{10.10b}$$

In the present study, we have taken a multi-layered configuration. That is why we have applied the slab model to calculate the effective refractive index of the structure under consideration. The expressions of reflection coefficients in the slab model [7,35] are already familiar.

$$r_P(\theta, h) = R_P \exp(i\phi_P) = \frac{r_P^{12} + r_P^{23} \exp(2ik_{2z}h)}{1 + r_P^{12} r_P^{23} \exp(2ik_{2z}h)} \tag{10.11a}$$

$$r_S(\theta, h) = R_S \exp(i\phi_S) = \frac{r_S^{12} + r_S^{23} \exp(2ik_{2z}h)}{1 + r_S^{12} r_S^{23} \exp(2ik_{2z}h)} \tag{10.11b}$$

where we have taken,

$$r_P^{ij} = \frac{\varepsilon_j k_{iz} - \varepsilon_i k_{jz}}{\varepsilon_j k_{iz} + \varepsilon_i k_{jz}} \tag{10.12a}$$

$$r_S^{ij} = \frac{k_{iz} - k_{jz}}{k_{iz} + k_{jz}} \tag{10.12b}$$

$$k_{iz} = \frac{2\pi}{\lambda} \sqrt{\varepsilon_i - \varepsilon_1 \sin^2\theta} \tag{10.12c}$$

superscripts/subscripts 'i' and 'j' refer to different layers of the multi-layered structure under consideration [36].

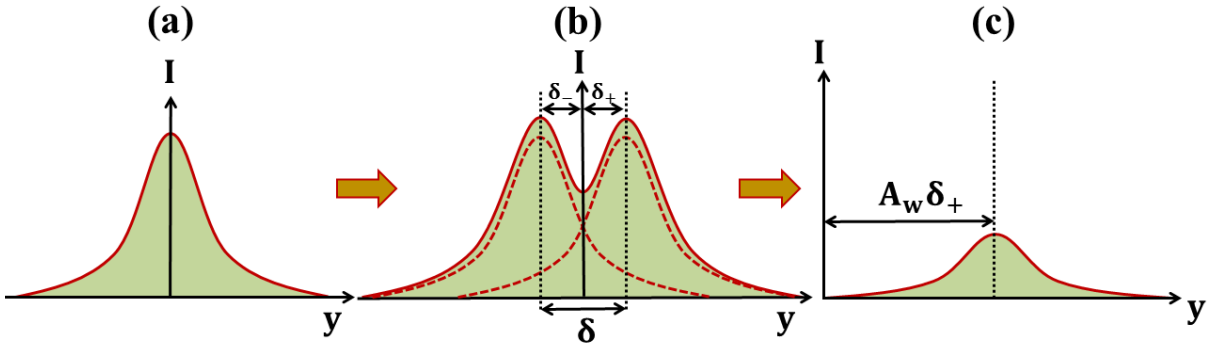

Figure 10.3. Weak value amplification (WVA) of the spin Hall shift by application of the proper post-selection scheme, **(a)** Intensity variation of the incident beam, **(b)** real value of the spin Hall shift, **(c)** application of post-selection to amplify the shift.

As we have already indicated, the value of this shift is too small to detect precisely. We have, therefore, amplified the shift by implementing the quantum weak measurement [26], in which, we have performed an additional post-selection of the reflected light in a state which is almost orthogonal to the pre-selected input state (either S or P-polarized) but deviated by a small angle Δ from it. If we subsequently apply the Jones vectors for the output polarizer (GLP2) and calculate the final post-selected output, we would find that after proper post-selection the resultant shift has been amplified by an amount A_w, many times greater than the original shift. The phenomenon is well-explained pictorially in Figure 10.3. The final weakly amplified output shift will be:

$$\left\langle y_{ps}^{P,S} \right\rangle = \frac{\iint y_r \left| E_{ps}^{P,S} \right|^2 dx_r dy_r}{\iint \left| E_{ps}^{P,S} \right|^2 dx_r dy_r} \tag{10.13}$$

After some rigorous mathematical steps, the spin Hall shifts for different input polarization states can be expressed as:

$$\left\langle y_{p2}^{P} \right\rangle = A_P \delta_P^y = \frac{2R_P \cot\theta \cot\Delta \left[R_P z_r + R_S z_r \cos\left(\phi_P - \phi_S\right) + R_S z_R \sin\left(\phi_P - \phi_S\right) \right]}{\cot^2\theta \cot^2\Delta \left[2R_P R_S \cos\left(\phi_P - \phi_S\right) + R_P^2 + R_S^2 \right] + 2R_P^2 k_r z_R + \left(\rho_P^2 + \varphi_P^2\right)} \tag{10.14}$$

$$\left\langle y_{p2}^{S} \right\rangle = A_S \delta_S^y = \frac{2R_S \cot\theta \cot\Delta\left[R_S z_r + R_P z_r \cos\left(\phi_P - \phi_S\right) - R_P z_R \sin\left(\phi_P - \phi_S\right)\right]}{\cot^2\theta \cot^2\Delta\left[2R_P R_S \cos\left(\phi_P - \phi_S\right) + R_P^2 + R_S^2 \right] + 2R_S^2 k_r z_R + \left(\rho_S^2 + \varphi_S^2\right)} \tag{10.15}$$

10.3 Experimental Setup

To perform the experiment (Figure 10.4), a He-Ne laser is used as the source. We fix the incident light's polarization using quarter-wave plate, half-wave plate, and linear polarizer. The light is externally reflected (as shown in Figure 10.2) from the MoS_2 interface. The motorized rotation system supports in evading any mechanical vibration. A high-quality monolayer MoS_2 is used for this experiment. Subsequently, the reflected light beam is post-selected by another linear polarizer. The final output state is supervised by a high-precision detector.

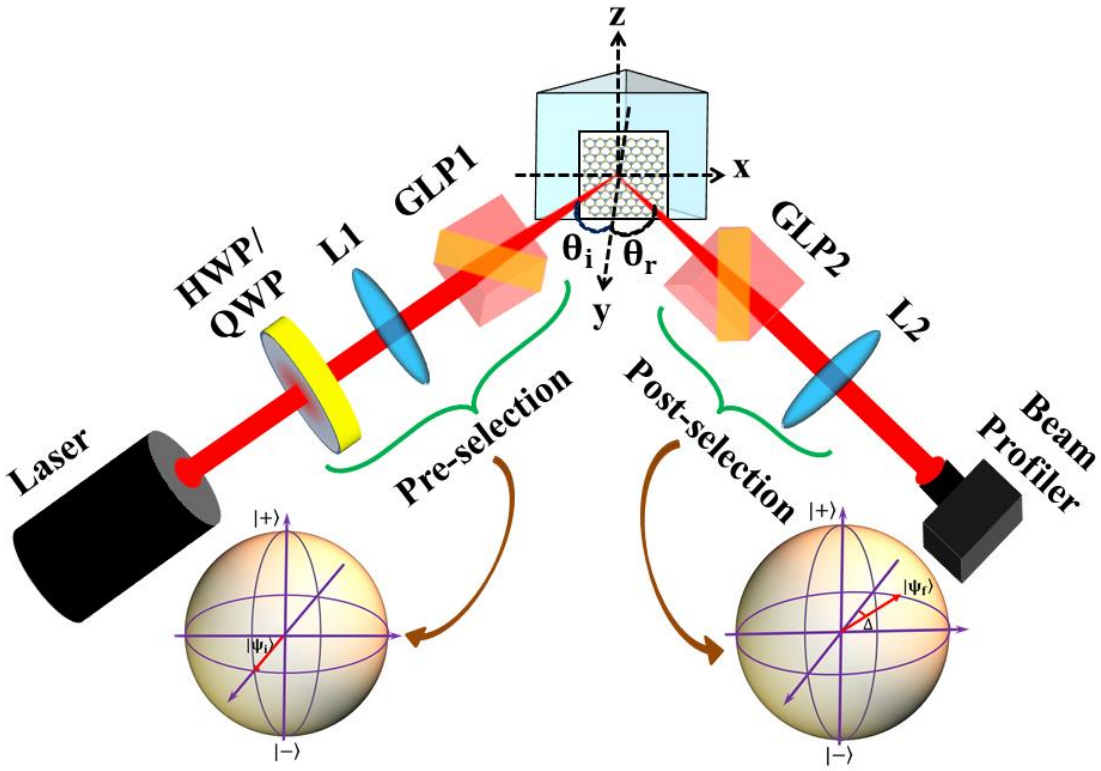

Figure 10.4. Photonic spin Hall shift measuring experimental setup, were **L1**, **L2**: lenses; **GLP**: linear polarizer; **HWP**: half-wave plate; **QWP**: quarter-wave plate. The polarization states at the pre-selection and post-selection states are also shown.

To perform the experiment, we first accomplish the pre-selection of the incident light to a specific (a) P-polarization or (b) S-polarization state by controlling the QWP/HWP and

GLP1 combination. After the external reflection (as shown in Figure 10.4) from the physical system, we accomplish the post-selection with another polarizer, GLP2. Propagation distance is set at 30 cm to get a sufficient beam enhancement $\left(\frac{z}{z_0}\right)$. The second polarizer is fixed at an exact orthogonal position with respect to the first polarizer for the anticipated orthogonality condition of quantum weak measurement. At this condition, the shift blows up and the resultant reflected light ruptures into two distinct Gaussian peaks separated by $\sqrt{2}w$ (along vertical direction) [37] (as shown in Figure 10.3). We rotate the analyzer GLP2 at angles Δ from this exact orthogonal position and term this as 'angle of deviation' or 'post-selection angle' [38,39]. GLP2 is rotated both clockwise (+) and anti-clockwise (-) by this angle Δ. The corresponding changes in the beam pattern are represented in Figure 10.5 below.

To compute the actual spin Hall shift from the output light's displacement, we take the beam centroid at $\Delta=0^0$ as the origin, and the final shift can be calculated by noting the beam centroid positions at $+\Delta$ or $-\Delta$, respectively. During the measurement, we have selected different values of the angle of deviation, Δ (0.5^0, 0.8^0, 1.1^0, 1.4^0, 1.7^0, and 2.0^0) to find out the proper value of Δ at which maximum spin Hall shift is observed.

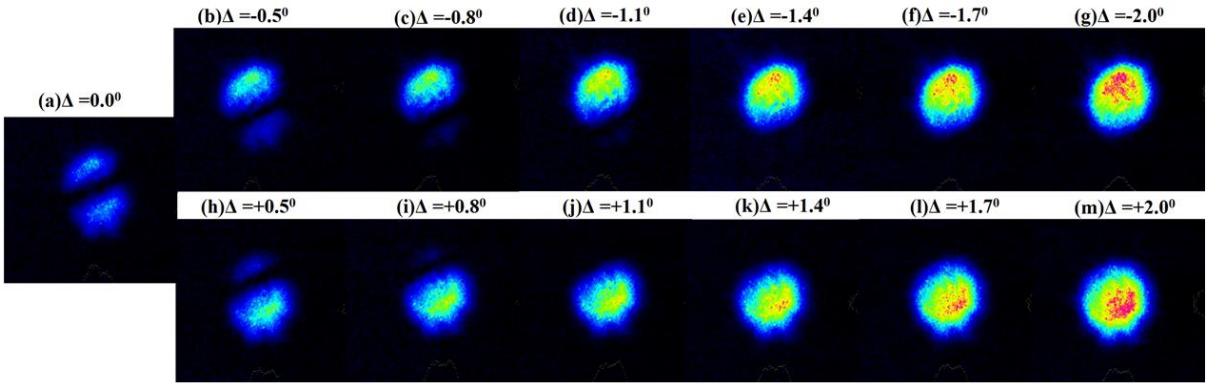

Figure 10.5. Variation of beam centroid intensity profile with the change in post-selection angle (Δ), upper panel: clockwise rotation of Glan-Thompson polarizer (GLP2), lower panel: anticlockwise rotation of GLP2.

10.4 Results & Discussions

Before starting the QWM, we first verified the monolayer quality of the MoS_2 sample. Here, the monolayer MoS_2 (2dsemiconductors, USA) is deposited upon the Si/SiO_2 substrate by the chemical vapour deposition (CVD) technique. We have performed Raman & Photoluminescence (PL) spectroscopy study (Figure 10.6). The Raman peaks designated as E^1_{2g} and A_{1g} are separated by 18 cm^{-1}. Here, the ratio $A_{1g}/E^1_{2g} = 1.06 \approx 1$, which confirms the good monolayer nature of the deposited MoS_2 [40,41]. In addition, the PL study exhibits a sharp peak at 1.88 eV which also indicates a clear signature of the monolayer MoS_2 [40].

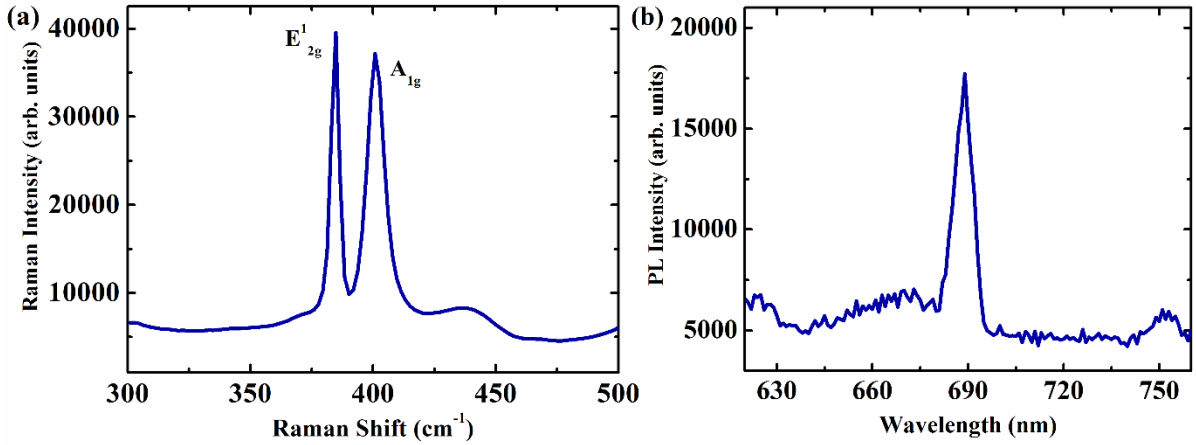

Figure 10.6. (a) Raman, and (b) Photoluminescence spectroscopy of monolayer MoS_2

As mentioned before, we have used two separate optical arrangements for the measurement of the spin Hall shift (SHS) in monolayer MoS_2, Air-MoS_2-Si/SiO_2 (**configuration 1**), and Air-Si/SiO_2-MoS_2 (**configuration 2**) (as described in Figure 10.2). We have selected different angles of deviation ($\Delta = 0.5^0$, 0.8^0, 1.1^0, 1.4^0, 1.7^0, and 2^0) to find the specific post-selection angle to get the maximum amplified spin shift. In Figure 10.7, we have shown the spin shift for the incident P polarized light (Figure 10.7(a)) for configuration 1, Air-MoS_2-Si/SiO_2 system.

If we select a particular post-selection angle and study the dependence on the angle of incidence, we witnessed that the spin Hall shift at first rises with the increasing angle of incidence. After reaching a maximum, SHS reduces and changes its sign by crossing over to zero value to smaller positive shifts at larger angles of incidence. We term this special angle at

which the spin Hall shift changes sign as 'zero-crossing angle' (θ_0). The significance of this point has been discussed later (TABLE 10.1) in this section. We have also compared the experimental data for the specific post-selection angle $\Delta=1.4^0$ with the theoretical model as shown in Figure 10.7(b). The theoretical model describes well the experimental results. But, at larger incident angles, experimentally observed spin Hall shifts deviate, and decrease to zero value. This is firstly due to the increased loss of incident light as the light comes almost parallel to the surface at larges incident angles. Secondly, the beam spot of interaction at the surface of the sample deviates in shape at larger angles causing a larger coverage of the surface during the interaction of light with the matter which contributes to increased scattering of the light beam.

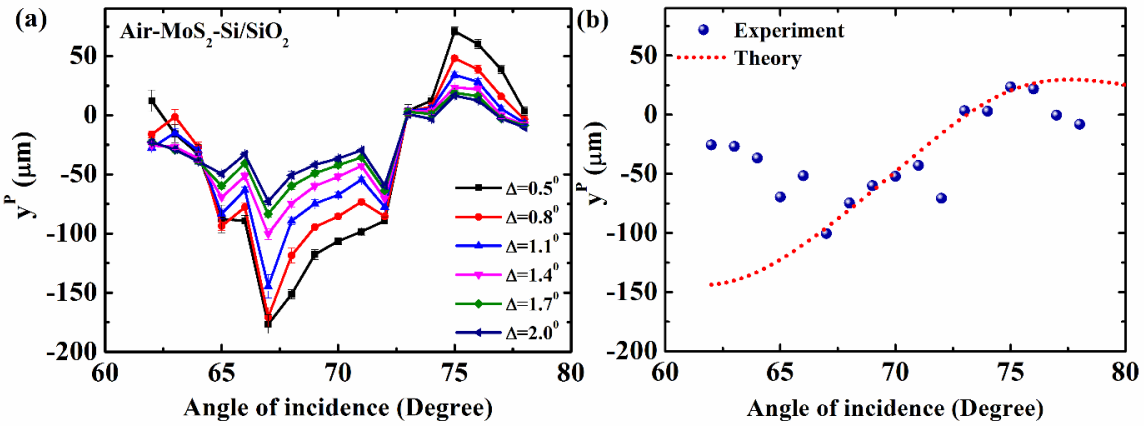

Figure 10.7 Spin Hall shift for pre-selected P polarized light incident upon MoS_2-Si/SiO_2 configuration: **(a)** experimental data for different post-selection angles (Δ), and **(b)** comparison with the theoretical model for post-selection angle, $\Delta=1.4^0$.

Similarly, when a P polarized light interacts with configuration 2 (Figure 10.8(a)), Air-Si/SiO_2-MoS_2 system, the spin Hall shift behaves differently in comparison to configuration 1. The nature of the spin shift gets reversed, i.e., here the shift starts from a positive value, which gradually decreases, crosses over to zero, and goes to a negative value. The transition from the positive to negative values occurs at a different angle (change in zero-crossing angle, θ_0) compared to the previous case. The theoretical model also agrees well with the experimental data (Figure 10.8(b)).

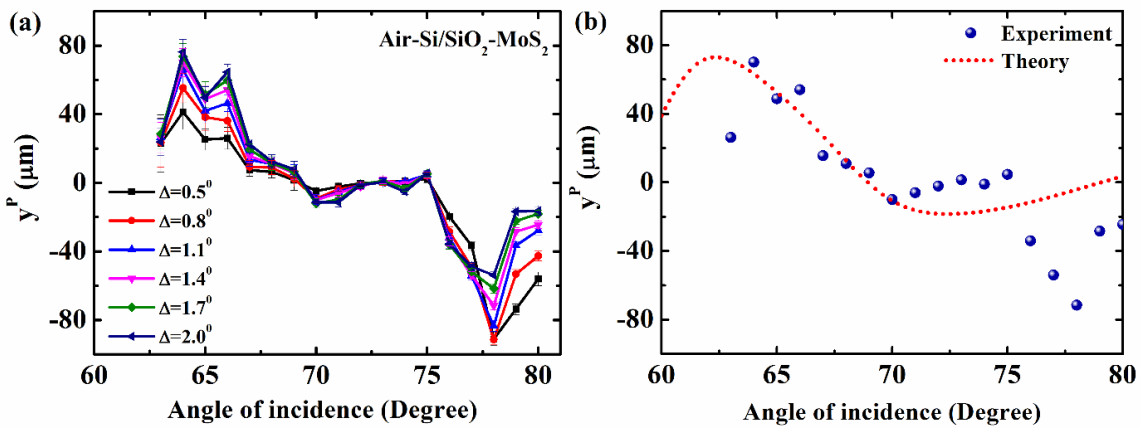

Figure 10.8 Spin Hall shift for pre-selected P polarized light incident upon Si/SiO_2-MoS_2 configuration: **(a)** experimental data for different post-selection angles (Δ), and **(b)** comparison with the theoretical model for post-selection angle, $\Delta=1.4^0$.

Next, we have altered the state of the incident light before interaction with the interface and preselect it in S polarized state by using QWP/HWP and GLP1 combination. In the case of configuration 1 (MoS_2-Si/SiO_2 system), the spin shift is again negative (Figure 10.9(a)) at lower angles similar to the case of the pre-selected P polarized state for configuration 1. The shift continuously decreases to zero and subsequently, crosses over to a small positive shift (Figure 10.9(a)). The transition from negative to positive shift occurs at the same angle of incidence that matches with the value of θ_0 for the P polarized light in configuration 1.

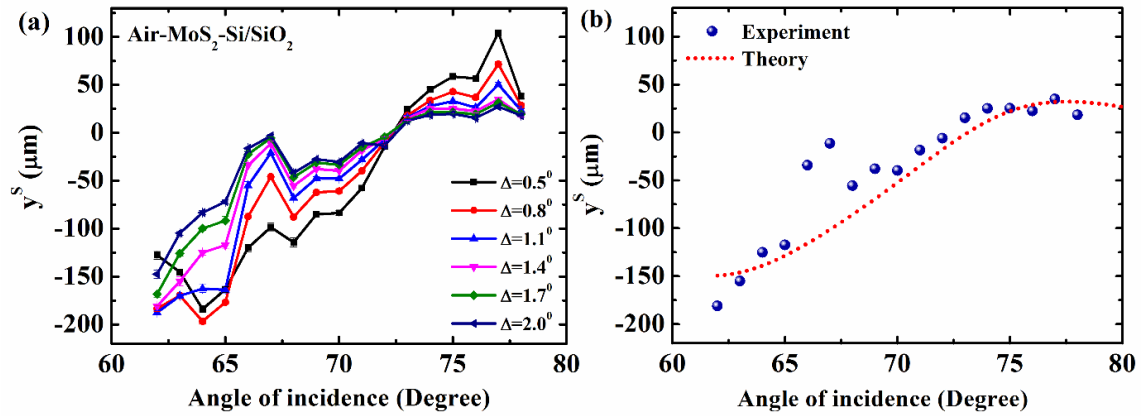

Figure 10.9 Spin Hall shift for pre-selected S polarized light incident upon MoS_2-Si/SiO_2 configuration: **(a)** experimental data for different post-selection angles (Δ), and **(b)** comparison with the theoretical model for post-selection angle, $\Delta=1.4^0$.

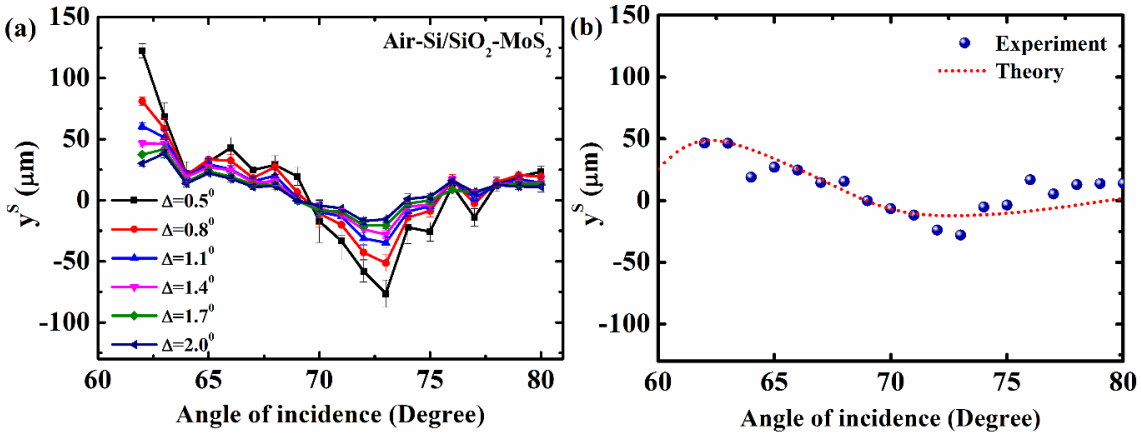

Figure 10.10 Spin Hall shift for pre-selected S polarized light incident upon Si/SiO_2-MoS_2 configuration: **(a)** experimental data for different post-selection angles (Δ), and **(b)** comparison with the theoretical model for post-selection angle, $\Delta=1.4^0$.

Similar to before, we now study the action of the incident pre-selected S-polarized beam on the second configuration Si/SiO_2-MoS_2 (Figure 10.10(a)). Again, the shift makes a transition from the positive to the negative shift at that particular value of θ_0 as observed in the case of P-polarized light in configuration 2. The theoretical model also supports the experimental data (Figure 10.10(b)).

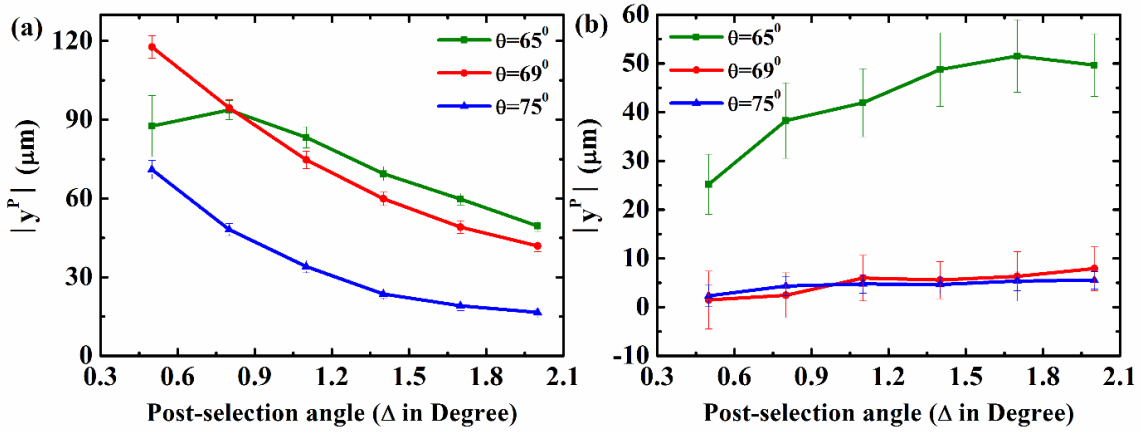

Figure 10.11 The magnitude of the Spin Hall shift at different post-selection angles (Δ) for three different incident angles ($\theta=65^0$, 69^0, 75^0) of pre-selected P polarized beam: **(a)** MoS_2-Si/SiO_2 configuration, and **(b)** Si/SiO_2-MoS_2 configuration.

In all the above cases, it is evident that the spin Hall shift is immensely dependent on the choice of the post-selection angle (Δ). To look into this dependence, we have presented the spin Hall shift against the post-selection angles (Figure 10.11).

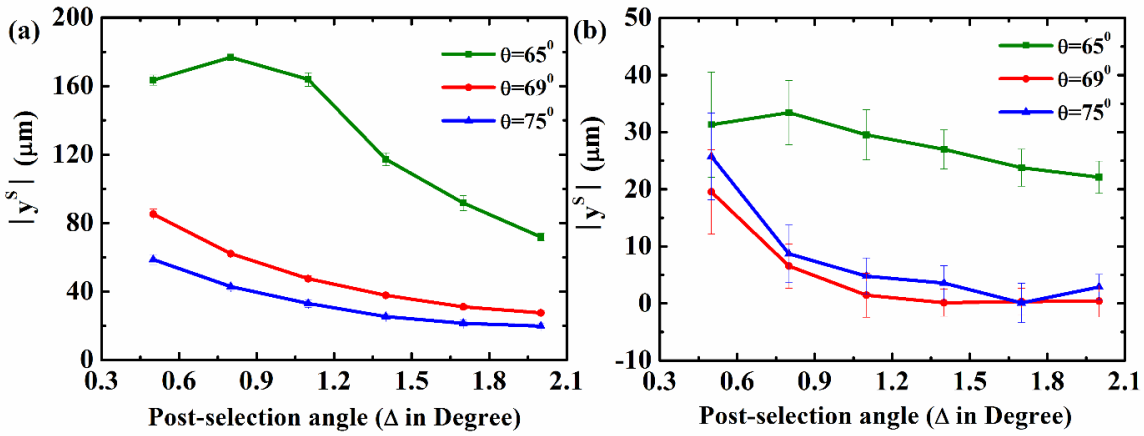

Figure 10.12 The magnitude of the Spin Hall shift at different post-selection angles (Δ) for three different incident angles ($\theta=65^0$, 69^0, 75^0) of pre-selected S polarized beam: **(a)** MoS_2-Si/SiO_2 configuration, and **(b)** Si/SiO_2-MoS_2 configuration.

For that, we have firstly fixed the angles of incidence at 65^0, 69^0, and 75^0 and plotted the absolute magnitude of the spin Hall shift for P (Figure 10.11) and S (Figure 10.12) polarized pre-selected beam, respectively. The above Figures 10.11(a) & 11(b) represents configuration 1, and configuration 2, respectively. In both of the cases, the spin Hall shift is larger for smaller angle of incidence and the shift also decreases with increasing post-selection angles, but, the slope of the curve is larger for configuration 1 pointing towards a greater dependence of the spin Hall shift on the post-selection angle.

In addition, we have made a comparison of the spin Hall shift in MoS_2 to that of the glass interface. The spin Hall shift for standard glass-air interface for P and S polarized pre-selected state is presented in Figures 10.13(a) & 10.14(a), respectively. For P as well as S polarized light, the spin Hall shift decreases monotonically towards zero, with an increasing angle of incidence. Moreover, the shift is larger for a smaller selection of post-selection angles.

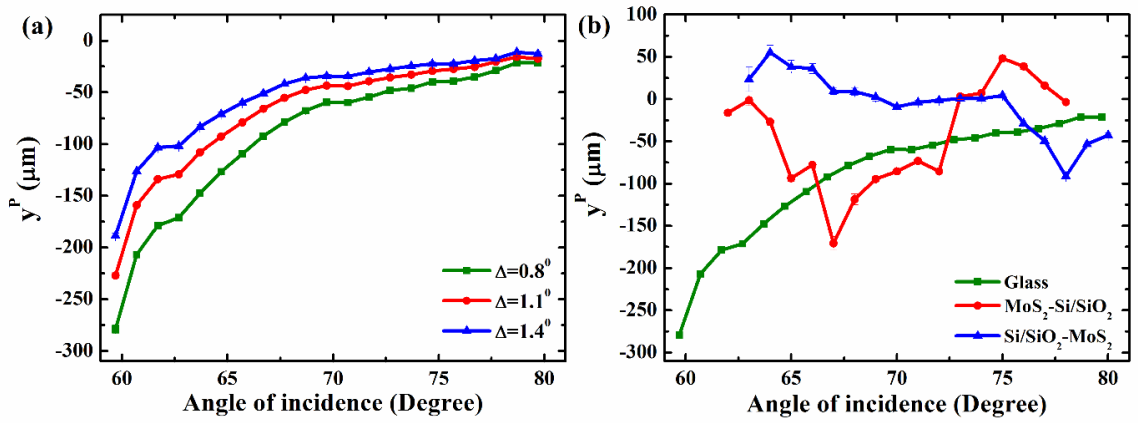

Figure 10.13 Spin Hall shift for pre-selected P polarized light: **(a)** in the air-glass system, and **(b)** comparison (for $\Delta=0.8^0$) for glass, MoS_2-Si/SiO_2, and Si/SiO_2-MoS_2.

The comparison of the spin shift for configurations 1 and 2 with the glass interface for P and S-polarization is shown in Figures 10.13(b) & 10.14(b), respectively. The spin Hall shift is entirely negative for the glass interface where no change in sign of the shift is observed. But, as already discussed previously, in configurations 1 and 2, there exists a zero crossing of the spin Hall shifts. The spin Hall shift is comparable in magnitude for the P polarized light, but not in the other case of the S polarization state.

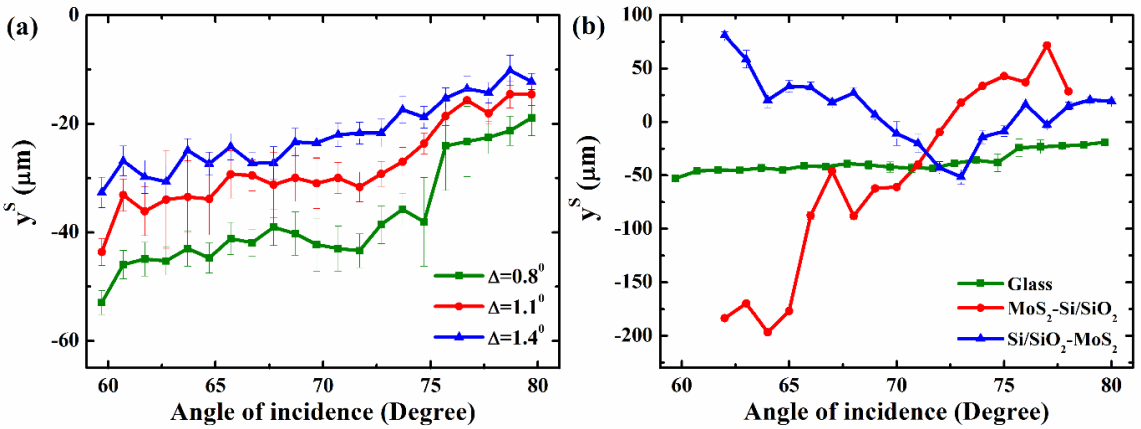

Figure 10.14. Spin Hall shift for pre-selected S polarized light: **(a)** in the air-glass system, and **(b)** comparison (for $\Delta=0.8^0$) for glass, MoS_2-Si/SiO_2, and Si/SiO_2-MoS_2.

Next, to study the zero crossing position and the inherent reason in detail, we present a table mentioning all the details of the transition points.

TABLE 10. 1

Sample configuration	**Polarization States**	**Post-selection angle (Δ)**	**Zero-crossing angle (θ_0) (Experimental)**	**Phase jump ($\delta\phi_0$) (Theoretical)**
MoS_2-Si/SiO_2	P	0.5^0	72.96^0	73.2^0
		0.8^0	72.97^0	
		1.1^0	72.95^0	
		1.4^0	72.95^0	
		1.7^0	72.96^0	
		2.0^0	72.99^0	
MoS_2-Si/SiO_2	S	0.5^0	72.37^0	73.2^0
		0.8^0	72.34^0	
		1.1^0	72.31^0	
		1.4^0	72.23^0	
		1.7^0	72.24^0	
		2.0^0	72.51^0	
Si/SiO_2-MoS_2	P	0.5^0	69.24^0	69.15^0
		0.8^0	69.21^0	
		1.1^0	69.38^0	
		1.4^0	69.36^0	
		1.7^0	69.34^0	
		2.0^0	69.41^0	
Si/SiO_2-MoS_2	S	0.5^0	69.53^0	69.15^0
		0.8^0	69.37^0	
		1.1^0	69.13^0	
		1.4^0	68.99^0	
		1.7^0	68.97^0	
		2.0^0	68.96^0	

From Table 10.1, we can observe the experimental angles of incidence for different configurations at which the zero-crossing occurs (θ_0). In the fifth column, we have presented the theoretically predicted angles of incidence at which the phase difference ($\phi_p - \phi_s$) of the reflection coefficients undergoes a discontinuity within our working region (60^0-80^0). The data shows a close agreement between the above two parameters as mentioned in the fourth and fifth columns of Table 10.1. It is already established that in the transmission mode of the photonic spin Hall effect the discontinuity in the phase difference is associated with the occurrence of geometric phases [9]. In our study with ML-MoS_2 in reflection mode, we have found a similar sharp jump of the phase difference ($\phi_p - \phi_s$) at specific angles for the two configurations (Table 10.1). At these specific angles, the special signature of zero-crossing of the photonic spin Hall shift is observed. This gives clear evidence of the presence of finite geometric phase also in the reflection mode observation of PSHS. Further investigations in TMDCs are necessary to find out the influence of inherent geometric phases on PSHS in detail.

10.5 Outlook & Summary

Here, we have accomplished a detailed investigation of the photonic spin Hall shift in monolayer MoS_2 deposited upon Si/SiO_2 substrate. We have observed the dependence of spin Hall shift on the surface of interaction, polarization states, and angle of incidence of the light beam. To maximize the beam shift, it is established in our study that a particular post-selected deviation angle and specific angle of incidence on the optical surface are of fundamental importance. To account for the experimental findings, we have also given a general theoretical model that supports the experimental results. In addition, we have found a coincidence of the angle of incidence at which the spin Hall shift changes its sign (zero-crossing) with the angle at which the phase difference suffers a discontinuous jump which points towards finite geometric phase existence. This observation opens up a new path to investigate the influence of the geometric phases in governing the nature of the photonic spin Hall shifts.

References

[1] S. Fu, C. Guo, G. Liu, Y. Li, H. Yin, Z. Li, and Z. Chen, Physical Review Letters **123**, 243904 (2019).

[2] O. Hosten and P. Kwiat, Science **319**, 787 (2008).

[3] X. Yin, Z. Ye, J. Rho, Y. Wang, and X. Zhang, Science **339**, 1405 (2013).

[4] H. Luo, X. Zhou, W. Shu, S. Wen, and D. Fan, Physical Review A **84**, 043806 (2011).

[5] Y. Qin, Y. Li, H. He, and Q. Gong, Opt. Lett. **34**, 2551 (2009).

[6] M. Onoda, S. Murakami, and N. Nagaosa, Physical Review Letters **93**, 083901 (2004).

[7] S. Chen, X. Zhou, X. Ling, W. Shu, H. Luo, and S. Wen, Applied Physics Letters **118**, 111104 (2021).

[8] K. Y. Bliokh, A. Niv, V. Kleiner, and E. Hasman, Nature Photonics **2**, 748 (2008).

[9] W. Zhu, H. Zheng, Y. Zhong, J. Yu, and Z. Chen, Physical Review Letters **126**, 083901 (2021).

[10] S. Chen, X. Ling, W. Shu, H. Luo, and S. Wen, Physical Review Applied **13**, 014057 (2020).

[11] X. Zhou, X. Lin, Z. Xiao, T. Low, A. Alù, B. Zhang, and H. Sun, Physical Review B **100**, 115429 (2019).

[12] K. Y. Bliokh and Y. P. Bliokh, Physical Review Letters **96**, 073903 (2006).

[13] K. Y. Bliokh, C. T. Samlan, C. Prajapati, G. Puentes, N. K. Viswanathan, and F. Nori, Optica **3**, 1039 (2016).

[14] V. G. Fedoseyev, Journal of Physics A: Mathematical and General **21**, 2045 (1988).

[15] K. Y. Bliokh, E. A. Ostrovskaya, M. A. Alonso, O. G. Rodríguez-Herrera, D. Lara, and C. Dainty, Opt. Express **19**, 26132 (2011).

[16] M. Merano, N. Hermosa, J. P. Woerdman, and A. Aiello, Physical Review A **82**, 023817 (2010).

[17] Y. Gorodetski, A. Niv, V. Kleiner, and E. Hasman, Physical Review Letters **101**, 043903 (2008).

[18] J.-M. Ménard, A. E. Mattacchione, H. M. van Driel, C. Hautmann, and M. Betz, Physical Review B **82**, 045303 (2010).

[19] W. J. M. Kort-Kamp, Physical Review Letters **119**, 147401 (2017).

[20] C. A. Dartora, G. G. Cabrera, K. Z. Nobrega, V. F. Montagner, M. H. K. Matielli, F. K. R. de Campos, and H. T. S. Filho, Physical Review A **83**, 012110 (2011).

[21] Y. Aharonov, D. Z. Albert, and L. Vaidman, Physical Review Letters **60**, 1351 (1988).

[22] I. M. Duck, P. M. Stevenson, and E. C. G. Sudarshan, Physical Review D **40**, 2112 (1989).

[23] N. W. M. Ritchie, J. G. Story, and R. G. Hulet, Physical Review Letters **66**, 1107 (1991).

[24] W. Wu, S. Chen, W. Xu, Z. Liu, R. Lou, L. Shen, H. Luo, S. Wen, and X. Yin, Photon. Res. **8**, B47 (2020).

[25] A. Das and M. Pradhan, J. Opt. Soc. Am. B **38**, 387 (2021).

[26] A. Das and M. Pradhan, Laser Physics Letters **17**, 066001 (2020).

[27] Y. Wu, L. Sheng, L. Xie, S. Li, P. Nie, Y. Chen, X. Zhou, and X. Ling, Carbon **166**, 396 (2020).

[28] X. Zhou, X. Ling, H. Luo, and S. Wen, Applied Physics Letters **101**, 251602 (2012).

[29] W. Zhang, W. Wu, S. Chen, J. Zhang, X. Ling, W. Shu, H. Luo, and S. Wen, Photon. Res. **6**, 511 (2018).

[30] K. F. Mak, C. Lee, J. Hone, J. Shan, and T. F. Heinz, Physical Review Letters **105**, 136805 (2010).

[31] S. Manzeli, D. Ovchinnikov, D. Pasquier, O. V. Yazyev, and A. Kis, Nature Reviews Materials **2**, 17033 (2017).

[32] D. Xiao, G.-B. Liu, W. Feng, X. Xu, and W. Yao, Physical Review Letters **108**, 196802 (2012).

[33] E. Cohen, H. Larocque, F. Bouchard, F. Nejadsattari, Y. Gefen, and E. Karimi, Nature Reviews Physics **1**, 437 (2019).

[34] L. Britnell *et al.*, Science **340**, 1311 (2013).

[35] M. Merano, Physical Review A **93**, 013832 (2016).

[36] Z. Qin, Q. Liu, C. Yue, Y. Lang, and X. Zhou, Review of Scientific Instruments **91**, 123111 (2020).

[37] W. Long *et al.*, Photon. Res. **7**, 1273 (2019).

[38] Z. Qin, Q. Liu, C. Yue, Y. lang, and X. Zhou, Journal of Physics D: Applied Physics **52**, 495106 (2019).

[39] L. Xie *et al.*, Opt. Express **26**, 22934 (2018).

[40] T. Han, H. Liu, S. Wang, S. Chen, W. Li, X. Yang, M. Cai, and K. Yang, Nanomaterials (Basel) **9**, 740 (2019).

[41] J. Wang, L. Chen, W. Lu, M. Zeng, L. Tan, F. Ren, C. Jiang, and L. Fu, RSC Advances **5**, 4364 (2015).

Chapter 11 Conclusion & Future Prospects

Here, we summarize the principal conclusions from this thesis. Depending on the present work, the scope of future development is also discussed.

11 Conclusion & Future Prospects

11.1 Concluding Remarks

In this thesis, our objective is to establish the presence of finite optical beam shifts in 2D materials establishing the theoretical formalism along with different experimental measurement technique and signifying the non-trivial nature of the optical beam shifts in such materials that makes them a potential candidate for future application in the optoelectronics and device industry.

We start this thesis with an elaborate discussion on the topic of optical beam shift and 2D materials in *Chapter* 1. In this *Chapter*, we have thoroughly described what are optical beam shifts, their nature and types, why are they important, how are they generated in the interaction of light with matter and how can they be measured. In the later sections of this chapter, we have described the general structure, electronic and optical behaviour, and the specific features of the well-known 2D materials with their possible application areas.

In *Chapters* 2 and 3 we have developed a theoretical model for the determination of the optical beam shifts following the stationary phase approximation method coupled with the transfer matrix method. This model is general and may be useful for the optical beam shift calculation in other layered materials. Analysis of the results provides us with several unusual features associated with the TMDCs (WS_2, WSe_2, MoS_2, and $MoSe_2$). Firstly, a giant shift is observed in the neighbourhood of the critical angle. This special signature is found to be a universal feature for the 2D materials that can help differentiating these materials over others. On top of that, we have found finite GH and IF shifts even outside the total internal reflection regime which is conventionally unusual. Generally, GH shift appears in case of total internal reflection only, but 2D materials again show here their non-trivial nature. The nature of both spatial and angular GH and IF shifts are explained over a large range of angles of incidence. The effect of wavelength and polarization states of the incident light beam on the GH and IF shifts in TMDCs are also evident from this *Chapter*. The observations are important as it provides us the freedom to select a particular wavelength to get the desired (maximum,

minimum, or zero) beam shifts in TMDCs. Additionally, the thickness effect is also described by comparing the GH and IF shifts of monolayer samples with their multilayer counterpart.

In *Chapter* 4, we again applied this theoretical model, but this time, for another 2D material graphene. Here, we have explicitly described the significance of the chemical potential of graphene in controlling the GH and IF shift in graphene. The study also considers a wide range of wavelengths establishing the role of wavelength in governing the optical beam shifts in graphene.

Chapter 5 gives an overview of the different experimental techniques that are available till date for the experimental determination of GH and IF shift. In this *Chapter*, the difficulty associated with the measurement process is explained along with the advantages and disadvantages of different techniques. From this *Chapter*, one can get the overall idea of the present status of all the experimental techniques that are available and that can be effective in different scenarios.

In *Chapter* 6, we have described the development the 'Quantum Weak Measurement' (QWM) technique for the measurement of GH shift. A detailed explanation of the weak value amplification scheme and the step-by-step method to measure the GH shift is explained here. The study is focussed on the glass-air interface for which the GH shift only appears in the total internal reflection regime and a large GH shift is found at the critical angle which continuously decreases over increasing incident angle. A comparison with the theoretical model supports our experimental findings.

In *Chapter* 7, we explained the effective way of applying this QWM method in TMDCs for measuring GH shift. As an example, we have considered a monolayer MoS_2 sample. The angular dependence of the corresponding GH shift is explained. The critical angle gets shifted due to the presence of the MoS_2. The GH shift is also lesser for MoS_2 than the glass surface as well as graphene. This less amount of shift is closely connected to the increased absorbance of monolayer MoS_2. The GH shift monotonically decreases from the maximum in the vicinity of critical angle with increasing incident angle. A comparison with the theoretical model.

In *Chapter* 8, we have studied the necessary experimental modifications of the QWM technique incorporating the Jones matrices before applying it to measure the IF shift. Again, we have taken monolayer MoS_2 for this study and measured the IF shift in this sample. The IF shift shows a non-trivial signature that is consistent with the theoretical model. We observe lesser amount of IF shift for monolayer MoS_2 than the glass surface. There also exits non-zero

IF shifts even below the critical angle which is a significant observation. Finally, the technique we have proposed here is a very general one that can be applied to other layered structures and coatings.

In *Chapter* 9, we have described the development of another method of 'Stokes Polarimetry' that can be used for GH and IF shift measurement purposes. This technique is simpler but an indirect one that can produce results over a short time. In this Chapter, we have elaborated on the GH and IF shifts in monolayer MoS_2. A comparison with the glass surface, we find a lesser shift for monolayer MoS_2. The critical angle is also slightly shifted for the monolayer MoS_2. Non-zero angular shifts exist below the critical angle. The effect of strong absorbance of MoS_2 is also discussed.

In *Chapter* 10, we shifted our attention to a new phenomenon of the 'Photonic spin Hall effect' that has created a lot of interest of late. We have again modified the QWM technique to measure the spin Hall shift. In monolayer MoS_2, we have observed finite spin Hall shift but over a small range of incident angles due to experimental difficulties. In the prescribed range, we have found a special phenomenon of sign changing (zero crossing angle) of the spin Hall shift that has a close connection with the finite geometric phases of light. This investigation can be extended for the multilayer sample and also for other 2D structures over a wider range of incident angles to get a detailed picture of this phenomenon.

11.2 Scope of Future Work

There are a lot of unanswered questions that remain in this particular field of research. We have just moved to the first step and a vast amount is yet unexplored. In the following, we have summarized a few proposals that require immediate attention.

Throughout this thesis, we have used a fundamental Gaussian beam for our study be it experimental or theoretical. But, there are higher-order complex beams (Hermite-Gauss, Laguerre-Gauss, and Bessel, etc.) that can yield interesting results.

In this thesis, we have proved the influence of the polarization of light on GH and IF shifts. Right and left circular polarization are nothing but the spin states of the light. But, in addition to this spin angular momentum, light can also have orbital angular momentum due to its phase evolution. In all of our studies, we have set this orbital angular momentum to zero which is true for a commonly used fundamental Gaussian beam. But, in modern technology, higher-order orbital angular momentum of light is under intense research interest due to their

application in information-carrying purpose. Hence, the study of GH and IF shift for higher-order orbital angular momentum modes would be really interesting.

Finally, the present measurement techniques are applied for solid materials with great success. But, it will be very interesting to find out the nature of GH and IF shift in the liquid state. Thus, it is an open field to search for applicable techniques for the accurate measurement of optical beam shifts in the liquid phase.